5-29-2019 11:00 AM

Optimization of Window Confirguration in Buildings for Sustainable Thermal and Lighting Performance

Meseret Tesfay Kahsay, *The University of Western Ontario*

Supervisor: Bitsuamlak, Girma T., *The University of Western Ontario*
Co-Supervisor: Tariku, Fitsum, *British Columbia Institute of Technology*
A thesis submitted in partial fulfillment of the requirements for the Doctor of Philosophy degree in Civil and Environmental Engineering

Abstract

In recent years, there is an urban architectural evolution towards significant use of glazing in high-rise buildings. Windows play a critical role in moderating the elements of the climate. Although good for outdoor viewing and daylighting, glazing has very little ability to control heat flow and solar heat gain. As a result, about 20 - 40% of the energy in a building is wasted through windows. Finding an optimal configuration of windows is a complex task due to its conflicting objectives, such as outdoor view, daylighting, and thermal comfort demands. Further buildings interact with the microclimate in a complex manner, the aerodynamics of the building as well as the location and shape of the window affect its energy performance primarily through convective heat transfer coefficient (*CHTC*). Various methods have been proposed to calculate *CHTC* in literature, but with significant differences, which can cause errors in energy demand calculations in the order of 20 - 40%. Most *CHTC*s used by building energy simulations (BES) tools are primarily derived from the experimental and numerical analysis carried out on low-rise buildings with smooth façade surfaces and are not suitable for high-rise buildings with various intricate surface architectural details. This thesis aims to develop a new simulation-based optimization framework of window configuration in a high-rise building that meets the objective of minimizing energy consumption of heating, cooling, and electric lighting. This framework integrates high resolution computational fluid dynamics (CFD) and heat transfer simulations, BES, and numerical optimizer. In this thesis, the effect of different building heights, external architectural features, and window configuration on annual energy consumption are investigated. A new concept of local-*CHTC* zoning, a CFD based procedure for accurate $CHTC\text{-}U_{10}$ correlations evaluation, and an optimum window configuration procedure for high-rise buildings are presented. Overall, the research accomplished in this thesis provides an advancement in knowledge of accurate energy consumption analysis and optimization of window configuration in buildings, particularly in high-rise buildings using a passive strategy that can satisfy the objectives of minimum energy consumption and maximum comfort in a sustainable way.

Keywords

Convective Heat Transfer Coefficient, natural convection, downdraft, high-rise building, glazing, external shading, window configuration, CFD, turbulence, steady RANS, Building Energy Simulation, optimization, Genetic Algorithm.

Co-Authorship Statement

This thesis has been prepared in accordance with the regulation for an Integrated-Article format thesis prepared by the Western University Graduate and Postgraduate studies and has been co-authored as:

Chapter 2: Numerical analysis of convective heat transfer coefficient for building facades is published in the *Journal of Building Physics* under the co-authorship of Meseret T. Kahsay, Girma T. Bitsuamlak, and Fitsum Tariku.

Chapter 3: CFD simulation of external convective heat transfer coefficient on high-rise building with and without external shadings is accepted with revision in the *Journal of Building and Environment* under the co-authorship of Meseret T. Kahsay, Girma T. Bitsuamlak, and Fitsum Tariku.

Chapter 4: Effect of exterior convective heat transfer on high-rise building energy consumption is accepted with revision in the *Journal of Building Simulation* under the co-authorship of Meseret T. Kahsay, Girma T. Bitsuamlak, and Fitsum Tariku.

Chapter 5: Effect of window configuration on the convective heat transfer rate of a window with natural convective heater will be submitted for publication under the co-authorship of Meseret T. Kahsay, Girma T. Bitsuamlak, and Fitsum Tariku.

Chapter 6: Optimization of window configuration on high-rise building will be submitted for publication under the co-authorship of Meseret T. Kahsay, Girma T. Bitsuamlak, and Fitsum Tariku.

To my honored parents,

my lovely wife, Simret,

my beloved daughter, Heran.

To my supervisors, Dr. Girma T. Bitsuamlak and Dr. Fitsum Tariku

for their inspiration, encouragement, guidance, constant source of knowledge during these years of hard work study period.

Acknowledgments

Foremost, I would like to praise the Almighty God for the courage and patience that He dwells in me.

I would like to express my sincere gratitude to my supervisors Prof. Girma Bitsuamlak and Prof. Fitsum Tariku for their excellent guidance, motivation, unparalleled support, dedication, encouragement, and understanding during this Ph.D. study. Their guidance helped me in all time of the research and writing of this thesis. Further, I am also grateful for the chance given to me to attend different international conferences.

I was fortunate to be surrounded by wonderful people who helped me in different stages of this research. I would like to thank the team of Alan G. Davenport wind-engineering group and the faculty and staff in the Department of Civil and Environmental Engineering at Western University. I would like to acknowledge the financial support from the Ontario Center of Excellence (OCE) through the Early Career Award and the South Ontario Smart Computing Innovation Platform (SOSCIP) grants. Special thanks shall go to the SharcNet and Compute/Calcul Canada for providing access to their High-Performance Computation (HPC) facility and excellent support from their technical staff.

Special thanks to my research group colleagues (Tibebu, Anwar, Matiyas, Kimberley, Barilelo, Abiy, Tsinuel, Anant, Hang, Hadil, Matthew, Muna, Tewodros, Thomas, Ameyu) for the time we spent together sharing ideas and learning from each other. I also would like to thank to all my old friends in Ethiopia who shared with me the journey of this study.

Last but not least, I would like to thank my wife, Simret, whose help, support, and love invaluable to me during all stages of this Ph.D. study. I would like to thank my beloved daughter, Heran, for filling my life with great happiness. I also would like to thank all Ethiopian community in London, ON and especially to Mr. Taddele’s and Mr. Kiros’s family. In addition, special thanks shall go to my parents, brothers, and sisters for supporting me through my life.

Table of Contents

List of Tables

List of Figures

List of Appendices

Nomenclature

Abbreviations

ASHRAE	American Society of Heating, Refrigerating and Air-Conditioning Engineers
ABL	Atmospheric Boundary Layer
BES	Building energy simulation
BESTEST	Building Energy Simulation Test
CV	Control volume
CD	Computational domain
CFD	Computational Fluid Dynamics
CHTC	Convective Heat Transfer Coefficient
DoE-2	Department of Energy
epw	EnergyPlus weather data (-)
GHG	Greenhouse gas emission
GA	Genetic Algorithm
HVAC	Heating Ventilation and Air-Conditioning
idf	Input data file
imf	Input macro file
LES	Large Eddy Simulation
LRNM	Low Reynolds Numerical Model
MOO	Multi-objective optimization
MoWiTT	Movable Window Thermal Test
NSGA-II	Non-dominated Sorting Genetic Algorithm
RANS	Reynolds Average Navier Stoke
rvi	Read variable input (-)
SHARCNET	Shared Hierarchical Academic Research Computing Network
SST	Shear Stress Transport
SHGC	Solar heat gain coefficient
TARP	Thermal Analysis Research Program
TMY	Typical metrological year
WWR	Window-to-Wall Ratio

Latin symbols

Symbol	Unit	Description
C_p	KJ/Kg K	Fluid specific heat capacity
Gr	-	Grahof number
H	m	Building height
h_h	m	Heater height
h_w	m	Window height
lx	Lumens	Illuminance
K	W/mK	Thermal conductivity
$K.E$	m^2/s^2	Turbulent kinetic energy
Nu	-	Nusselt Number
Pr	-	Prandtl number
q_c	W/m^2	Heat flux
R	m^2K/W	Thermal resistance
Re	-	Reynolds Number
Ra	-	Rayleigh Number
T	K	Temperature
T_{ref}	K	Reference Temperature
$T\infty$	K	Free stream Temperature
T_{surf}	K	Surface temperature
T_{air}	K	Air temperature
ΔT	K	Change Temperature
T^+	-	Dimensionless temperature ($= (T_s - T_p)/(T_s - T_{ref})$)
U_{10}	m/s	Reference velocity at 10 m height
$U\infty$	m/s	Free stream velocity
u^*	m/s	Friction velocity
$\overline{u'u'}, \overline{v'v'}$	m^2/s^2	Reynolds normal stress components
$\overline{u_j'T'}$	K.m/s	Turbulent heat flux
$\overline{u'v'}$	m^2/s^2	Reynolds shear stress component
u_i	m/s	Instantaneous velocity

u_i'	m/s	Fluctuating velocity component
$\bar{u}_i$	m/s	Mean velocity
ϑ_t	m^2/s	Eddy-viscosity
K_T	m^2/s	Turbulent heat diffusivity
Pr_t	-	Turbulent Prandtl number
u_r	m/s	Downdraft velocity
y^+	-	Dimensionless wall distance ($=u^* y_p/\nu$)
z_0	m	The aerodynamic roughness length
z	m	For wind speed height above ground
Z_{g-met}	m	Boundary layer thickness at the meteorological station
z_{met}	m	Height above ground of the wind speed sensor

Greek symbols

Symbols	Unit	Description
θ	-	Dimensionless temperature
α_1	-	Wind speed profile exponent at the meteorological station
ρ	Kg/m^3	Density
ν	m^2/s	Kinematic viscosity
μ	Kg/m.s	Dynamic viscosity
ε	m^2/s^3	Turbulence dissipation rate
k	-	von Karman constant (~0.42)
ω	s^{-1}	Specific rate dissipation ($=K/\varepsilon$)
g	m/s^2	Gravity
β	$^0C^{-1}$	Volumetric thermal expansion coefficient
α	m^2/s	Thermal diffusion

Chapter 1

1 Introduction

1.1 Background

Buildings use about 40% of global energy and emit approximately 33% of GHG emissions (UNEP, 2017). In Canada, buildings use 29% of the total energy, out of this, residential building use 58.6% and commercial and institutional buildings use 41.4% (NRCan Energy facts, 2015) as illustrated in Figure 1-1. Realizing the significant amount of energy consumption in buildings, it is essential to investigate the accuracy of building energy consumption estimation and provide passive strategies to improve building energy efficiency in the long-term.

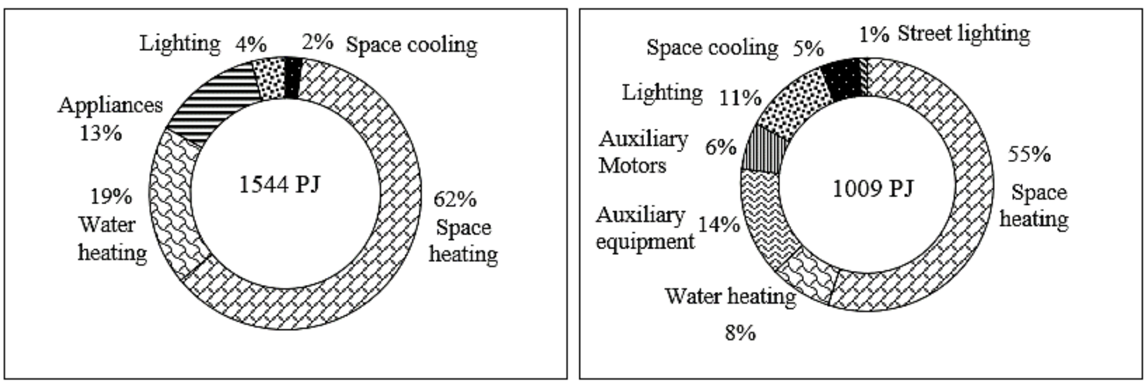

Figure 1-1: Energy use facts of Canada 2018 -2019; a) Residential appliances b) commercial and institutional (NRCan, 2018)

Building windows play a critical role in moderating the elements of the climate. Numerous studies have reported that design and selection of a proper window system is one of the most critical passive strategies for saving energy in buildings (Greenup, 2004; Tzempelikos, 2005; Ghisia et al., 2005; Bokel, 2007; Haglund, 2010; Ochoa, 2012; Straube, 2012). In recent years, there is an urban architectural evolution towards the use of glazing in high-rise buildings as illustrated in Figure 1- 2. Although good for outside view and lighting, glazing has very little ability to control heat flow and solar radiation. For example, the study by Straube (2012) has shown that the overall heat transfer coefficient

(U-factor) of windows usually is five times greater than other components of a building's façade, e.g., walls, doors, roof, etc. For a building having an opaque wall, the windows alone could be the most significant heat flow contributors. About 20% - 40% of the energy consumed in a building is wasted through windows (Lee et al., 2013). Accordingly, improving the windows climate performance should take priority over improving the opaque wall thermal resistance.

Figure 1-2: The façade of this condominium tower is covered with low thermal resistance and high solar gain curtain wall (Straube, 2012)

Therefore, to assess the impact of window configuration on the energy efficiency of buildings, the first research question that should be asked is that what makes a window energy efficient? The energy efficiency of a window is dependent on its: *thermal attributes* such as U-factor, Solar Heat Gain Coefficient (SHGC), glazing components; *daylighting attributes* such as visible transmittance; *size and location attribute* such as a size of the window, an aspect ratio of the window, its location on a wall, building orientation, etc.; and *other attributes* such as the purpose of the room. While some of these attributes work concurrently with each other, others contradict the benefit of the other. Thus, requiring an optimal design process under constraints.

A literature review covering various aspect related to convective heat transfer performance of building façade is provided in this introductory chapter. The review includes previously researched *CFD* based *CHTC* analysis, the impacts of the existing-*CHTC* accuracy on building energy performance, effects of glazing on building energy performance, and a general review on window to wall ratio configuration impact on thermal performance is provided. The research gaps, the thesis scope and organization are then outlined.

1.2 Literature review

1.2.1 Computational fluid dynamics and heat transfer simulation

In buildings, a large part of the energy consumption is caused by heat transfer from the external surface. This heat transfer consists of two parts: radiation and convection. The radiation heat loss is a function of surface temperature and emissivity while the convective heat loss is a function various parameter such as wind speed, wind direction, topography, flow pattern, building geometry, building architectural elements, and the temperature difference between indoor and outdoor. Figure 1-3 illustrates a convective heat transfer from hot surface to air by convection.

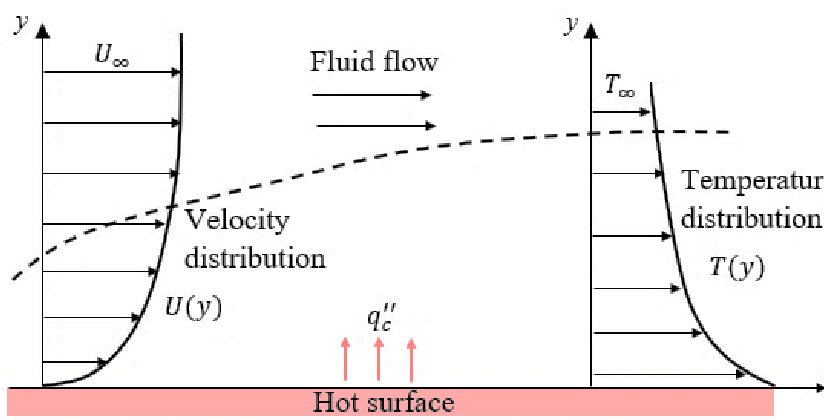

Figure 1-3: Convective heat transfer

The amount of heat transferred from a surface can be expressed using Newton's law of cooling as the amount of heat transferred from a unit area to the surrounding is due to the temperature difference between the surface and the bulk fluid flowing over it and a parameter *CHTC* that characterizes the flow behavior. Hence, the external convective heat transfer is defined as in Equation 1-1:

$$CHTC = \frac{q_c''}{(T_{sur} - T_{air})} \qquad \text{Equation 1-1}$$

where *CHTC* (W/m^2.K) is convective heat transfer coefficient, q_c is local surface heat flux (W/m^2), T_{sur} is surface temperature (K), and T_{air} is the reference air temperature (K).

The *CHTC* is dependent on conditions in the boundary layer. These include, but not limited to, nature of fluid motion, fluid thermodynamics and transportation properties, surface geometry, surface texture, surface orientation (windward & leeward in case of buildings), surface to air temperature difference (ΔT), wind speed, wind direction, and topography (Blocken et al., 2009; Defraeye et al., 2011; Mirsadeghi et al., 2013; Montazeri et al., 2015; Jubayer et al., 2016).

Since the 1930s, many methods have been proposed to calculate *CHTC*, but each method has had significant differences (Yazdanian and Klems, 1994; Palyvos, 2008; Mirsadeghi et al., 2013). Some of the existing methods for evaluating *CHTC* correlations includes wind-tunnel experiments (Meinders et al., 1998, 1999; Nakamura et al., 2001) and full-scale measurements on buildings facades (Sharples, 1984; Yazdanian and Klems, 1994; Loveday and Taki, 1996). However, the existing-*CHTC* correlations have limitations in considering all of those parameters stated above and their interaction with the complex microclimate parameters. Thus, the improper use of the existing correlations can easily cause errors in energy demand calculations in the order of 20 – 40% (Palyvos, 2008). For example, EnergyPlus, one of the widely used in building energy simulation (BES) programs, offers a wide selection of *CHTC* correlations based on low-rise buildings, flat plate, and vertical window (Palyvos, 2008; Defraeye et al., 2011). However, limited information is available for high-rise buildings and buildings with complex architectural detail.

In addition to the physical experiments, the physical interaction of air flow around the boundary layer can be modeled using Computational Fluid Dynamics (CFD) and Heat transfer numerical simulation. The numerical simulation has some advantages over physical experiments. It allows for simulating the actual size of the building with its complex architectural form, and therefore, it avoids the potential scaling effects related to the property of fluids. Also, numerical simulation allows for generating detailed information about the flow and temperature field in both time and space compared with experiments.

CFD is a computer-based mathematical modeling tool capable of dealing with the spatial and temporal distribution of velocity, temperature, and pressure by solving the conservative equation of the flow and energy transfer (Versteeg & Malalasekera, 2007). It has been used intensively as a tool for analyzing outdoor and indoor environment of buildings as well asits interaction with the building façade (Blocken et al., 2009; Jiru et al., 2010; Dagnew & Bitsuamlak, 2014; Jubayer et al., 2016). Numerous studies (Franke et al., 2007; Zhang et al., 2008; Dalal et al., 2009; Roeleveld et al., 2010; Peetersa et al., 2011; Kim, 2013; Younes & Shdid, 2013, Montazeri and Blocken, 2018) have investigated building interaction with the environment using CFD. As learned from the studies above-mentioned, CFD has been useful for building design and analyses where it has been applied with considerable success.

A steady-state Reynolds-Average Navier-Stoke (RANS) simulation is used in numerous numerical studies such as Franke et al. (2007); Blocken et al. (2009); Defraeye et al. (2011); Karava et al. (2012); which provide a time average flow field. Large eddy simulation (LES) undeniably provide more accurate and more reliable information about the flow field than the RANS approach; however, it requires substantially greater computing resources (Peng & Davidson, 2001; Ampofo & Karayiannis, 2003; Dagnew & Bitsuamlak, 2014; Blocken, 2018). In addition, in building heat transfers, most of the convective heat is transferred very near to the wall. Thus, to resolve the entire boundary layer, including the viscous sublayer and the buffer layer, which dominates the convective heat resistance, the fact that turbulent eddies are very small and resolving them with LES could be very computationally expensive.

Therefore, in this thesis, a RANS turbulence model will be used for to the building energy simulation (BES). Since the prediction accuracy of air flow and heat transfer in CFD depend on the accuracy of its boundary conditions, emphasis is given to defining realistic microenvironment and geometrical boundary conditions. In recent years, many studies have used CFD to predict *CHTC*-U_{10} correlations, such as Emmel et al. (2007); Blocken et al. (2009); Defraeye et al. (2010); however, the existing correlations are surface-averaged correlations and based on a generic building geometrical configuration of a 10 m cubical. An exception is a study by Montazeri et al. (2015, 2017, 2018), which used a narrow floor plan dimension of 10 m width, 20 m depth, and various height configurations ranging from 10 to 80 m, where a correlation of $CHTC/(U_{10}^{0.84})$ relatively insensitive to U_{10} for each building was developed by averaging the maximum and minimum values of the case study buildings. Although all of the above studies provide very useful insights on building convective heat transfer analysis, none of these studies discussed the local-*CHTC* variations, the effect of external shadings (see Figures 1-4 & 1-5) , the existing-*CHTC* correlations, and the local-*CHTC* distribution on building energy performance and window configurations.

Figure 1-4: A case study on high-rise buildings model a) without shading b) horizontal shading c) vertical shading and d) egg-crate shading

Therefore, these missing aspects will be investigated in this thesis by introducing a novel concept on analyzing of local-*CHTC* using zoning approach, new *CHTC*-U_{10} correlations for different building geometries, the impact of the existing-*CHTCs* on building energy consumption, and a framework for simulation-based optimization of window configuration in a high-rise building . To perform this investigation, an integration of CFD, BES, and an optimizer algorithm is applied using a simplified high-rise building geometry model.

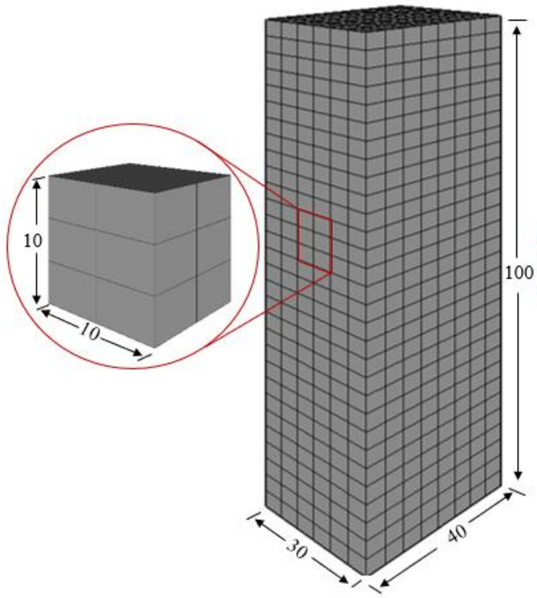

a) Without shading (smooth facade)

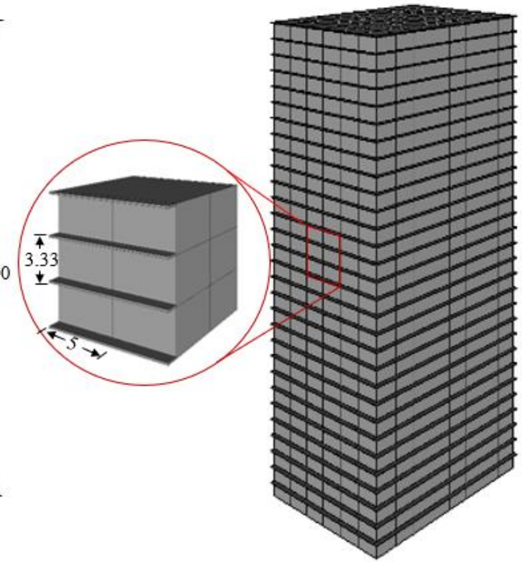

b) Horizontal shading

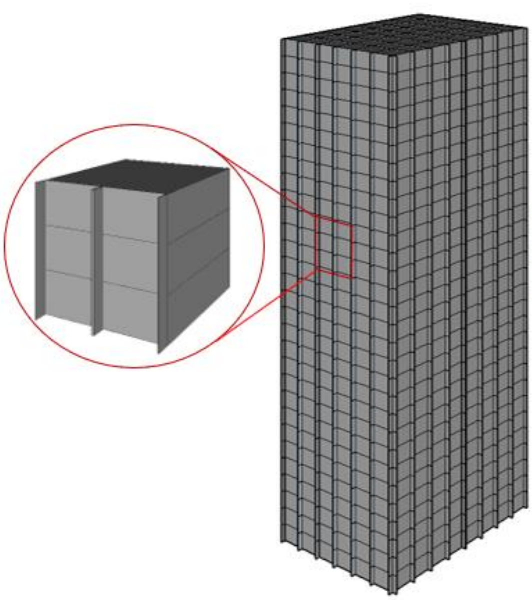

c) With vertical shading

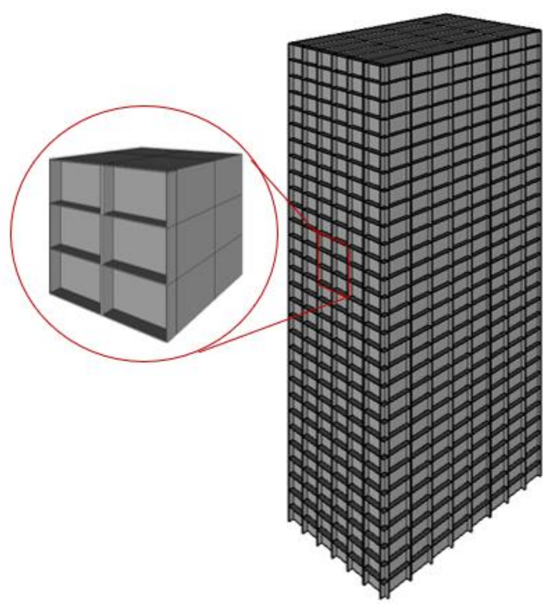

d) Egg-crate shading

Figure 1-5: Model of high-rise buildings a) without-shading – smooth façade, b) horizontal shading, c) vertical shading, and d) egg-crate shading

CFD analysis of the flow field around a bluff body with sharp edges have some limitations (Murakami, 1998). To mention some: difficulties related to high Reynolds number which requires fine grid resolution, the complex nature of the 3D flow field in the separation, reattachment, and vortex shading zones, and the numerical difficulties associated with flow at sharp corners and consequences for discretization schemes. The recent studies by Blocken (2015 and 2018) have indicated that RANS is by far the most often used, despite its deficiencies, in both research and engineering practices. However, to asses the accuracy and reliability of the CFD analysis, a validation through comparison with previous experimental work is done, and detail of the validation and verification of the CFD is covered as shown in Chapter 2 of this thesis.

1.2.2 Studies on the effect of existing-*CHTC* correlations on building energy consumption

To date, the *CHTC*s used by BES tools are primarily derived from experimental and numerical analysis carried out on a low-rise building with smooth façade surfaces (Palyvos, 2008; Defraeye et al., 2011; Mirsadeghi et al., 2013). However, the external shading elements, as well as the height of the building have a significant effect on the *CHTC*. Therefore, the application of the existing *CHTC*s for non-smooth facades and high-rise buildings may not be accurate. Within the building industry, there is an increasing concern about a mismatch between the predicted energy performance of a building and actual measured performance referred to as “the performance gap” (De Wilde, 2014). For instance, Menezes et al. (2012) have investigated the energy performance gap between the predicted versus actual energy performance of non-domestic buildings using post-occupancy evaluation data suggesting that the measured energy use can be as much as 2.5 times the predicted use. These are attributed to shortcomings of the current modeling programs, poor assumptions, poor construction quality, as well as lack of monitoring following construction. Bridging the gap between the predicted and measured performance is crucial for designers. Therefore, understanding the interaction of a building with the microclimate in detail is essential to evaluate the *CHTC*-U_{10} correlation and hence to model the energy consumption accurately. Further, the estimation of an accurate *CHTC* distribution on the surface of the façade is used in analyzing local effects on surface condensation, heating, cooling & moisture (HAM) transfer studies.

1.2.3 Studies on window configuration effect on building energy consumption

Previous studies of Greenup & Edmonds (2004); Tzempelikos (2005); Ghisia et al. (2005); Ochoa et al. (2012), Kahsay et al. (2017) have shown that design and selection of a proper window system is one of the essential passive strategies for saving energy in buildings. Thus, choosing a window system and its corresponding configuration is a fundamental decision in the early design stage, which is costly to be changed later. Due to this, ASHRAE standard 90.1 provides a guideline on the Window-to-Wall Ratio (WWR) stating that: *"the total vertical window area shall be less than 40% of the gross wall area".* While this is useful, this general guideline on the WWR does not provide any explicit way to evaluate whether a given WWR size will give satisfactory results regarding thermal and lighting performance for different window configurations having the same WWR. For example, consider the following four window configurations as shown in Figure 1-6 that have the same area of 20% WWR but with different configurations that lead to different thermal and lighting performance. Accordingly, it is vital for the guideline to accommodate for a question such as which of the four window configurations (see Figure 1-6) is more energy efficient and thermally comfortable.

Therefore, window configuration has to be optimized for more than one objective due to its influence on heating, cooling, and lighting performance. Hence, obtaining the optimum size of WWR and the configuration of a window for a generic room building that complies with the multi-objective is one of the main aims of this thesis, which is discussed in detail in Chapter 5 and 6 of this thesis.

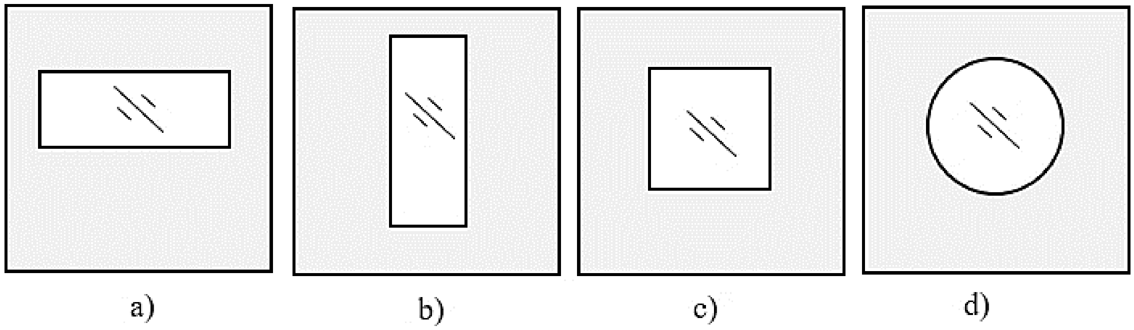

Figure 1-6: Model window configurations with 20% WWR that represent a) horizontal rectangular b) vertical rectangular c) square and d) circular

1.2.4 Studies on optimization of a window configuration

To investigate the effect of window configuration on building energy consumption, one of the most straight forward methods in assessing building energy consumption is by changing a design parameter while the other parameters are constant (Susorova, 2013). As building energy simulation programs are based on a scenario-by-scenario process, this procedure is often extremely time-consuming and may be infeasible in action. In this respect, coupling a proper optimization procedure with a building energy simulation tool makes it possible to analyze and optimize the characteristics and performance of buildings in the least time (Caldas & Norford, 2002; Rapone, 2012; Nguyen, 2014; Delgarm et al., 2016).

Therefore, due to the iterative nature of the procedure, simulation-based optimization tools will be used. *Simulation-based optimization* is a procedure that couples an optimization program to a simulation program whose function is to calculate a specific performance of a model. Today, simulation-based optimization has become an efficient measure to reach a cost-effective building design with reliable performance in a short time (Rapone, 2012; Nguyen, 2014). Therefore, in this thesis, a new approach of simulation-based optimization of window configuration in high-rise buildings by integrating CFD, BES, and an optimizer tool is developed.

In this thesis, an optimization of window configuration in high-rise buildings for sustainable thermal and lighting performance is carried out; where a detail investigation interaction of the microclimate with buildings and its effect on building energy performance is performed. The topic of optimization of window configuration in buildings is an active research areas in building physics and sustainable building design today due to the following reasons:

- Research conducted on this topic is limited; there is insufficient information about window configurations on high-rise buildings.
- High-rise buildings with glazed cladding or having large window-to-wall ratio are the most vulnerable to high heat losses and solar heat gains.
- The existing Convective Heat Transfer Coefficient (*CHTC*) correlations available in building energy simulations (BES) programs are derived from a low-rise building and the use of these correlations on high-rise building energy consumption analysis may not be accurate.
- The existing-*CHTC* correlations are based on smooth facades; it does not account for a building having external architectural features.
- Local-*CHTC* correlations can provide accurate energy consumption information than averaged surface correlations particularly, for buildings with glazed claddings.
- Window system is one of the most complex components of a building façade with conflicting objectives such as heating, cooling, and lighting demands and its architectural forms. Hence, it requires a simulation-based optimization analysis to optimize the configuration of the window that satisfies the objective functions.

1.3 Research gap

Thermal comfort and lighting performance inside a building is highly dependent on window configuration as the selection of optimal window configuration often involves many factors such as micro-climate condition, building location, orientation, height, and purpose of the room. However, windows are mainly configured based on their aesthetic value rather than their thermal comfort, due to this there is a lack of consistency with external convective heat transfer rate distribution on the façade of the building. Consequently, different studies have shown that 20% - 40% of the building's energy wasted through windows (Lee et al., 2013). Although ASHRAE standard (ASHRAE standard 90.1-2010) provides a general guideline on the WWR percentage; building height effect, airflow around a building effect, a shape of the buildings, and architectural details on the surface of the building are not considered in detail. Furthermore, this guideline does not provide any explicit way to evaluate the thermal and lighting performance of the window with respect to the orientation of the building. Moreover, it is also well understood that during window configuration conflict will arise in optimizing heating, cooling, and light performance simultaneously. Most often, as a small window size is preferred for reducing heat loss during winter and less solar heat gain during summer; in contrast a large window size is preferred for better views of the outside environment, solar heat gain during winter and daylighting. Both sizes may be preferred simultaneously by the occupants; however, the designer will be challenged to optimize these two sizes simultaneously without having any specific objective guidelines or tools.

In addition, the effect of wind on convective heat transfer rate of the building is not explored in detail. Aerodynamics around a building varies with the geometry. As a result, the external convective heat transfer rate also varies on the surface of the building due to this, the value of the external *CHTC* is unknown and determined by the empirical correlation of wind speed, building height, and shape. To this effect, many methods have been proposed to calculate *CHTC*, but each method has had significant differences (Yazdanian and Klems, 1994; Palyvos, 2008; Mirsadeghi et al., 2013). Thus, the improper use of these correlations can easily cause errors in energy demand calculations in the order of 20% – 40% (Palyvos, 2008). To date, the *CHTC*s used by building energy simulations (BES) tools are primarily derived from experimental and numerical analysis carried out on a low-rise building with smooth façade surfaces (Palyvos, 2008; Defraeye et al., 2011; Mirsadeghi et al., 2013). However, the external shading elements, as well as the height of the building have a significant effect on the *CHTC*. Therefore, the application of the existing *CHTC*s for non-smooth facades and high-rise buildings may not be accurate. Numerous studies have shown that within the building industry; there is an increasing concern about a mismatch between the predicted energy performance of a building and actual measured performance, typically addressed as “the performance gap” (De Wilde, 2014).

Therefore, understanding the convective heat transfer of a building in detail is essential to estimate the *CHTC* accurately, and it is currently one of the fundamental challenges in the analysis of building energy consumption. BES cannot configure the optimal position of a window. As a result, there is a lack of generalized approach to enable window configuration optimization with respect to energy consumption, thermal comfort, and lighting performance simultaneously. There is a limitation on the study of window configuration based on wind exposure and accurate external *CHTC* distribution on the surface of a building. There is a need to develop effective approach to assess the impacts of building geometry and its architectural features on the local-*CHTC* distribution and use this info to optimize window configurations of high-rise buildings. Therefore, the primary objective of the thesis is to develop a new framework for simulation-based optimization of window configuration in high-rise building under opposing constraints of energy and comfort (thermal and lighting), thus, contributing to the sustainable built-environment of the future. The technique involves CFD to develop the wind-driven $CHTC\text{-}U_{10}$ correlations, BES to analyze building energy consumption, and a numerical optimizer to optimize window configuration as illustrated in Figure 1-7. The detail of this approach and its applications are presented in this thesis in Chapter 6.

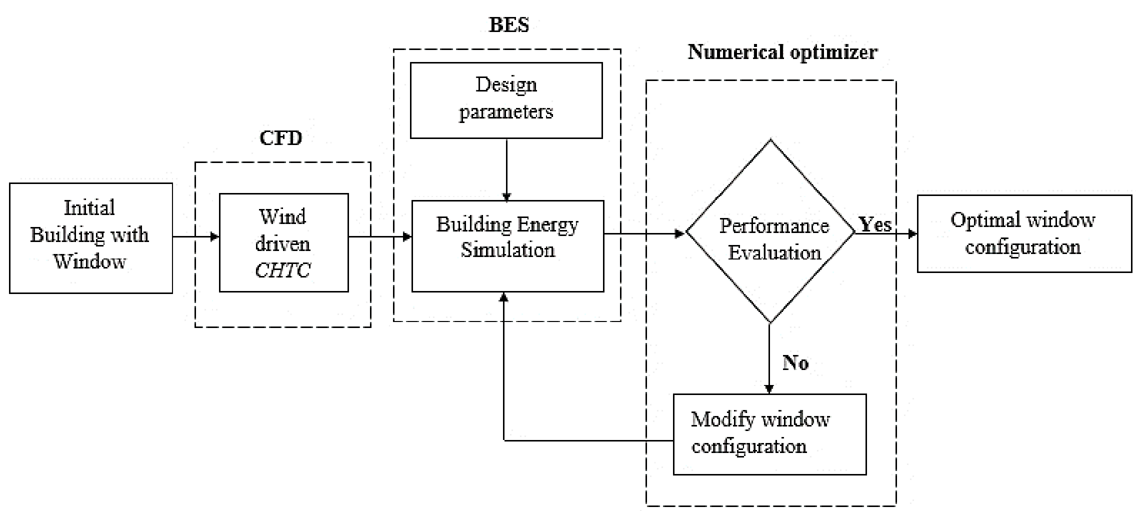

Figure 1-7: Flow chart of simulation-based window configuration optimization

1.4 Scope of the thesis

The thesis aims to address the research gaps mentioned in the above section. As such the objectives of the thesis are:

- To investigate the effect of building height on the external-*CHTC* distribution and develop *CHTC*-U_{10} correlations using validated numerical approaches.
- To develop a generalized approach for evaluating *CHTC* distribution using a local *CHTC*-zoning approach.
- To developing *CHTC*-U_{10} correlations for building with different forms of external shadings.
- To investigate the effect of different window configurations on the convective heat transfer rate of a window
- To investigate the impact of the existing-*CHTC* correlations on the accuracy of energy consumption assumptions.
- Developing a new framework for simulation-based optimization of window configuration in a high-rise building under opposing constraints of energy and comfort (thermal and lighting) and examining these procedures on high-rise building.

1.5 Organization of the thesis

This thesis has been prepared in an “Integrated-Article” format. In Chapter 1, a review of studies on the existing-CHTC development and the effect of window configuration on building energy consumption is provided. These objectives are addressed in detail in the following six chapters.

1.5.1 Numerical analysis of convective heat transfer coefficient for building façades

Chapter 2 discusses first on the numerical validation of a CFD with a previous experimental study of a small scale as a fundamental base for this study. Then based on the validated computational procedure and techniques, applied to full-scale of low- and high-rise buildings to investigate the impact of building on averaged-*CHTC* distribution. In this study, five buildings with heights of 10.1 m, 33.7 m, 50.6 m, 67.4 m, and 100 m, respectively, are used. A new local- and surface-averaged *CHTC* correlations are developed. Further, a new concept on local-*CHTC* zoning is introduced and the aerodynamics effects are discussed in detail.

1.5.2 CFD simulation of external convective heat transfer coefficient on high-rise building with and without external shading

In chapter 3, a comparison of local-*CHTC* distribution between buildings with and without shading elements for rooms located in different floor heights and in locations of the building is performed. Wind directionality and external shading effect on $CHTC\text{-}U_{10}$ distribution is investigated in detail. Thus, new $CHTC\text{-}U_{10}$ correlations are developed for different external shading forms and depths.

1.5.3 Effect of exterior convective heat transfer coefficient on high-rise-building energy consumption

Chapter 4, the impact of the existing-*CHTC* on energy consumption of a high-rise building is investigated. In this study, a high-rise building which is located in different climate conditions is considered as a case study. First, a new-*CHTC* correlation is developed that considered wind speed and building height using a CFD. Then the existing- and new-*CHTC* correlations are compared using the EnergyPlus building energy simulation program to illustrate the wind impact on the building energy consumption.

1.5.4 Effect of window configuration on the convective heat transfer rate of a window with a natural convective heater

Chapter 5, the effect of different window configuration on the convective heat transfer rate of a window with natural a convective heater is numerically investigated. In this study, initially, a CFD validation with an experimental study is carried out. Then, a downdraft velocity and convective heat transfer rate of a window are computed for different full-scale windows configurations are performed.

1.5.5 Optimization of window configuration on high-rise building

Chapter 6 discusses the utilization of simulation-based optimization of optimal window configuration in high-rise buildings. The techniques involved in this study are CFD, BES, and a numerical optimizer for optimal window configuration. The optimization process aims to reduce both heating and cooling energy demands and maximize daylight entrance to the room.

1.6 References

ASHRAE, A. (2011). ASHRAE/USGBC/IES standard 189.1-2014, standard for the design of high-performance green buildings. *American Society of Heating, Refrigerating and Air-Conditioning Engineers, Inc., Atlanta, GA*.

ASHRAE. (2009). Fundamentals, SI ed. *American Society of Heating, Refrigerating and Air Conditioning Engineers: Atlanta, GA, USA*.

Book, E. F. (2018). *Book 2018–2019*. Tech. Rep., Natural Resources Canada. Available at: (https://www.nrcan.gc.ca/energy-facts), 2018 (accessed 03.03. 19)

Blocken, B. (2018). LES over RANS in building simulation for outdoor and indoor applications: a foregone conclusion? In *Building Simulation* (pp. 1-50). Tsinghua University Press.

Blocken, B. (2015). Computational Fluid Dynamics for urban physics: Importance, scales, possibilities, limitations and ten tips and tricks towards accurate and reliable simulations. *Building and Environment*, *91*, 219-245.

Blocken, B., Defraeye, T., Derome, D., & Carmeliet, J. (2009). High-resolution CFD simulations for forced convective heat transfer coefficients at the facade of a low-rise building. *Building and Environment*, *44*(12), 2396-2412.

Bokel, R. (2007). The effect of fenestration position and fenestration size on the energy demand for heating, cooling and electric lighting. Proceedings: *Building Simulation*, 117-121.

Caldas, L. G., & Norford, L. K. (2002). A design optimization tool based on a genetic algorithm. *Automation in construction*, *11*(2), 173-184.

Dagnew, A. K., & Bitsuamlak, G. T. (2014). “Computational evaluation of wind loads on a standard tall building using LES. *Wind and Structures*, *18*(5), 567-598.

Delgarm, N., Sajadi, B., Delgarm, S., & Kowsary, F. (2016). A novel approach for the simulation-based optimization of the building’s energy consumption using NSGA-II: Case study in Iran. *Energy and Buildings*, *127*, 552-560.

Defraeye, T., Blocken, B., Carmeliet, J., (2011). Convective heat transfer coefficients for exterior building surfaces: Existing correlations and CFD modeling. Energy Conversion and Management, 52(1), pp.512-522.

Defraeye, T., Blocken, B., Carmeliet, J. (2010). “CFD analysis of convective heat transfer at the surfaces of a cube immersed in a turbulent boundary layer.” Int. J Heat Mass Transf; 53:297–308.

De Wilde, P. (2014). The gap between predicted and measured energy performance of buildings: A framework for investigation. *Automation in Construction*, *41*, 40-49.

Emmel, M.G., Abadie, M.O., Mendes, N. (2007). “New external convective heat transfer coefficient correlations for isolated low-rise buildings.” Energy Build; 39:335–42.

Greenup, P. J., & Edmonds, I. R. (2004). Test room measurements and computer simulations of the micro-light guiding shade daylight redirecting device. *Solar Energy*, *76*(1), 99-109.

Ghisi, E., & Tinker, J. A. (2005). An ideal window area concept for energy efficient integration of daylight and artificial light in buildings. *Building and environment*, *40*(1), 51-61.

Greenup, P. J., & Edmonds, I. R. (2004). Test room measurements and computer simulations of the micro-light guiding shade daylight redirecting device. *Solar Energy*, *76*(1), 99-109.

Haglund, K. L. (2010). Decision-making methodology & selection tools for high-performance window systems in US climates. In *BEST2 Conference, Portland*.

Jubayer, C. M., Siddiqui, K., & Hangan, H. (2016). CFD analysis of convective heat transfer from ground mounted solar panels. *Solar Energy*, *133*, 556-566.

Kahsay, M., Bitsuamlak, G., & Tariku, F., (2017). Numerical study of the effect of window configuration on the convective heat transfer rate of a window. 15th Canadian Conference on Building Science and Technology.

Kahsay, M. T., Bitsuamlak, G., & Tariku, F. (2018). Numerical analysis of convective heat transfer coefficient for building facades. *Journal of Building Physics*,

Karava, P., Jubayer, C. M., Savory, E., Li, S. (2012). "Effect of incident flow conditions on convective heat transfer from the inclined windward roof of a low-rise building with application to photovoltaic-thermal systems." Journal of Wind Engineering and Industrial Aerodynamics, 104, 428-438.

Loveday, D.L., Taki, A.H. (1996). "Convective heat transfer coefficients at a plane surface on a full-scale building facade. Int. J Heat Mass Transf; 39:1729 – 42.

Liu, J., Srebric, J., Yu, N. (2013). "Numerical simulation of convective heat transfer coefficients at the external surfaces of building arrays immersed in a turbulent boundary layer." Int. J. Heat Mass Transf; 61:209 25.

Lee, J. W., Jung, H. J., Park, J. Y., Lee, J. B., & Yoon, Y. (2013). Optimization of building window system in Asian regions by analyzing solar heat gain and daylighting elements. *Renewable energy*, *50*, 522-531.

Meinders, E.R., Hanjalic, K., Martinuzzi R.J. (1999). "Experimental study of the local convection heat transfers from a wall mounted cube in turbulent channel flow." Trans ASME J Heat Transf. 121:564–73.

Meinders, E.R. (1998). "Experimental study of heat transfer in turbulent flows over wall mounted cubes." PhD thesis. Technische Universiteit Delft.

Menezes, A. C., Cripps, A., Bouchlaghem, D., & Buswell, R. (2012). Predicted vs. actual energy performance of non-domestic buildings: Using post-occupancy evaluation data to reduce the performance gap. *Applied Energy*, *97*, 355-364.

Mirsadeghi, M., Cóstola, D., Blocken, B., & Hensen, J. L. M. (2013). Review of external convective heat transfer coefficient models in building energy simulation programs: implementation and uncertainty. *Applied Thermal Engineering*, *56*(1), 134-151.

Montazeri, H., Blocken, B., Derome, D., Carmeliet, J., Hensen, J. L. M. (2015). "CFD analysis of forced convective heat transfer coefficients at windward building facades:influence of building geometry." Journal of Wind Engineering and Industrial Aerodynamics, 146, 102-116.

Montazeri H., Blocken B. New generalized correlations for forced convective heat transfer coefficients at building facades and roofs. Building and Environment 119 (2017) 153-168.

Montazeri, H., & Blocken, B. (2018). Extension of generalized forced convective heat transfer coefficient correlations for isolated buildings taking into account oblique wind directions. *Building and Environment*, *140*, 194-208.

Murakami, S. (1998). Overview of turbulence models applied in CWE–1997. *Journal of Wind Engineering and Industrial Aerodynamics*, *74*, 1-24.

Nakamura, H., Igarashi, T., Tsutsui, T. (2001). "Local heat transfer around a wall- mounted cube in the turbulent boundary layer." Int J Heat Mass Transf.; 44:3385– 95.

NRCan Energy facts, (2015) (https://www.nrcan.gc.ca/energy-facts) accessed March 2019.

Nguyen, A. T., Reiter, S., & Rigo, P. (2014). A review on simulation-based optimization methods applied to building performance analysis. *Applied Energy*, *113*, 1043-1058.

Ochoa, C. E., Aries, M. B., van Loenen, E. J., & Hensen, J. L. (2012). Considerations on design optimization criteria for windows providing low energy consumption and high visual comfort. *Applied Energy*, *95*, 238-245.

Palyvos, J.A. (2008). "A survey of wind convection coefficient correlations for building envelope energy systems modeling." Appl. Therm. Eng., 28, 801–808.

Rapone, G. (2012). Optimisation of office building facades by means of genetic algorithms.

Straube, J. (2012). "High performance Enclosure: design guide for institutional, commercial and industrial buildings in cold climate." Building Science press, 2nd edition, ISBN: 978-0- 9837953-9

Sharples, S. (1984). "Full-scale measurements of convective energy losses from exterior building surfaces." Build Environ; 19:31–9.

Susorova, I., Tabibzadeh, M., Rahman, A., Clack, H. L., & Elnimeiri, M. (2013). *Energy and Buildings*, *57*, 6-13.

Standard, A. S. H. R. A. E. (2010). 90.1 2007.―Energy Standard for Buildings Except Low-Rise Residential Buildings. *American Society of Heating, Refrigerating and Air-Conditioning Engineers, Inc*.

Tzempelikos, A. (2005). *A methodology for integrated daylighting and thermal analysis of buildings* (Doctoral dissertation, Concordia University).

United Nations Environment Program. (2017). https://www.unenvironment.org/explore-topics/resource-efficiency/what-we-do/cities/sustainable-buildings (March 2019).

Yazdanian, M., Klems, J.H. (1994). "Measurement of the exterior convective film coefficient for windows in low-rise buildings." ASHRAE Trans; 100(1): 1087–96.

Yazdanian, M., Klems, J.H. (1994). "Measurement of the exterior convective film coefficient for windows in low-rise buildings." ASHRAE Trans; 100(1): 1087–96.

Chapter 2

2 Numerical analysis of convective heat transfer coefficient for building facades

2.1 Introduction

Modern architecture utilizes significant glazing in buildings. Although glazing is good for viewing, daylighting, and other solar design features, it poorly controls heat flow. Quantifying the heat exchange between the building surface and the external environment requires a detailed understanding of the external convective heat transfer coefficient (*CHTC*) distribution. The convective heat transfer is governed by Newton's law of cooling as shown Equation 2-1:

$$q_s'' = h(T_s - T_{ref}) \qquad \text{Equation 2-1}$$

where q_s'' is the local surface heat flux (W/m^2), h is the local convective heat transfer coefficient (W/m^2 K), T_s is the surface temperature (K), and T_{ref} is a characteristic temperature of the fluid moving over the surface (K). However, this linear relationship is only an approximation. The flow condition can vary from one point to another on the surface and both q_s'' and h can vary as a function of time. *CHTC* cannot be defined without defining a T_{ref}. Therefore, there are an infinite number of *CHTC* and T_{ref} combinations that give rise to the same surface heat flux.

Accurate *CHTC*s evaluations are particularly important for the thermal analysis of critical building enclosure components such as glazed curtain walls, fenestration configuration, and double-skin facades. Previous studies (Palyvos, 2008; Defraeye et al., 2011; Mirsadeghi et al., 2013, Kahsay et al., 2017) on the exterior surface *CHTC* computation indicated that their inappropriate use can result in 20% - 40% errors in the building energy consumption. Numerous studies have also shown that *CHTC* on building facades is dependent on the simultaneous interactions of the wide range of parameters. These include, but not limited to, building geometry, surface slope angle, surface texture, surface orientation (windward & leeward), surface to air temperature difference (ΔT), wind speed, wind direction, sheltering by nearby buildings, and topography (Blocken et al., 2009; Defraeye et al., 2011; Mirsadeghi et al., 2013; Montazeri, et al., 2015).

Table 2-1: *CHTC-U*$_{10}$ correlations derived from wind-tunnel experiments on bluff body for windward façade for flow approaching at 0° incident angle

Authors name	Approach flow	Reference speed	Reynolds number range	Correlations
Meinders et al. (1999)	Developing turbulent channel flow	Bulk velocity	2.7×10^3 - 4.9×10^3	$Nu = aRe^{0.65}$
Nakamura et al. (2001)	Turbulent, BL thickness 1.5 -1.83 of cube height	Free stream velocity	4.2×10^3 - 33×10^3	$Nu = 0.71Re^{0.52}$
Chyu and Natarajan (1991)	Turbulent BL thickness of ± ¼ height of the cube	Free stream velocity	3.1×10^4 - 11×10^4	$Sh=0.868Re^{0.53}$
Wang and Chiou (2006)	Fully-developed channel flow	Maximum velocity at the inlet	8.0×10^2 - 5.0×10^3	$Sh=0.961Re^{0.52}$

Sh: Sherwood number, *a*: correlation coefficient for wind speed and direction, the *CHTC* can be derived from heat transfer and mass transfer analog

Existing methods for evaluating *CHTC* correlations include wind-tunnel experiments (Meinders et al., 1998, 1999; Nakamura et al., 2001), full-scale measurements on buildings facades (Sharples, 1984; Yazdanian and Klems, 1994; Loveday and Taki, 1996), and numerical simulations (Emmel et al., 2007; Blocken et al., 2009; Defraeye et al., 2010; Karava et al., 2012; Liu et al., 2013; Montazeri et al., 2015).

In the wind tunnel studies, wide range of flow parameters have been used. Table 2-1 summarizes relevant correlation parameters related to windward, vertical, and smooth surfaces used in these studies. More comprehensive review of these correlations can be found in studies by Palyvos (2008) and Mirsadeghi et al. (2013). Most of these experiments were not performed in the context of building aerodynamics immersed in the atmospheric boundary layer. They were rather carried out for thin turbulent boundary layers compared to the body height and at relatively low *Reynolds numbers* (e.g. $Re = 10^2\text{-}10^4$). Therefore, these flow characteristics may not directly represent the atmospheric boundary layer flow around buildings (Defraeye et al., 2010). In reality, the flow structure around buildings is more complex (Holmes, 2015). In addition, the existing wind-tunnel studies do not consider the variations of the *CHTC* correlation over the surface.

Full-scale experiments in literature are summarized in Tabel 2-2. In these full-scale experiments, *CHTC* were correlated to wind speed at different reference locations. Linear and power-law correlations were developed shown in Table 2-2 for relevant full-scale experiments. The reported results are not holistic as the spatial resolution, building geometry configurations, control on boundary conditions, and the experimental setups are usually case-specific (Mirsadeghi et al., 2013). However, they are very valuable for benchmarking numerical and model-scale experiments, as these full-scale experiments provide realistic *CHTC* data for exterior building surfaces.

On the numerical side, Computational Fluid Dynamics (CFD) and heat transfer-based simulations to predict $CHTC\text{-}U_{10}$ correlations have been used, as summarized in Table 2-3. These studies consider the influence of wind speed (Emmel et al., 2007; Blocken et al., 2009; Defraeye et al., 2010; Karava et al., 2012; Liu et al., 2013), wind direction (Blocken et al., 2009) and building geometry (Montazeri et al., 2015). The existing correlations, summarized in Table 2-3, are developed primarily for a generic geometrical configuration, for example, a 10 m cube. An exception is the study by Montazeri et al. (2015), which used a narrow floor plan dimension of 10 m width, 20 m depth, and various height configurations ranging from 10 to 80 m. However, it is reasonable to conclude that the existing correlations do not account for variations in building surrounding, building type, building geometry, and topography (Mirsadeghi et al. 2013).

Table 2-2: *CHTC*-U correlation derived from full-scale measurements on building facade for windward for flow approaching at 0° incident angle.

Author name	Building geometry	Wind speed Range (m/s)	Wind speed measurement location	Correlation
ASHRAE task group (1975) (incorporating results of Ito et al., 1972)	Open L-shaped building, 18 m high	0.5 - 3.5	0.3 m from the facade	$h_c = 18.6U_s^{0.605}$ $U_s = 0.25U_{10}$ For $U_{10} > 2\ m/s$
Sharples (1989)	Center of the 18th floor (20 x 36 x 78) m	0.5 - 20	1 m from the facade	$h_c = 1.4U_{10} + 6.5$
MoWiTT[a] (Yazdanian and Klems, 1994)	Low rise building	0 - 12	*U_{10}*	$h_c = \sqrt{\left(0.84\Delta T^{\frac{1}{3}}\right)^2 + (2.38U_{10}^{0.89})^2}$
Loveday and Taki (1996)	L-shape building (21 x 9 x28) m	0.5 - 9	1 m from the facade	$h_c = 16.15U_s^{0.397}$
Liu and Harris (2007)	Low rise building (8.5 x 8.5 x 5.6) m	*U_{10}*	0-16	$h_c = 1.53U_{10} + 1.43$
Zhang et al. (2004)	Low rise building (3 x 3 x 3) m	0.5 m from facade	0- 0.35	$h_c = 6.31U_{loc} + 3.32$

U_s: local wind speed near the façade, [a] MoWiTT (Mobile Window Thermal Test)

In the present study, the influence of building geometry on the *CHTC*-U_{10} correlations is examined. Full-scale, 3D steady RANS simulations are carried out to evaluate surface-averaged *CHTC*s. Five different building heights, 10.1 m, 33.7 m, 50.6 m, 67.4 m, and 101.1 m respectively with a rectangular floor plan dimension of 30 m x 42 m have been investigated. Furthermore, for the 101.1 m high building, a spatial distribution of *CHTC* over the entire windward façade is investigated by dividing the building height into ten cubical floor zones, which highlights the necessity of zonal treatments of *CHTC* for tall buildings. The current studies are carried for five different wind directions, namely 0°, 22.5°, 45°, 67.5°, and 90° wind angles of attacks, respectively.

Table 2-3: *CHTC*-U correlations derived from CFD simulation on bluff body for windward facade for flow approaching at 0° incident angle

Author name	Building Geometry H x W x D (m)	Near wall region modeling	U_{10} range (m/s)	*CHTC*-U_{10} correlation for windward
Emmel et al. (2007)	2.7 x 6 x 8	Wall function	1.0 -15.0	$h_c = 5.15U_{10}^{0.81}$
Blocken et al. (2009)	10 x 10 x 10	Low-*Reynolds Number* Modeling	1.0 - 4.0	$h_c = 4.60U_{10}^{0.89}$
Defraeye et al. (2009)	10 x 10 x 10	Low-*Reynolds Number* Modeling	0.5 – 5.0	$h_c = 5.01U_{10}^{0.85}$
Defraeye et al. (2010)	10 x 10 x 10	Low-*Reynolds Number* Modeling	0.15 - 7.5	$h_c = 5.15U_{10}^{0.82}$
Montazeri et al. (2015)	H = 10 - 80 W = 10 D = 20	Low-*Reynolds Number* Modeling	1.0 - 5.0	$h_c = aU_{10}^{0.84}$

a: correlations coefficients for windward

This chapter is organized as follows: In section 1 (this section), an introduction to the previous *CHTC* correlations development studies is presented. Section 2 describes the CFD validation process of surface temperatures prediction in comparison with an experimental study from literature. Section 3 describes the new CFD based evaluation of *CHTC* for low- and high-rise buildings and finally, and Section 4 concludes the chapter.

2.2 CFD validation

2.2.1 Experimental data description

Experimental data by Meinders et al. (1999) for a cube placed in a turbulent channel flow is used to validate the present numerical model (see Figure 2-1). The salient features of the experiment are provided in Figure 2-4. The physical properties used in the simulations are presented in Table 2-4. Details of experimental set-up can be found Meinders et al. (1999). It is to be noted that ideally the validation data would have been a boundary layer flow, however the current choice is due to the lack of available high-resolution boundary layer wind-tunnel *CHTC* data at high *Reynolds numbers* for building applications.

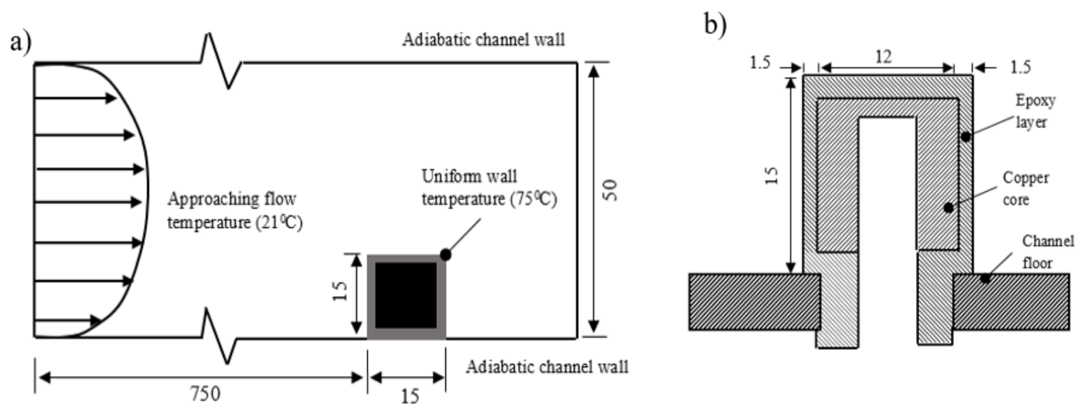

Figure 2-1: Experimental setup of Meinders et al. (1999): (a) general setup (b) detail of the heated cube. All dimensions are in mm (figure not to scale)

Table 2-4: Physical property of Air and Epoxy

Physical Properties	Air	Epoxy
Density (kg/m^3)	1.225	1191
Specific heat capacity (J/KgK)	1006.4	1650
Thermal conductivity (W/mK)	0.0242	0.237
Dynamic viscosity (Kg/ms)	1.7894 x 10^{-5}	-

2.2.2 Numerical model for validation

A computational domain (CD) that mimics the experimental setup is employed based on the recommendation of Franke et al. (2007); Tominaga et al. (2008); Dagnew and Bitsuamlak (2013). However, it deviates from these recommendations for height of the CD adopted, which is set as 3.3*H* to replicate the experimental channel (see Figure 2-2) where *H* represent the height of the cube. Other dimensions of the CD follow the recommendations, where an upstream length of 5*H* and a downstream length of 15*H* and side distance of 5*H* from the cube are adopted. Two simulations are conducted; the first one consists of an empty CD later used to produce inflow condition to the main CD. The second one is the main CD that consists of the study cube.

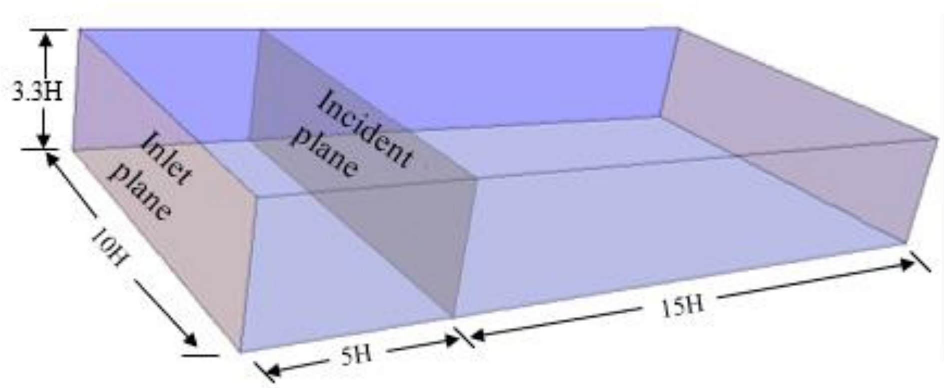

Figure 2-2: Empty CD for velocity and turbulence intensity extraction at the inlet and incident planes

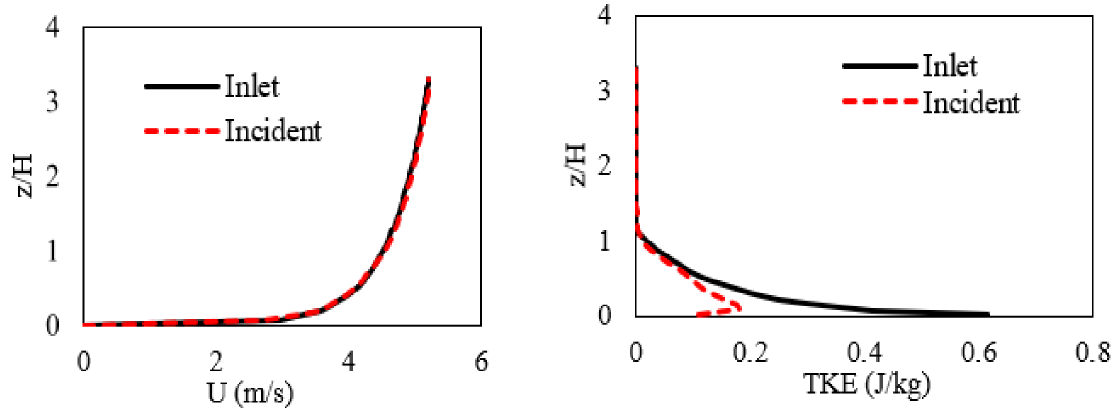

Figure 2-3: a) Vertical inlet velocity mean wind profile, b) vertical profile of turbulent kinetic energy *k* for measured (inlet) and modeled (incident)

For the empty domain simulation with smooth ground surface, inflow and turbulence intensity profiles at inlet are extracted from Meinders et al. (1999) experimental data at *Reynolds number* of 4440. Similarly, the velocity and turbulence intensity profiles have been extracted and stored for later use as inlet boundary conditions by the main CD (see Figure 2-3). These profiles fit into a log-law with aerodynamic roughness length $z_0 = 6.6 \times 10^{-6}$ m and a friction velocity $u* = 0.25$ m/s. A uniform temperature of 348 K was specified in the copper core of the cube. Using conjugative heat transfer, an interface between solid and fluid has been applied. The exterior cube surfaces are specified as no-slip boundaries with zero roughness. For the ground boundary of the domain, no-slip boundary conditions and adiabatic surface are assumed. Zero static pressure at the outlet and symmetry boundary conditions at the top and sides of the CD are specified. In addition, the bulk velocity, $U_{bulk} = 4.47$ m/s, and uniform temperature, $T = 283$ K are specified at the domain inlet. The simulations are conducted using a commercial CFD package (STAR-CCM+ v.10.12, 2015) and the SHARCNET (www.sharcnet.ca, 2015) high-performance computing (HPC) facility at Western University.

The local *CHTC* at each node ($CHTC_{node}$) is calculated using the standard wall function as shown in Equation 2-2:

$$CHTC_{node} = \frac{\rho(y_p)C_p(y_p)u_*}{T^+\left(y^+(y_p)\right)} \quad \text{Equation 2-2}$$

where ρ is the fluid density, C_p is the fluid-specific heat capacity, u_* is a velocity scale that is based on the wall shear stress, $T^+ = (T_s - T_p)/(T_s - T_{ref})$ is the dimensionless temperature, $y^+ = u_* y_p/v$ is a dimensionless wall distance, y_p and T_p are the normal distance and temperature of the near-wall cell, respectively, and v is the kinematic viscosity.

The standard wall functions are a set of semi-empirical functions that are used to satisfy the flow physics in the near-wall region where the relationships for T^+ and u_* is given in terms of the laminar and turbulent *Prandtl* numbers, the dimensionless near-wall flow velocity, and the turbulent kinetic energy. However, in this chapter, all internal convective heat transfer coefficient (*CHTC*) values are determined based on the upstream T_{ref}, which is unaffected by the presence of the building. . Therefore, to perform post-processing for the target surface building using user defined T_{ref}, Equation 2-3 will be used.

$$CHTC_{user} = CHTC\,\frac{(T_s - T_p)}{(T_s - T_{ref})} \quad \text{Equation 2-3}$$

where *CHTC* is defined based on the approach-flow temperature T_{ref}, and $CHTC_{node}$, T_p, and T_s is determined from the CFD simulation near the wall.

2.2.3 Comparison of CFD with experimental results

For validation, computationally evaluated surface temperature along a mid-plane vertical centerline and a mid-height horizontal line is compared with experimental results (see Figure 2-4). The temperature distribution on the surface of the cube is analyzed by resolving the entire boundary layer, including the viscous sublayer and the buffer layer, which dominate the convective heat resistance. In this simulation, a minimum grid distance of 130 μm from the cube surface has been employed to achieve the required $y+$ to capture important details of the temperature gradients and flow structures near the walls. The comparison of the simulated temperature distribution value at the windward surface of the leading cube with the experimental data is shown in Figure 2-4. Both two-equation models i.e. *SST k-ω* model and Realizable *k-ε* model combined with the one-equation Wolfshtein model perform well at the windward surface. The average difference between experimental data and results obtained with the *SST k-ω* turbulence model in the windward is approximately on average less than 3% deviation, whereas the Realizable *k-ε* model with an average deviation of up to 5% is found.

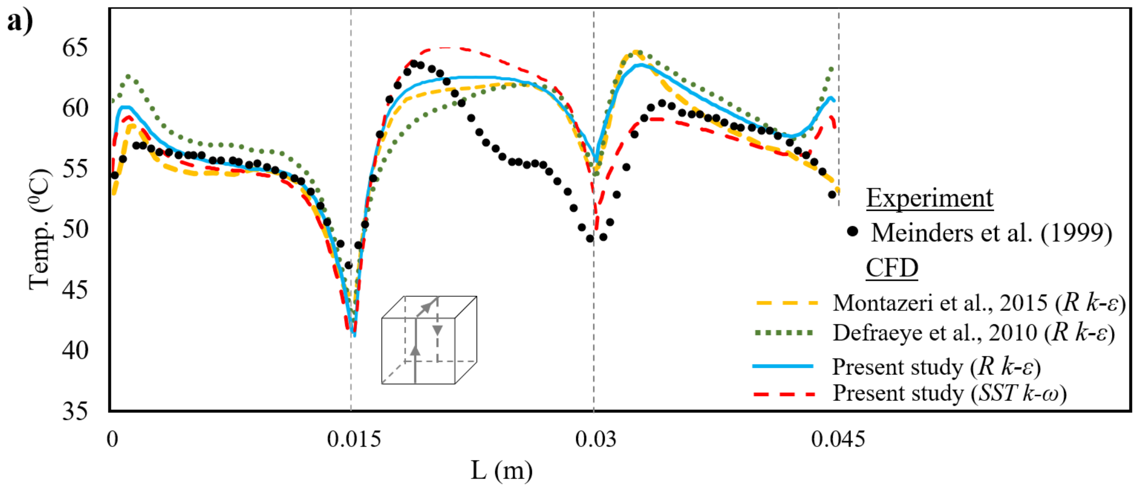

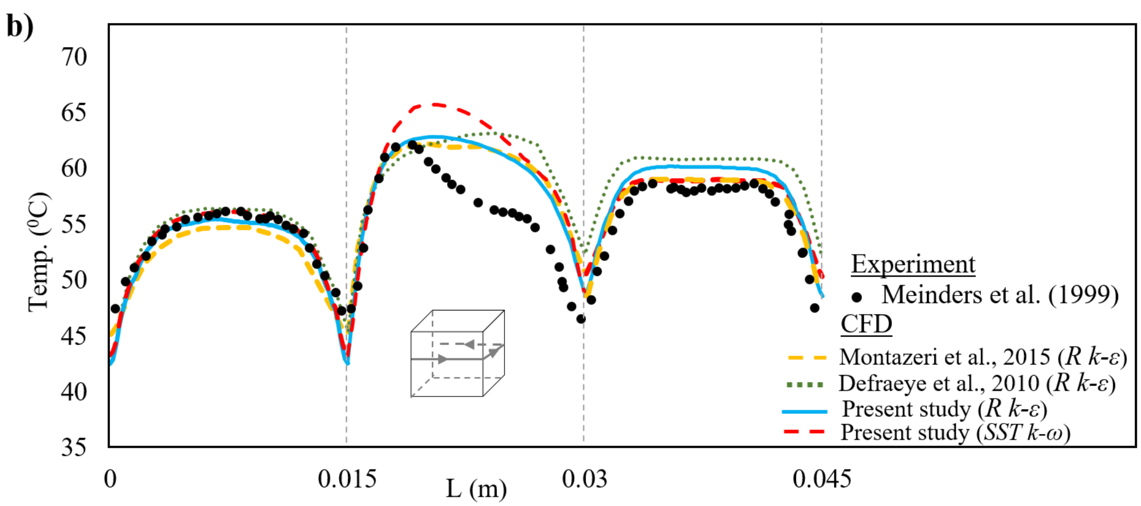

Figure 2-4: Comparison of experimental measured and simulated temperature distribution on the surfaces of the cube in a vertical (a) and horizontal (b) center plane

The worst agreement with the experimental data shows an overestimation for local temperatures of more than 10% at the top and lateral surface of the cube. This discrepancy could be attributed to the inaccurate predictions of flow field in the separation and reattachment zones of the top and sidewalls resulting in larger temperature values predictions. This has also been pointed out by Blocken et al. (2009) and Defraeye et al. (2010). For the leeward surface, the distribution of the predicted surface temperatures by the *SST k-ω* model agrees on average about 5% deviation with the experimental results, especially for the mid plane, whereas the realizable *k-ε* models overestimated by more than 15%. Therefore, the *SST k-ω* turbulence model will be used in the full-scale computational study.

2.3 CFD based evaluation of *CHTC* for low- and high- rise buildings

2.3.1 Computational domain

The size of the 3-D computational domain, defined with respect to *H* (i.e. height of study building), is the same as the validation study as mentioned above except the height of the domain is 5*H* based on Franke et al. (2007) and Dagnew and Bitsuamlak (2014) guidelines (see Figure 2-5). A blockage ratio of 1.8% is obtained, which is sufficiently low (Franke et al., 2007). The distance between the inflow boundary and the building is 5*H*, with the outflow boundary at 15*H* downstream of the building to allow for wake flow redevelopment. Lateral boundaries are set at 5*H* from the building surfaces. In all cases, the inflow direction is normal to the vertical façade.

2.3.2 Boundary conditions

Five different wind speeds U_{10} = 1, 2, 3, 4, and 5 m/s, respectively, are simulated at the reference height of 10 m. Accordingly, the *Reynolds numbers* range from 0.7×10^6 to 28×10^6 based on the building heights (*H*). At the inlet of the CD, an atmospheric boundary layer (ABL) is imposed (see Figure 2-7). This boundary layer can be described by the logarithmic law, which constitutes a vertical profile of the mean horizontal wind speed, turbulent kinetic energy *K* (m^2/s^2) and turbulence dissipation rate *ε* (m^2/s^3) (Richards and Hoxey, 1993) as shown in Equations 2-4 – 2-6. These profiles represent a neutral ABL, where the turbulence originates only from friction and shear:

$$u(z) = \frac{u_*}{k} ln\left(\frac{z+z_0}{z_0}\right) \qquad \text{Equation 2-4}$$

$$K = 3.3u_*^2 \qquad \text{Equation 2-5}$$

$$\varepsilon = \frac{u_*^3}{k(z+z_0)} \qquad \text{Equation 2-6}$$

where u_* is friction velocity (m/s), z_0 is the aerodynamic roughness length which is assumed that the buildings are situated on a large grass-covered terrain z_0 = 0.03 m (ESDU, 2001), k is the von Karman constant (~0.42). The thermal boundary conditions are a uniform inlet air temperature of T_{ref} = 283 K and a fixed surface temperature of T_w = 303 K for the building. An adiabatic boundary condition is used for the ground surface. Symmetry boundary conditions are applied at the top and lateral sides of the domain. The ground surface is modeled as a no-slip wall with zero roughness height k_s = 0 because in Low Reynolds Number Modeling (LRNM) surface roughness values cannot be specified (Blocken et al., 2009; Defraeye et al., 2010; Karava et al., 2012). Zero static pressure is applied at the outlet plane.

2.3.3 Grid dependency analysis

In this case, a generic low-rise with height H of 10 m cube has been used to accurately adopt the LRNM turbulence closure and grid resolutions at full-scale. The CD is discretized using polyhedral control volumes with a refined grid near the building exterior surfaces (Figures 2-5 and 2-6). Two levels of grid density with G1 (1.166×10^6 cells) and G2 (1.517×10^6 cells) are used to assess grid independency and ensure optimum mesh size. Properties of the two grids are summarized in Table 2-5, and different grid zones are used as illustrated in Figure 2-5. CV_3 is located close to the building and its surroundings where fine grids are deployed to achieve small y+ to capture vital details of the temperature gradients near the wall and the flow structures. A refinement ratio of 1.5 has been used in each dimension. Whereas, CV_1 and CV_2 are away from the building.

Table 2-5: Grid distributions

Control volumes	G1	G2
Control volume 1 (CV_1)	H/10	H/10
Control Volume 2 (CV_2)	H/15	H/20
Control Volume 3 (CV_3)	H/20	H/25
Total grids	1,066, 000	1,517,000

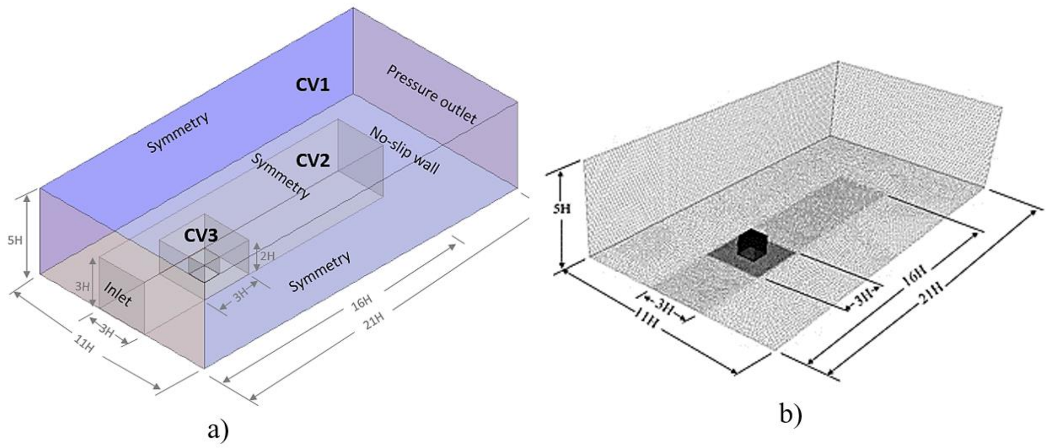

Figure 2-5: a) Perspective view of different control volume distributions, b) detail view of grid distributions

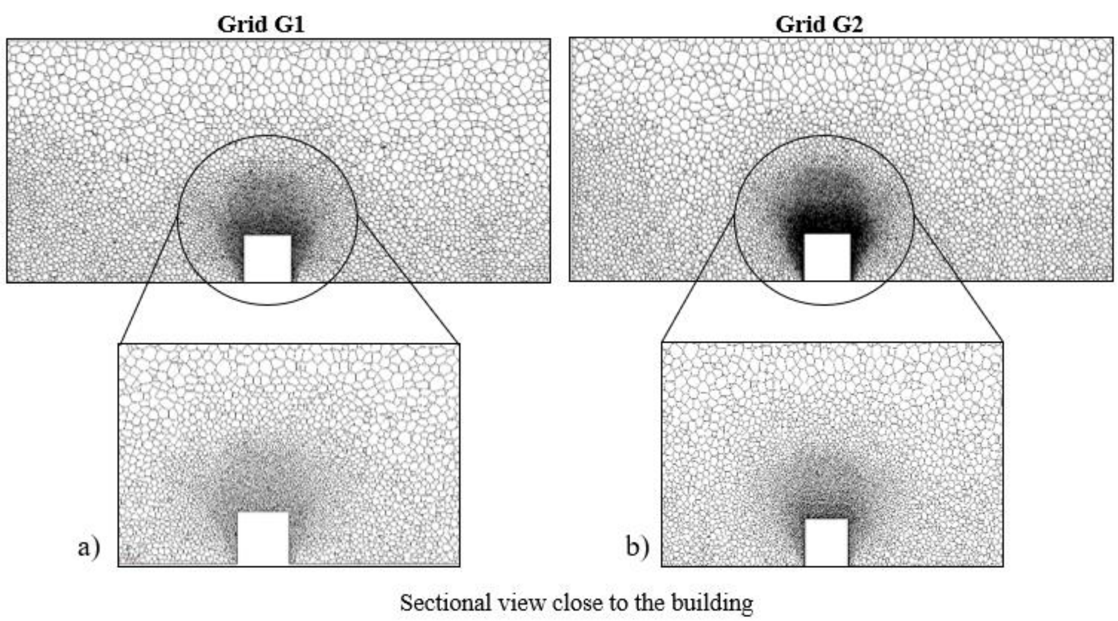

Figure 2-6: Comparison between grid G1 and G2

A viscous boundary layer with 10 prism layers is generated on the surfaces of the cubical model thus producing the required y^+ values. A stretching factor of 1.05 is used to resolve the boundary layer at all solid-fluid interfaces of CV_3. LRNM using the *Realizable k-ε (R k-ε)* and the *Shear Stress Transport k-ω (SST k-ω)* turbulence models has been used in the present work. The LRNM requires very high grid resolution near the wall. The simulation has employed grid with cell centers at a minimum distance of 130 μm from the cube surface to resolve the entire boundary layer, including the viscous sublayer and the buffer layer, which dominate the convective heat resistance. The simulated *CHTC* result does not change significantly between the two grids. Therefore, the grid distribution of G2 has been adopted in the present studies of five isolated buildings. A total of 2.1 $\times10^6$, 2.4 $\times10^6$, 2.64 $\times10^6$, 3.37 $\times10^6$, and 4.83 $\times10^6$ grid cells are deployed, for (i.e. 3, the 10, 15, 20, and 30 story building, respectively.

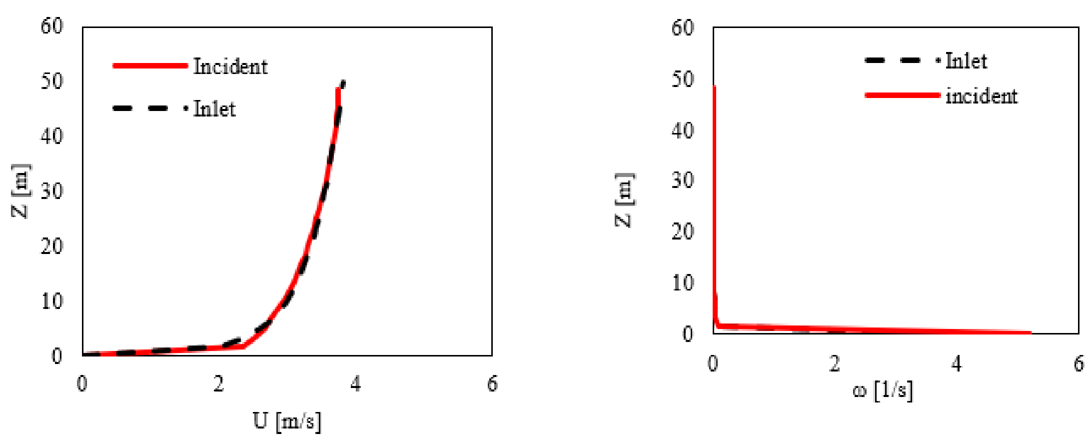

Figure 2-7: Comparison of simulated inlet and incident mean wind and specific turbulence dissipation rate (ω) profiles for U_{10} = 3 m/s case

2.3.4 Surface-average *CHTC* distributions

Bluff bodies are characterized with flow separation at the leading-edge corners. The separated flows at the edges forms vortices. The geometry of a building plays a crucial role in the flow structure and hence the *CHTC* distribution. Figures 2-8 and 2-9 illustrate that, as the stagnation pressure forces the impinging wind flow towards the top, bottom and side corners of the building. Near wall velocity increases around the leading-edge corners, which leads to higher surface friction velocity. As a result, higher values of *CHTC* are observed at the leading top and side corners of the building (see Figures 2-10. a - e). However, around the stagnation position and closer to the base of the buildings, lower values of *CHTC* are observed. Further, the standing and horseshoe vortices around the base of the buildings, which increases the residence time of the air, leads to a higher local air temperature resulting in lower values of *CHTC*.

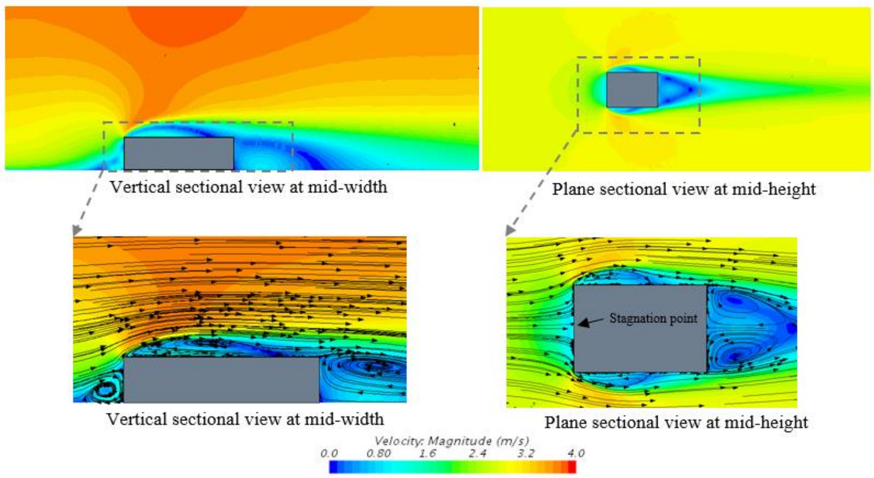

Figure 2-8: Wind velocity contours for the 10.1 m tall building (Ref. speed = 3 m/s at the inlet)

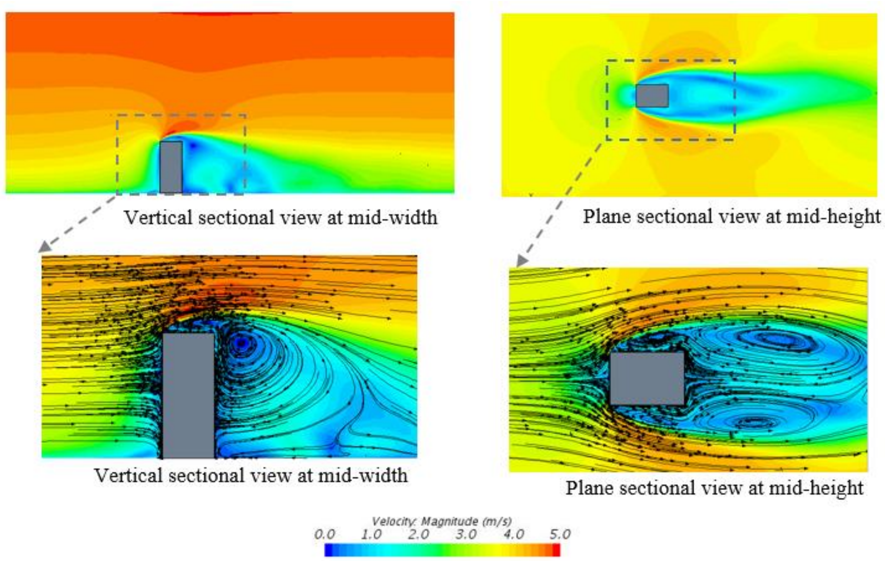

Figure 2-9: Wind velocity contour for 101.1 m tall building (ref. speed = 3m/s at the inlet)

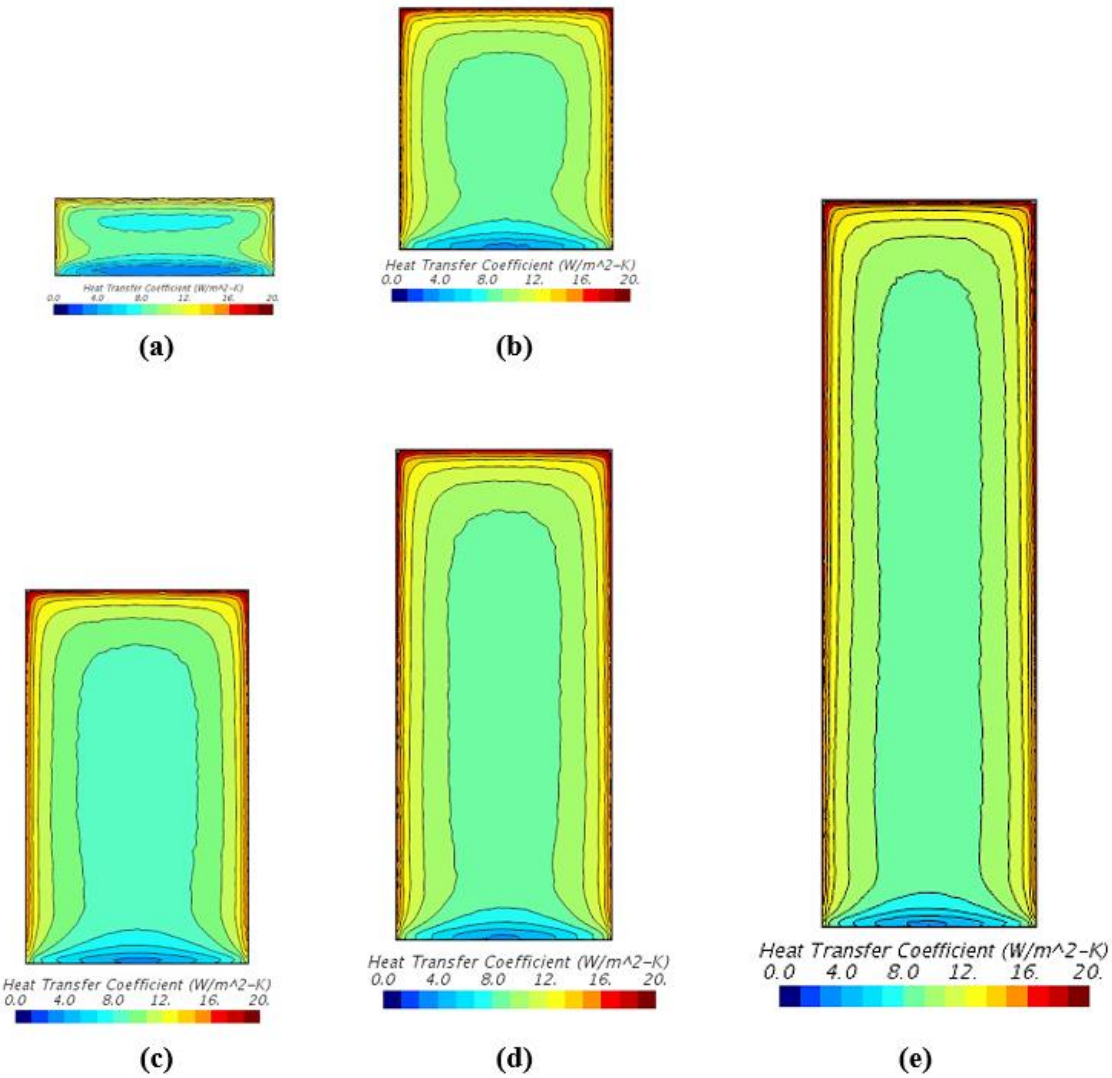

Figure 2-10: Windward *CHTC* distribution (for Ref. wind speed of 3 m/s at the inlet of building height) for building with a) 10.1 m, b) 33.7 m, c) 50.6 m, d) 67.4 m and e) 101.1 m heights

2.3.5 *CHTC* distribution on 10 m cubical building

The steady RANS is not capable of modeling the inherently transient nature of separation and circulation that occur downstream of the windward façade and of von Karman vortex shedding in the wake (Blocken et al., 2009). Therefore, calculating results in the downstream regions are generally deficient (Tominaga et al., 2008; Blocken et al., 2009). However, steady RANS with *SST k-ω* has a capability for the calculation of the mean wind speed upstream of the building façade and for the calculation of the *CHTC* for the windward face of the cube used in the validation. For this reason the *CHTC* analysis in in the present study focuses on windward façade of the buildings. The present study utilizes power-law relationship to represent forced convective heat transfer. A similar approach is considered by previous studies (Emmel et al., 2007; Blocken et al., 2009; Defraeye et al., 2010; Montazeri et al., 2015). A correlation between the *CHTC* and U_{10} averaged over the windward façade for a wind speed of 1-5 m/s is derived with high coefficients of determination (R^2). Close correlations are observed with the average deviation less than 5% is (see Figure 2-11) when compared with previous studies (Blocken et al. 2009; Defraeye et al. 2009; Defraeye et al. 2010). However, the study of Montazeri et al. (2015) deviates by 10%.

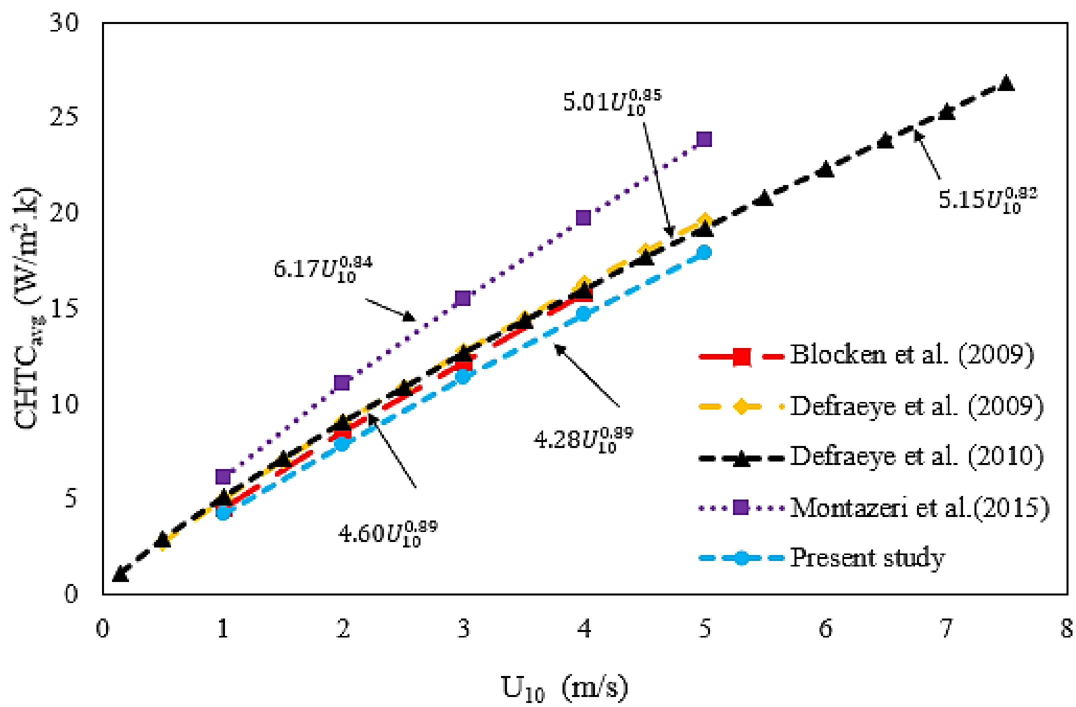

Figure 2-11: Comparison of surface-average *CHTC*-U_{10} correlation for windward façade of a 10 m cubical building

2.3.6 *CHTC*-U_{10} correlation

For each of the building configurations where H ranges from 10.1 m to 101.1 m and the reference wind speed 1 – 5 m/s, a power-law correlation for the surface-average of *CHTC* is derived with high coefficients of determination (R^2) as shown in Table 2-6 and illustrated as in Figure 2-12. The local and surface-averaged *CHTC* at the surfaces of each building is highly dependent on the immediate flow structure. The coefficient of the correlation shows that as the building height increases, the surface-average *CHTC* increases.

Table 2-6: Surface-average *CHTC* correlations

Building height (H x W x D) m	Reference wind speed range (m/s)	$CHTC_{avg}$-U_{10} correlation for windward (W/m²K)	R^2 (-)
10.1 x 30 x 42	1 – 5	$CHTC_{avg} = 3.142\ U_{10}^{0.84}$	0.9978
33.7 x 30 x 42	1 – 5	$CHTC_{avg} = 3.95U_{10}^{0.83}$	0.9997
50.6 x 30 x 42	1 – 5	$CHTC_{avg} = 4.005U_{10}^{0.89}$	0.9994
67.4 x 30 x 42	1 – 5	$CHTC_{avg} = 4.11U_{10}^{0.94}$	0.9985
101.1 x 30 x 42	1 – 5	$CHTC_{avg} = 4.385U_{10}^{0.96}$	0.9999

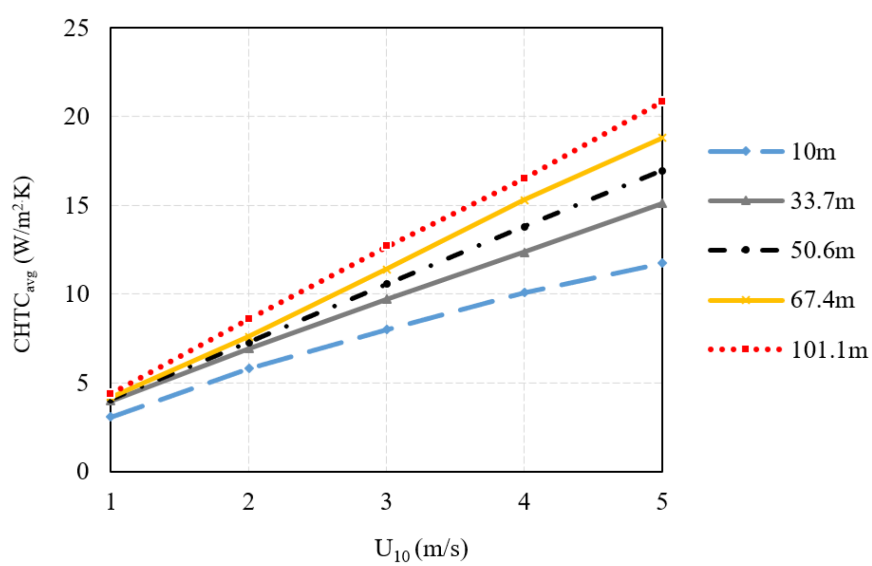

Figure 2-12: Surface-average *CHTC* correlation as a function of U_{10}

2.3.7 *CHTC* and building height correlation

To assess the surface–average *CHTC* variations with respect to the building height for a reference wind speed of 1-5 m/s, a correlation is derived with high coefficients of determination (R^2) as shown in Equation 2-7.

$$CHTC_{avg} = 4.67H^{0.21} \quad \text{Equation 2-7}$$

Thus, as H increases from 10.1 m to 101.1 m, the surface-average *CHTC* also increases by about 55% (see Figure 2-13).

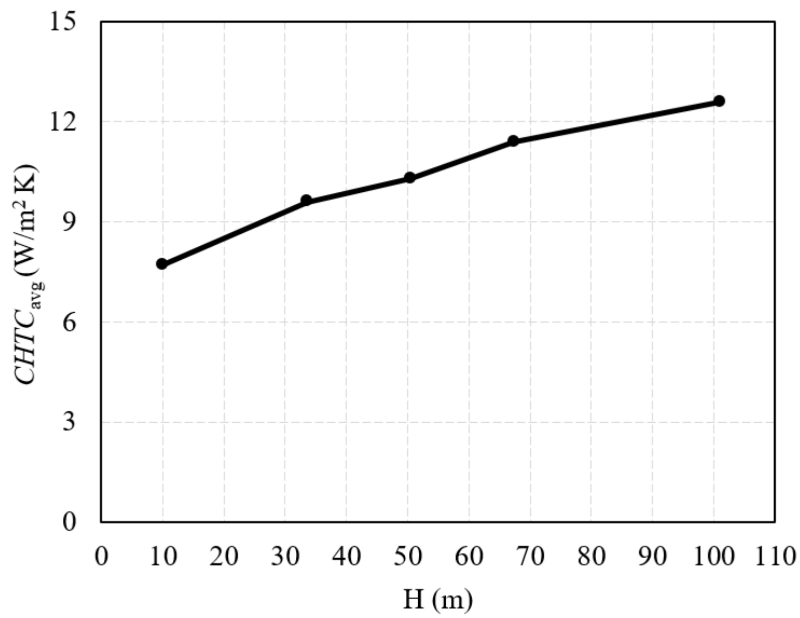

Figure 2-13: Surface- average *CHTC* as a function of building height for U_{10} = 1-5 m/s

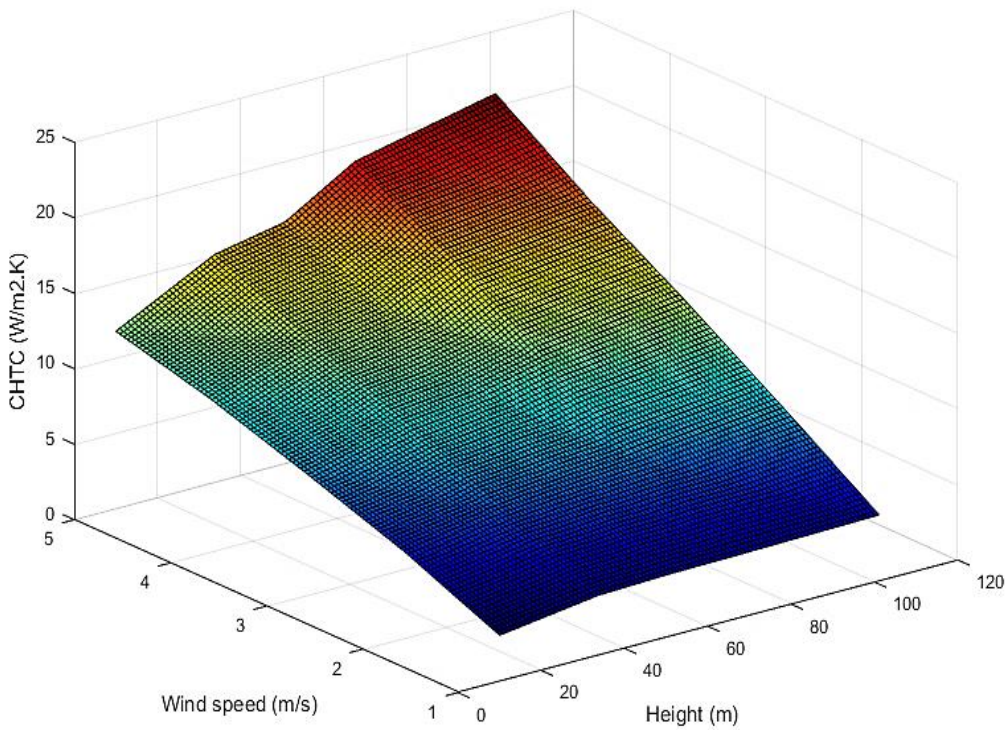

Figure 2-14: Plot of surface-average *CHTC* as a function of wind speed U_{10} and height (H)

Moreover, a new *CHTC* correlation as a function of reference wind speed (U_{10}) and building height (H) (see Figure 2-14) is developed as shown in Equation 2-8, where the coefficients are with 95% of confidence bound.

$$CHTC_{avg} = 0.62U_{10}^{1.81} + H^{0.45} \qquad \text{Equation 2-8}$$

2.3.8 Effect of wind direction on spatial distribution of *CHTC*

Spatial distribution of *CHTC* is calculated for the wind speed of U_{10} =1-5 m/s and for wind directions of θ= 0°, 22.5°, 45°, 67.5° and 90° at high-resolution. Note that θ= 0° represent wind direction perpendicular to the façade.

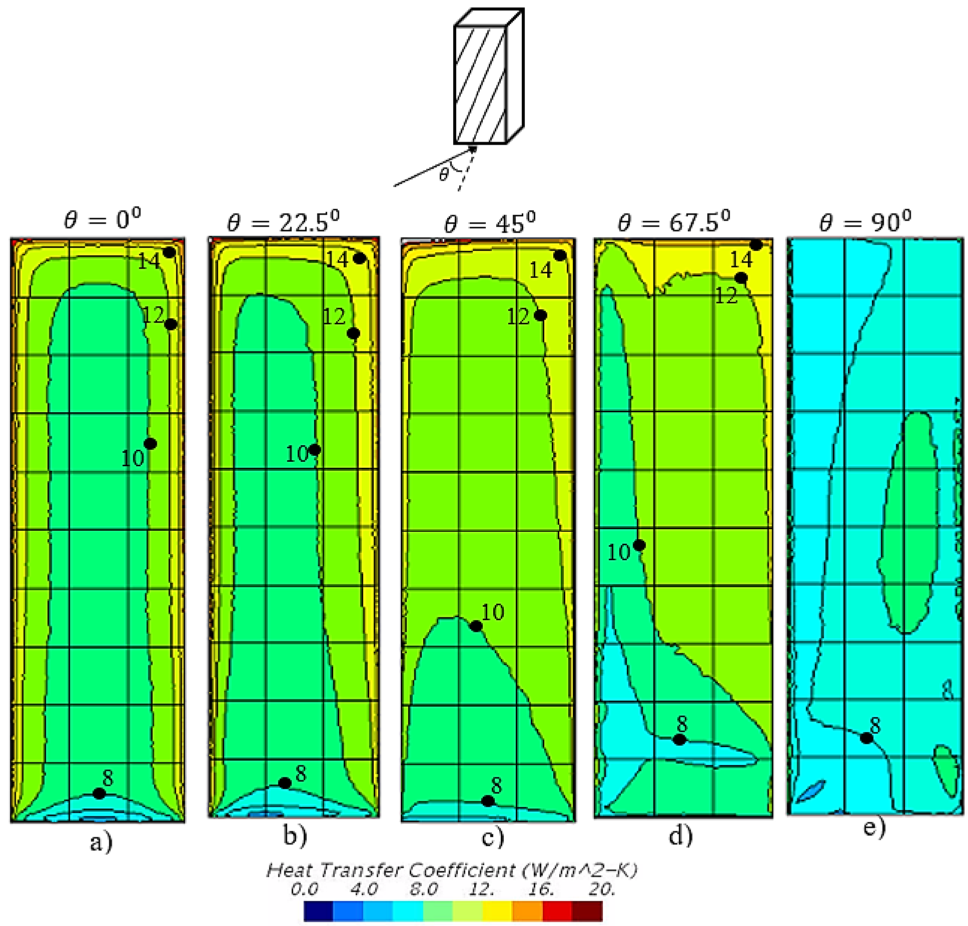

Figure 2-15: *CHTC* distribution on the windward façade for wind direction of : a) 0°, b) 22.5° c) 45°, d) 67.5°, and e) 90° for U_{10} of 3 m/s

CHTC value increases from bottom to top-corners zones in all cases as shown in Figure 2-15. This is due to the increase on the surface wind velocity from the stagnation point towards the edges and along the height of the building. The average-*CHTC* was similar for all wind directions except for the wind direction of 90° (see Figure 2-16) for the simulated wind speed ranges (i.e. 1-5 m/s). For the 90° wind direction, the façade under consideration is inside the separated flow that increases the residence time of the air, which can lead to a higher local air temperature and lower values of *CHTC*. For highly insulated wall systems average values may be good, however, for facades having low thermal resistance components such as windows or facades with curtain wall, local *CHTC* have an impact on the energy performance of the building attesting the need for wind directionality considerations.

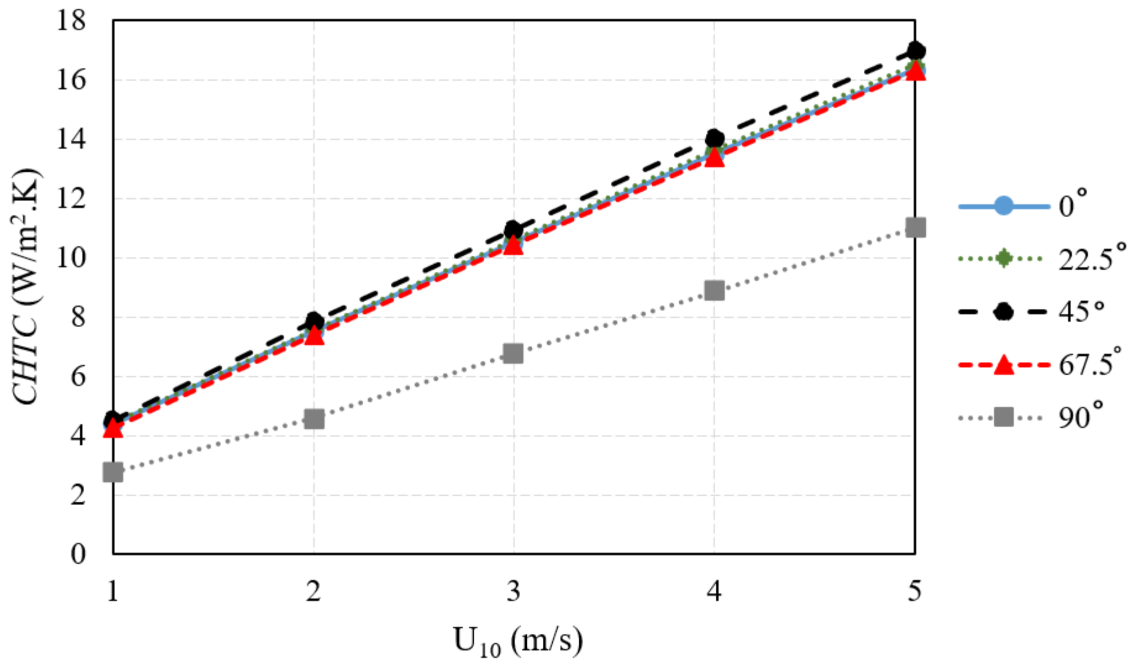

Figure 2-16: Average-*CHTC* distribution across windward façade for wind speed of U_{10} (1 – 5 m/s)

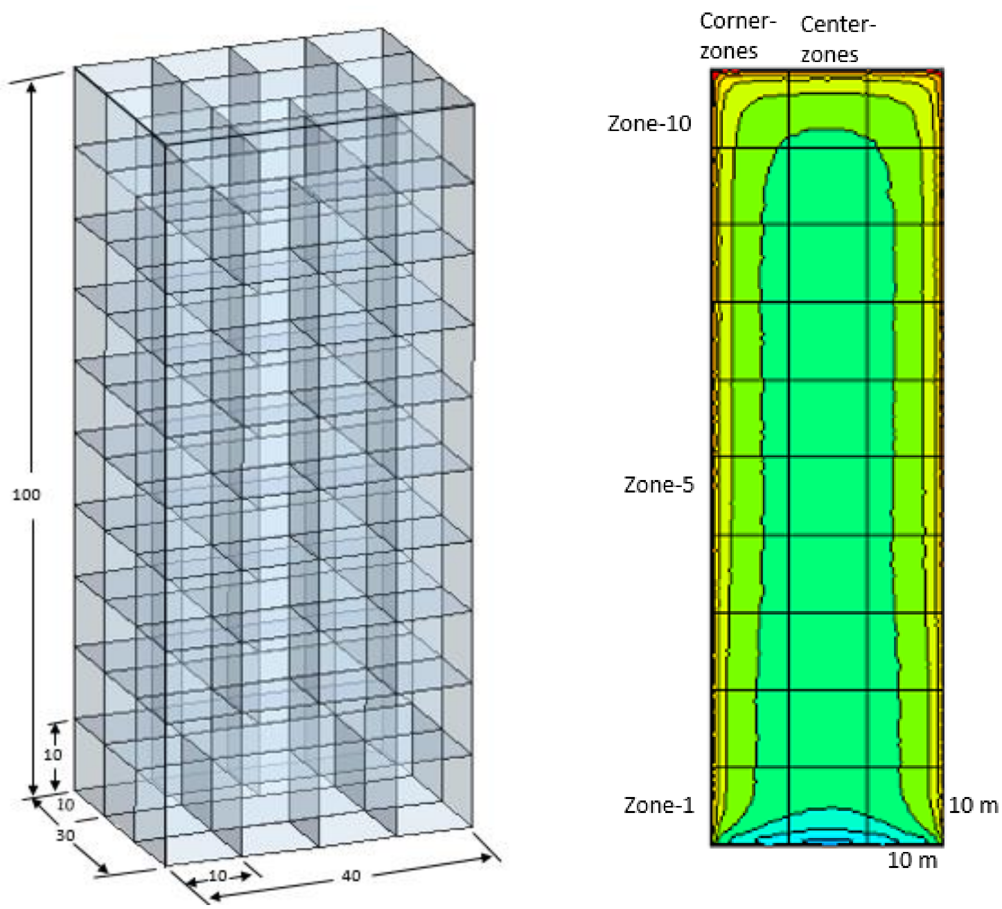

Figure 2-17: Zoning: A 101.1 m high-rise building divided into different thermal zones (10 m cube)

2.3.9 *CHTC* distribution effect on window and curtain walls

To analyze the *CHTC* distribution effect on window configurations and building energy consumption, a high-resolution spatial distribution of *CHTC* across the entire windward façade of the 101.1 m height building is considered. The façade is divided into ten vertical thermal zones, where one thermal zone is 10 m cube. In this study, for comparison purpose, rooms are categorized as *center-zone* where all rooms located in the mid-floors whereas rooms around the edges are considered as a *corner- zones* (see Figure 2-17).

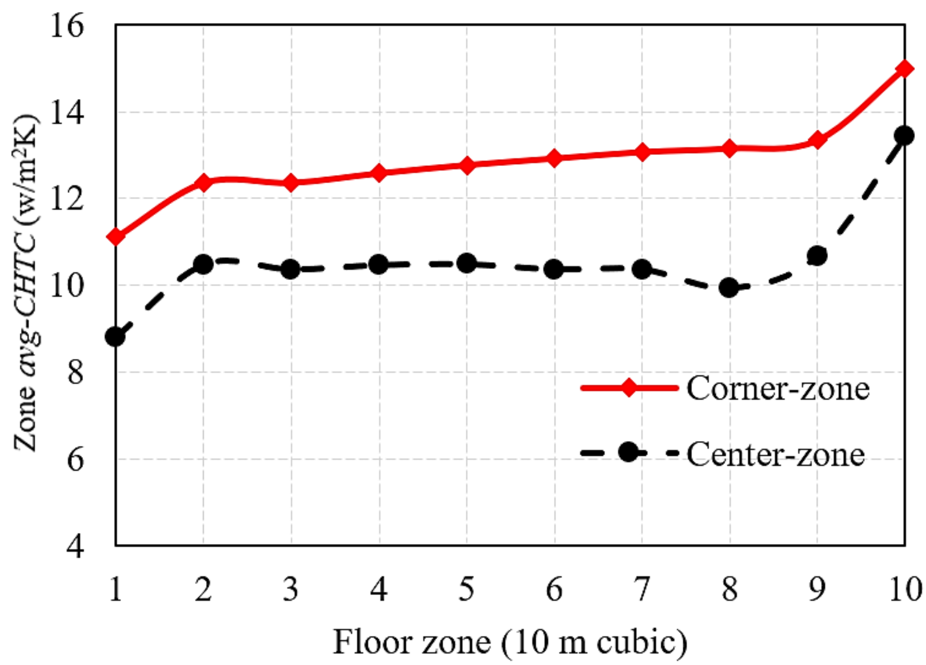

Figure 2-18: Average-*CHTC* distribution on different zones of 101.1 m height building for windward speed of U_{10} = 1 – 5 m/s, and wind direction of 0^0

2.3.10 *CHTC*- zoning

In building energy simulation, regardless of the window position, modelers use a single average-*CHTC* value to perform energy consumption analysis. The windward façade average-*CHTC* value is 12.08 W/m^{2}K for a wind speed of U_{10} 1-5 m/s. However, the top-corner zone (zone-10) of the building is 24% higher whereas at the base-center zone (zone-1) of the building it is lower by 27% decrement is observed. The local- *CHTC* distribution varies spatially across the entire façade of the building. The overall energy consumption analysis of a building, particularly curtain walls, where the least thermal resistance has, shall be analyzed consistent with this *CHTC* variation, to conserve the energy consumption of a building. Therefore, consideration of spatially varying *CHTC* for tall building energy analysis may be necessary. A previous study by Straube, J. (2012) reported that the overall heat transfer coefficient (U-factor) of highly insulated windows is normally five times greater than other components of a building's envelope e.g., wall, door, roof etc. Therefore, selection of optimal window configuration of a building consistent with the local *CHTC* distribution is one of the most important passive strategies, for saving energy. Thus, an architect's decision to position windows and to select a glazing type for high-rise building facades plays a key role in energy saving of the buildings. This is particularly for high-rise buildings that have curtain wall or large window-to-wall ratio.

2.4 Conclusion

Five different building configurations were investigated using high-resolution 3D steady RANS simulations for the analysis of convective heat transfer at the façade of a building. Surface-average *CHTC* – U_{10} correlations were determined. Firstly, validation of the numerical model with an experimental study conducted by Meinders et al. (1999) was carried out. This comparative validation also showed that the *Shear Stress Transport k-ω* (*SST k-ω*) provide more accurate results for convective heat transfer at the windward surface of reduced-scale cubic models. Based on the validated computational procedures and techniques, the surface-average *CHTC*-U_{10} correlations were computed for full-scale low- and high-rise buildings. The local and surface-averaged *CHTC* values at the surfaces of each building were observed to be highly dependent on the local flow structure. For example, the *CHTC* value increases as building height increases, and consistent with the increase of wind speed with height in the atmospheric boundary layer. In addition, *CHTC* distribution increases as the surface friction velocity increases. For the considered building plan dimensions and U_{10} (1-5 m/s), the surface-average *CHTC* increases by about 55% as H increases from 10.1 m to 101.1 m. For the top-corner zone (zone-10) of the building, the *CHTC* values were higher by 24% compared to the surface average *CHTC* and average *CHTC* values that were 27% lower compared to the surface average were observed at the base-center zone (Zone-1) of the building. This implies the necessity of zonal treatment of *CHTC* to enhance tall building energy simulation accuracy.

2.5 References

ASHRAE Task Group. (1975). "Procedure for determining heating and cooling loads for computerizing energy calculations, Algorithms for building heat transfer subroutines", New York.

Blocken, B., Defraeye, T., Derome, D., Carmeliet, J. (2009). "High-resolution CFD simulations for forced convective heat transfer coefficients at the facade of a low-rise building." Build Environ; 44:2396–412.

CD-Adapco StarCCM+, User Guide, CD-Adapco, Melville, NY, USA, 2015.

Chyu, M.K., Natarajan, V. (1991). "Local heat/mass transfer distributions on the surface of a wall-mounted cube". Trans ASME J Heat Trans; 113(4):851–7.

Dagnew, A. K., & Bitsuamlak, G. T. (2014). "Computational evaluation of wind loads on a standard tall building using LES. *Wind and Structures*, *18*(5), 567-598.

Dagnew, A., Bitsuamlak, G. T. (2013). "Computational evaluation of wind loads on buildings: a review." Wind Struct, 16(6), 629-660.

Defraeye, T., Blocken, B., Carmeliet, J. (2010). "CFD analysis of convective heat transfer at the surfaces of a cube immersed in a turbulent boundary layer." Int. J Heat Mass Transf; 53:297–308.

Defraeye, T., Blocken, B., Carmeliet, J., (2011). "Convective heat transfer coefficients for exterior building surfaces: Existing correlations and CFD modelling." Energy Conversion and Management, 52(1), pp.512-522.

Emmel, M.G., Abadie, M.O., Mendes, N. (2007). "New external convective heat transfer coefficient correlations for isolated low-rise buildings." Energy Build; 39:335–42.

Engineering Sciences Data Unit (ESDU) 85020. (2001). "Characteristics of atmospheric turbulence near the ground." Part II: Single point data for strong winds.

Franke, J., Hellsten, A., Schlünzen, H., Carissimo, B. (2007). "Best practice guideline for the CFD simulation of flows in the urban environment COST 2007." Action 732.

Handbook, A.S.H.R.A.E. (2001). "Fundamentals". American Society of Heating, Refrigerating and Air Conditioning Engineers, Atlanta, 111.

Holmes, J. D. (2015). "Wind loading of structures." CRC Press.

Ito, N., Kimura, K., Oka, J. (1972). “A field experiment study on the convective heat transfer coefficient on exterior surface of a building”. ASHRAE Trans; 78(1): 184–91.

Kahsay, M.T., Bitsuamlak, G., Tariku, F., (2017). “Numerical simulation of forced convective heat transfer coefficients on the facade of low-and high-rise buildings.” International conference on resilience of the integrated building: A community focus, Oklahoma City, Oklahoma, USA, April, 2017. http://dx.doi.org/10.1061/9780784480502.022#sthash.t0wtjbau.dpuf

Karava, P., Jubayer, C. M., Savory, E., Li, S. (2012). “Effect of incident flow conditions on convective heat transfer from the inclined windward roof of a low-rise building with application to photovoltaic-thermal systems.” Journal of Wind Engineering and Industrial Aerodynamics, 104, 428-438.

Liu, J., Srebric, J., Yu, N. (2013). “Numerical simulation of convective heat transfer coefficients at the external surfaces of building arrays immersed in a turbulent boundary layer.” Int. J. Heat Mass Transf; 61:209 25.

Liu, Y., Harris, D.J. (2007). “Full-scale measurements of convective coefficient on external surface of a low-rise building in sheltered conditions”. Build Environ; 42(7):2718–36.

Loveday, D.L., Taki, A.H. (1996). “Convective heat transfer coefficients at a plane surface on a full-scale building facade. Int. J Heat Mass Transf; 39:1729–42.

Nakamura H, Igarashi T, Tsutsui T. (2001). “Local heat transfer around a wall-mounted cube in the turbulent boundary layer”. Int J Heat Mass Trans; 44(18): 3385–95.

Meinders, E.R., Hanjalic, K., Martinuzzi R.J. (1999). “Experimental study of the local convection heat transfers from a wall mounted cube in turbulent channel flow.” Trans ASME J Heat Transf. 121:564–73.

Meinders, E.R. (1998). “Experimental study of heat transfer in turbulent flows over wall mounted cubes.” PhD thesis. Technische Universiteit Delft.

Mirsadeghi, M., Costola, D., Blocken, B., Hensen, J.L. (2013). “Review of external convective heat transfer coefficient models in building energy simulation programs: Implementation and uncertainty.” Appl. Therm. Eng., 56, 134–151.

Montazeri, H., Blocken, B., Derome, D., Carmeliet, J., Hensen, J. L. M. (2015). “CFD analysis of forced convective heat transfer coefficients at windward building facades: influence of building geometry.” Journal of Wind Engineering and Industrial Aerodynamics, 146, 102-116.

Nakamura, H., Igarashi, T., Tsutsui, T. (2001). “Local heat transfer around a wall-mounted cube in the turbulent boundary layer.” Int J Heat Mass Transf.; 44:3385–95.

Palyvos, J.A. (2008). “A survey of wind convection coefficient correlations for building envelope energy systems modeling.” Appl. Therm. Eng., 28, 801–808.

Richards, P.J., Hoxey, R.P. (1993). “Appropriate boundary conditions for computational wind engineering models using the k-ϵ turbulence model.” J. Wind Eng. Ind. Aerodyn; 46:145–53.

SHARCNET is a consortium of colleges, universities and research institutes operating a network of high-performance computer clusters across south western, central and northern Ontario [Online]. Available: <www.sharcnet.ca>; 2015.

Sharples, S. (1984). “Full-scale measurements of convective energy losses from exterior building surfaces.” Build Environ; 19:31–9.

STAR CCM+. CD-ADAPCO product. (2015). www.cdadapco.com/products/star-ccm (accessed on Sep. 12, 2015)

Straube, J. (2012). “High performance Enclosure: design guide for institutional, commercial and industrial buildings in cold climate.” Building Science press, 2nd edition, ISBN: 978-0-9837953-9.

Tominaga, Y., Mochida, A., Yoshie, R., Kataoka, H., Nozu, T., Yoshikawa, M., Shirasawa, T. (2008). “AIJ guidelines for practical applications of CFD to pedestrian wind environment around buildings.” Journal of wind engineering and industrial aerodynamics, 96(10), 1749-1761.

Wang K, Chiou R. (2006). “Local mass/heat transfer from a wall-mounted block in rectangular channel flow”. Heat Mass Trans; 42(7):660–70.

Yazdanian, M., Klems, J.H. (1994). “Measurement of the exterior convective film coefficient for windows in low-rise buildings.” ASHRAE Trans; 100(1): 1087–96.

Zhang, L., Zhang, N., Zhao, F., Chen, Y. (2004). “A genetic-algorithm-based experimental technique for determining heat transfer coefficient of exterior wall surface”. Appl Therm Eng; 24(2–3):339–49.

Chapter 3

3 CFD simulation of external *CHTC* on high-rise building façade with and without external shadings

3.1 Introduction

Improving the building's energy efficiency and reducing energy demand are widely believed as the likely means to mitigate climate changes. There have been several studies reporting that building envelope plays a curial role in moderating the elements of the climate (Hien & Istiadji, 2003; Lee & Tavil, 2007; Tzempelikos & Athienitis, 2007; Simmler & Binder, 2008; Kirimtat et al., 2016). To this effect, designers usually prescribe high R-value walls and windows etc. Glazed areas provide natural light and external views but represent the weakest thermal performance creating high heating and cooling loads. The requirements to minimize energy consumption is partially satisfied by integrating architectural shading features such as balconies, mullions, and egg-crates on their façade systems particularily to reduce the cooling load during summer. There are many studies in literature that focussed on shading devices energy performance assessment in buildings by using simulation programs (Awadh, 2013; Bueno et al., 2015; Stazi et al., 2014; Bellia et al., 2013; Kirimtat et al., 2016). Further, external shadings modify the flow regime near the surface, which in turn affect the convective heat transfer and air infiltration process significantly. Building have very diverse architectural design details (as illustrated in Figure 3-1 for city of Toronto with complex and varied facade system) that can lead to complex interaction of the building facade with the environment. It is expected that each architectural form (aerodynamics) interact with the environment differently than the other. Therefore, careful treatment of external convective heat transfer is necessary.

In a building, a large part of the energy consumption is caused by heat transfer from the external surfaces, which consists of radiation and convection. The radiation heat loss is a function of surface temperature and emissivity while the convection heat loss is a function of various parameters such as wind speed, wind direction, topography, flow pattern, building form and other architectural detials (i.e. aerodynamics), and the temperature difference between indoor and outdoor (Blocken et al., 2009; Bergman and Incropera, 2011; Kahsay et al., 2018). Thus, the external convective heat transfer is modeled using Newton's law of cooling as in Equation 3-1:

$$CHTC = \frac{q_c}{(T_{sur} - T_{air})} \qquad \text{Equation 3-1}$$

where *CHTC* (W/m^2. K) is convective heat transfer coefficient, q_c is local surface heat flux (W/m^2), T_{sur} is surface temperature (K), and T_{air} is reference air temperature (K). Therefore, considering these parameters, the analysis of heat transfer makes it complex to get accurate estimates, particularly of the convective heat transfer rate. External *CHTC* is affected by surface roughness, such as the window sash, the wall texture and the building external shading elements. Consequently, the prediction and evaluation of *CHTC* is extraordinarily complex (Maruta et al., 1998).

Figure 3-1: High-rise buildings with interacted façade system, Toronto

To date, the *CHTC*s used by building energy simulations (BES) tools are primarily derived from experimental and numerical analysis carried out on a low-rise building with smooth façade surfaces (Palyvos, 2008; Defraeye et al., 2011; Mirsadeghi et al., 2013). However, the external shading elements, as well as the form and size of the building have a significant effect on the *CHTC*. Therefore, the application of the existing *CHTC*s for non-smooth facades and high-rise buildings may not be accurate. Within the building industry, there is an increasing concern about a mismatch between the predicted energy performance of a building and actual measured performance referred as "the performance gap" (De Wilde, 2014). For instance, Menezes et al. (2012) have investigated the energy performance gap between the predicted versus actual energy performance of non-domestic buildings using post-occupancy evaluation data suggesting that the measured energy use can be as much as 2.5 times the predicted use. These are attributed to shortcomings of the current modeling programs, poor assumptions, poor construction quality, as well as lack of monitoring following construction. Bridging the gap between the predicted and measured performance is crucial for designers. Understanding convective heat transfer of a building in detail is essential to estimate the *CHTC* and hence model energy consumption accurately.

One of the most widely used simulation programs for energy consumption analysis is EnergyPlus (Kirimtat et al., 2016), which offers a wide selection of different values of *CHTC* correlations. The commonly existing-*CHTC* correlations in EnergyPlus are DoE-2 as default, Simple Combined, TARP, and MoWiTT as shown in Table 3-1. In recent years, there are numerous numerical studies on the investigation of *CHTC* correlations such as Blocken et al. (2009); Defraeye et al. (2010); Montazeri et al. (2015); Montazeri and Blocken (2017 & 2018); however, in these studies, only a smooth façade was considered. Besides there are also previous studies on the impact of external shading in building energy consumption, yet, in these studies, the existing- *CHTC* correlations are used which are primarily developed from smooth facades (Kirimtat, 2016). Thus, the present study investigates compartively the effects of smooth facade, balconies, mullions, and egg-crates on the convective heat transfer rate of a high-rise building. The *CHTC* is evaluated using high-resolution 3D computational heat transfer and fluid dynamics simulations. A steady RANS with *SST k-ω* model at full-scale simulation on the study building, an isolated 100 m tall building with smooth façade and covered with different forms of external shading elements. The influence of the external shading elements on the surface-average *CHTC* value distribution is investigated at different Reynolds Numbers ranging from 6.67×10^6 to 33×10^6 to define new-*CHTC* correlations as a function of reference wind speed.

Table 3-1: The common existing-*CHTC* correlations in EnergyPlus

Reference	*CHTC* correlations	Comment
Nusselt & Jurges (1922)	$7.13V^{0.78}$	WTM, plate, parallel flow, 5 < V_w < 24 m/s, ASHRAE proposes exponent= 7.2 for 5 $\leq V_w \leq$ 30.
McAdams (1954)	$7.6V^{0.78}$	V > 5 m/s, rough surface
Mitchell (1971)	$6.6V^{0.6}$	Vertical surface behind a wedge-separated subsonic flow
Ito et al. (1972)	5.8 + 2.9V	Nocturnal field measurement, wall, V_f > 3 m/s, windward (if leeward and V_f > 4 m/s, h_w = 13 W/m^2 K)
ASHRAE task group (1975)	$18.65V^{0.605}$	FM, V_w–Kimura's ‘‘6th floor model” V_w = 0.25Vf for V_f > 2 m/s, V_w = 0.5 for V_f =2 m/s (windward) and V_w = 0.3 + 0.05Vf (leeward)
TARP (Walton, 1983)	$2.537W_f R_f \frac{PU_{loc}}{A} + c\lvert\Delta T\rvert^{1/3}$	Reduced scale experiment, Windward: W_f = 1.0, Leeward: W_f = 0.5, For rough brick, roughness index R_f = 1.67 Vertical surface, c = 1.31
Sharples (1984)	5.8 + 2.9V	FM on facade of tall building, V_w =1.8V_f + 0.2 windward.
DoE-2 (LBL, 1994)	$\sqrt{\left[aU_{loc}^{b}\right]^2 + [c\lvert\Delta T\rvert^{1/3}]^2}$	On-site full-scale experiment with $U_{10,}$ Windward: a=3.26, b=0.89, Leeward: a=3.55, b=0.617
Loveday & Taki (1996)	$16.15V^{0.397}$	FM, flat vertical panel, windward, V_w = f(V_f) = 0.68V_f < 0.5 and 0.2V_f < 0.1
Taki & Loveday (1996)	$14.82V^{0.42}$	FM on a 6th floor vertical surface in 200 mm recess, windward,

Hagishima & Tanimoto (2003)	4.47 + 10.21V	Multipoint FM, V= $\sqrt{avg(u^2+v^2+w^2)}$, on a vertical wall
Emmel et al. (2007)	$5.15V^{0.81}$	FM, walls of isolated, low-rise building, 0^0angle of attack, ΔT= surface-to-air temperature difference = 10 K, wind speed 1 – 5 m/s
MoWiTT (Booten et al., 2012)	$\sqrt{\left[aU_{loc}^b\right]^2+[c\lvert\Delta T\rvert^{1/3}]^2}$	On-site full-scale experiment of low-rise building with U_{10}, Windward: a = 3.26, b = 0.89, c = 0.84, Leeward: a = 3.55, b = 0.617, c = 0.84
Simple-combined (DoE, 2016)	$D+EU_{loc}+FU_{loc}^2$	A simple algorithm, For rough brick, roughness coefficient D=12.49, E=4.065, F=0.028

h_n: Natural convection; U_{loc}: local wind speed calculated at the height above ground of the surface centroid; V: wind speed at a reference height of 10 m; P: Perimeter; A: Area; FM: Field measurements; WTM: wind tunnel measurement.

The remaining sections of the chapter are organized as follows: Section 2 describes validation process and the methodology used for evaluating *CHTC* and *CHTC*-U_{10} correlations. Section 3 presents the results and discussion, and section 4 concludes the chapter.

3.2 Methodology

The methodology consists of two parts. In the first part, experimental data from literature has been used to validate the proposed CFD simulation; and in the second part the present study case and the study cases and numerical model and its boundary conditions has been described. The validated CFD model has been used to assess effect of different external shading forms on high-rise building convective heat transfer coefficients, and to develop *CHTC* correlations.

3.2.1 CFD model validation

To validate the CFD model, an experimental data from literature by Meinders et al. (1999) for a cube in a turbulent channel flow is used. The validation detail study has been presented by Kahsay et al. (2018a), in this study a brief description of the method is presented for completeness. In the experiment, the convective heat transfers at the surfaces of a cube placed in turbulent channel flow were evaluated. The channel had a rectangular test section with a height of 50 mm, the width of 600 mm and a depth of 600 mm. A single cube having an internal copper core of 12 mm in length covered with an epoxy layer of 1.5 mm thickness and external side dimensions of 15 mm is placed at the center of the channel. For the validation study, a Reynolds number of 4440 resulting in a bulk velocity of 4.47 m/s is considered based on the cube height. The approaching airflow temperature is set to 283K and is taken as the reference temperature to calculate the *CHTC*s. The 3D steady RANS with SST κ-ω turbulent model closure is used. Ccommercial CFD solver (STAR-CCM+ v 11.06.011, 2018) has been adopted in the present study.

Computationally evaluated surface temperature along a mid-plane vertical centerline and a mid-height horizontal line are compared with experimental results (see Figure 3-2) for validation purposes. At the windward surface indicates that the low Reynolds number (LRNM) model namely the two-equation *SST* κ-ω model perform well in this region. The average difference between experimental data and results obtained with the *SST* κ-ω turbulence model in the windward facade along the vertical and horizontal lines is about 1.34 and 1.48%, respectively. This is inline with previous CFD studies by Montazeri et al., (2015) and Defraeye et al., (2010). Nevertheless, some overestimations can be clearly seen close to the ground, and it could be attributed to the additional heat loss through the base wall in the experiment, which is not considered in the simulation. Some studies also reason out that is may be due to an incorrect prediction of the size and shape of the standing vortex due to the upstream longitudinal gradients in the approach-flow profiles Montazeri et al. (2018). Further, an overestimation about 10% is observed on the top and lateral surface of the cube. This discrepancy could be attributed to the inaccurate predictions of the flow field in the separation and reattachment zones of the top and sidewalls resulting in larger temperature values predictions. This has also been pointed out by Blocken et al. (2009); Defraeye et al. (2010); and Montazeri, et al. (2015). For the leeward surface, the distribution of the predicted surface temperatures by the *SST* k-ω model is within 5% deviation from the experimental results, especially for the midplane. Therefore, it is fair to assume the adopted model can yield reliable results for the windward facade. The temperature predicted with *SST k-ω* provides sufficient accuracy on the surface of a cube, and therefore the same set of parameters will be used in the next full-scale computational section.

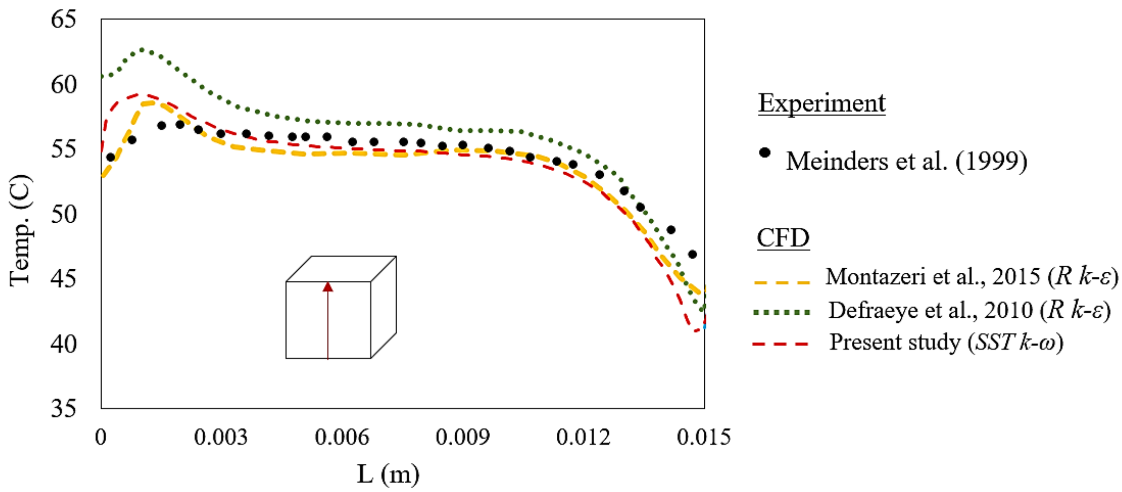

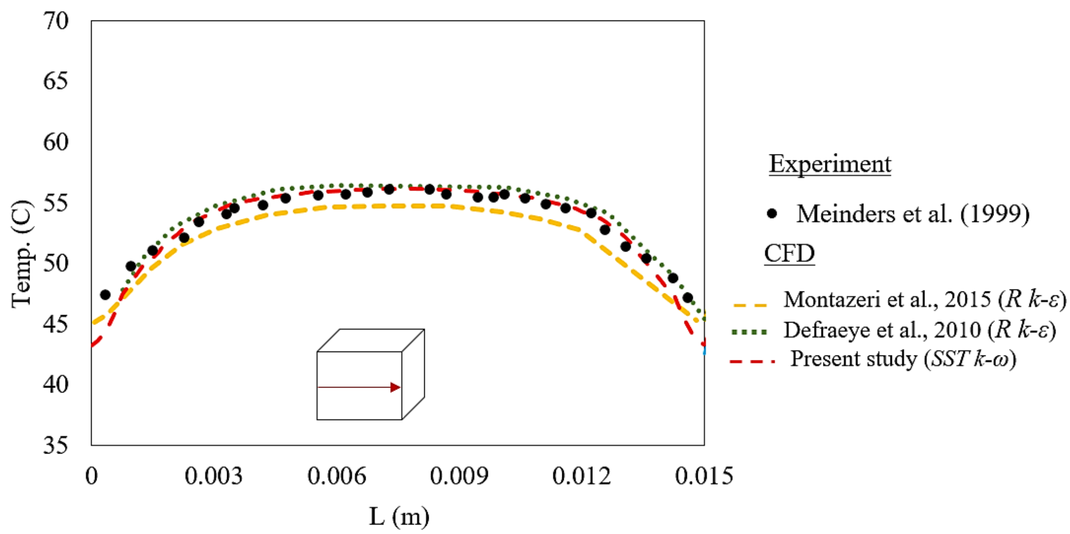

Figure 3-2: Comparison of experimental measured and simulated temperature distribution on the windward surfaces of the cube in a) vertical center plane (b) horizontal center plane

3.2.2 High-rise building case study

The study building has a dimension of 30 m x 40 m x 100 m (width, depth, height) but with three different forms of external shading elements namely horizontal, vertical, and egg-crate and fourth smooth façade case as illustrated in Figure 3-3. The detail dimensions of the shading elements are provided in Table 3-2. The horizontal shading or balconies are common structures frequently used in buildings, and they have different forms of walls or fences, however, in this study, balconies with free edges are considered. The depth of the balconies range between 0.2 m and 1 m. Vertical shading or mullions on the external wall of a building are also common cladding elements. In this study, a vertical ribs depth ranging between 0.2 m and 1 m are used. Further, egg-crate shading that represent a combination of both horizontal and vertical shades to provide higher shading effect under the hot-humid climate (Lau et al., 2016) is modeled. Like the other cases, the depth of the shading range between 0.2 m to 1m. Details of different shading elements that are used for the numerical model are described in deatial in Figure 3-4.

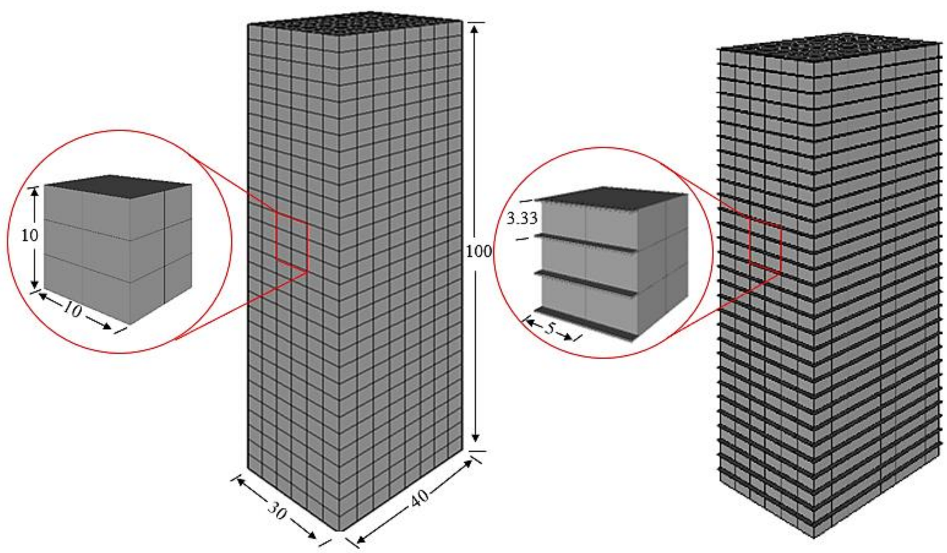

a) Without shading (smooth facade)

b) Horizontal shading

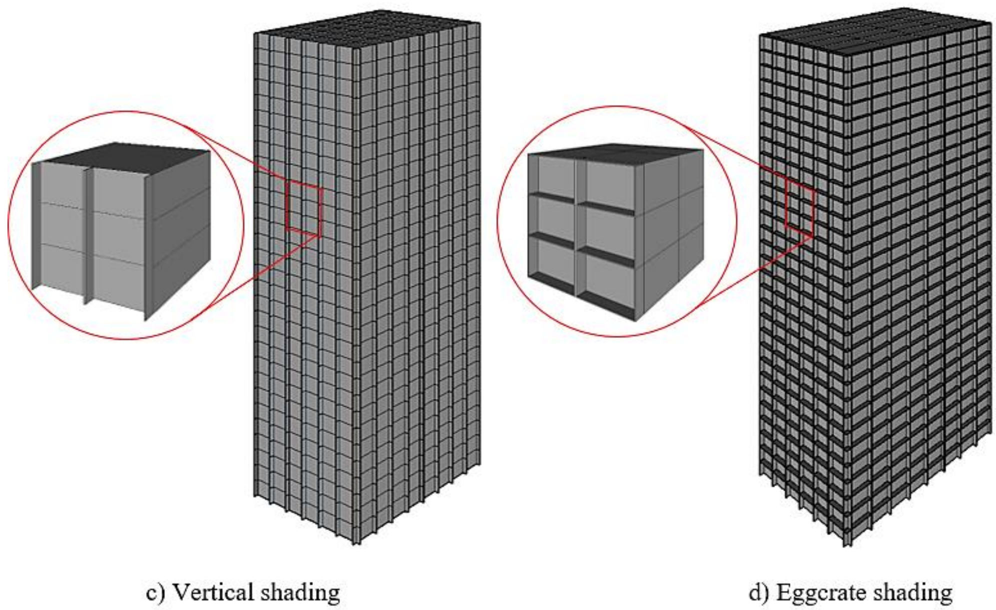

Figure 3-3: Model of high-rise buildings a) without-shading – smooth façade, b) horizontal shading, c) vertical shading, and d) egg-crate shading

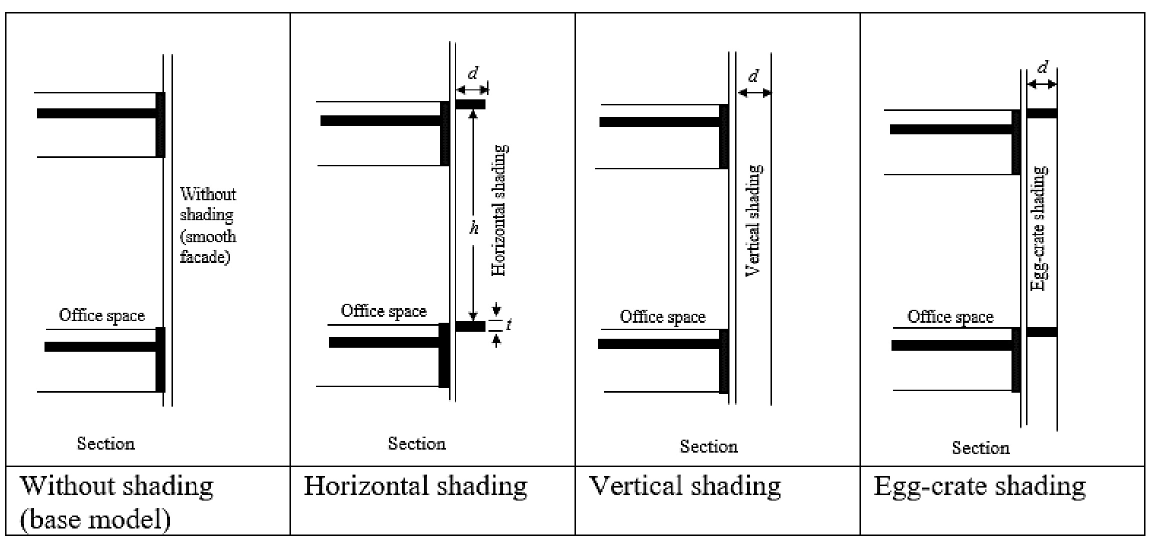

Figure 3-4: Types of shading details

Table 3-2: Numerical simulation case study

Study cases	*Width (w) m*	*Height (h) m*	*Depth (d) m*	*Thickness (t) m*
Case1	5	3.3	0.2	0.15
Case 2	5	3.3	0.5	0.15
Case 3	5	3.3	1	0.15

3.2.3 Numerical modeling

The dimensions of the 3-D computational domain (CD) are defined based on the height of the study building (*H*). The dimensions and boundary conditions of the CD are selected based on the recommendations of Franke et al. (2007); Tominaga et al. (2008); Dagnew & Bitsuamlak (2014), as illustrated in Figure 3-5. A blockage ratio of 1.8% is obtained, which is sufficiently low to minimize effects due to blockage in the numerical results (Franke et al. 2007). In this analysis, different wind speeds at the reference height of 10 m of U_{10} = 1, 2, 3, 4 and 5 m/s are used. In all cases of the study, the wind inflow direction is normal to the vertical façade of the building is considered. Atmospheric boundary layer (ABL) flow is imposed at the inlet of the domain where the velocity profile is described by the logarithmic law, which constitutes a vertical profile of the mean horizontal wind speed, turbulent kinetic energy K (m^2/s^2) and turbulence dissipation rate ε (m^2/s^3) (Richards and Norris, 2011) as shown in Equations 3-2 – 3-4:

$$u(z) = \frac{u_*}{k} ln\left(\frac{z+z_0}{z_0}\right) \quad \text{Equations 3-2}$$

$$k = 3.3u_*^2 \quad \text{Equation 3-3}$$

$$\varepsilon = \frac{u_*^3}{k(z+z_0)} \quad \text{Equation 3-4}$$

where u_* is friction velocity (m/s), z_0 is the aerodynamic roughness length which is assumed that the buildings are situated on a large grass-covered terrain z_0 = 0.03 m (ESDU, 2001), κ is the von Karman constant (~0.42). The thermal boundary conditions are a uniform inlet air temperature of T_{ref} = 283 K and a fixed surface temperature of T_w = 303 K for the building. An adiabatic boundary condition is used for the ground surface. Symmetry boundary conditions are applied at the top and lateral sides of the domain. The ground surface is modeled, as a no-slip wall with zero roughness height (k_s), since in *LRNM* surface roughness values cannot be specified (Blocken et al., 2009; Defraeye et al., 2010). Zero static pressure is applied to the outlet plane.

In order to effectively discretize the computational domain, three different grid density are constructed with different control volumes (see Figures 3-5 and 3-6) where dense grids are allocated near study building and the ground where flow gradients changes significantly. The grid distributions are CV_1 (H/10), CV_2 (H/20), and CV_3 (H/25). In CV_3 to achieve a high-resolution (*LRNM*) grid with cell center at a minimum distance of $y_p = 130\ \mu m$ from the building surface is used to resolve the entire boundary layer, including the viscous sublayer and the buffer layer, which dominate the convective heat resistance. In this study, different grid cells are used, such as for the case of building without shading a total of 2.66×10^6 cells, for the building with horizontal shading a total of 3.35×10^6, for the building with vertical shading a total of 3.42×10^6 cells, and for a building with egg-crate shading a total of 4.92×10^6 cells are deployed. *Low-Reynolds number modeling, Shear Stress Transport* $k-\omega$ *(SST* $k-\omega$*)* turbulence models have been used in the present work.

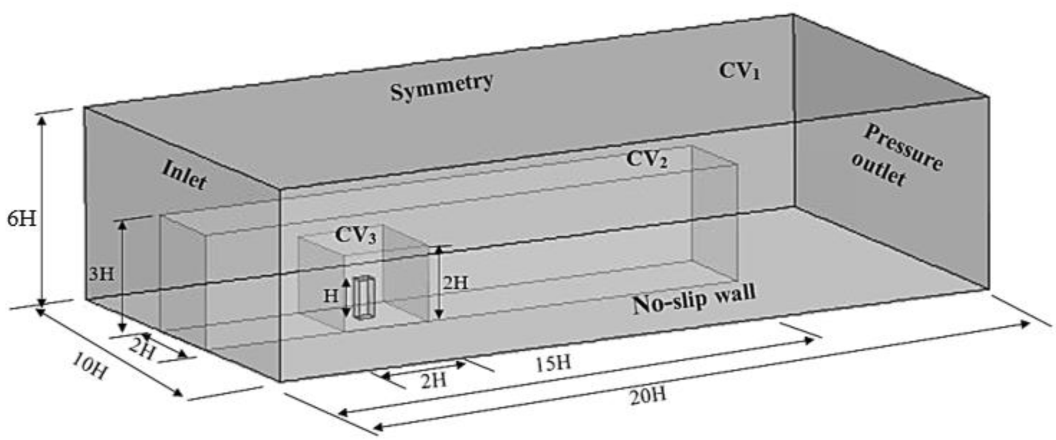

Figure 3-5: Computational domain

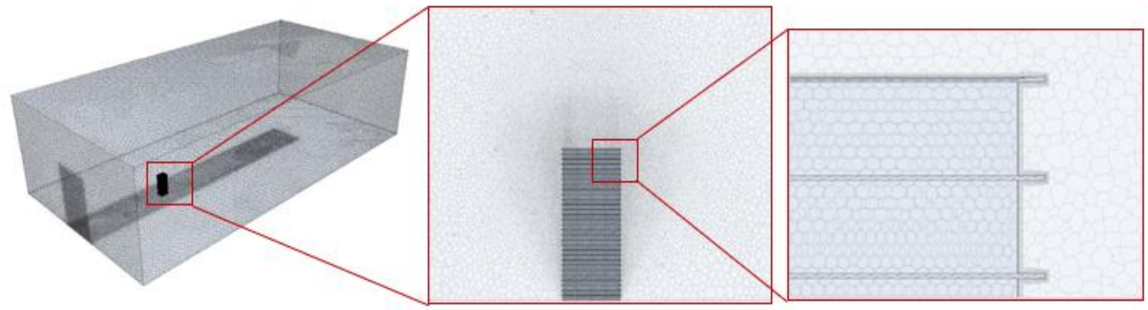

Figure 3-6: High-resolution mesh distribution

3.3 Results and discussions

In this section, the influence of wind speed, wind direction, and three external shading elements and one smooth façade on *local-CHTC* distribution on a high rise will be discussed. In addition, a correlation on surface-averaged *CHTC* and a reference wind speed (U_{10}) for all study cases will be presented.

3.3.1 Wind speed effect on the *local-CHTC* distribution

Wind speed affects the convective heat transfer coefficient; the higher the speed of the air flowing around a building, the more heat will be drawn from the building convectively. Overall, providing building surface roughness such as shading decreases the airflow near the surface of the building; however, depending on the geometrical details and the arrangement of the shading elements their effect on the *local-CHTC* varies as discussed in the following sections.

3.3.2 Building without external shading – smooth facade

For a case of building without shading, the simulation result shows that for a windward façade of a building, as the stagnation pressure forces the impinging wind flow towards the top, bottom and side corners of the building, the separated layer flows at high shear form vortices around the edge as illustrated in Figure 3-7. Near-wall, velocity increases around the leading-edge corners, which leads to higher surface friction velocity. As a result, a higher value of *CHTC* is observed at the leading top and side corners of the building. In addition, a variation on the convective rate at the corner and center zones of the building is observed, which leads to higher heat losses from the corner-zones rooms than that of center zone rooms are observed as shown in Figure 3-7. However, around the stagnation position and closer to the base of the buildings, lower values of velocities are observed, which increases the residence time of the air, leads to a higher local air temperature resulting in lower values of *CHTC*.

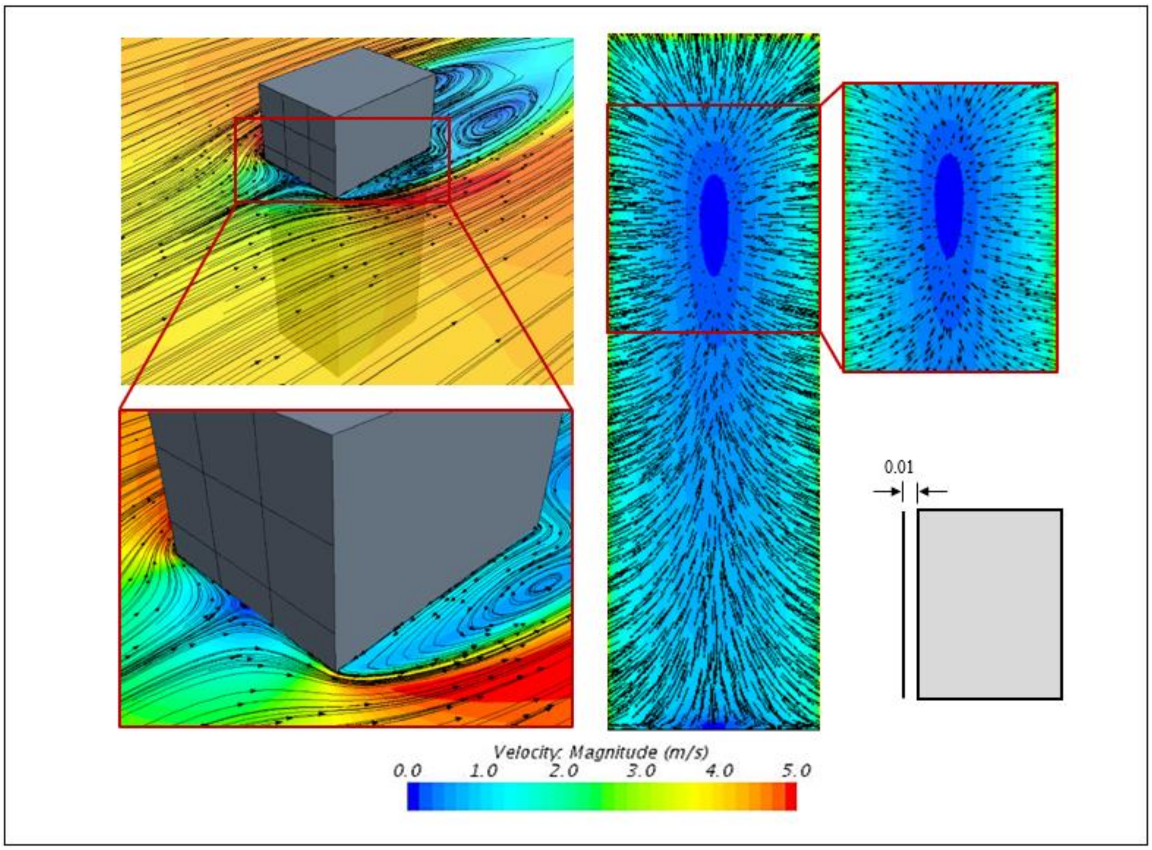

Figure 3-7: Wind velocity contour and vector plots at distance of 0.01m from the wall for a smooth wall building (Ref. speed U_{10} = 3 m/s at the inlet)

Further, at different floor height of the building and room locations, the variation on local-*CHTC* distribution is investigated. As the building height increases, the convective heat transfer rate also increases; this is due to the exposure of the zones to higher wind speed as illustrated in Figure 3-8. Thus, local-*CHTC* comparison on zone 1, 5, and 10 between the corner and the center zones are performed. Compared to the center zone, the corner-zone has increased by 30.2%, 25.7%, and 12.8%, respectively.

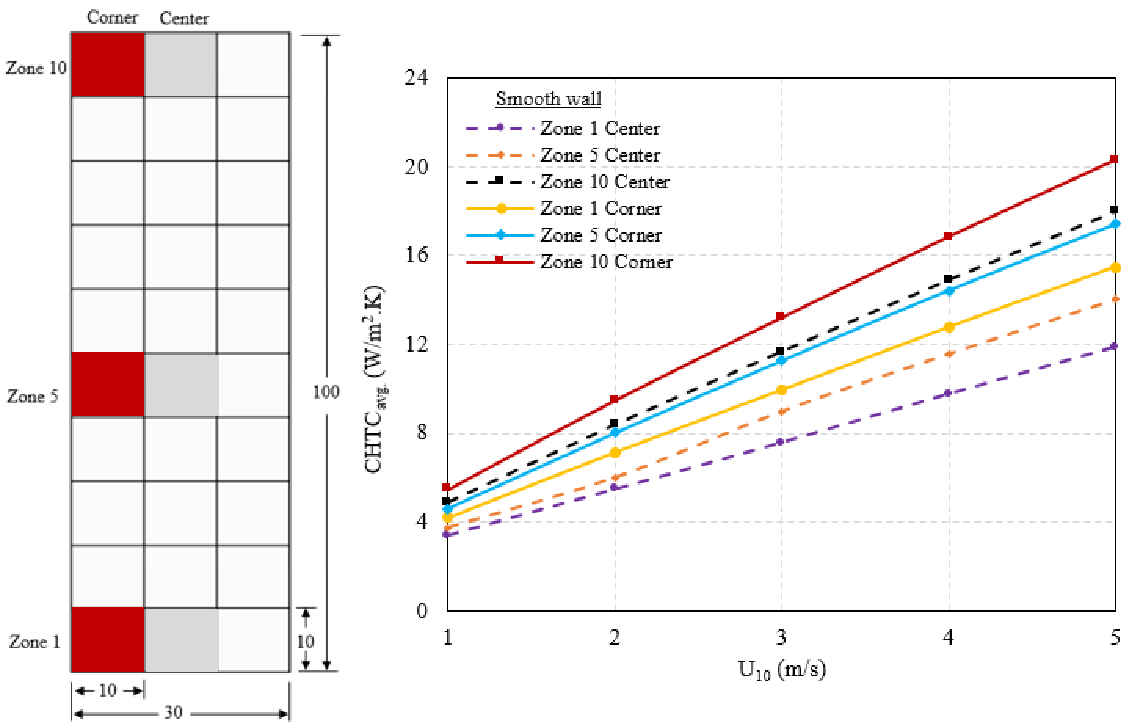

Figure 3-8: Surface-averaged *CHTC* correlation for windward façade at the ref. U_{10} wind speed

3.3.3 Building with horizontal shading

For the case of building with horizontal shading elements, considering the windward façade of the building, at near the wall, the stagnation pressure forces the impinging wind flow primarily towards the side corners of the building, and this is due to the horizontally aligned balconies (see Figure 3-9). Therefore, the separated layer flows at a high shear velocity around the side edges. As a result, a higher *CHTC* value is observed at the side corners than the center zone of the buildings. However, around the stagnation location and down to the base of the buildings, lower values are observed as illustrated in Figure 3-9.

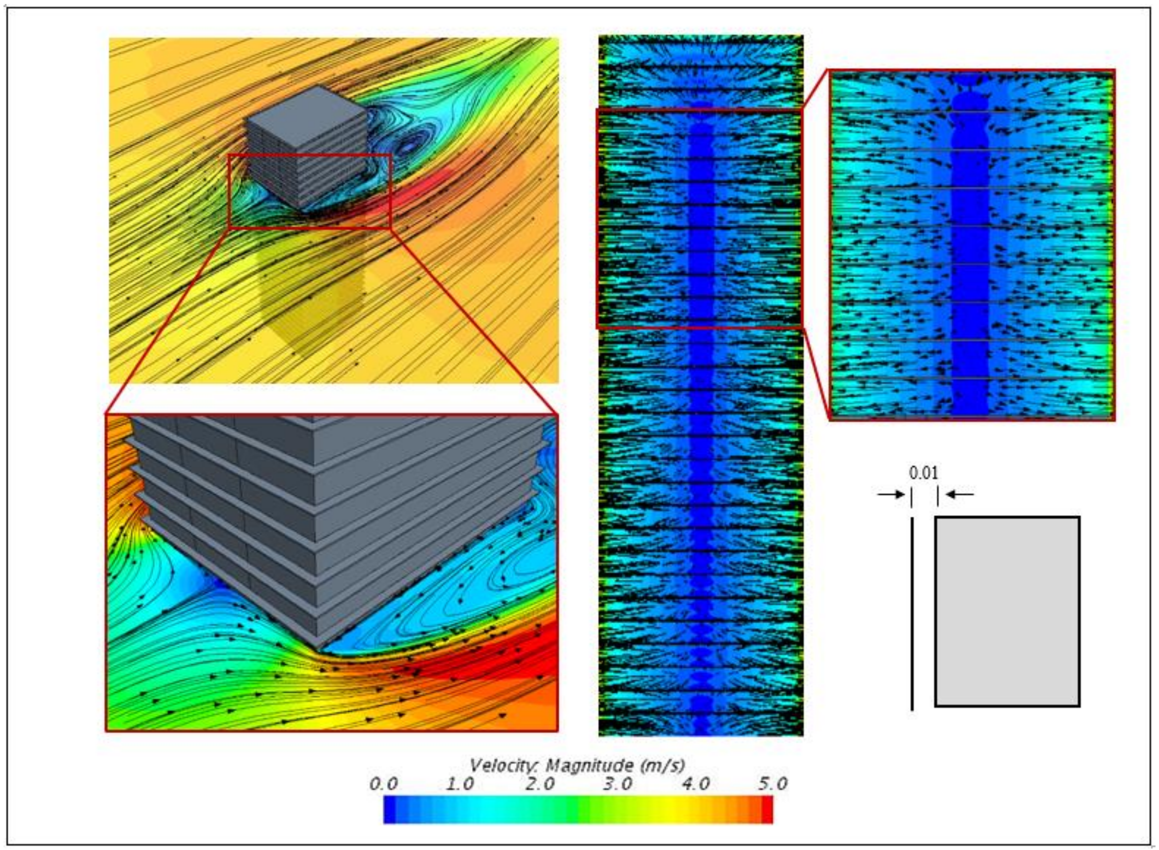

Figure 3-9: Wind velocity vector and contour plots at distance of 0.01m from the wall for a building with horizontal shading (Ref. speed U_{10} = 3 m/s at the inlet)

Therefore, a comparison between the corner and center zones of the building on local-*CHTC* distribution is made at different zone 1, 5, and 10 of the building heights (see Figure 3-8). For instance, for the case of a building having 1 m depth of external shading, the *CHTC* value at the corner-zone has increased by 34%, 35%, and 27% on zone 1, 5, and 10, respectively compared to the center zone (as illustrated in Figure 3-10).

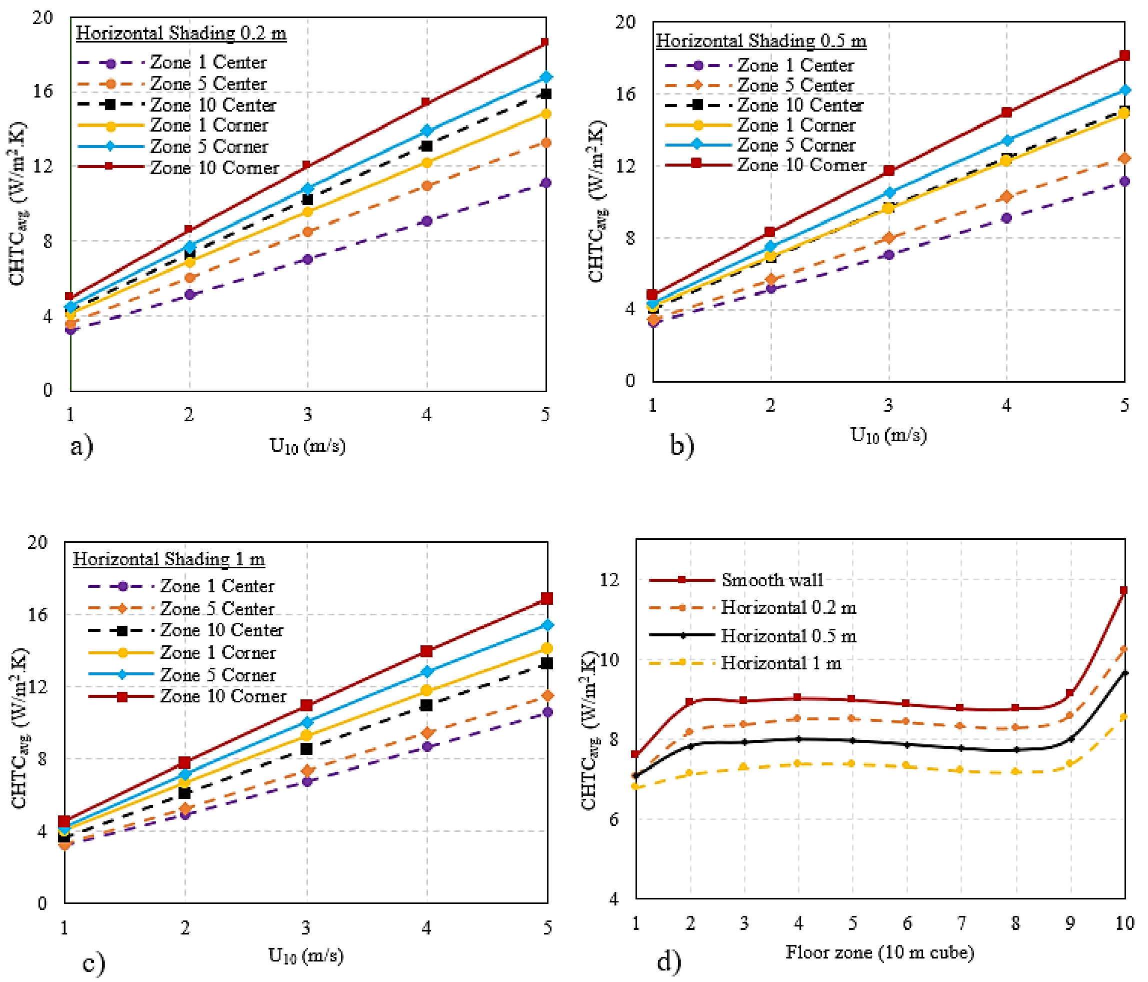

Figure 3-10: Surface-averaged per zone *CHTC* comparison for buildings without and with horizontal shading depth of a) 0.2 m, b) 0.5 m, c) 1.0 m, and d) Surface-averaged per floor comparison between different shading depths

3.3.4 Building with vertical shading

For the case of buildings with vertical shading elements and considering the windward façade, the stagnation pressure forces the impinging wind flow primarily towards the top corner and the ground, and this is due to the obstruction of the mullions (see Figure 3-11). Near-wall velocity increases towards the leading top corner, which leads to higher surface friction velocity. As a result, a higher *CHTC* value is observed at the top corners of the building.

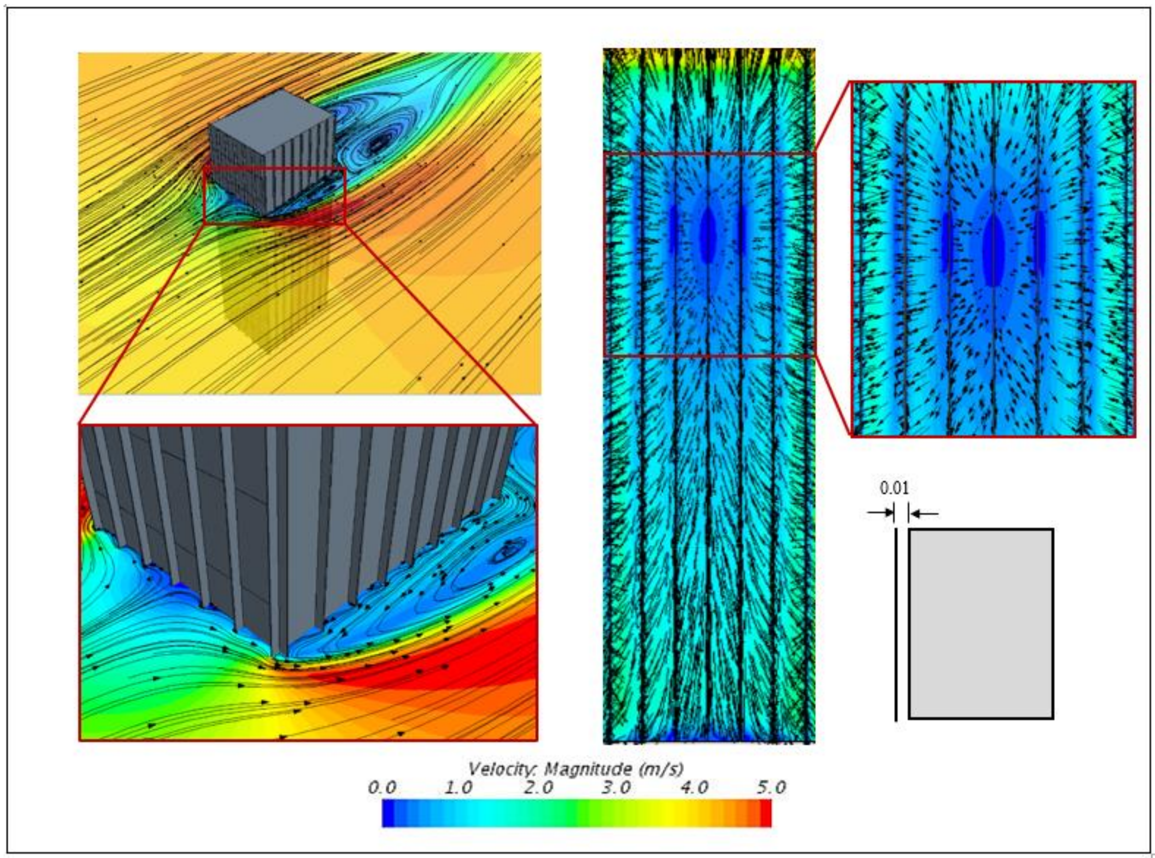

Figure 3-11: Wind vector and contour plots at distance of 0.01m from the wall for a building with vertical shading (Ref. speed U_{10} = 3 m/s at the inlet)

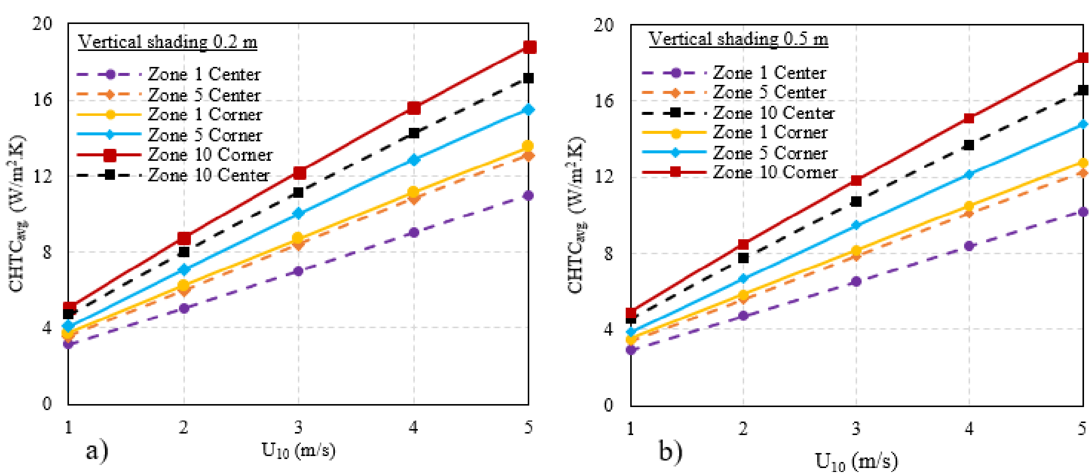

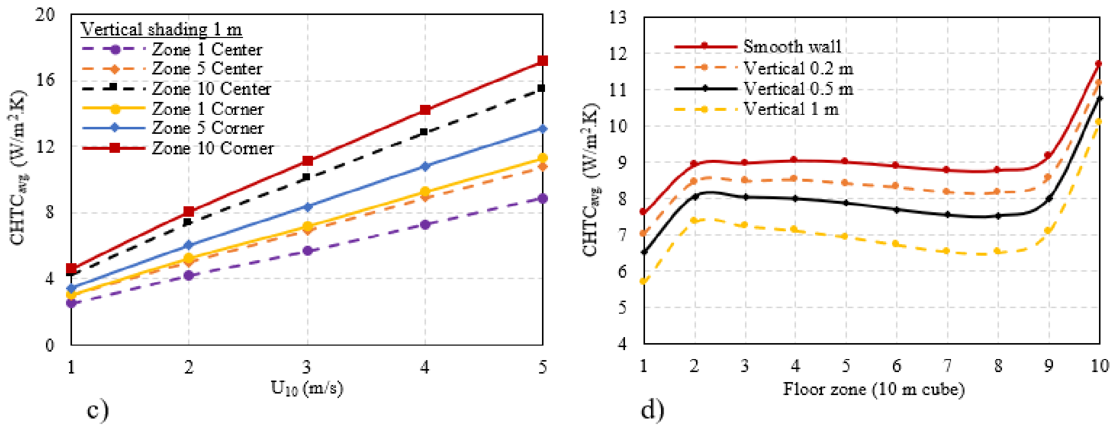

Figure 3-12: Surface-average per zone *CHTC* comparison for buildings without and with vertical shading depth of a) 0.2 m, b) 0.5 m, c) 1.0 m, and d) Surface-averaged per floor comparison between different shading depths

In addition, a comparison on the corner and center of zone 1, 5, and 10 is analyzed. For instance, for the case of a building having 1 m depth external shading, the local-*CHTC* value in the corner-zone has increased by 24.4%, 20.3%, and 10.4% on zone 1, 5, and 10, respectively compared to the center zone as illustrated in Figure 3-12.

3.3.5 Building with egg-crate shading

For the case of buildings with egg-crate shading elements, both the horizontal and vertical shading elements restrict the flow on the surface of the building, this increases the residence time of the air on the building surface resulting in low *CHTC* values as illustrated in Figure 3-13.

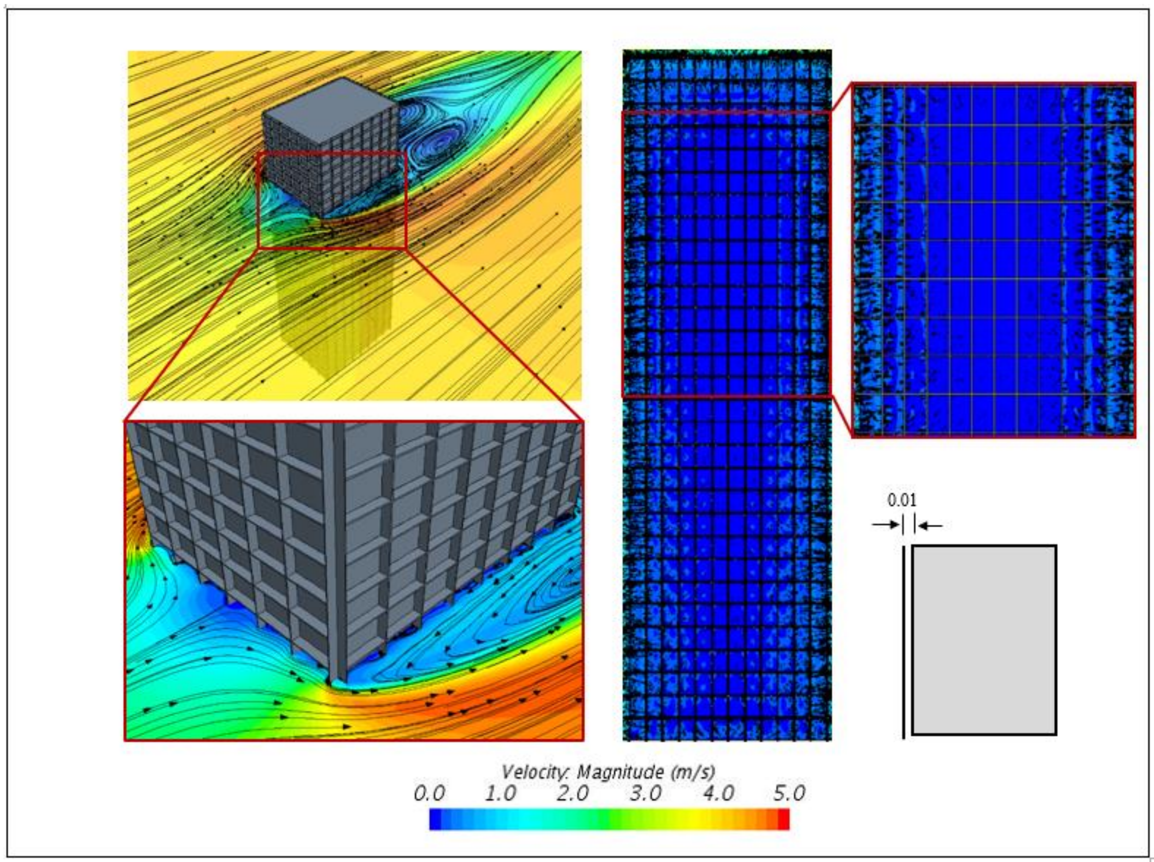

Figure 3-13: Wind velocity vector and contour plots at distance of 0.01m from the wall for building with egg-crate shading (Ref. speed U_{10} = 3 m/s at the inlet)

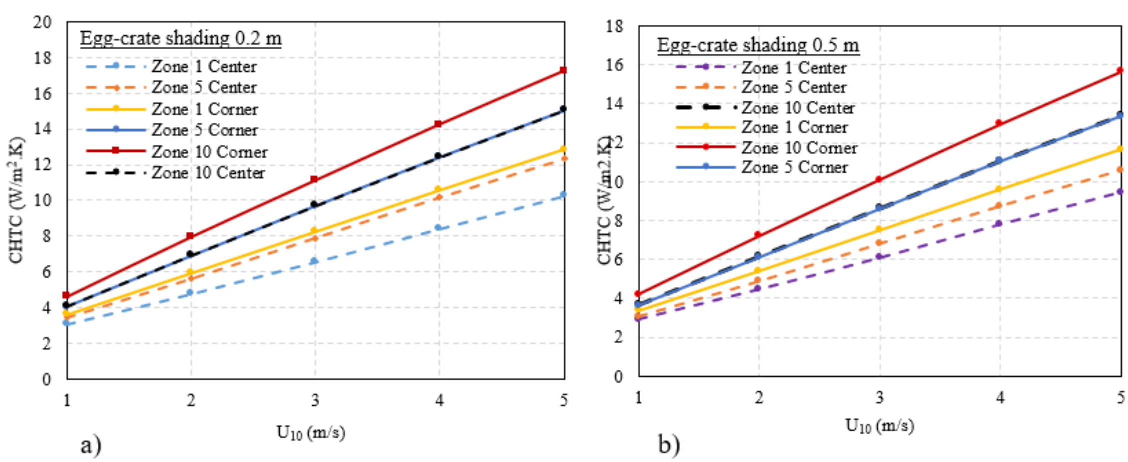

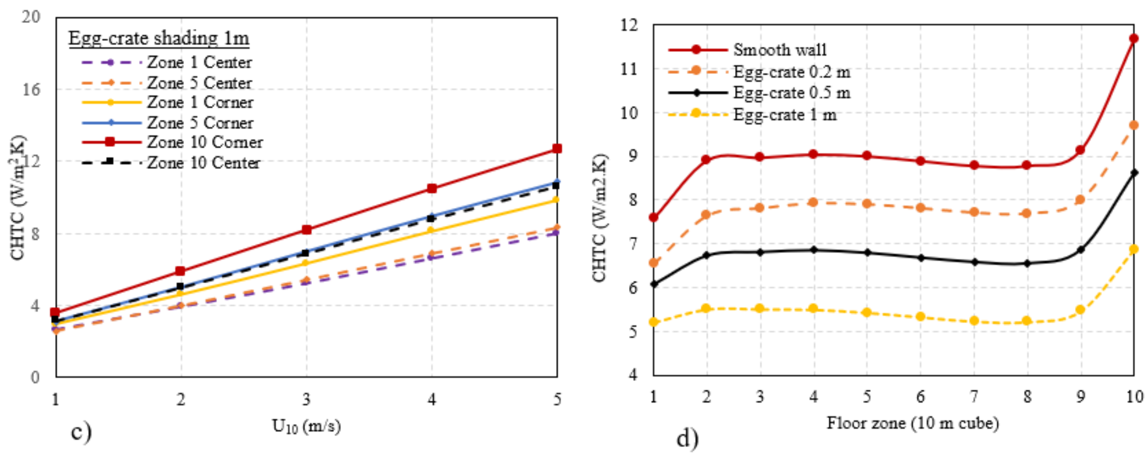

Figure 3-14: Surface-averaged per zone *CHTC* comparison for buildings without and with egg-crate shading depth of a) 0.2 m, b) 0.5 m, c) 1.0 m, and d) Surface-averaged per floor comparison between different shading depths

A comparison between the corner and center zones of the building on local-*CHTC* is made for zones 1, 5, and 10 of the building heights. For the case of a building with 1 m depth of egg-crate external shading, the *CHTC* value at the corner-zone has increased by 20.6%, 28.2%, and 18.9% on zone 1, 5, and 10, respectively, compared to the center zone as illustrated in Figure 3-14.

3.3.6 Wind direction effect on convective heat transfer

Wind direction effect on the *local-CHTC* distribution of buildings with external shading elements is investigated. *CHTC* distribution across the windward façade, calculated for a wind speed of 3 m/s and wind directions of $\theta = 0^{\circ}$, $\theta = 22.5^{\circ}$, $\theta = 45^{\circ}$, $\theta = 67.5^{\circ}$, and $\theta = 90^{\circ}$. In all cases, the surface-average *CHTC* distributions increases from bottom to top and from stagnation point to the edges of the facades. Thus, the highest values are found at the top corners. This is due to the accelerated surface friction velocity that reduces the thickness of the boundary layer. The results with each case of the building external shading configurations are presents below.

3.3.7 Building without external shading

The local-*CHTC* distribution pattern shows some changes with a change in wind direction. The *CHTC* distribution is similar for all wind directions except for the wind direction of 90° (see Figure 3-15) for the simulated wind speed of 3 m/s. For the 90° wind direction, the façade under consideration is inside the separated flow that increases the residence time of the air, which can lead to higher local air temperature and lower *CHTC* value as illustrated in Figure 3-16.

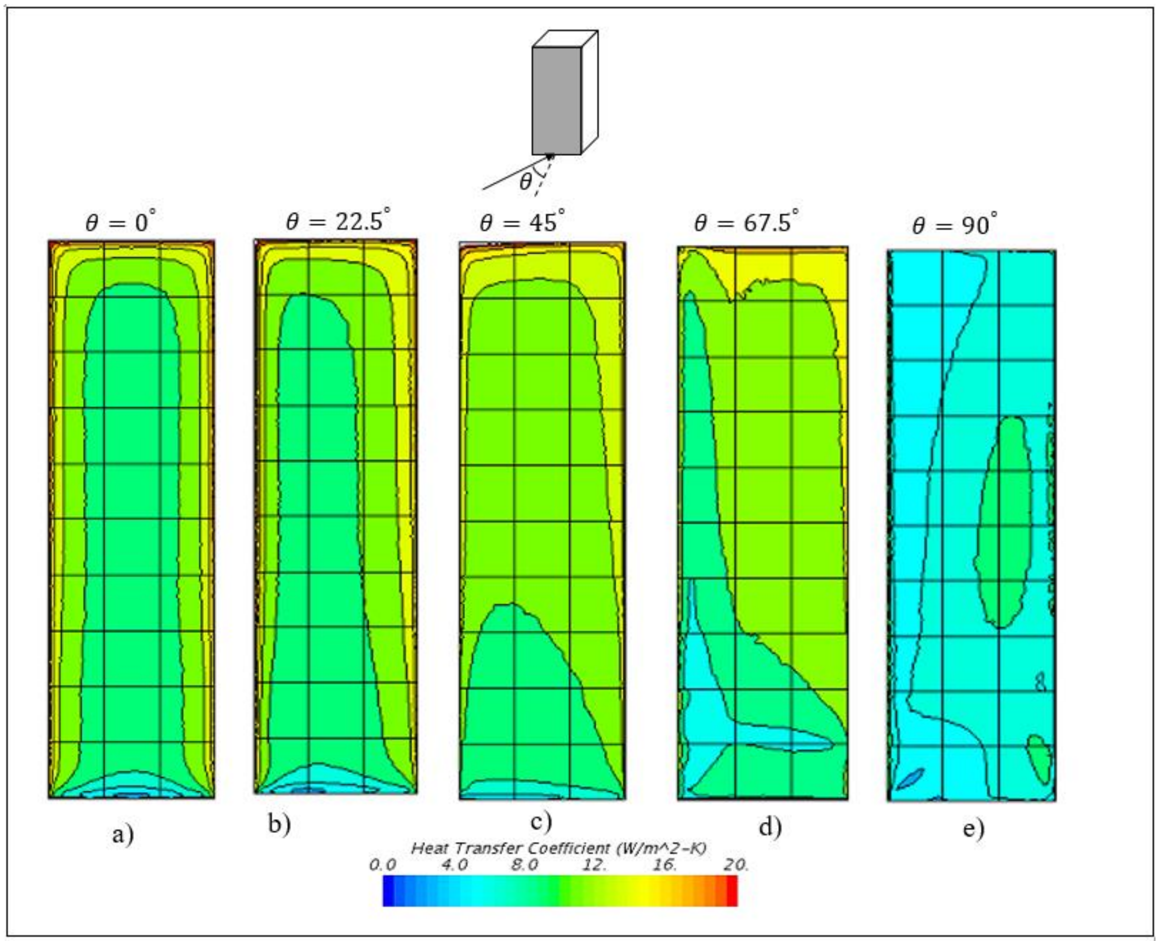

Figure 3-15: *CHTC* distribution on windward façade of smooth wall for wind direction of: a) 0°, b) 22.5°, c) 45°, d) 67.5°, and e) 90° for U_{10} of 3 m/s

It can be seen that (see Figure 3-15) at wind direction of $\theta = 45^{\circ}$, the maximum *CHTC* value occurs at the top and lateral edges where the wind speed is also relatively high. For highly insulated façade systems, the average values do not show significant changes, however, for curtain walls with low thermal resistance such as a window, the *local-CHTC* distribution has an impact on the energy performance of the building attested the need for wind directionality consideration.

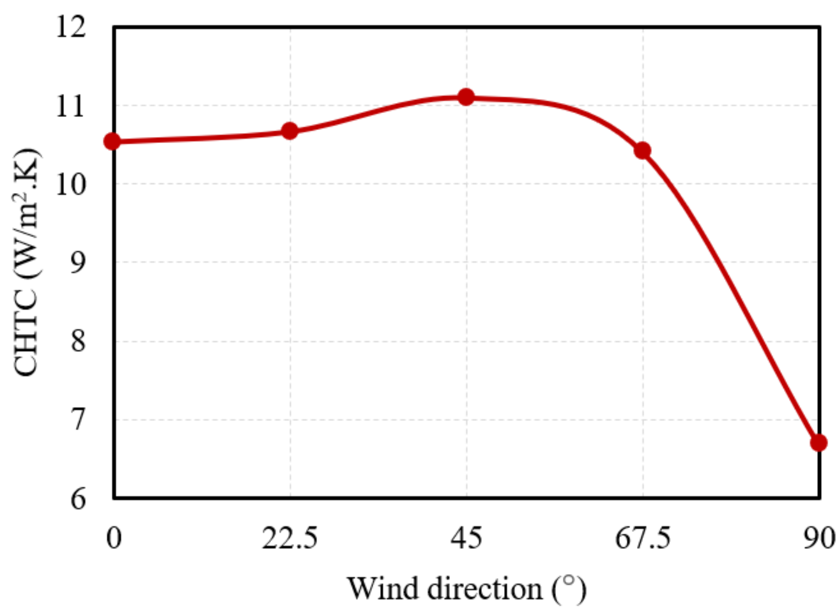

Figure 3-16: Surface-averaged *CHTC* on smooth wall building for U_{10} of 3 m/s

3.3.8 Building with horizontal shading

Due to the horizontally aligned shading effects, the wind flow is guided toward the side corner of the building. Therefore, higher local-*CHTC* values are observed as illustrated in Figure 3-17. This has a significant impact on the rooms, which are located on the corner sides of the building.

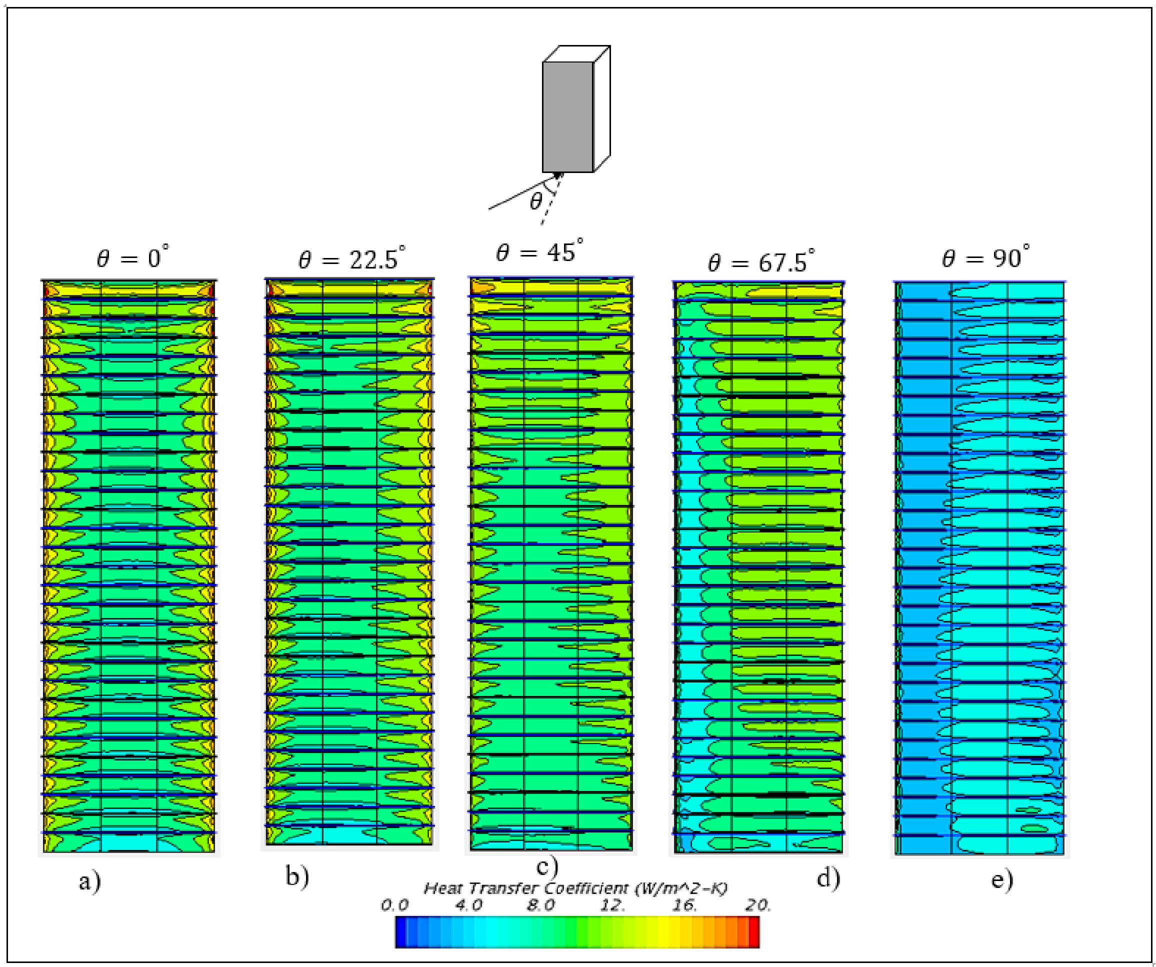

Figure 3-17: ***CHTC*** **distribution on the windward façade of building with horizontal shading for wind direction of: a) 0°, b) 22.5°, c) 45°, d) 67.5°, and e) 90° for** $\mathbf{U_{10}}$ **of 3 m/s**

Figure 3-18 shows a wind direction of $\theta = 45^{\circ}$, the maximum *CHTC* value occurs when the wind speed is relatively high. Since the vertical airflow is restricted by the external shading, the wind directionality will have an effect of the side edges of a building particularly, buildings having large window-to-wall ratio at the corners.

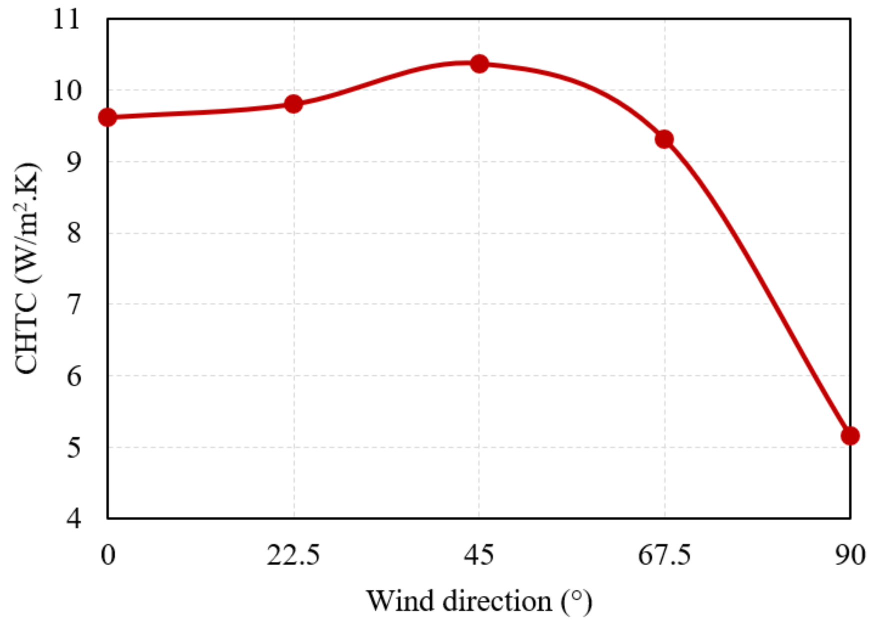

Figure 3-18: Surface- averaged *CHTC* on building with horizontal shading for U_{10} of 3 m/s

3.3.9 Building with vertical shading

Due to the vertical arrangement of external shadings, the surface-average *CHTC* distribution pattern does not show significant changes with a change in wind direction except for the wind direction of 90° (see Figure 3-19) for the simulated wind speed of 3 m/s. However, higher local-*CHTC* are observed at the top edge of the building. This is due to the vertical shading alignment that guides the airflow vertically.

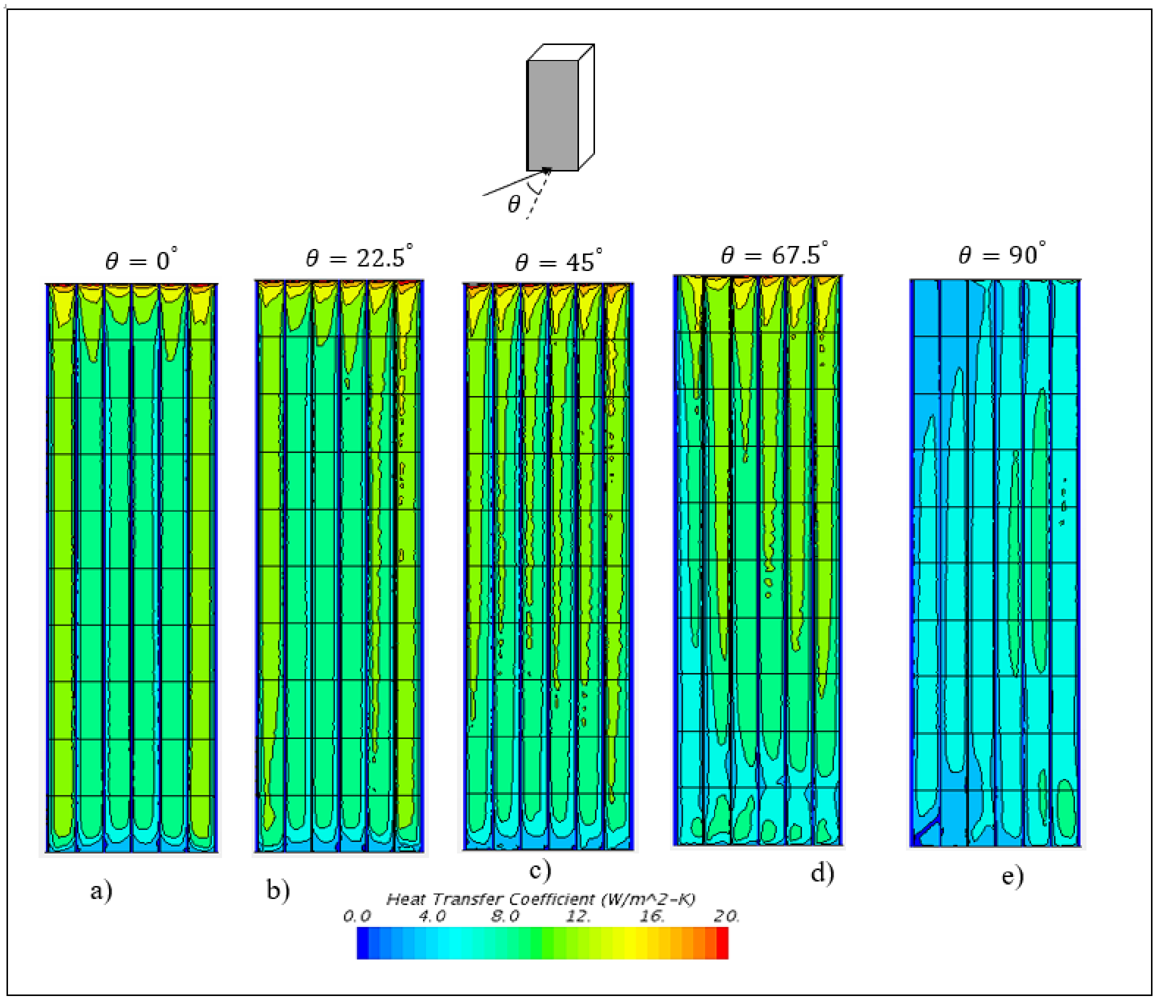

Figure 3-19: *CHTC* distribution on the windward façade of building with vertical shading for wind direction of: a) 0°, b) 22.5°, c) 45°, d) 67.5°, and e) 90° for U_{10} of 3 m/s

In Figure 3-20, it confirms that the relative insensitivity of the *CHTC* distribution at the windward façade to wind direction except at wind direction of $\theta = 90^{\circ}$. This will have an effect mainly at the top edge of the room having a large window-to-wall ratio.

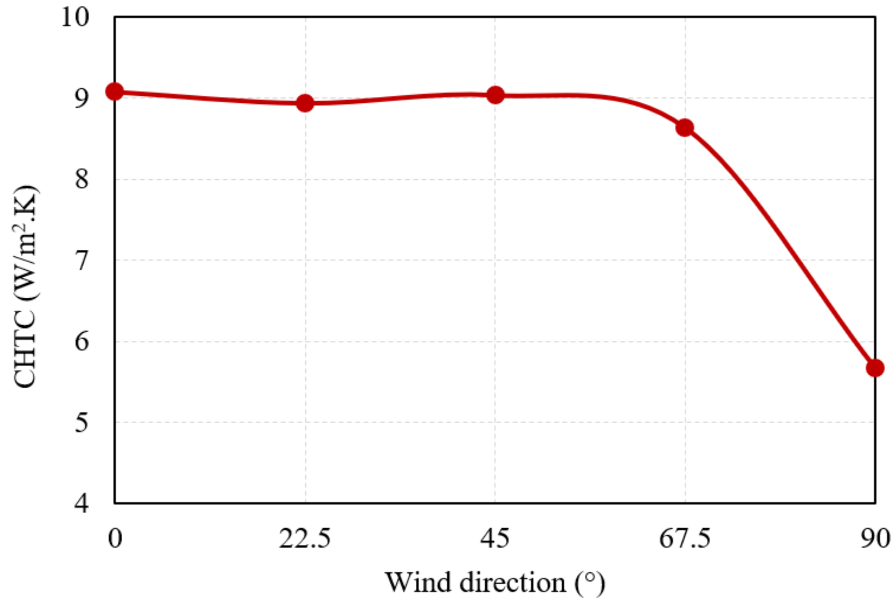

Figure 3-20: Surface- averaged *CHTC* on building with vertical shading for U_{10} of 3 m/s

3.3.10 Building with egg-crate shading

Figure 3-21 shows for egg-crate shaped external shading, the *CHTC* distribution decreases with the wind direction except for the case of 22.5° Angle of Attack (AOA). As the wind direction changes from 0° to 22.5°, the circulated air inside the egg-crate are extracted by the accelerated wind speed leads to a lower resident time of the air, which lowers the thermal resistance of the boundary layer (see Figure 3-22) and shows higher local-*CHTC* values.

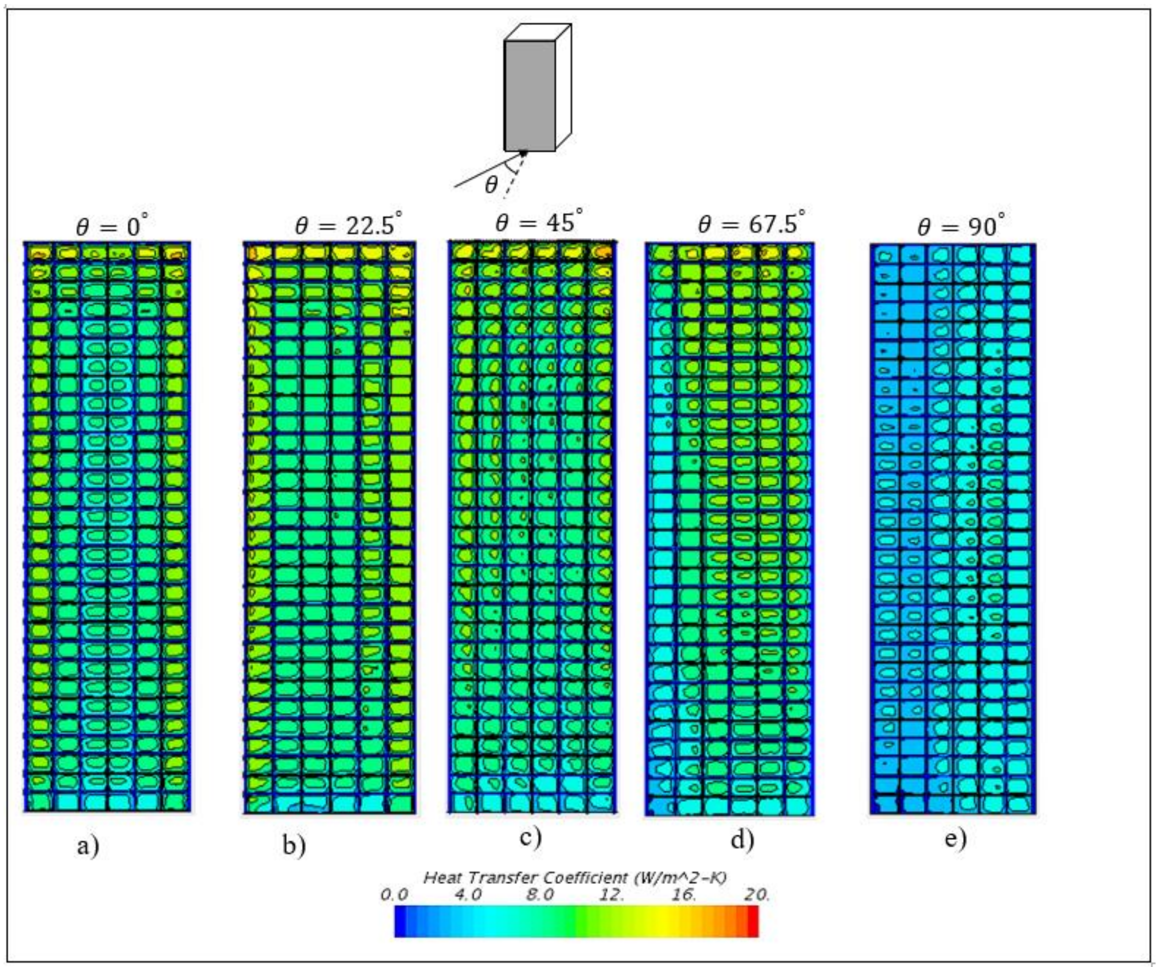

Figure 3-21: ***CHTC*** **distribution on the windward façade of building with egg-crate shading for wind direction of: a) 0°, b) 22.5°, c) 45°, d) 67.5°, and e) 90° for U_{10} of 3 m/s**

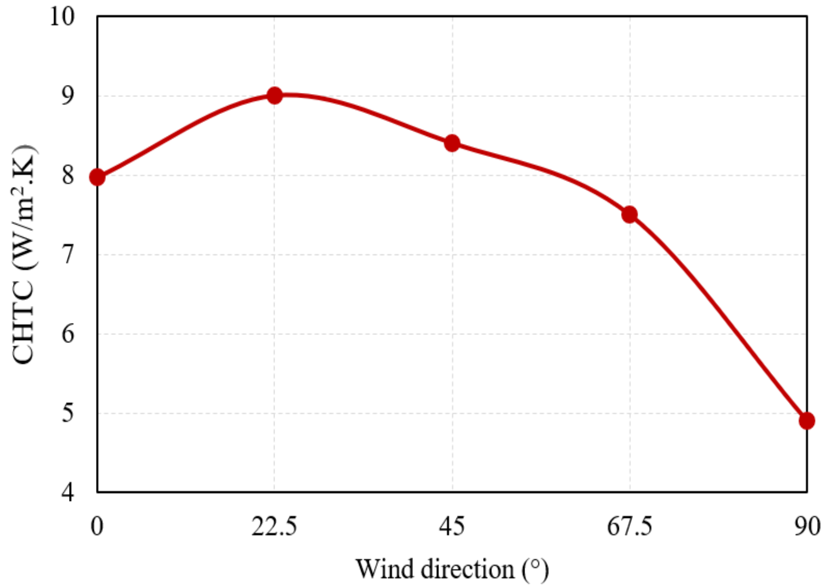

Figure 3-22: Surface- averaged *CHTC* on a building with egg-crate shading for U_{10} of 3 m/s

Overall, for higher R-value wall systems, the average values of *CHTC* may not have an effect. However, for curtain walls or a room with large window-to-wall ratio positioned at the edge side of the building, the local-*CHTC* has an impact on the energy consumption of the particular room and the overall building. Further, it may have impact on surface condensations, thus, it is good practice to assess the effect of wind directionality on buildings with external shading elements.

3.3.11 Shading depth effect

The effect of different external shading forms with three different depths considered for shading elements on the local-*CHTC* distribution of the building is assessesed. A comparison of *CHTC* distribution on the surface of a building is made between a building with and without shading at different zones of the building for U_{10} of 3 m/s.

For Case 1 (see Table 3-2) where the building has a horizontal shading of 1 m depth, the local-*CHTC* at the corner-zone is decreased by 7.6%, 11%, and, 17.2% on the 1st, 5th, and 10th zones, respectively compared with the smooth façade building. For Case 2 where the building has a vertical shading of 1 m depth, the local-*CHTC* at the corner-zone is decreased by 27.3%, 25.3%, and 15.5% on the 1st, 5th, and 10th zones, respectively compared with the smooth facade building. For Case 3 where the building has an egg-crate external shading with 1 m depth, the local-*CHTC* at the corner-zone is decreased by 35.9%, 37.4%, and 37.5% on the 1st, 5th, and 10th zones, respectively compared with the smooth façade building as illustrated in Figures 3-23.

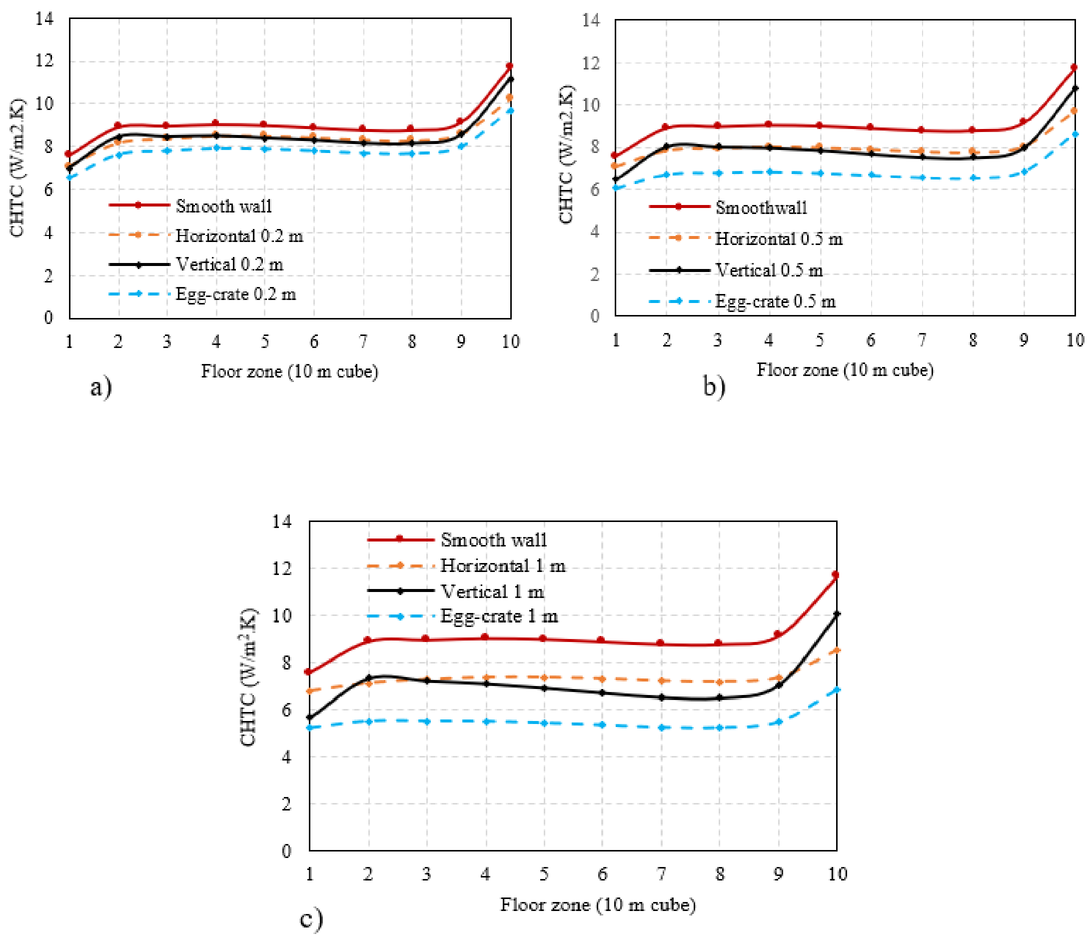

Figure 3-23: Surface- average *CHTC* comparison on four shading with shading depth of a) 0.2 m, b) 0.5 m and c) 1.0 m

Further, for the case where the building has a shading depth of 0.2 m (Case 1), on average 5%, 9%, and 19% of decrement is shown on horizontal, vertical, and egg-crate shading, respectively, compared with smooth facade. For Case 2 i.e. a building with shading depth of 0.5 m, on average 9%, 15%, and 30% decrement are shown on horizontal, vertical, and egg-crate shading, respectively, compared with smooth facade. For case 3 where the building has shading depth of 1 m, on average 13%, 22%, and 46% decrement is shown in horizontal, vertical, and egg-crate shadings respectively, compared to smooth façade.

3.3.12 *CHTC* – U_{10} correlations

The impact of external shading on the *CHTC*-U_{10} correlations is investigated. The results from the previous sections show that local and surface-averaged *CHTC* at the building surface is highly dependent on the immediate flow structure around it that is strongly affected by the shading element details. Thus, average-surface correlations for each of the shading type (smooth, horizontal, vertical, egg-crate) and depth (0.2 m, 0.5 m, and 1 m) are developed. In order to easily integrate the correlations with BES programs, power-law correlations between *CHTC* and U_{10} are derived with a high coefficient of determinations (R^2) as shown in Table 3-3.

Table 3-3: *CHTC* correlation for high-rise building with external shadings

Building type	U_{10} range (m/s)	Shading depth (m)	*CHTC* correlation (W/m^2K)	R^2(-)
Without shading	1 -5	-	$CHTC_{avg} = 4.38U_{10}^{0.96}$	0.9989
Horizontal shading	1 -5	0.2	$CHTC_{avg} = 4.14U_{10}^{0.81}$	0.999
		0.5	$CHTC_{avg} = 4.03U_{10}^{0.8}$	*0.9988*
		1	$CHTC_{avg} = 3.86U_{10}^{0.78}$	*0.9985*
Vertical shading	1 -5	0.2	$CHTC_{avg} = 3.93U_{10}^{0.81}$	*0.999*
		0.5	$CHTC_{avg} = 3.71U_{10}^{0.82}$	*0.9978*
		1	$CHTC_{avg} = 3.37U_{10}^{0.8}$	*0.9992*
Egg-crate shading	1 -5	0.2	$CHTC_{avg} = 3.76U_{10}^{0.8}$	*0.9986*
		0.5	$CHTC_{avg} = 3.4U_{10}^{0.79}$	0.9976
		1	$CHTC_{avg} = 2.89U_{10}^{0.76}$	0.9962

3.4 Conclusion

This study numerically investigated the impact of external shading on the convective heat transfer coefficients. A building with different external shading forms and depths are investigated using a high-resolution 3D steady RANS simulation of convective heat transfer at the façade of a building. Based on the results obtained, the following conclusions can be drawn.

- Validation: A good agreement is achieved on the validation between the experimental and CFD simulated temperature profile, hence, it affirms that the *SST k-ω* turbulent model can be used to predict convective heat transfer on the windward building facades.
- Local aerodynamics: The local and surface-averaged *CHTC* values at the surfaces of each building are dependent on building aerodynamics and forms of the shading element depth. In all cases, the *CHTC* value has reduced with the increase on the building shading depth.
- Surface zone variation: For the case of a building having horizontal shading element with 1 m depth, the local-*CHTC* at the corner-zone is decreased by 7.6%, 11%, and, 17.2% on the 1^{st}, 5^{th}, and 10^{th} zone, respectively compared with the smooth wall building. For a case building having vertical shading with 1 m depth, the local-*CHTC* at the corner-zone is decreased by 27.3%, 25.3%, and 15.5% on the 1^{st}, 5^{th}, 10^{th} zone, respectively compared with the smooth wall building. For the case of a building having egg-crate shading with 1 m depth, the local-*CHTC* at the corner-zone is decreased by 35.9%, 37.4%, and 37.5% on the 1^{st}, 5^{th}, and 10^{th} zone, respectively compared with the smooth wall building.
- Shading elelment depth effect: Considering the surface-averaged *CHTC*, for Case 1 of the study where a building having a shading depth of 0.2 m, on average 5%, 9%, and 19% of decrement is shown on horizontal, vertical, and egg-crate shading respectively. For the case of 2 where a building is having shading depth of 0.5 m, on average 9%, 15%, and 30% decrement are shown on horizontal, vertical, and egg-crate shading respectively. For case 3 where the building has shading depth of 1 m, on average 13%, 22%, and 46% decrement is shown in horizontal, vertical, and egg-crate shadings respectively.
- Wind directionality effect: Wind direction affects the *CHTC* distribution regardless of whether a building is with or without shading. Particularly, rooms located at the side edge of the building shows higher local-*CHTC* values.

- New *CHTC* correlations: To integrate the new-*CHTC* correlations derived from the CFD into BES programs, power-law correlations between *CHTC* and U_{10} are derived with a high coefficient of determinations.
- Local effects: For buildings with high R-value cladding systems, the use of an average value of *CHTC* may not have an effect. However, for curtain walls or a room with large window-to-wall ratio positioned at the edge side of the building, the local-*CHTC* has an impact on the energy consumption of the building, therefore, this study shows the importance of local effect assessment.

In summary, the external feature (i.e. aerodynamics) of a building has an impact on moderating the microclimate effects. Thus, the egg-crate shading form shows the highest *CHTC* reduction compared to vertical, horizontal shadings. Building with horizontal shading shows higher local-*CHTC* value at the side edge of the building, however, for the case of a building with vertical shading higher local-*CHTC* values are observed at the top edge of the buildings, this is due to accelerated wind speed guided by the shading elements. Since a type of shading element and its depth play a critical role in the convective heat transfer rate of a building, it is recommended that the shading elements should be designed by optimizing for the solar effect mitigation and convective wind effects. For further study, the new-*CHTC* correlations that are developed from CFD can be be compared with the existing-*CHTC* correlations in order to investigate the impact of external shadings on the annual energy consumption for high-rise buildings.

3.5 References

A.H. Taki, D.L. Loveday. (1996). "External convection coefficients for framed rectangular elements on building facades." Energy. Build. 24 (1996) 147–154.

ASHRAE Task Group. (1975). Procedure for determining heating and cooling loads for computerizing energy calculations. Algorithms for building heat transfer subroutines, ASHRAE, New York, 1975, pp. 76–78.

A. Hagishima, J. Tanimoto. (2003). Field measurements for estimating the convective heat transfer coefficient at building surfaces, Build. Environ. 38 (7) (2003) 873–881.

Awadh, O. F. (2013). The Impact of External Shading and Windows' Glazing and Frame on Thermal Performance of Residential House in Abu-Dhabi.

Bellia, L., De Falco, F., & Minichiello, F. (2013). Effects of solar shading devices on energy requirements of standalone office buildings for Italian climates. *Applied Thermal Engineering*, *54*(1), 190-201.

Bergman, T. L., & Incropera, F. P. (2011). *Fundamentals of heat and mass transfer*. John Wiley & Sons.

Booten, C., N. Kruis, and C. Christensen. (2012). Identifying and Resolving Issues in EnergyPlus and DOE-2 Window Heat Transfer Calculations. National Renewable Energy Laboratory. NREL/TP-5500-55787. Golden, CO.

Blocken, B., Defraeye, T., Derome, D., Carmeliet, J. (2009). "High-resolution CFD simulations for forced convective heat transfer coefficients at the facade of a low-rise building." Build Environ; 44:2396–412.

Bueno, B., Wienold, J., Katsifaraki, A., & Kuhn, T. E. (2015). Fener: A Radiance-based modelling approach to assess the thermal and daylighting performance of complex fenestration systems in office spaces. *Energy and Buildings*, *94*, 10-20.

Dagnew, A. K., & Bitsuamlak, G. T. (2014). Computational evaluation of wind loads on a standard tall building using LES. *Wind and Structures*, *18*(5), 567-598.

DoE, U. S. (2016). EnergyPlus engineering reference. *The reference to energyplus calculations*.

De Wilde, P. (2014). The gap between predicted and measured energy performance of buildings: A framework for investigation. *Automation in Construction*, *41*, 40-49.

Dubois, M. C. (1997). Solar shading and building energy use. *Lund University*.

Defraeye, T., Blocken, B., Carmeliet, J. (2010). “CFD analysis of convective heat transfer at the surfaces of a cube immersed in a turbulent boundary layer.” Int. J Heat Mass Transf; 53:297–308.

Defraeye, T., Blocken, B., & Carmeliet, J. (2011). Convective heat transfer coefficients for exterior building surfaces: Existing correlations and CFD modeling. *Energy Conversion and Management*, *52*(1), 512-522.

D.L. Loveday, A.H. Taki. (1996). “Convective heat transfer coefficients at a plane surface on a full-scale building façade.” Int. J. Heat Mass Transfer 39 (8) (1996) 1729–1742.

E.M. Sparrow, S.C. Lau. (1981). “Effect of adiabatic co-planar extension surfaces on wind-related solar-collector heat transfer coefficients.” Trans. ASME J. Heat Transfer 103 (1981) 268–271.

Engineering Sciences Data Unit (ESDU) 85020. (2001). “Characteristics of atmospheric turbulence near the ground.” Part II: Single point data for strong winds.

Franke, J., Hellsten, A., Schlünzen, H., Carissimo, B. (2007). “Best practice guideline for the CFD simulation of flows in the urban environment COST 2007.” Action 732.

Kahsay, M. T., Bitsuamlak, G., & Tariku, F. (2018a). Numerical analysis of convective heat transfer coefficients for building Façade. Journal of building physics.

Kahsay, M., Bitsuamlak, G., & Tariku, F., (2018b). Influence of external shading on convective heat transfer of high-rise buildings. Building Performance Analysis Conference and Sim-Build co-organized by ASHRAE and IBPSA-USA Chicago, IL September 26-28, 2018.

Kirimtat, A., Koyunbaba, B.K., Chatzikonstantinou, I. and Sariyildiz, S. (2016). Review of simulation modeling for shading devices in buildings. *Renewable and Sustainable Energy Reviews*, *53*, pp.23-49.

J.W. Mitchell. (1971). “Base heat transfer in two-dimensional subsonic fully separated flows”. Trans. ASME J. Heat Transfer (1971) 342–348.

Hien, W. N., & Istiadji, A. D. (2003, August). Effects of external shading devices on daylighting and natural ventilation. In *Proceedings of the 8th International IBPSA Conference, Eindhoven, The Netherlands* (pp. 475-482).

Lau, A. K. K., Salleh, E., Lim, C. H., & Sulaiman, M. Y. (2016). Potential of shading devices and glazing configurations on cooling energy savings for high-rise office buildings in hot-humid climates: The case of Malaysia. *International Journal of Sustainable Built Environment*, *5*(2), 387-399.

Lee, E. S., & Tavil, A. (2007). Energy and visual comfort performance of electrochromic windows with overhangs. *Building and Environment*, *42*(6), 2439-2449.

Lawrence Berkeley Laboratory (LBL) (1994). DOE2.1E-053 Source Code.

Maruta, E., Kanda, M., & Sato, J. (1998). Effects on surface roughness for wind pressure on glass and cladding of buildings. *Journal of Wind Engineering and Industrial Aerodynamics*, *74*, 651-663.

M. Yazdanian, J.H. Klems. (1994) "Measurement of the exterior convective film coefficient for windows in low-rise buildings". ASHRAE Trans. 100 (1) (1994) 1087–1096.

Menezes, A. C., Cripps, A., Bouchlaghem, D., & Buswell, R. (2012). Predicted vs. actual energy performance of non-domestic buildings: Using post-occupancy evaluation data to reduce the performance gap. *Applied Energy*, *97*, 355-364.

Mirsadeghi, M., Costola, D., Blocken, B., Hensen, J.L. (2013). "Review of external convective heat transfer coefficient models in building energy simulation programs: Implementation and uncertainty." Appl. Therm. Eng., 56, 134–151.

M.G. Emmel, M.O. Abadie, N. Mendes. (2007). "New external convective heat transfer coefficient correlations for isolated low-rise buildings." Energ. Build. 39 (2007) 335–342.

Montazeri, H., Blocken, B., Derome, D., Carmeliet, J., & Hensen, J. L. M. (2015). CFD analysis of forced convective heat transfer coefficients at windward building facades: influence of building geometry. *Journal of Wind Engineering and Industrial Aerodynamics*, *146*, 102- 116.

Montazeri, H., & Blocken, B. (2017). New generalized expressions for forced convective heat transfer coefficients at building facades and roofs. *Building and Environment*, *119*, 153-168.

Montazeri, H., & Blocken, B. (2018). Extension of generalized forced convective heat transfer coefficient expressions for isolated buildings taking into account oblique wind directions. *Building and Environment*, *140*, 194-208.

Norris, N. E. I. L., Lawton, M., & Roppel, P. (2012, April). The concept of linear and point transmittance and its value in dealing with thermal bridges in building enclosures. In *Building enclosure science & technology conference*.

N. Ito, K. Kimura, J. Oka. (1972). "A field experiment study on the convective heat transfer coefficient on exterior surface of a building." ASHRAE Trans. 78 (1972) 184–191.

Nielsen, M. V., Svendsen, S., & Jensen, L. B. (2011). Quantifying the potential of automated dynamic solar shading in office buildings through integrated simulations of energy and daylight. *Solar Energy*, *85*(5), 757-768.

Palyvos, J.A. (2008). "A survey of wind convection coefficient correlations for building envelope energy systems modeling." Appl. Therm. Eng., 28, 801–808.

Richards, P. J., & Norris, S. E. (2011). Appropriate boundary conditions for computational wind engineering models revisited. *Journal of Wind Engineering and Industrial Aerodynamics*, *99*(4), 257-266.

SHARCNET is a consortium of colleges, universities and research institutes operating a network of high-performance computer clusters across southwestern, central and northern Ontario [Online].Available: <www.sharcnet.ca>; 2015.

S. Sharples. (1984). “Full-scale measurements of convective energy losses from exterior building surfaces.” Build. Environ. 19 (1984) 31–39.

Stazi, F., Marinelli, S., Di Perna, C., & Munafò, P. (2014). Comparison on solar shadings: Monitoring of the thermo-physical behaviour, assessment of the energy saving, thermal comfort, natural lighting and environmental impact. *Solar Energy*, *105*, 512-528.

Simmler, H., & Binder, B. (2008). Experimental and numerical determination of the total solar energy transmittance of glazing with venetian blind shading. *Building and Environment*, *43*(2), 197-204.

STAR CCM+. CD-ADAPCO product. (2015). www.cdadapco.com/products/star-ccm

Tzempelikos, A., & Athienitis, A. K. (2007). The impact of shading design and control on building cooling and lighting demand. *Solar Energy*, *81*(3), 369-382.

Tzempelikos, A., & Athienitis, A. K. (2007). The impact of shading design and control on building cooling and lighting demand. *Solar energy*, *81*(3), 369-382.

Tominaga, Y., Mochida, A., Yoshie, R., Kataoka, H., Nozu, T., Yoshikawa, M., Shirasawa, T. (2008). “AIJ guidelines for practical applications of CFD to pedestrian wind environment around buildings.” Journal of Wind Engineering and industrial aerodynamics, 96(10), 1749-1761.

Yao, J. (2014). An investigation into the impact of movable solar shades on energy, indoor thermal and visual comfort improvements. *Building and environment*, *71*, 24-32.

Yazdanian, M., Klems, J.H. (1994). “Measurement of the exterior convective film coefficient for engineering models using k-e turbulence model.” J. Wind Eng. Ind. Aerodyn. 46:145–53 windows in low-rise buildings.” ASHRAE Trans; 100(1): 1087–96.

W. Nusselt, W. Ju¨rges, (1922). “Die Ku¨hlung einer ebenen Wand durch einen Luftstrom (The cooling of a plane wall by an air flow), Gesundheits Ingenieur 52. Heft, 45. Jahrgang, (30 Dezember 1922) pp. 641–642.

W.H. McAdams. (1954). “Heat Transmission, third ed., McGraw-Hill Kogakusha, Tokyo, Japan, 1954, p. 249.

W. Ju¨ rges. (1924). “Der Wa¨rmeu¨bergang an einer ebenen Wand (Heat transfer at a plane wall)”. Beiheft Nr. 19 zum ‘‘Gesundh.- Ing.” (1924), appearing in Gesundheits-Ingenieur 9. Heft, 48. Jahrg., 1925, p. 105.

Walton, G.N. (1983). Thermal Analysis Research Program Reference Manual, NBSSIR 83e2655, National Bureau of Standards.

Chapter 4

4 Effect of exterior convective heat transfer on high-rise building energy consumption

4.1 Introduction

Buildings use about 40% of global energy and emit approximately 33% of GHG emissions (UNEP, 2017). Realizing the significant amount of energy consumption in buildings, it is essential to investigate the accuracy of the estimation of energy consumption predictions by the Building Energy Simulation (BES) programs at the early design stages to achieve long-term sustainability. Many BES programs can be used to analyze the energy consumption by low-rise buildings efficiently; however, they have some fundamental limitations when applied to high-rise buildings. Some of the limits include a size of the building, changes in microclimate at different altitudes, and the uncertainties associated with the existing convective heat transfer coefficients (*CHTC*) correlations. The height of a high-rise building means that there are many thermal-zones, which are a collection of spaces having a similar space-conditioning requirement and the same heating and cooling set point. For instance, considering a 70-story office building where each floor has four perimeter zones, a core zone, and a plenum zone, the modeling would require 420 thermal-zones (70 floors * 6 zones) (Ellis and Torcellini, 2005). Consequently, the user requires extensive input data to define the energy analysis problem, which can be computationally expensive. Furhter, the size of a building introduces some challenges in the building energy analysis. For instance, as the building width increases, the aerodynamics around the building will be changed. Large width leads to more air blockage near the center and accelerated airflow near the corners. This will result in lowers convective heat transfer at the center and more convective heat loss near the corner. These types of variations are not commonly considered in the current practices. In addition, as the building size increases rooms energy requirements increase such as, light and thermal scheduling couple with a purpose of the rooms, cafeteria, office etc., and these lead to complex system design of the thermal load analyzes.

To deal with these limitations, the common practice is to select and simulate only a few floors at the mid-height of the high-rise building and then multiply the results by a factor to estimate the energy consumption of the entire building (Ellis and Torcellini, 2005). EnergyPlus has a built-in multiplier to perform this action. The main problem with this kind of multiplier approach is that it may decrease the accuracy of the overall energy prediction, which may lead to local thermal discomfort in individual rooms and unexpected surface condensations. This is because the selected representative floor or rooms may not adequately capture the energy consumption variations along the building height. Further, high-rise buildings are exposed to different wind speeds along the building height that significantly effects the local *CHTC* distributions. Due to these variations in airflow characteristics, the energy consumption of each room at different floor heights of the building also varies.

Buildings interact with the atmosphere through convective heat transfer between the outside air and the exterior surface of the building façade, and through the exchange of air between the outside and inside of the building through infiltration/exfiltration. The external convective heat transfer is defined as in Equation 4-1:

$$CHTC = \frac{q_c}{(T_{sur} - T_{air})} \qquad \text{Equation 4-1}$$

where *CHTC* $(\mathrm{W/m^2.K})$ is convective heat transfer coefficient, q_c is local surface heat flux ($\mathrm{W/m^2}$), T_{sur} is surface temperature (K), and T_{air} is the reference air temperature (K).

Since the 1930s, many methods have been proposed to calculate this coefficient, but each method has had significant differences (Yazdanian and Klems, 1994; Palyvos, 2008; Mirsadeghi et al., 2013). Thus, the variations on these correlations can easily cause errors in energy demand calculations in the order of 20% – 40% (Palyvos, 2008). For example, EnergyPlus, one of the widely used BES programs, offers a wide selection of *CHTC* correlations based on low-rise buildings, flat plate, and vertical windows (Palyvos, 2008; Defraeye et al., 2011). The common existing-*CHTC*s correlations in EnergyPlus are DoE-2 (LBL, 1994), Simple Combined (DoE, 2016), Thermal Analysis Research Program -

TARP (Walton, 1983), and Mobile Window Thermal Test - MoWiTT (Yazdanian and Klems, 1994; Booten et al., 2012).

The DoE-2 model is a combination of the MoWiTT and Building Load Analysis and system Thermodynamics - BLAST (Sparrow et al., 1979) convectional models. This model considers different surface textures, windward and leeward orientations, and different surface slope angles but its application is limited to low-rise building with very smooth surfaces e.g. glass (Mirsadeghi et al., 2013; DoE, 2016). The simple combined is based on simple second-degree polynomial equations proposed by ASHRAE (2009). This simple algorithm uses surface roughness and local surface wind speed to calculate the exterior heat transfer coefficient. The roughness correlation is taken from the ASHRAE Handbook of Fundamentals (ASHRAE, 2009).

The MoWiTT algorithm offers a reasonable balance between accuracy and ease of use (Palyvos, 2008). This model is based on measurements taken at the Mobile Window Thermal Test facility (Yazdanian and Klems, 1994). This correlation also applies to very smooth, vertical surfaces (e.g. window glass) in low-rise buildings. The original MoWiTT model has been modified for use in EnergyPlus so that it is sensitive to the local surface's wind speed, which varies with the height above ground. However, the MoWiTT algorithm may not be appropriate for rough surfaces (e.g. external architectural features) or high-rise buildings (DoE, 2016). TARP is an important predecessor of EnergyPlus (Walton 1983). Walton developed a comprehensive model for exterior convection by blending correlations from ASHRAE and flat plate experiments by Sparrow et al. (1979). The model was reimplemented to use Area and Perimeter values for the group of surfaces that make up a facade or roof, rather than the single surface being modeled (DoE, 2016). The Building Loads Analysis and System Thermodynamics (BLAST) model is based on wind tunnel experiments performed by Sparrow et al. (1979). While this model is rather comprehensive, it does not consider variations in building type (high-rise, medium, or low-rise), and surface orientation (Mirsadeghi et al., 2013). Previous study of Liu et al. (2015) has investigated the impact of the existing-*CHTC* correlations on a low-rise building energy consumption in urban neighborhoods with different plan area densities, and the result indicated that there is a direct impact of the urban microclimate variation on the energy performance of buildings. All the equations shown in Table 4-1 are derived from a low-rise building (Mirsadeghi et al., 2013). The use of these correlations for the analysis of the energy consumption of high-rise buildings will have an impact on the accuracy of the estimation. This is because the wind flow pattern around a building is highly dependent upon the geometry and height of the building, resulting in local-*CHTC* variations. Further, rooms of a similar size, on the same floor, positioned at the edge or center zone of the building may have different energy consumption rates.

In recent years, numerous studies have used CFD to develop surface-averaged *CHTC*-U_{10} expression, such as the influence of wind speed (Emmel et al., 2007; Blocken et al., 2009; Defraeye et al., 2010; Montazeri et al., 2016; Jousef et al., 2017; Montazeri et al., 2017 & 2018), wind direction (Blocken et al., 2009; Montazeri et al, 2018) and building geometry (Montazeri et al., 2015, 2017, and 2018). Further, a study by Montazeri et al. (2015), which used a various height configuration ranging from 10 to 80 m a correlation of $CHTC/(U_{10}^{0.84})$ relatively insensitive to U_{10} for each building was developed by averaging the maximum and minimum values of the case study buildings. However, in the present study, the impact of local-*CHTC* variations on energy consumption focusing on a high-rise building with curtain claddings is investigated. For this purpose, detail CFD simulations will be conducted considering the specificity of the study building and its local microclimate.

More specifically, a 100 m tall building, exposed to open wind field conditions, having floor dimensions of 30 m width by 40 m in-depth and exposed to different microclimate conditions will be considered. The floor plan is adopted from the CAARC (Commonwealth Advisory Aeronautical Research Council) building which is a typical building used as a benchmark for various aerodynamics studies (Dagnew and Bitsuamlak 2014). Different window-to-wall ratios and analysis for rooms located at different positions in the building are considered. Consequently, the aerodynamic effect on the existing-*CHTC* will be investigated for wind speeds ranging from 1 to 5 m/s. First, at the windward façade of the building, the spatial distribution of the *CHTC* will be calculated using a CFD simulation. The calculated *CHTC* values are then used to define a new surface-averaged *CHTC* correlation as a function of the reference wind speed (U_{10}) for the windward face. Then the new-*CHTC* correlations will be implemented and compared with the existing-*CHTC* correlations in EnergyPlus program. In this approach, the high-resolution CFD and heat transfer simulations have enabled extraction of high spatial resolution of *CHTC* for a wide range of wind speeds accurately.

Table 4-1: Existing-*CHTC* correlations used by the EnergyPlus simulation tool

Correlation name	Correlations	Remarks
DoE-2 (LBL, 1994)	$\sqrt{h_n^2 + \left[aU_{loc}^b\right]^2}$	Windward: a=3.26, b=0.89 Leeward: a=3.55, b=0.617
Simple-combined (DoE, 2016)	$D + EU_{loc} + FU_{loc}^2$	For rough brick, roughness coefficient, D=12.49, E=4.065, F=0.028
TARP (Walton, 1983)	$2.537 W_f R_f \frac{PU_{loc}}{A} + c\lvert\Delta T\rvert^{1/3}$	Windward: W_f = 1.0, Leeward: W_f = 0.5, For rough brick, roughness index R_f = 1.67 Vertical surface, c = 1.31
MoWiTT (Booten et al., 2012)	$\sqrt{\left[aU_{loc}^b\right]^2 + [c\lvert\Delta T\rvert^{1/3}]^2}$	Windward: a = 3.26, b = 0.89, c = 0.84, Leeward: a = 3.55, b = 0.617, c = 0.84

h_n: Natural convection; U_{10}: *local wind speed calculated at the height above ground of the surface centroid;P: perimeter; A: Area*

This chapter is organized into four sections. Section 1 presents an introduction and literature review on the challenges of analyzing the energy consumption for high-rise buildings. Section 2 presents the development of new *CHTCs* using high-resolution CFD and heat transfer simulations. Section 3 presents the application of the new *CHTCs* and other widely used correlations in building energy modeling using BESs and discusses the results comparatively, and Section 4 concludes the chapter.

4.2 New-*CHTC* development using CFD

The study is conducted in two parts. In the first part of the study, an accurate *CHTC* at the windward façade of the building was generated by using high-resolution CFD and heat transfer simulations. In the second part of the study, energy consumption rates, using the newly generated and existing-*CHTC* correlations are compared using EnergyPlus to quantify the impact *CHTC*s have on building energy simulation results. For this study, a 100 m tall building with 3.33 m floor-to-floor height rooms that are exposed to open wind field is considered. The building is described as shown in Figure 4-1. To investigate, in detail, the effect of the room position and window size, two different zones were considered: the corner-zone (all rooms at the edge of the building along the height) and center-zone (all rooms at the center of the building along the height) as shown in Figures 1 and 2.

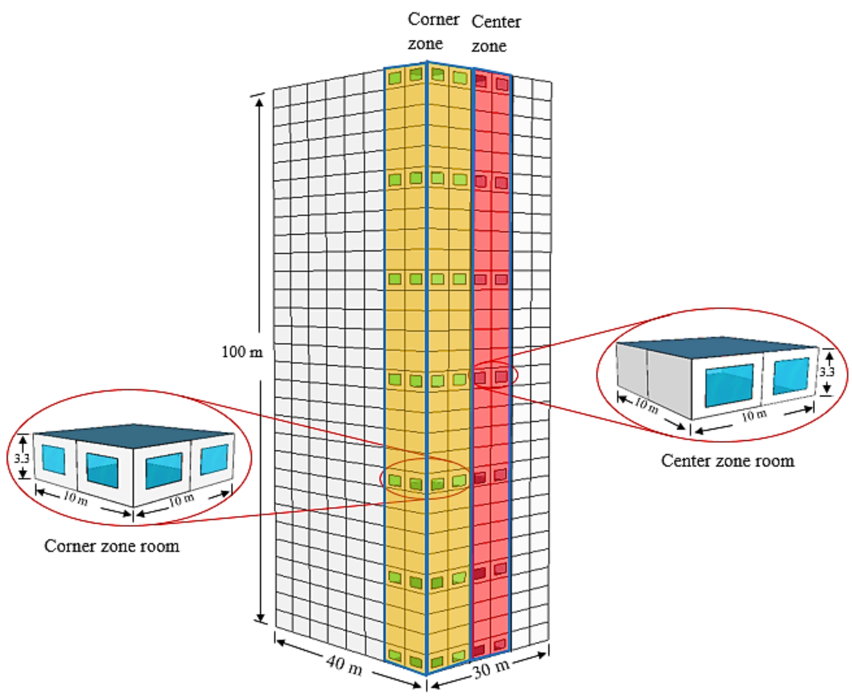

Figure 4-1: High-rise building with 40% window-to-wall ratio

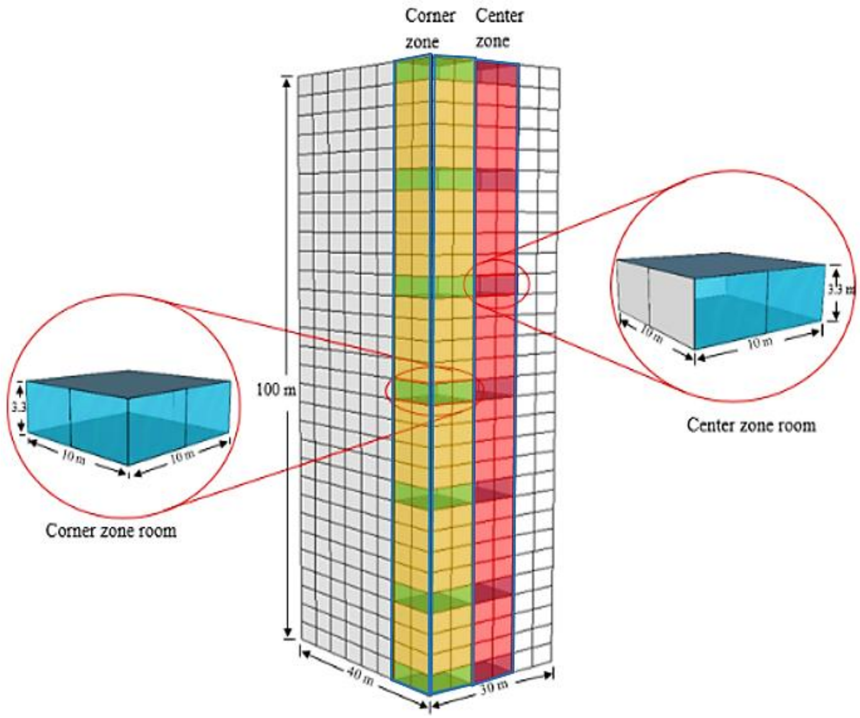

Figure 4-2: High-rise building with 100% window-to-wall ratio

4.2.1 CFD setup

A building exposed to open terrain conditions for five different wind speeds U_{10} = 1, 2, 3, 4 and 5 m/s at the reference height of 10 m is considered. The outdoor air temperature is kept constant at T_{ref} = 283 K, and the building has a fixed surface temperature of T_w = 303 K. The dimensions of the 3-D computational domain (CD) were defined based on the height of the building (H) and recommendations by Franke et al. (2007) and Tominaga et al. (2008) as illustrated in Figure 4-3. The distance between the inflow boundary wall and the building is 5H, with the outflow boundary 15H downstream of the building, to allow the wake-flow to develop. The lateral boundaries are set at 5H from the building surfaces, and the CD height is 5H from the top of the highest building surface. Three sub-computational domain volumes (in short CV) with different grid density and grid distributions were constructed to capture high-velocity gradient zones such as those near the study building and near the ground, behind the study building, etc. Further a low Reynolds number model near the wall region that resolves the viscous sublayer and the buffer layer, which dominates the convective heat transfer in the CD, has been used. The sub-computational domain volume distributions are CV_1 (H/10), CV_2 (H/20), CV_3 (H/25) as illustrated in Figure 4-3. The CD is discretized using polyhedral control volumes with a refined sub-grid near the exterior surfaces of the building. As illustrated in Figure 4-4, the surfaces of the buildings have a viscous boundary layer with ten prism layers, producing $y^+ < 5$ values. A dimensionless wall distance $y^+ = (u_* y_p)/v$, is used to characterize the grid resolution near the wall, where, u_* is friction velocity (m/s), y_p is the distance from the center point of the wall adjacent cell to the wall (m), and v is kinematic viscosity (m^2/s). The simulation uses a sub-grid with cell centres at a minimum distance of 130 μm from the building surface. Hence, a stretching factor of 1.05 is used to resolve the boundary layer at all solid-fluid interfaces of CV3 satisfying the recommendations of Franke et al. (2007) and Tominaga et al. (2008). Grid independency test with grid refinement ratio is 1.5 was carried. More details on grid dependency analysis can be found in the previous study by the same author Kahsay et al. (2018). A total of 4.83 $x10^6$ grid cells are deployed. Convergence is assumed when all the scaled residual values level off and reach 10^{-7} for *x*, *y*, *z* momentum and energy, 10^{-5} for continuity and 10^{-6} for *k* and *ε*.

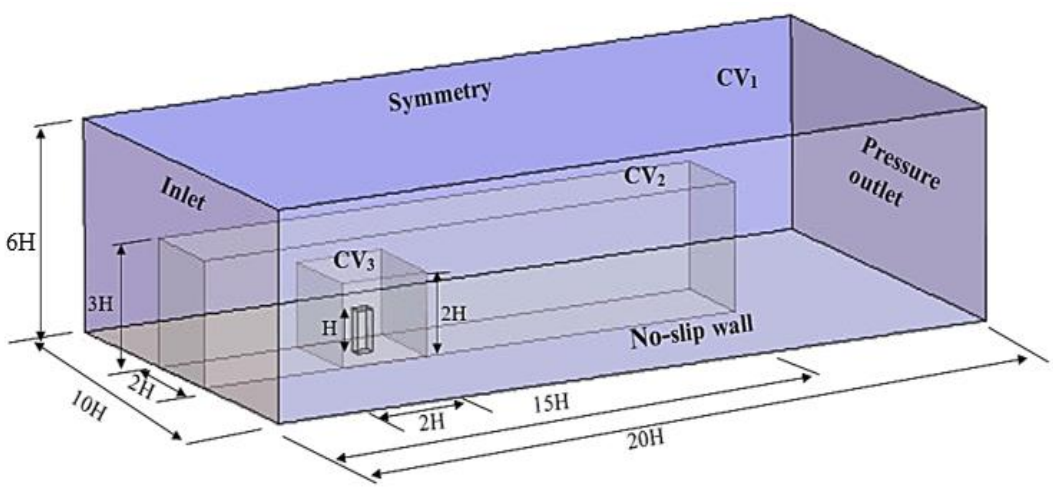

Figure 4-3: Computational domain geometry

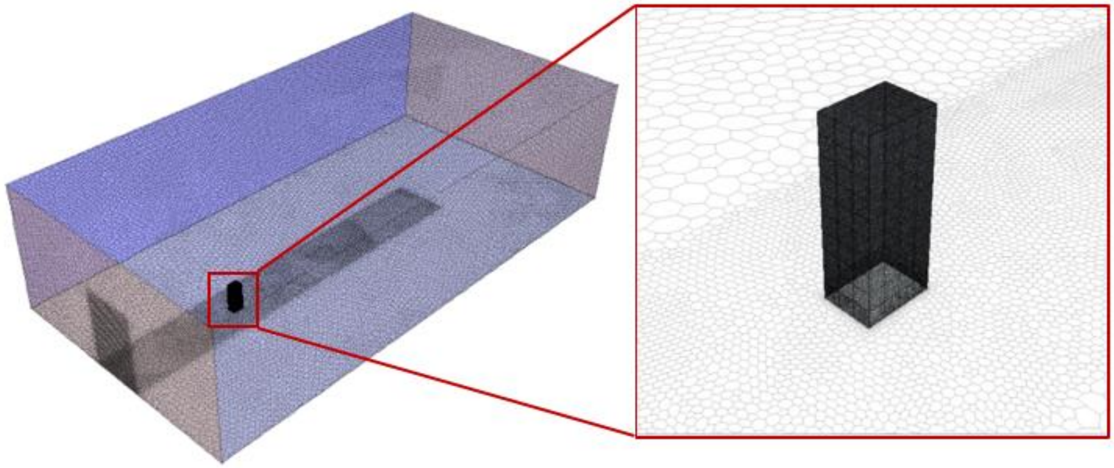

Figure 4-4: Grid distribution

4.2.2 Boundary conditions

The mean velocity and turbulent profile are generated assuming an open terrain exposure. At the inlet of the domain, an atmospheric boundary layer (ABL) is imposed. This boundary layer can be described by the logarithmic law, which constitutes a vertical profile of the mean horizontal wind speed, turbulent kinetic energy K (m^2/s^2) and turbulence dissipation rate ε (m^2/s^3) (Richards and Norris, 2011). These profiles represent a neutral ABL, where the turbulence originates only from friction and shear:

$$u(z) = \frac{u_*}{k} ln\left(\frac{z+z_0}{z_0}\right) \quad \text{Equation 4-2}$$

$$\text{K} = 3.3u_*^2 \quad \text{Equation 4-3}$$

$$\varepsilon = \frac{u_*^3}{k(z+z_0)} \quad \text{Equation 4-4}$$

where u_* is friction velocity (m/s), z_0 is the aerodynamic dynamic roughness length which is assumed that the buildings are situated on a large grass-covered terrain z_0 = 0.03 m (ESDU, 2001), and k is the von Karman constant (~ 0.42). An adiabatic boundary condition is used for the ground surface. Symmetry boundary conditions are applied at the top and lateral sides of the computational domain. The ground surface is modeled as a no-slip wall with no roughness height (k_s = 0) since in LRNM (Low Reynolds Number Model) surface roughness values cannot be specified (Defraeye et al., 2010). Zero static pressure is applied to the outlet plane. Note that in this simulation, only a forced convection heat transfer is considered. The turbulent closure of standard $k - \omega$ allows for a more accurate near-wall treatment and automatically switches a wall function to a low-Reynolds number formulation based on grid spacing (Wilcox, 1988). One of the shortcomings on the $k - \omega$ is that the model strongly depends on the free-stream values of ω that are specified outside the shear layer. Menter (1994) proposed $SSTk - \omega$, which combines the original $k - \omega$ model used near walls and the standard $k - \varepsilon$ model (Launder, 1974) away from walls using a blending function. Thus, SST $k - \omega$ is recommended for more accurate boundary layer simulation and is therefore used in this study. Details on the CFD simulation validation with experimental data of Meinders et al. (1999) and grid sensitivity analysis are provided in Kahsay et al. (2018). The simulations are conducted using a commercial CFD package (STAR-CCM+ v.10.12, 2015) and the SHARCNET (www.sharcnet.ca, 2017) high-performance computing (HPC) facility at Western University.

4.2.3 *CHTC* results and discussion

To evaluate building energy consumption accurately, knowledge of the *CHTC* distribution over the facade of the building is essential. Thus, in this study, the evaluation of surface-averaged *CHTC* with the wind free stream velocity is the primary target, and the correlations are then integrated into building energy simulation.

The geometry of a building plays a crucial role in the flow structure and 77 the *CHTC* distribution. Figure 4-5 illustrates how the incoming wind flow is forced around the structure both on the sidewalls and the roof. Near-wall velocity increases around the leading-edge building corners, leading to higher surface friction velocity. As a result, a higher value of *CHTC* is observed at the leading top and corners zones of the building as illustrated in Figure 4-6. However, around the stagnation position and closer to the base of the buildings, lower values of *CHTC* are observed. Further, the standing and horseshoe vortices around the bottom of the building, which increases the residence time of the air, leads to lower velocity, resulting in lower values of *CHTC.* The local surface-averaged *CHTC* distribution for a specified room is dependent on its location on the building with respect to these different flow region zones.

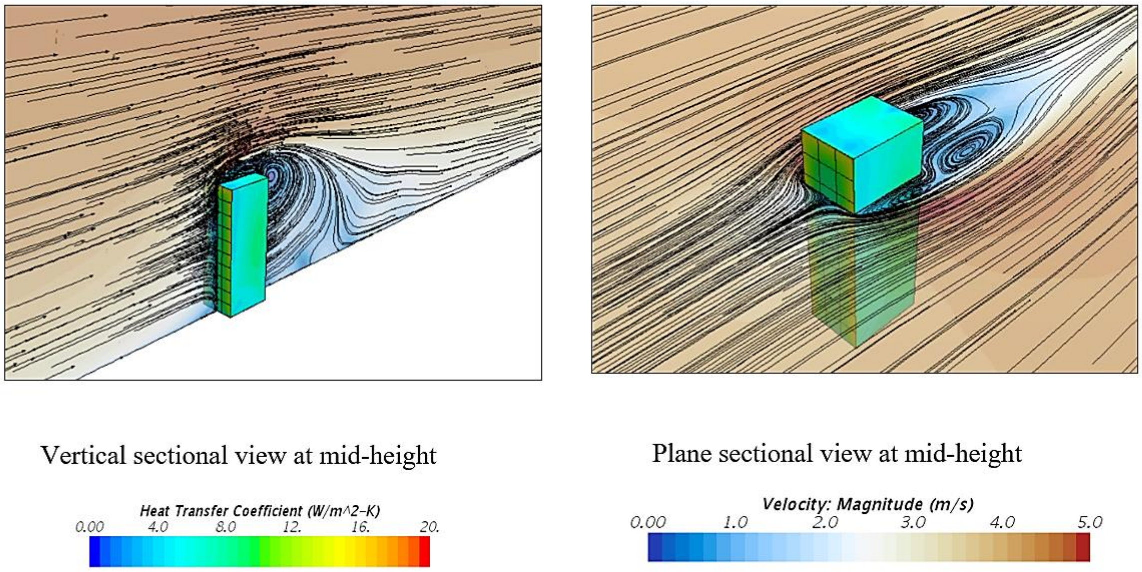

Figure 4-5: Velocity magnitude contours and *CHTC* distribution (for a wind speed of 3 m/s at 10 m ref height at the inlet)

Figures 4-7 and 4-8 show the averaged-surface *CHTC* values for different wind speeds at corner and center-zones of a building, respectively. The windward *CHTC*-U_{10} expression for the corner and center zones are presented with a high coefficient of determinations in Table 4-2. At a lower wind speed (1 m/s), the *CHTC* variations are insignificant. However, the *CHTC* variations along the height increase as the wind speed increase to 5 m/s. Moreover, at the center-zone of the building, since the air velocity is lower, the variations in *CHTC*s are lesser. However, at the corner-zones of the building, high variations in *CHTC*s are observed due to higher surface velocity.

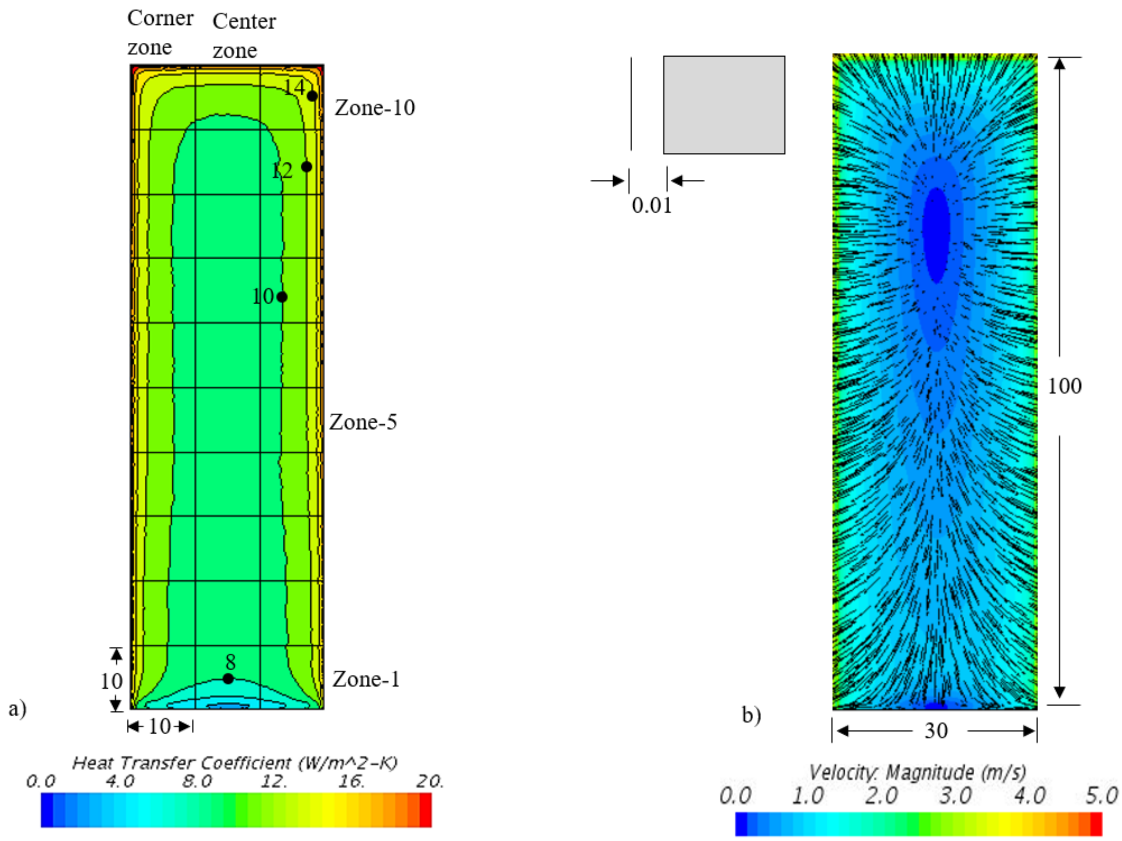

Figure 4-6: a) Windward *CHTC* distribution for a wind speed of 3 m/s at 10 m ref height at the inlet, b) Wind field vector and contour on a plane taken in front of the windward façade at 0.01 m from the wall of a building

Table 4-2: Local-*CHTC* correlations

Building zones	Reference wind speed range (m/s)	$CHTC - U_{10}$ correlation for windward (W/m²K)	R^2 (-)
Zone 1 center	1 -5	$CHTC = 3.29U_{10}^{0.78}$	0.9966
Zone 5 center	1 -5	$CHTC = 3.60U_{10}^{0.83}$	0.9943
Zone 10 center	1 -5	$CHTC = 4.83U_{10}^{0.81}$	0.9996
Zone 1 corner	1 -5	$CHTC = 4.16U_{10}^{0.8}$	0.9991
Zone 5 corner	1 -5	$CHTC = 4.58U_{10}^{0.83}$	0.9997
Zone 10 corner	1 -5	$CHTC = 5.43U_{10}^{0.82}$	0.9998

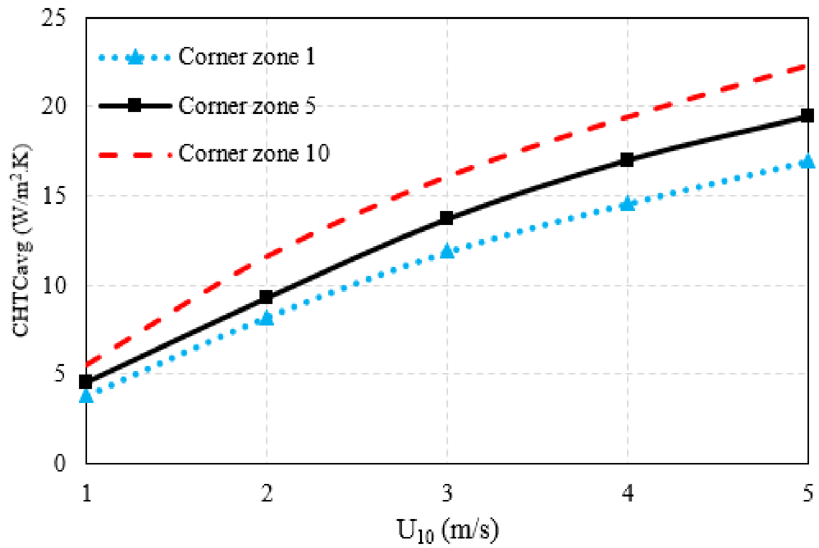

Figure 4-7: Surface-averaged *CHTC* distribution on different corner-zones of a 100 m tall of building on the windward side

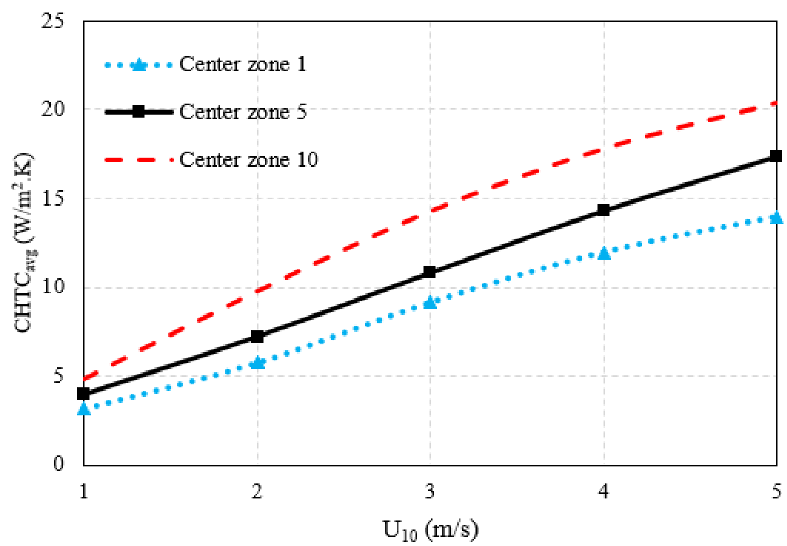

Figure 4-8: Surface-average *CHTC* distribution on different center-zones of a 100 m tall of building on the windward side

These new-*CHTCs* that are developed for the corner and center-zone of the buildings, as shown in Figures 7 and 8 respectively, are then integrated into EnergyPlus. The energy consumption that uses the new CHTC correlation can then be compared and analyzed against the energy consumption of the existing-*CHTC* correlation as discussed in the next section.

4.3 Application of *CHTC* on energy modeling

BES programs are essential in building design to predict energy consumptions. In this study, EnergyPlusV8.6.0, developed by the U.S. Department of Energy (DoE, 2016) is used. EnergyPlus is a building energy simulation program that calculates the heating and cooling loads necessary to keep the thermal control set points throughout the HVAC system. The building thermal zone calculation is a based-on heat balance model as shown in Equation 4-5 that uses the following assumptions: the air in the thermal zone has a uniform temperature; the temperature of each surface is uniform; the surface irradiation is diffusive, and the heat conduction through the surfaces is one-dimensional.

$$C_z \frac{dT_z}{dt} = \sum_{i=1}^{N_i} Q_i + \sum_{i=1}^{N_{surf.}} h_i A_i (T_s - T_a) + \sum_{i=1}^{N_{zone}} m_i C_p (T_i - T_a) + \dot{m}_{inf} C_p (T_\infty - T_a) + \dot{m}_{sys} C_p \left(T_{sup} - T_a\right)$$

Equation 4-5

where $C_z \frac{dT_z}{dt}$ is heat stored in the air, $\sum_{i=1}^{N_i} Q_i$ is the sum of convective internal loads, $\sum_{i=1}^{N_{surf.}} h_i A_i (T_s - T_a)$ is the convective heat transfer from the zone surface, $\sum_{i=1}^{N_{zones}} m_i C_p (T_i - T_a)$ is the heat transfer due to inter-zone air mixing, $\dot{m}_{inf} C_p (T_\infty - T_a)$ is heat transfer due to infiltration of outside air, and $\dot{m}_{sys} C_p \left(T_{sup} - T_a\right)$ is the air system in and out.The correlations used in the EnergyPlus simulations are DoE-2, MoWiTT, TARP, and new-*CHTC* for external convective and TARP for internal convective. The energy consumption of a high-rise building using the existing-*CHTC* is compared with evaluations based on the new-*CHTC* correlations. These comparative studies are carried out for case studies where the study building is exposed to two different weather conditions located in two different cities. The buildings exposed to different wind speeds are considered. The first case study analyzes the building located in London, ON, which is located at 42.9^0 north latitude, 81.2^0 west longitude, and at an altitude of 251 m. The annual average wind speed is 3.8 m/s, and the annual average temperature high is 13^0C and the low is 3^0C. In the second case study, the building is located in Boston, MA, which is located at 42.2^0 north latitude and 71.03^0 west longitude and an altitude of 43 m. The annual wind speed is 5.5 m/s, and the annual average temperature high is 15^0C and the low is 7^0C. Weather data from a typical metrological year (TMY) is used in the building energy simulation for both London, ON, and Boston, MA. The TMY consists of hourly data that includes ambient temperature, relative humidity, wind speed and direction, solar radiation, cloud cover and other metrological data over a year. The TMY weather data is available at the National Renewable Energy Laboratory, U.S. Department of Energy. For both study cases, different window configurations, i.e. 40% WWR and 100 % WWR have been considered. Rooms located in different parts of the building are investigated to assess the effects of wind flow around a building (aerodynamics). The representative floors are placed at the 1st, 5th, 10th, 15th, 20th, 25th, and 30th floor of the building, at the corner and center of one side of the building. Rooms in the corner-zone are oriented to south and west direction while rooms at the center-zone are oriented to south only as illustrated in Figures 1 and 2. Each room has a size of 10 m in width, 10 m in length, and is 3.33 m high. A total of 448 simulations is performed to cover the case studies illustrated in Table 4-3.

Table 4-3: Case studies

Building location	**Window configuration**	**Room location**	**Model room floor**	***CHTC* correlations**
London, ON	40WWR	Corner	1st, 5th, 10th, 15th, 20th,25th, and 30th	DoE-2, MoWiTT, TARP, and New-*CHTC*
		Center		
	100WWR	Corner		
		Center		
Boston, MA.	40WWR	Corner		
		Center		
	100WWR	Corner		
		Center		

4.3.1 Building envelope description:

The schematic diagram of the buildings, which are considered for energy simulation, is illustrated in Figures 1 and 2. The building is made of lightweight construction and has dimensions of 30 m width, 40 m length, and 100 m height. The case where the building has a 40% window-to-wall ratio on the south wall and west wall also has two identical windows with dimensions of 3.3 m width and 2 m height. The exterior walls consist of 19 mm thick gypsum board on the interior, followed by a 13 mm wall airspace, and then a 128 mm thick insulation panel with 1.5 mm thick metal cladding on the exterior. The roof consists of a 19 mm thick gypsum board, followed by a 650 mm thick fiberglass quilt, finally 100 mm thick concrete on top. The floor slab is composed of 100 mm thick concrete, followed by 100.3 mm insulation, and 19.1 mm thick acoustic tile. The partition wall is composed of 19 mm thick of gypsum board, followed by 15 mm partition airspace, and 19 mm thick gypsum board. The physical and thermal properties of all these materials are presented in Table 4-4.

4.3.2 Boundary conditions and building operating conditions

The exterior boundary conditions for the walls and roof are generated from the weather data file while a constant 10^0C ground temperature is assumed for the floor. The building is assumed to operate with a continuous ventilation rate of 0.5 ACH (air-exchange per hour), and constant internal sensible heat gain of 800 W; 60% of the total heat gain is assumed to be radiative and the remaining 40% is convective. It is assumed that all units are maintained at the same temperature so that there is no heat exchange between units and adiabatic boundary conditions are enforced. This assumption is valid for all units except the top and bottom floors. An ideal loads air system is used to control the temperature in the rooms. The room is equipped with a 10 W/m^2 compact fluorescent lamp (CFL) lighting system. Moreover, the model has a day-lighting controller sensor to automatically dim the lighting system with a threshold of 500 lx. When illuminance surpasses 500 lx, artificial lighting is not required, and the lighting system turns off. The cooling and heating set-points are 20^0C and 24^0C. A generic office occupancy of 0.05 people/m^2 with an activity schedule of 8 am to 7 pm on workdays is considered.

Table 4-4: Thermophysical properties of materials that make up the building.

Materials	Thermal conductivity (W/m K)	Thickness (m)	Thermal resistance (m^2 K/W)	Density (Kg/m^3)	Specific heat capacity (J/Kg K)
Exterior wall assembly					
Metal clad	44.96	0.0015	3.33×10^{-5}	7688.86	410
Wall insulation	0.045	0.128	2.85	265	836
Wall airspace		0.013	0.15		
Gypsum board	0.16	0.019	0.11875	800	1090
Insulated glass unit cladding					
Clear-glass	0.9	0.006	0.0067	2500	800
Window airspace		0.013	0.15		
Clear-glass	0.9	0006	0.0067	2500	800
Partition wall					
Gypsum board	0.16	0.019	0.11875	800	1090
Partition airspace		0.013	0.15		
Gypsum board	0.16	0.019	0.11875	800	1090
Ceiling					
Heavy weight concrete	1.95	0.1	0.051	2240	900
Ceiling air resistance			0.15		
Acoustic tile	0.06	0.0191	0.32	368	590
Floor					
Heavy weight concrete	1.95	0.1	0.051	2240	900
Insulation	0.04	0.1003	25.075		
Acoustic tile	0.06	0.0191	0.32	368	590
Roof					
Heavy weight concrete	1.95	0.1	0.051	2240	900
Fiberglass quilt	0.040	0.65	16.25	12.0	
Gypsum board	0.16	0.019	0.11875	800	1090

4.3.3 Results and discussions

A comparison between the energy consumption of a building using the existing- and new-*CHTC* is performed using EnergyPlus to quantify the impact that building geometry and microclimate changes with height on the annual energy consumption. The energy consumption deviation using the coefficients is calculated as shown in Equation 4-6. The evaluation approach is based on an analytical verification and comparative diagnostic procedure of the International Energy Agency (IEA) building energy simulation test (BESTEST) of whole-building energy simulation (Judkoff and Neymark, 1995).

$$Deviation\ (\%) = 100\ x\ \frac{E_{Existing\_CHTC} - E_{New\_CHTC}}{E_{New\_CHTC}} \qquad \text{Equation 4-6}$$

Comparison between the new and existing-*CHTC* on annual energy consumption is illustrated in Figures 10 to 13. It is important to note that the default correlation used in EnergyPlus program is DoE-2, thus, the average deviations between the DoE-2 and the new-*CHTC* correlation are presented while a comparison to other correlations is summarized in tabulated form below. Considering the first case study, when a building that has 40% WWR is exposed to London, ON weather conditions, the deviation between the existing- and the new-*CHTC* show insignificant deviations. For instance, rooms located at the corner and center zone of the building on the 1st, 5th,10th, 15th, 20th, 25th, and 30th floors show an average annual heating energy consumption deviation of 1.78% and 1.53%, respectively. For the annual cooling energy consumption, a deviation of 1.54% and 1.71% was seen respectively in Figure 4-9.

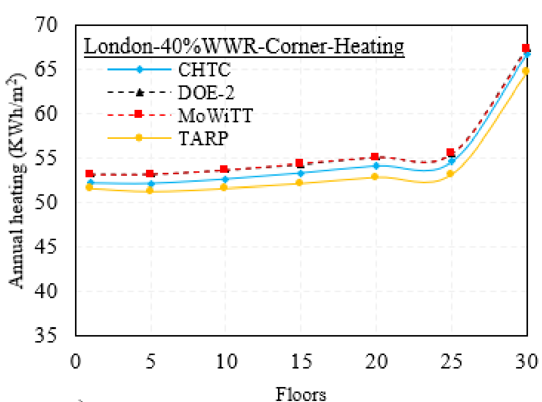

a)

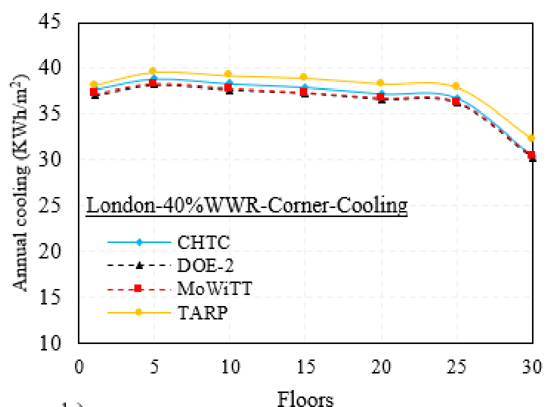

b)

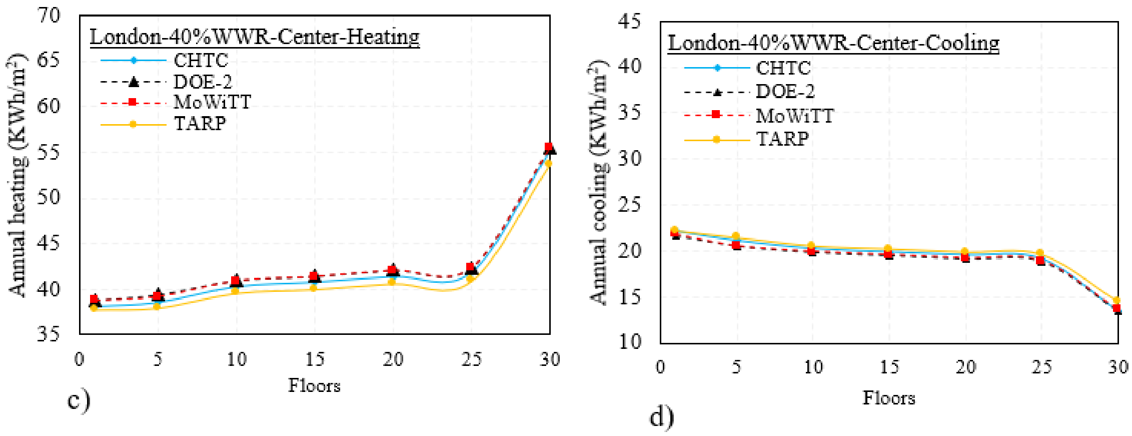

Figure 4-9: Annual energy consumption for a building located in London, ON with 40% WWR: a) corner-zone rooms heating b) corner-zone rooms cooling c) center-zone rooms heating, and d) center-zone rooms cooling

However, for the case of a building having a 40% WWR and exposed to the Boston, MA weather conditions, a higher deviation is observed. This is due to the intense winds in Boston, MA compared to London, ON. For the selected rooms, in the 1st, 5th,10th, 15th, 20th, 25th, and 30th floor, at the corner-zone and the center-zone of the building, an average deviation on annual heating energy consumption reached 2.82% and 3.54%, respectively. Whereas the annual cooling energy consumption deviation reached 2.53% and 3.02%, respectively as shown in Figure 4-10. The comparison between the existing- and new-*CHTC* correlations for the chosen floors are summarized in Table 4-5 for average deviations and Table 4-6 for local deviations.

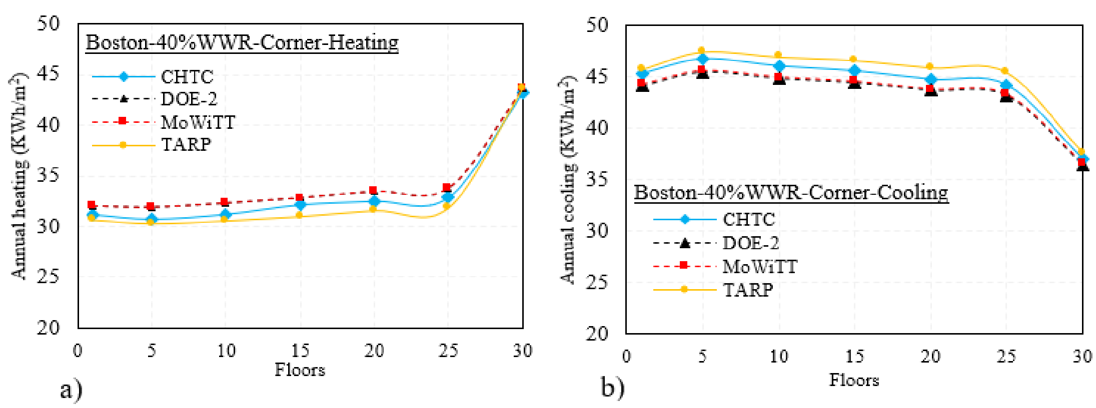

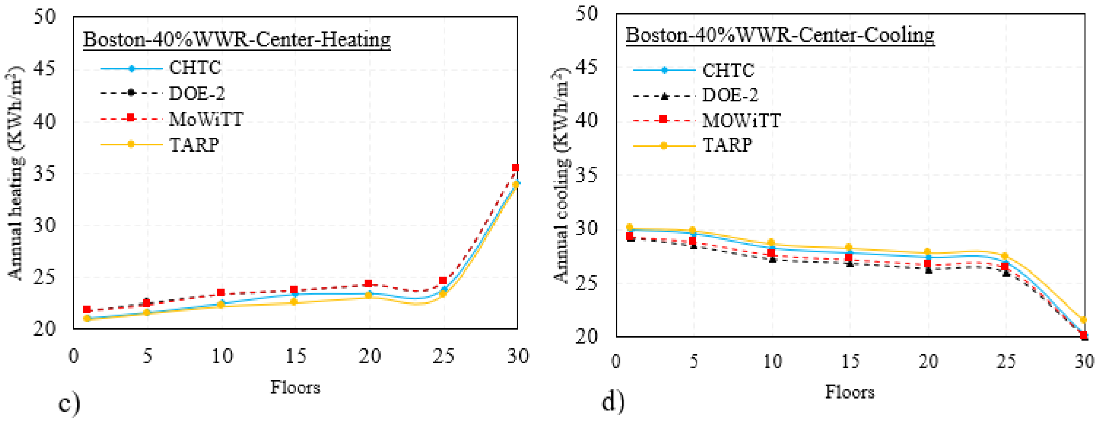

Figure 4-10: Building located in Boston, MA for the case of 40%WWR, the annual energy consumption for a) corner-zone rooms heating b) corner-zone rooms cooling, c) center-zone rooms heating, and d) center-zone rooms cooling

Table 4-5 gives a summary of the absolute average deviation results of the heating and cooling loads of buildings located in London and Boston for the case of 40%WWR. Overall, due to the small window size and the higher thermal resistance of the opaque wall, on average lesser deviations on the *CHTC*s correlations are seen. Table 4-5 shows that for individual rooms, for instance, the 5th floor, a deviation of 4.4% and 3.7% on heating and cooling, respectively, is observed.

Table 4-5: Absolute annual average deviation of the heating and cooling load for a building with 40% WWR

Existing-*CHTC* correlation	**London, ON 40% WWR corner-zone**		**London, ON 40% WWR center-zone**		**Boston, MA 40% WWR corner-zone**		**Boston, MA 40% WWR center-zone**	
	Heating	Cooling	Heating	Cooling	Heating	Cooling	Heating	Cooling
DoE-2	1.78%	1.54%	1.53%	1.71%	2.82%	2.35%	3.54%	3.02%
MoWiTT	1.64%	1.26%	1.30%	1.45%	2.69%	2.22%	3.27%	1.88%
TARP	2.25%	2.83%	1.85%	2.38%	1.87%	1.89%	1.37%	2.06%

Table 4-6: Absolute annual deviation of the heating and cooling load between DoE-2 and new-*CHTC* for a building with 40% WWR.

Floors	London, ON 40% WWR corner-zone		London, ON 40% WWR center-zone		Boston, MA 40% WWR corner-zone		Boston, MA 40% WWR center-zone	
	Heating	Cooling	Heating	Cooling	Heating	Cooling	Heating	Cooling
5th floor	2.1%	1.8%	2.2%	2.6%	4.1%	2.6%	4.4%	3.7%
15th floor	1.9%	1.7%	1.5%	1.8%	2.2%	2.4%	3.8%	3.8%
25th floor	1.7%	1.6%	1.2%	1.4%	2.9%	2.3%	3.1%	3.3%

Considering the second case study where a building has 100% WWR, a higher deviation between the existing- and the new-*CHTC* correlations are observed in both exposures, as illustrated in Figures 11 and 12. For instance, considering a building exposed to the London, ON weather conditions, and for rooms that are located in the corner and center zones of the 1st, 5th,10th, 15th, 20th, 25th, and 30th floors of the building, the annual average heating energy consumption deviated by 3.84% and 5.44%, respectively. Whereas, the average annual cooling energy consumption deviated by 3.35% and 3.94%, respectively. However, considering individual rooms such as the 5th floor, a deviation of 7.1% and 4.1% on heating and cooling, respectively, is observed.

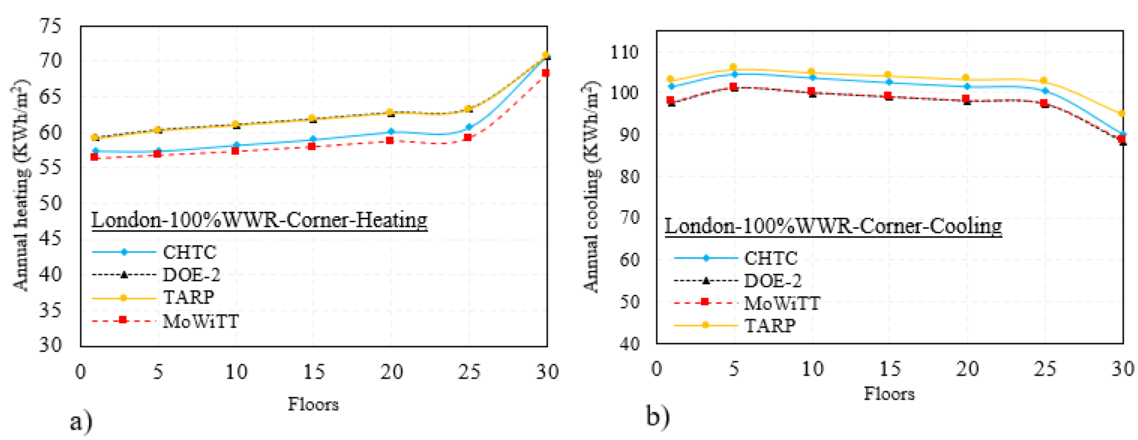

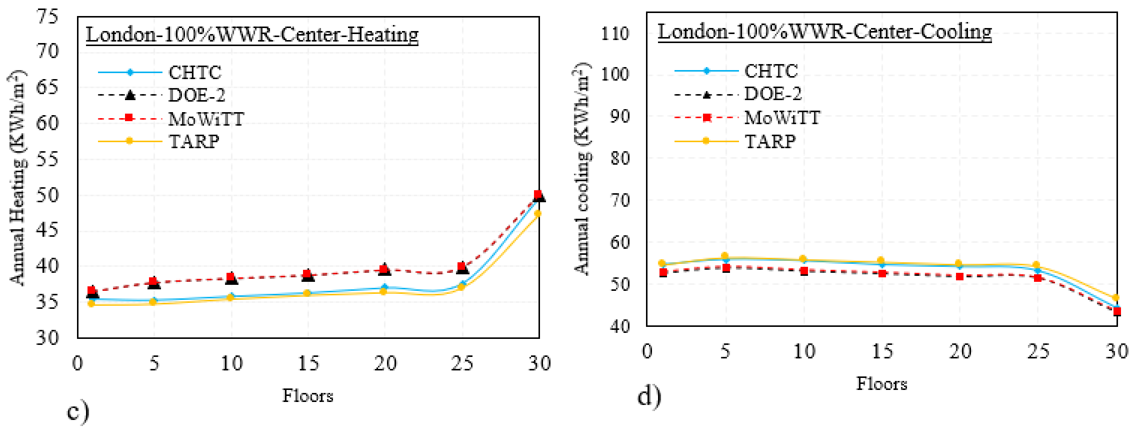

Figure 4-11: Building located in London, ON, for the case of 100% WWR, annual energy consumption for a) corner-zone rooms heating b) corner-zone rooms cooling, c) center-zone rooms heating d) center-zone rooms cooling

Further, significant deviations on the annual average energy consumption of a building are observed when the building with 100% WWR is exposed to Boston's windy environment. For instance, for the case of a building exposed to the Boston, MA, weather condition, where rooms are located on the 1st, 5th,10th, 15th, 20th, 25th, and 30th floors in the corners and center of the building, a deviation of 5.68% and 8.53% of the average annual heating energy consumption is observed, respectively. Whereas, a deviation of 3.9% and 3.84% on annual average cooling energy consumption, respectively, is observed. However, considering individual rooms such as the 15th floor, a deviation of 11.2% and 4.7% on heating and cooling, respectively, is observed. Details on the comparison between the existing- and new-*CHTC* correlations for the chosen floors and are summarized in Table 4-7 for average deviations and Table 4-8 for local deviations.

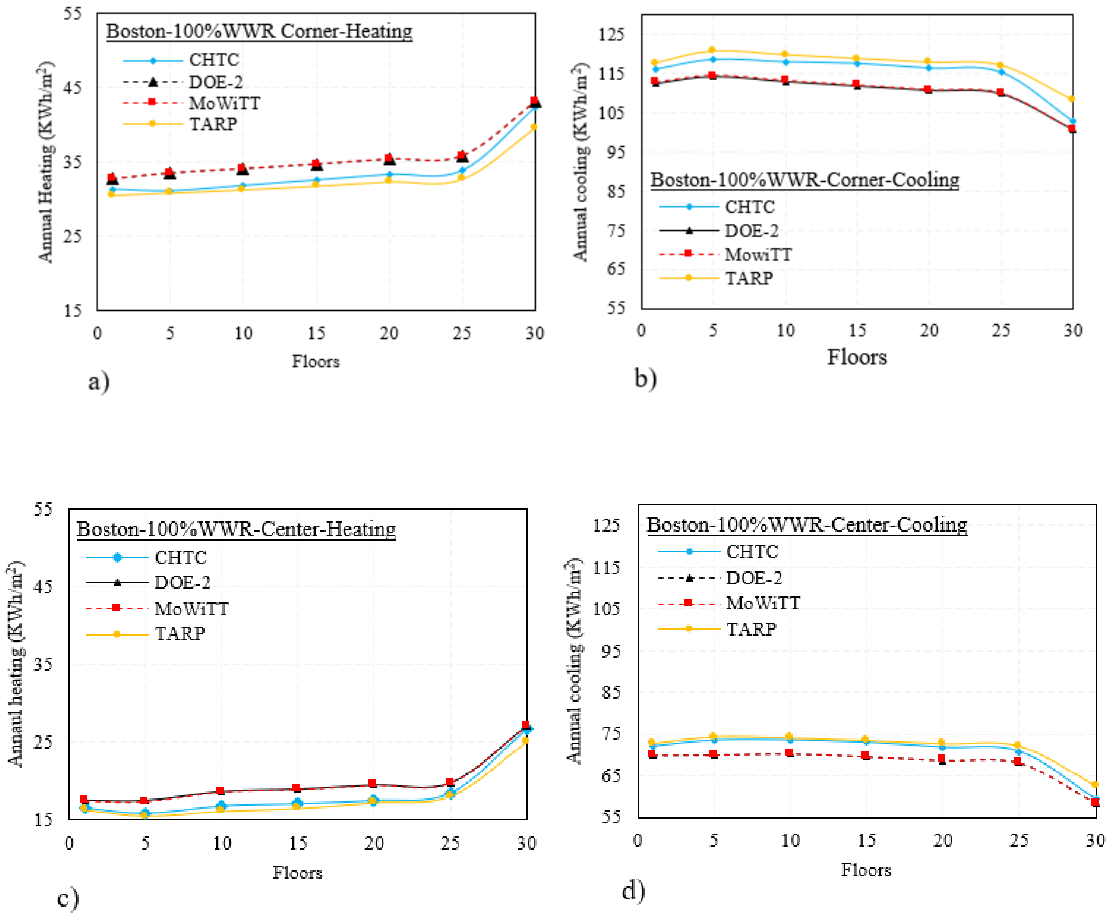

Figure 4-12: Building exposed to Boston, MA, weather condition for the case of 100% WWR, annual heating energy consumption for a) corner-zone rooms b) center-zone rooms, annual cooling consumption for c) corner-zone rooms d) center-zone rooms

Table 4-7: Annual average deviation of heating and cooling load for a building with 100% WWR.

Existing-*CHTC* correlations	**London, ON 100% WWR Corner -zone**		**London, ON 100% WWR Center-zone**		**Boston, MA 100% WWR Corner-zone**		**Boston, MA 100% WWR Center-zone**	
	Heating	cooling	Heating	Cooling	Heating	cooling	Heating	Cooling
DoE-2	3.84%	3.35%	5.44%	3.94%	5.64%	3.9%	8.53%	3.84%
MoWiTT	3.61%	3.09%	5.22%	3.34%	5.51%	3.8%	8.28%	3.73%
TARP	2.13%	2.08%	1.91%	1.46%	2.84%	1.86%	2.94%	1.71%

Table 4-8: Absolute annual deviation on heating and cooling load between DoE-2 and new-*CHTC* for a building with 100% WWR.

Floors	London, ON 100% WWR corner-zone		London, ON100% WWR center-zone		Boston, MA 100% WWR corner-zone		Boston, MA 100% WWR center-zone	
	Heating	Cooling	Heating	Cooling	Heating	Cooling	Heating	Cooling
5th floor	5.1%	3.4%	7.1%	4.1%	7.7%	3.7%	10.6%	4.7%
15th floor	4.9%	3.5%	6.9%	4.1%	6.5%	4.9%	11.2%	4.7%
25th floor	4.33%	3.3%	4.1%	3.0%	5.8%	4.7%	7.2%	3.9%

Therefore, for a building with a curtain wall exposed to a windy environment such as that located in Boston, MA, higher deviations of the *CHTC* coefficients are observed. These deviations are highly noticeable when comparing individual rooms. Hence, the existing-*CHTC* correlations are very sensitive to the local microclimate such as wind effects.

4.3.4 Multiplier effect on high-rise building energy consumption

The common practice in energy simulation for high-rise buildings is to select and simulate only a few representative floors and then multiply the results by a factor to estimate the energy consumption of the entire building. Previous studies by Ellis and Torcellini (2005) have recommended that rooms located at mid-height will closely approximate the average energy consumption of the entire building. However, the main problem with the multiplier approach is that it can decrease the accuracy of the thermal comfort requirement of individual rooms, as this approach may not capture the average-energy consumption variation between the rooms in the bottom and top floors of the building as well as corner and center zones.

Table 4-9: Absolute deviations of annual energy consumption for room positioned at the center-zone of the building.

Location of building	Window configuration	Mid-height (15th floor) deviation from 5st -floor room		Mid-height (15th floor) deviation from 25st -floor room	
		Heating	Cooling	Heating	Cooling
London, ON	40% WWR	5.7%	5.8%	2.6%	3.9%
	100% WWR	2.8%	2.3%	3.4%	2.7%
Boston, MA	40% WWR	8.1%	5.9%	2.0%	3.4%
	100% WWR	7.8%	1.0%	7.6%	3.2%

In the present study, significant deviations in the energy consumption between the mid-height (15th) and the 5th and 25th floors are observed. For instance, the middle floor of a building exposed to Boston, MA, weather condition and having 100%, WWR has an additional 7.8% average annual heating compared to the 5th floor. Whereas compared to the 25th floor, the average annual heating decreased by 7.6%. A summary of the details of these comparisons is presented in Table 4-9. Therefore, the use of a representative floor at the mid-height of the building may lead to a variation in the estimation of the annual energy consumption of individual rooms. Consequently, this can lead to thermal discomfort and unexpected surface condensation on surfaces at the individual room level. Accordingly, multiple representative floors should be selected based on the *CHTC* distribution on the surface of the building using CFD analyses.

4.4 Conclusion

During the early design stages of high-rise building numerical analyses of the energy consumption of the building is an effective strategy to achieve energy efficiency. However, high-rise buildings pose unique challenges for BES programs. A few of these limitations of BES include the size of the building, the changes in a microclimate with altitudes, and the uncertainties regarding the correlation of the existing convective heat transfer coefficients (*CHTC)*. Introducing CFD and heat transfer simulations help solve these issues and improve the current BES. In this study, a 100 m tall isolated building is investigated as a case study for two different weather condition (Boston, MA, and London, ON). First, a new-*CHTC* correlation is developed that considered for a high-rise building for different wind speed by using CFD and heat transfer simulations. Then, EnergyPlus simulations are carried out by using the new and existing-*CHTC* correlations to comparatively illustrating the impact of aerodynamics on energy consumption, and the following conclusions can be drawn:

- The existing-*CHTC*s correlations are more sensitive to windy environments such as in Boston MA than to the calmer weather in London, ON. For the case of a building located in London, ON, having rooms located in the 1^{st}, 5^{th},10^{th}, 15^{th}, 20^{th}, 25^{th}, and 30^{th} floors and positioned at the center-zone of the building, a deviation of 5.44% on heating and 3.94% on cooling is observed. However, for a building located in Boston, MA, a deviation of 8.53% on heating and 3.84% on cooling is observed.

- As the WWR is increased, a higher deviation between the new-*CHTC* and the existing-*CHTC* correlations are observed. For instance, considering a building exposed to Boston, MA, weather condition, a room located on the 5^{th} floor at the center-zone of the building, and for the case of 40% WWR, a deviation of 4.4% on heating and 3.7% on cooling is observed; however, as the WWR increases to 100%, a deviation of 10.6% on heating and 4.7% on cooling is observed.

- Using a representative room located at the mid-height of a building as a multiplier may lead to thermal discomfort in individual rooms located on other zones. For instance, for the case of a building with 40% WWR exposed to Boston, MA, weather condition, the energy consumption difference between the representative and the 5^{th} floor and 25^{th} floor was compared. This comparison showed that the annual heating consumption of the representative mid-height room is 7.8% higher than the 5^{th} floor room. However, compared to the 25^{th} floor room, the annual heating consumption 7.6% lower. Thus, the use of a representative floor or multiplier at mid-height can have a significant impact on the local thermal comfort of each room and may lead to unexpected surface condensations.

It is fair to say that case-specific CFD and heat transfer simulation can be used to generate *CHTC* for each room of a high-rise building in a relatively simple and accurate way that could result in an accurate building energy consumption analysis. Further studies can optimize window configurations based on the local-*CHTC* distributions and needs for thermal comfort of individual rooms by representing the urban microclimate in a realistic way.

4.5 References

ASHRAE. (2009). Fundamentals, SI ed. *American Society of Heating, Refrigerating and Air Conditioning Engineers: Atlanta, GA, USA.*

Blocken, B., Defraeye, T., Derome, D., & Carmeliet, J. (2009). High-resolution CFD simulations for forced convective heat transfer coefficients at the facade of a low-rise building. *Building and Environment*, *44*(12), 2396-2412.

Booten, C., N. Kruis, and C. Christensen. (2012). Identifying and Resolving Issues in EnergyPlus and DOE-2 Window Heat Transfer Calculations. National Renewable Energy Laboratory. NREL/TP-5500-55787. Golden, CO.

CD-Adapco StarCCM+, User Guide, CD-Adapco, Melville, NY, USA, 2017.

Defraeye, T., Blocken, B., & Carmeliet, J. (2010). CFD analyzes of convective heat transfer at the surfaces of a cube immersed in a turbulent boundary layer. *International Journal of Heat and Mass Transfer*, *53*(1), 297-308.

Defraeye, T., Blocken, B., Carmeliet, J. (2011). Convective heat transfer coefficients for exterior building surfaces: Existing correlations and CFD modeling. Energy Conversion and Management, 52(1), pp.512-522.

DoE, U. S. (2016). EnergyPlus engineering reference. *The reference to energyplus calculations*.

Ellis, P. G., & Torcellini, P. A. (2005). Simulating tall buildings using EnergyPlus. In *International IBPSA conference* (pp. 279-286).

Emmel, M.G., Abadie, M.O., Mendes, N. (2007). New external convective heat transfer coefficient correlations for isolated low-rise buildings. Energy Build; 39:335–42.

Engineering Sciences Data Unit (ESDU) 85020. (2001). Characteristics of atmospheric turbulence near the ground. Part II: Single point data for strong winds.

Franke, J., Hellsten, A., Schlünzen, H., Carissimo, B. (2007). Best practice guideline for the CFD simulation of flows in the urban environment COST 2007. Action 732.

Iousef, S., Montazeri, H., Blocken, B., & Van Wesemael, P. J. V. (2017). On the use of non-conformal grids for economic LES of wind flow and convective heat transfer for a wall-mounted cube. *Building and Environment*, *119*, 44-61.

Judkoff, R.; Neymark, J. (1995). Building Energy Simulation test (BESTEST) and diagnostic method. *NREL/TP-472-6231*. Golden, CO National Renewable Energy Lab

J. Liu, M. Heidarinejad, S. Gracik, J. Srebric, (2015). The impact of exterior surface convective heat transfer coefficients on the building energy consumption in urban neighborhoods with different plan area densities, Energy and Buildings. 86 (2015) 449-463.

Kahsay, M., Bitsuamlak, G., & Tarik, F. (2018). Numerical analysis of convective heat transfer coefficient for building facades. Journal of building physics.

Lawrence Berkeley Laboratory (LBL) (1994). DOE2.1E-053 Source Code.

Launder, Brian Edward, and Dudley Brian Spalding. (1974). "The numerical computation of turbulent flows." *Computer methods in applied mechanics and engineering* 3, no. 2: 269-289.

Meinders, E. R., Hanjalic, K., & Martinuzzi, R. J. (1999). Experimental study of the local convection heat transfer from a wall-mounted cube in turbulent channel flow. *Journal of heat transfer*, *121*(3), 564-573.

Menter, F. R. (1994). Two-equation eddy-viscosity turbulence models for engineering applications. *AIAA journal*, *32*(8), 1598-1605.

Mirsadeghi, M., Cóstola, D., Blocken, B., & Hensen, J. L. (2013). Review of external convective heat transfer coefficient models in building energy simulation programs: implementation and uncertainty. *Applied Thermal Engineering*, *56*(1), 134-151.

Montazeri, H., Blocken, B., Derome, D., Carmeliet, J., & Hensen, J. L. (2015). CFD analysis of forced convective heat transfer coefficients at windward building facades: influence of building geometry. *Journal of Wind Engineering and Industrial Aerodynamics*, *146*, 102-116.

Montazeri, H., & Blocken, B. (2017). New generalized expressions for forced convective heat transfer coefficients at building facades and roofs. *Building and Environment*, *119*, 153-168.

Montazeri, H., & Blocken, B. (2018). Extension of generalized forced convective heat transfer coefficient expressions for isolated buildings taking into account oblique wind directions. *Building and Environment*, *140*, 194-208.

Natural Resources Canada (NRCan) (2016). Energy Fact Book 2016-2017.

Nusselt, W., & Jurges, W. (1922). The cooling of a flat wall by an air stream (Die Kuhlung einer ebenen Wand durch einen Luftstrom. *Gesundheits Ingenieur)*, *52*(45), 641-642.

Richards, P. J., & Norris, S. E. (2011). Appropriate boundary conditions for computational wind engineering models revisited. *Journal of Wind Engineering and Industrial Aerodynamics*, *99*(4), 257-266.

SHARCNET is a consortium of colleges, universities, and research institutes operating a network of high-performance computer clusters across southwestern, central, and northern Ontario [Online]. Available: <www.sharcnet.ca>; 2015.

Sparrow, E. M., Ramsey, J. W., & Mass, E. A. (1979). Effect of finite width on heat transfer and fluid flow about an inclined rectangular plate. *Journal of Heat Transfer*, *101*(2), 199-204.

Standard, A. S. H. R. A. E. (2010). 90.1 (2013). Energy Standard for Buildings Except Low-Rise Residential Buildings.' In *American Society of*.

STAR CCM+. CD-ADAPCO product. (2015). www.cdadapco.com/products/star-ccm (accessed on Sep. 12, 2015)

U.N-habitat, Energy (2017). https://unhabitat.org/urban-themes/energy/ (accessed on 21/08/2017)

Walton, G.N. (1983). Thermal Analysis Research Program Reference Manual, NBSSIR 83e2655, National Bureau of Standards.

Weather and science facts. Retrieved from https://www.currentresults.com/Weather/Massachusetts/Places/boston-temperatures-by-month-average.php. Accessed on 21/04/2018.

Wilcox, D. (1988). Reassessment of the scale-determining equation for advanced turbulence models. *AIAA journal*, *26*(11), 1299-1310.

Yazdanian, M., Klems, J.H. (1994). "Measurement of the exterior convective film coefficient for windows in low-rise buildings." ASHRAE Trans; 100(1): 1087–96.

Chapter 5

5 Effect of window configuration on the convective heat transfer rate of a window with natural convective heater

5.1 Introduction

The amount of energy consumed in a building through heating, cooling, and lighting can be lost in different ways through the façade components. The study by Lee et al. (2013) has shown that about 20% - 40% of energy in a building is wasted through windows. The energy performance of a building is therefore strongly influenced by its window systems and configuration. Windows provide daylight, view, and fresh air to occupants; hence, it plays a crucial role both in the energy exchange of the building as well as the occupant's psychological satisfaction. Windows are configured on buildings in different forms as illustrated in Figure 5-1.

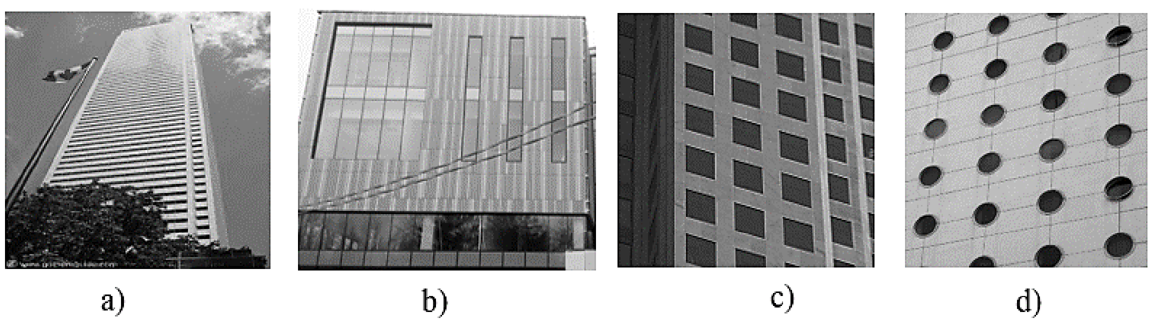

Figure 5-1: Window configuration examples: a) horizontal rectangular, b) vertical rectangular, c) square, and d) circular

Previous studies by Greenup & Edmonds (2004); Tzempelikos (2005); Ghisia et al. (2005); Ochoa et al. (2012), Kahsay et al. (2017) have shown that design and selection of a proper window system is one of the essential passive strategies for saving energy in buildings. Choosing a window system and its corresponding configuration is a fundamental decision in the early design stage, which is costly to change later. ASHRAE standard 90.1 provides a guideline on the Window-to-Wall Ratio (WWR) stating that: *"the total vertical window area shall be less than 40% of the gross wall area".* While very useful and pragmatic, this general guideline on the WWR does not provide any explicit way to evaluate whether a given WWR size will give satisfactory results regarding thermal and lighting performance for different window configurations having the same WWR. For example, consider the following four window configurations as shown in Figure 5-2 that have the same area 20% WWR. Since the design and selection of a proper window system is one of the most effective strategies for conserving the energy of a building, it is important to determine which of the four window configurations more energy efficient and thermally comfortable is.

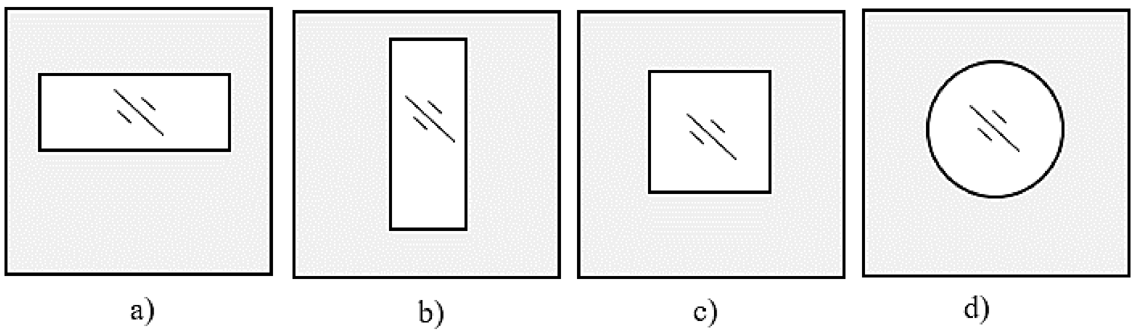

Figure 5-2: Model window configurations with 20% Window-to-Wall Ratio (WWR) that represent a) horizontal rectangular b) vertical rectangular c) square, and d) circular.

In winter, outdoor environmental conditions primarily influence the indoor surface temperature of the window, and this leads to a temperature gradient in the indoor environment that induces a downdraft and affects the thermal comfort of occupants. This phenomenon is sensitive to the configuration and the location of windows. Although it is well understood that high-performance windows can reduce building energy consumption, a better understanding of the effects of window configuration on thermal comfort would lead to further savings.

Window's effect on thermal comfort varies during summer and winter, which is governed by the U-factor (the overall heat transfer coefficient including surface film thermal resistance), visual transmittance, and solar heat gain coefficient of the window and the temperature difference between indoor and outdoor. The existing guidelines, such as ASHRAE handbook in the Fenestration chapter (ASHRAE, 2017) offers basic guidance about windows and comfort. The guideline suggests that "*In heating-dominated climates, windows with the lowest U-factor tends to give the best comfort outcomes…In cooling-dominated climates for orientations where cooling loads are of concern, window with lowest rise in the surface temperature for a given SHGC tends to give the best comfort outcomes*." However, this may not provide an accurate way to evaluate window configurations and their corresponding thermal comfort rating. Further, it does not refer to the full range of modern products such as Low-E glazing and the current standard in high-performance glazing systems (Lyons et al., 2000). Despite such recognition on the thermal discomfort, there is no standard method to quantify the extent of the discomfort. To counteract the draft effect and increase the indoor thermal comfort and reduce possible window condensation risk, convective heaters are often mounted below the window in buildings. This alters the airflow patterns, temperature distributions near the window and the rate of convective heat transfer on the window.

Based on the fundamental principles of the downdraft, when the window temperature is low; indoor air near the window loses heat by convective heat exchange. The cooler air downpours to the floor. This forms a cold air layer near the floor as illustrated in Figure 5-3a. The local cooling effect caused by air movement can create thermal convective discomfort. However, as the convective heater temperature increases, the flow pattern of the downdraft is pushed up from the floor. This behavior of the airflow field and its sensitivity to the configuration of windows numerically investigated in this study.

The effect of different window configurations on the energy performance of a building are examined using the fundamentals of a vertical heated plate, experimentally (Churchill and Chu, 1975), analytically (Eckert and Jackson, 1950) and numerically (Zitzmann et al., 2005). In addition, several studies have investigated flow near window-wall heater systems (Oosthuizen, 2011; Oosthuizen & Naylor, 2009). Although there have been many studies of flow near window-wall heater systems, most of these studies are two-dimensional and based on the assumption that the flow remains laminar and steady. There are limited studies that consider both laminar and turbulent flows (Oosthuizen, 2011). In most of the previous studies, only one window configuration was considered. Studies on the effect of different window configurations on the convective thermal discomfort, and convective heat transfer rate are very limited. Therefore, the present study aims at investigating the influence of different window configurations on the indoor convective thermal discomfort and convective heat transfer rate of a window. For this purpose, an approximate numerical model of the convective heat transfer for various window shapes below which a natural convective heater is mounted is considered.

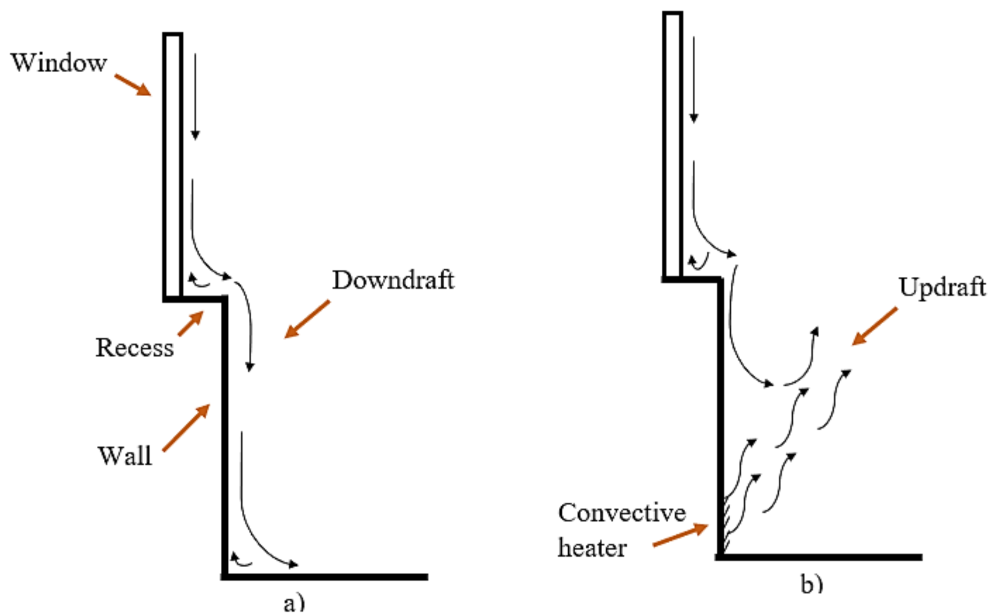

Figure 5-3: Cold downdraft from window a) without a convective heater and b) with convective heater below a window.

The heater and the window are modeled as isothermal plane boundaries; the window is colder than the room air temperature, and the heater is hotter than the room air temperature. The sensitivity of window Nusselt number and room temperature distributions to various window configurations have been examined. Parameters investigated in this study include the window configuration and heater temperature. The results are discussed and compared with previous analytical, numerical, and experimental works whenever applicable.

The remaining sections of the chapter are organized as follows: section 2 provides validation of CFD simulations with previous experimental and computational studies on vertical isothermal planes. Section 3 describes the details of the simulation and the parameters included in the computational fluid dynamics and heat transfer model. Section 4 presents result and discusses, and finally, section 5 concludes the chapter.

5.2 CFD validation study

5.2.1 Experimental data for validation

To validate the numerical study, an experimental data by Churchill & Chu (1975) and numerical data by Oosthuizen (2011) for flow over a vertical heated isothermal plate is used. In this experiment, the Nusselt number for the entire Rayleigh number (Ra = 10^7-10^{12}) range- laminar, transition, turbulent -natural convective are evaluated.

The heat transfer rate from a vertical wall in the presence of turbulence in the boundary layer has been measured experimentally and correlated as a function, $\overline{Nu_y}\left(Ra_y, Pr\right)$, where Ra_y is Rayleigh number, Pr is Prandtl number, and $\overline{Nu_y}$ is an alternative notation for overall Nusselt number Nu_{0-y} (Bejan, 2013). An empirical isothermal-wall correlation that relates the wall averaged Nusselt number $\overline{Nu_y}$ for the entire Rayleigh number range – laminar, transition, turbulent-was constructed by Churchill & Chu (1975) as presented in Equation 5-1.

$$\overline{Nu_y} = \left\{0.825 + \frac{0.387Ra_y^{1/6}}{\left[1+(0.492/\mathrm{Pr})^{9/16}\right]^{8/27}}\right\}^2 \qquad \text{Equation 5-1}$$

where $\overline{Nu_y}$ is surface averaged Nusselt number, Ra_y is the Rayleigh number, y is window vertical height, and Pr is ratio of viscosity diffusion rate to thermal diffusion rate ($Pr = (C_p\ \mu)/k$). The physical properties used in the definition of $\overline{Nu_y}$, Ra_y and Pr are evaluated at the film temperature $(T_w - T_a)/2$ (Bejan, 2013). The boundary layer flow remains laminar if y is small enough so that the Rayleigh number Ra_y does not exceed a critical value. The transition to turbulent flow occurs at a y position where $Ra_y \sim 10^9 Pr$ where ($10^{-3} \leq Pr \leq 10^3$).

5.2.2 Numerical model for validation case

To validate the wall-averaged Nusselt number with the empirical correlation of Churchill and Chu (1975), a computational domain (see Figure 5-4) that represents a two-dimensional heat transfer in a vertical isothermal window is used. In this study, the vertical right-side boundary is an open boundary, and the inflow on this boundary has a constant air temperature of T_∞ (290 K). The wall is assumed adiabatic to isolate the window effects and the window is uniformly fixed at T_w (310 K) as shown in Table 5-1. The Nusselt number is evaluated for laminar, transition to turbulent regimes.

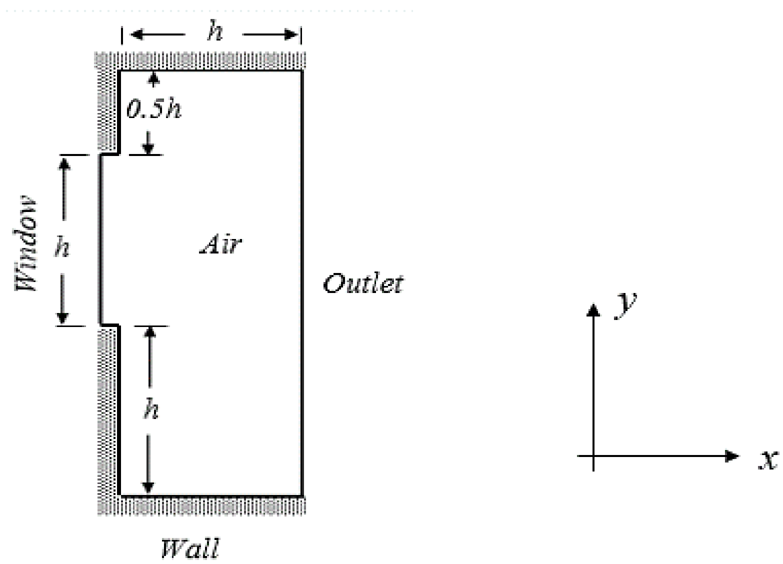

Figure 5-4: Model boundary conditions

Table 5-1: Boundary conditions

Name	**Boundary conditions**
Wall	Adiabatic* (*u= v=0, q=0*)
Window	T_w = 310 K (isothermal)
Outlet	Pressure outlet, T_∞ = 290 K

**u and v are velocities and q is a heat flux*

In this study, a high-resolution, steady Reynolds-Averaged Navier-Stokes (RANS) CFD simulations using *Shear Stress Transport* (*SST*) $k - \omega$ Low Reynolds number modeling (LRNM) approach has been used to resolve the near-wall heat transfer in conjunction with the buoyancy force. The buoyancy force is what causes the fluid motion in free convection. In addition, fluid properties are treated as constant values, except when changes in temperature lead to changes in density and the development of a buoyancy force. In other words, this scenario is treated using the Boussinesq approach. The simulations are conducted using a commercial CFD solver (STAR-CCM+ v.11.06.11, 2018) and the SHARCNET (www.sharcnet.ca) high-performance computing (HPC) facility at Western University.

The solution is obtained by numerically solving the full two-dimensional governing equations. In this analysis, the height of the window, h, is used as the length scale and the magnitude of the overall temperature difference $|(T_w - T_a)|$ is used as the temperature scale. These parameters show the same essential characteristics for all cases of window configurations. The effect of the radiative heat transfer has been excluded. The governing equations are (Equation 5-2 – Equation 5-4):

Continuity:

$$\frac{\partial u}{\partial x} + \frac{\partial v}{\partial y} = 0 \qquad \text{Equation 5-2}$$

Momentum in the y-direction:

$$u\frac{\partial u}{\partial x} + v\frac{\partial u}{\partial y} = -\frac{1}{\rho}\frac{\partial p}{\partial x} + \vartheta\left(\frac{\partial^2 u}{\partial x^2} + \frac{\partial^2 u}{\partial y^2}\right) + \beta g(T - T_a) \qquad \text{Equation 5-3}$$

Energy:

$$u\frac{\partial T}{\partial x} + v\frac{\partial T}{\partial y} = {}^{k}/_{\rho C_p}\left(\frac{\partial^2 T}{\partial x^2} + \frac{\partial^2 T}{\partial y^2}\right) \qquad \text{Equation 5-4}$$

where C_p is specific heat capacity of air, β is volumetric thermal expansion coefficient, g is gravitational acceleration, h, *is* window height, and ϑ is kinematic viscosity of air. Density changes, due to temperature variation in a fluid at constant pressure, are represented by β the volumetric thermal expansion coefficient (Equation 5-5), which is a thermodynamic property of a fluid:

$$\beta = -\frac{1}{\rho}\left(\frac{\partial \rho}{\partial T}\right)_p \qquad \text{Equation 5-5}$$

It should be noted that the Boussinesq approximation could only be used when the temperature variation in the solution domain is not significant (Equation 5-6).

$$\beta(T - T_a) \ll 1 \qquad \text{Equation 5-6}$$

5.2.3 Grid sensitivity analysis

The quality of the mesh has a significant effect on the accuracy of the results that are obtained from the simulation. Accordingly, the computational domain is discretized using polyhedral control volumes with a refined grid near the vertical heated plate "window" interior surfaces. Three levels of grid density with G1 (24,000 cells), G2 (34,090 cells), and G3 (52,400 cells) as illustrated in Figure 5-5 is used to assess the grid independence and to ensure that the optimum mesh size and computational accuracy for Low Reynolds Number Modeling (LRNM) simulations are met. The control volume is located close to the window where fine grids are deployed to capture essential details of the temperature gradients near the window and the flow structures.

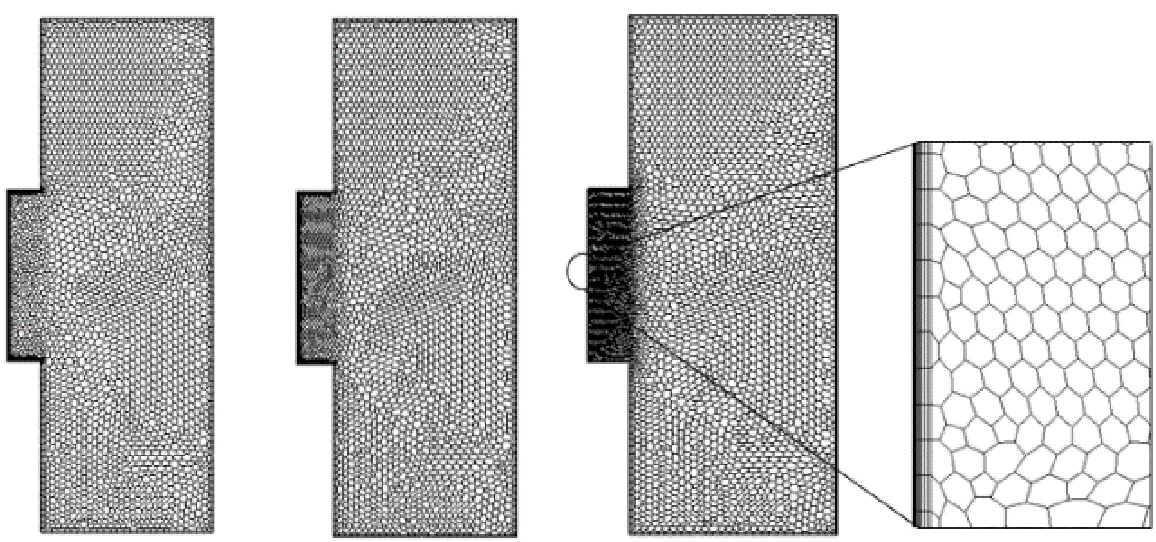

Figure 5-5: Grid distribution resolution and sensitivity analysis

On the surfaces of the window, a viscous boundary layer with 10 grid layers is generated. A stretching factor of 1.05 is used to resolve the boundary layer at all solid-fluid interfaces of the computational domain. Low-Reynolds number modeling (LRNM), Shear Stress Transport *k-ω* (*SST k-ω*) turbulence model, has been used in the present work. The LRNM requires a very high grid resolution near the wall that is computationally expensive.

The simulation has employed a grid with cell centers at a minimum distance of 120 μm from the window surface to resolve the entire boundary layer, including the viscous sublayer and the buffer layer, that dominate the convective heat resistance. For a grid independence study of G1 (coarse), G2 (medium) and G3 (fine), a Nusselt number on the surface of the window is compared. The similarly of the results from grid distribution of G3 (fine) and G2 (mean) confirmed that results are independent of the grid sizes as shown in Figure 5-6. Conservatively, the grid distribution of G3 has been adopted in the reminder of the study. Convergence is assumed when all the scaled residuals level off and reach the values 10^{-7} for x, y, z-momentum and energy, 10^{-5} for continuity and 10^{-6} for k and ε.

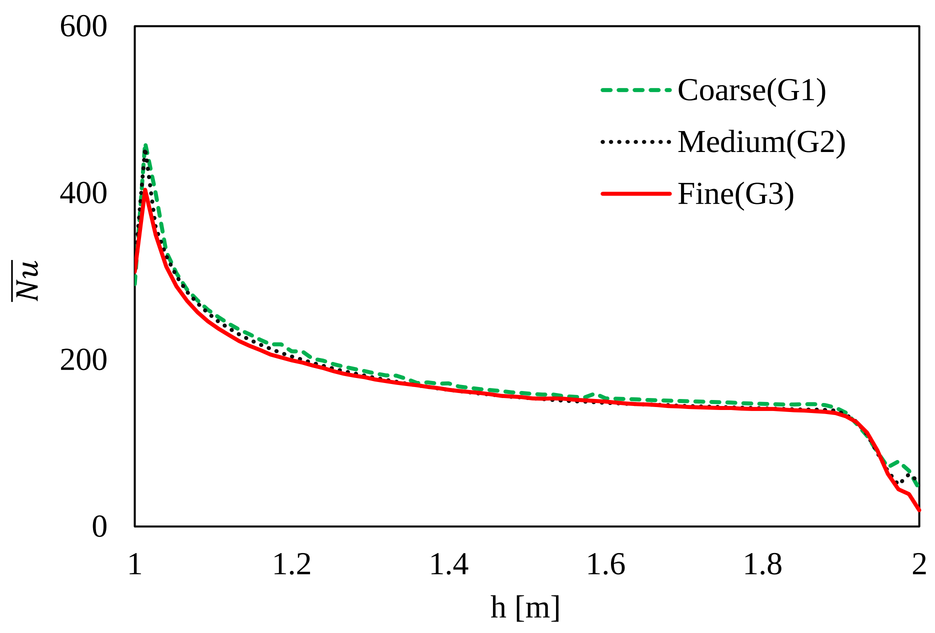

Figure 5-6: Grid sensitivity analysis: variation of Nusselt number along the window height.

5.2.4 Validation of CFD in comparison with experimental results

For validation, a computationally evaluated average Nusselt number is compared to a vertical centerline with experimental and previous computational results (see Figure 5-7). Since the property of air is considered constant except for the density, the approximate value of air is calculated to be *Pr* is 0.7. The range of the study includes laminar cases that exist at lower Rayleigh number, and turbulent flow that exists at the higher Rayleigh number. The solution parameters are $\overline{Nu}_w$ and Ra_w, where $\overline{Nu}_w$ is the mean Nusselt number based on the reference window height (Equation 5-7).

$$\overline{Nu}_w = \frac{\overline{q'_w}\, h_w}{k(T_a - T_w)} \qquad \text{Equation 5-7}$$

where $\overline{q'_w}$ is the mean heat transfer rate from the window surface, h_w is window height, k, is thermal conductivity of air, T_a , is room air temperature, and T_w, window temperature. The window Rayleigh number is expressed in the following Equation 5-8 – 5-10.

$$Ra_w = Pr.Gr = \frac{C_p\mu}{k}\left(\frac{\beta g(T_w - T_a){h_w}^3}{\vartheta^2}\right) \qquad \text{Equation 5-8}$$

$$Pr = \frac{C_p\mu}{k} \qquad \text{Equation 5-9}$$

$$Gr = \frac{\beta g(T_w - T_a){h_w}^3}{\vartheta^2} \qquad \text{Equation 5-10}$$

where *Gr* is Grashof number, μ is the dynamic viscosity of air, C_p is the specific capacity of air, β is volumetric thermal expansion coefficient, g is gravitational acceleration, and ϑ is kinematic viscosity of air. The numerical results obtained in the present study for the case of a vertical heated window are in good agreement with experimental measurements of Churchill & Chu (1975) and previous numerical study of Oosthuizen (2011). The computational results are similar in the lower laminar region where the values gradually increase until the transition region. The computational results give lower values in the turbulent region than the experimental correlation; however, the overall average deviation is less than 10%.

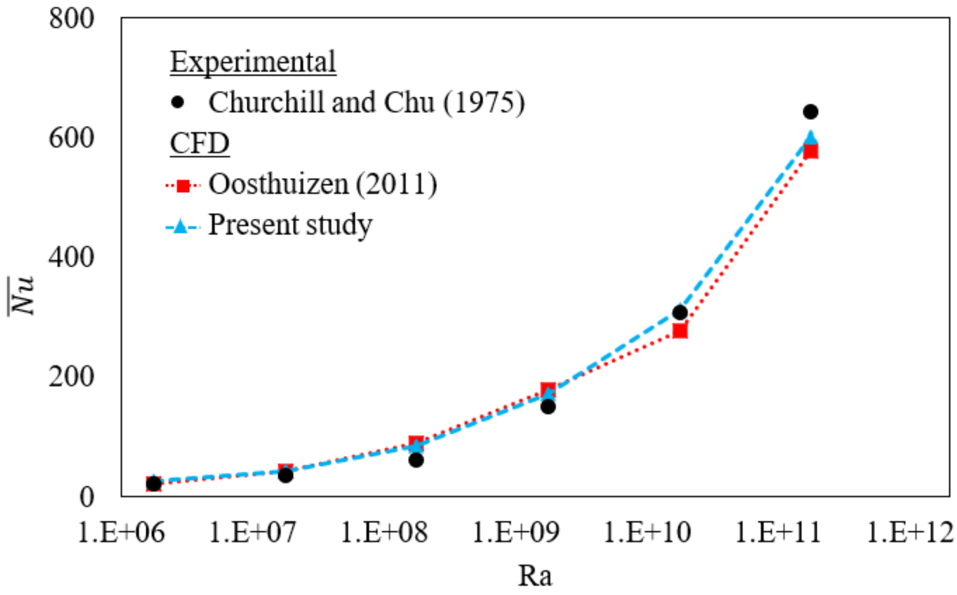

Figure 5-7: Comparison of experimental and numerical results of window Nusselt number for Rayleigh number

Therefore, the Nusselt number determined from the CFD numerical simulation can be relied upon with confidence. The same set of parameters will be used in the next full-scale 3D computational section.

5.3 Numerical evaluation of thermal comfort and convective heat transfer rate

5.3.1 Computational domain

In this study, an office room of 4 m width, 3 m depth, and 2.5 m height is considered as a computational domain as illustrated in Figure 5-8. Four different window configurations are evaluated having the same 20% WWR (Figure 5-9). The basic situation considered in the present study is an approximate model of most typical cases of window configurations. As shown in Figure 5-8, the heater width has been assumed greater than the window width, which leads to a complex three-dimensional flow near the vertical edges of the window. The presence of the heater below the window alters the flow and temperature distributions. Hence, the main focus of this study is to investigate the lowest heater temperature that ensures the cold downward flow from the window is diverted away from the floor by the hot upward flow from the heater for different window configurations.

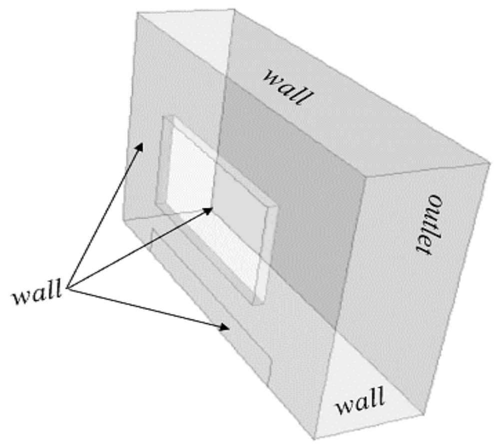

Figure 5-8: Computational domain for horizontal rectangular window configuration

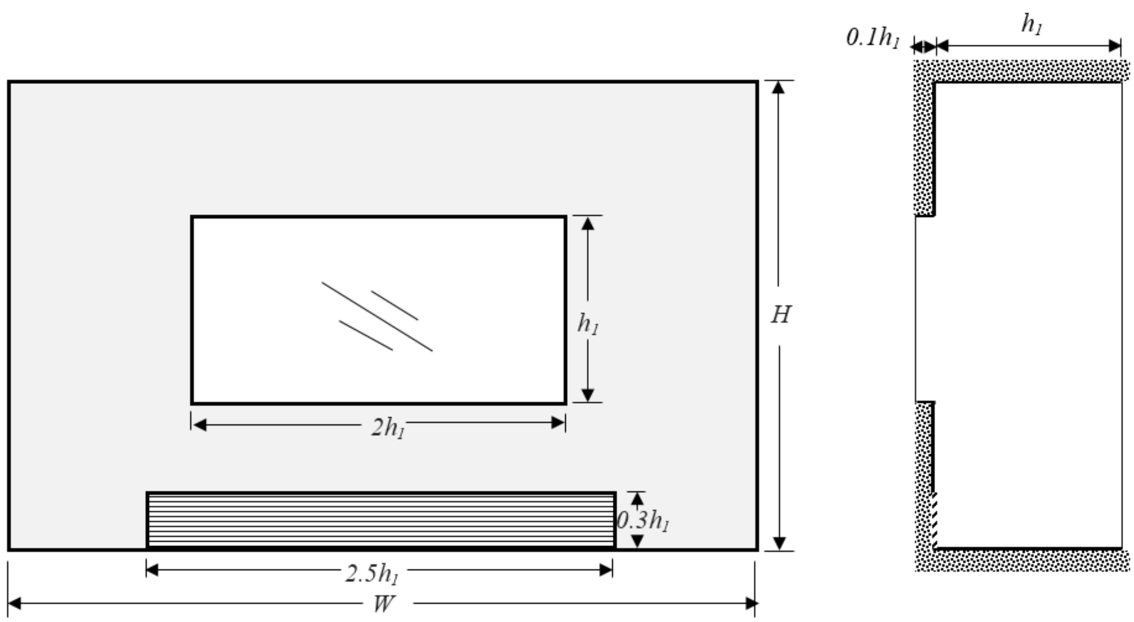

a)

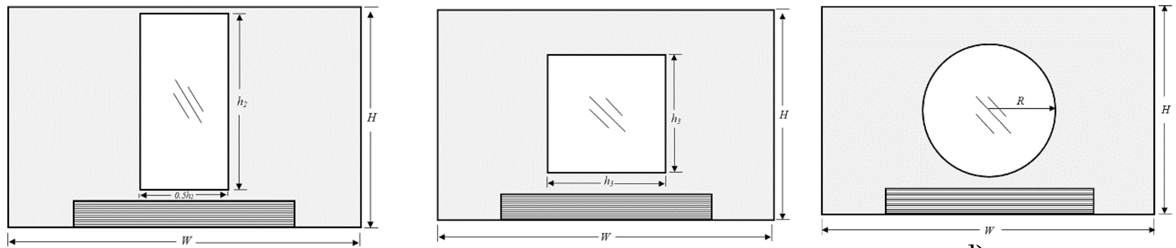

b) c) d)

Figure 5-9: Schematic of physical models used for parametric study a) horizontal b) vertical c) square, and d) circular

5.3.2 Boundary condition

In this study, only natural convection heat transfer is considered. Thus, to isolate the window effect, the heater and the window are modeled as plane isothermal boundaries, the window being colder, and the heater is hotter than the room air temperature as shown in Table 5-2. In the computational domain, the velocity is assumed zero on all the walls. The vertical right-side boundary is an open boundary, the inflow on this boundary is assumed to be constant air temperature, T_a, and walls are assumed to be adiabatic. The dimensionless heater temperature (θ) is expressed as in Equation 5-8.

$$\theta = \frac{(T_h - T_a)}{(T_a - T_w)} \qquad \text{Equation 5-11}$$

where T_h is heater temperature, T_a is room air temperature, and T_w is window temperature.

Table 5-2: Boundary conditions

Name	Boundary Condition
Wall	Adiabatic* (*u= v=w=0, q=0*)
Window	Isothermal, T_w = 273 K
Heater	Isothermal, $T_h > T_a$
Outlet	Pressure outlet, T_a = 294 K

**u, v, and w are velocities and q are heat flux*

5.4 Results and discussions

5.4.1 Cold draft analysis

As the cold air flows down past the cold surface of a window the thickness of the air layer increases from the top to the bottom. At a certain distance, along with the window, the airflow will become turbulent. This phenomenon caused more discomfort. Accordingly, as the window height increased, the turbulent effect has also increased. Thus, the window geometry has an impact on the comfort of an individual. The closer a person is to a window or the larger the size of the window, the higher the impact on comfort. Therefore, ASHRAE Standard (2013) has defined the comfort occupied zone as 0.6 m away from the window. Further, a study of Manz & Frank (2004) suggests that 0.1 m above floor height is an appropriate height for measuring thermal comfort since people usually wear shoes. Therefore, in this section, the influence of window configuration on convective heat transfer and the effect of downdraft at 0.6 m away from the window is analyzed, and results are presented.

5.4.2 Case study I: No natural convective heater below the window

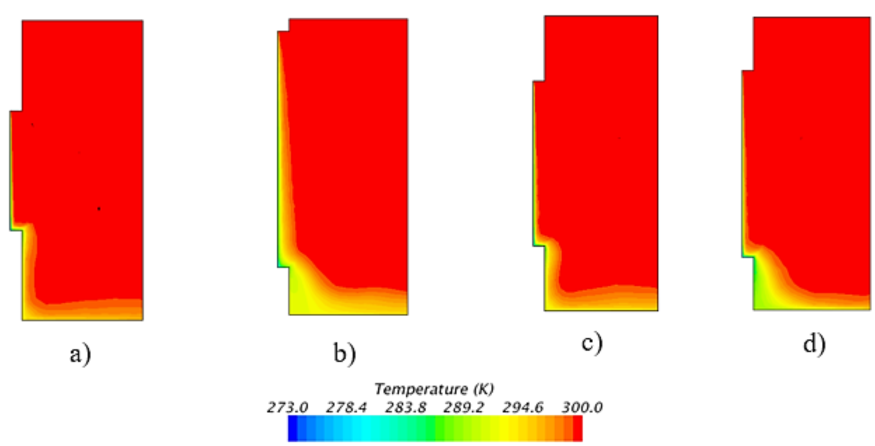

Figure 5-10: Temperature contour on vertical plane section for the cases of a) horizontal-, b) vertical-rectangular c) square, and d) circular with no heater and for $Ra_w = 10^9$

At a certain distance, the airflow will become turbulent and increase in velocity near the floor as illustrated in Figures 5-11 and 5-12. Accordingly, in all cases, the cold airflow touches the floor and may cause discomfort on the occupants.

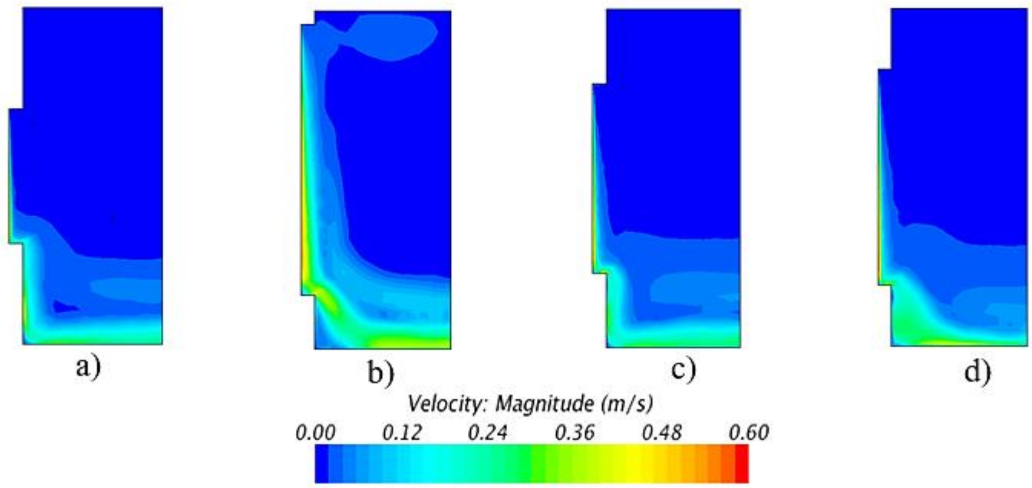

Figure 5-11: Vertical contours on vertical plane section for the case of a) horizontal-, b) vertical-rectangular, c) square, and d) circular with no heater for $Ra_w = 10^9$

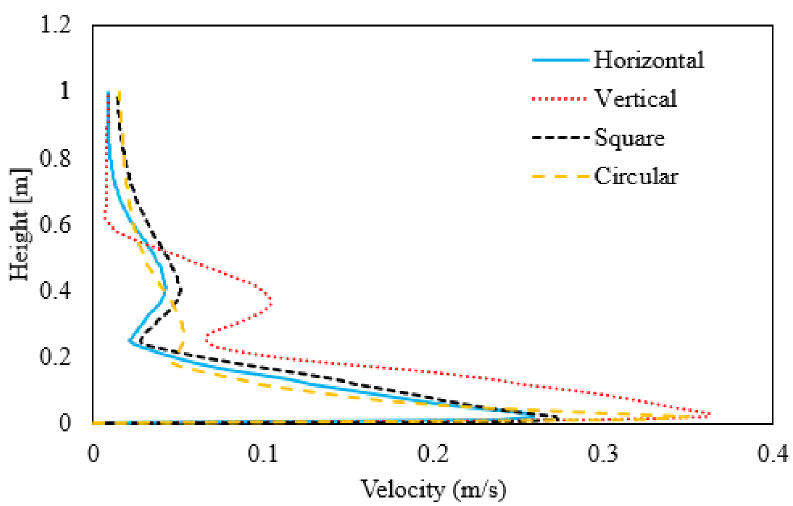

Figure 5-12: Variation of downdraft velocity at a distance of 0.6 m (No heater, $Ra_w = 10^9$)

Therefore, at the height of 0.1 m above the floor, considered to be an appropriate height as proposed by (Manz & Frank, 2004), the vertical rectangular window configuration shows the worst draft speed that is about 86% higher than the horizontal rectangular configuration as illustrated in Figure 5-12. The window's Nusselt number (see Figure 5-13), at lower values of Rayleigh numbers the variations are independent of the window configuration because the flow is laminar. However, at higher Rayleigh numbers, changes are dependent on the window configuration. Thus, comparing the average Nusselt number value, the horizontal configuration shows the least, and the vertical window configuration is the largest.

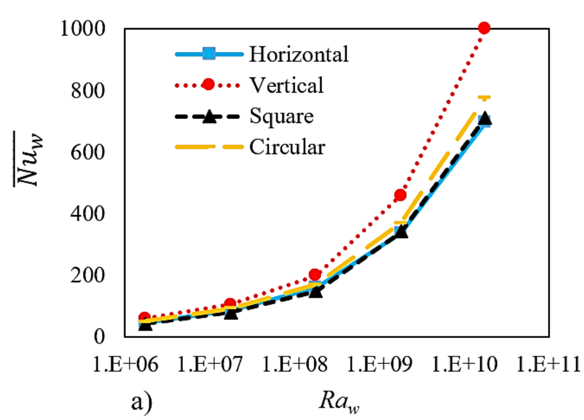

Figure 5-13: a) Variation of window Nusselt number with Rayleigh number for the case of no heater and b) variation of downdraft temperature at a distance of 0.6 m from the window for the case with no heater (Ra_w =10^9)

5.4.3 Case study II: Where there is a natural convective heater below the window

For the case with a convective heater below the window, the solution parameters are draft velocity (v), room air temperature at the suggested occupied zone (0.6 m from the window), and the heater Rayleigh number (Ra_h) and heater dimensionless temperature (θ). Where the analysis is based on the Ra_h as shown in Equation 5-12. The typical variations of window Nusselt numbers with heater Rayleigh number for dimensionless heater temperatures (θ) of 1 and 2 and for four window configurations are presented in the following Figures 5-15 and 5-18. The mean Nusselt number (Nu_w) (Equation 5-7) has been presented as a function of the reference window height (h_w) (see Figures 5-16 and 5-19). At the lower values of Ra_h ($1.77*10^6$ - $1.77*10^8$) considered, the windows Nusselt number variations are identical to the previous case where there is no heater below the window. However, at the higher values of Ra_h ($1.77*10^9$ -$1.77*10^{11}$) the window Nusselt numbers are higher due to the turbulent flow (see Figures 5-14 and 5-17).

$$Ra_H = \frac{\beta\rho(T_H - T_a)h_h^3}{\vartheta\alpha} \qquad \text{Equation 5-12}$$

where h_h is height of heater.

5.4.3.1 For the case of $\theta = 1$

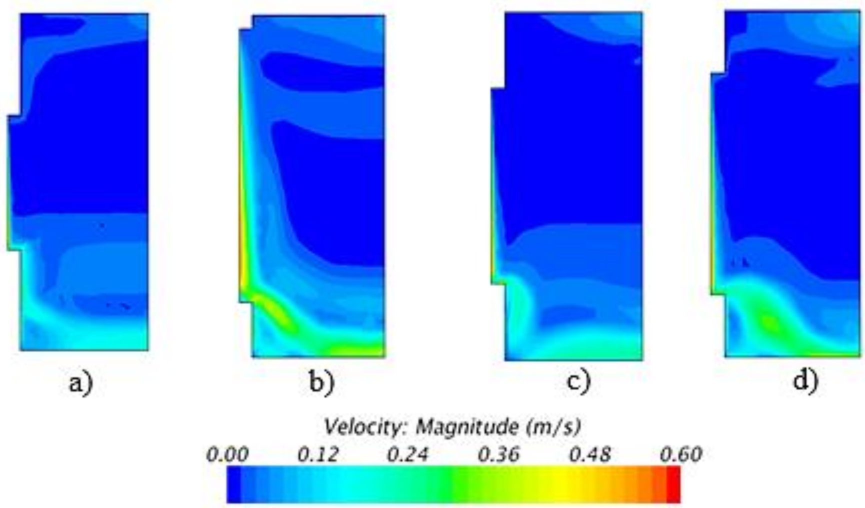

Figure 5-14: Plane section view of velocity contour for $\theta = 1$ and for the case of Ra_h = 10^9 a) horizontal b) vertical c) square, and d) circular window configuration

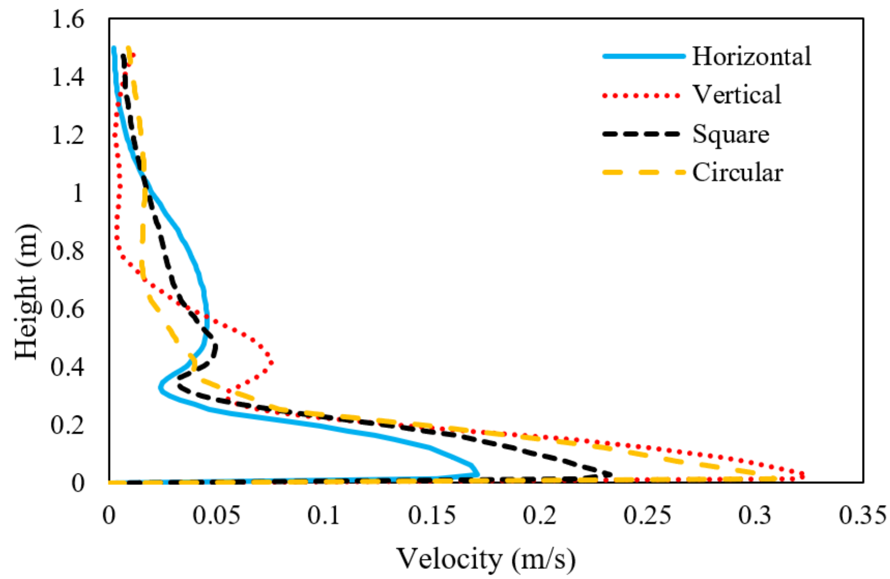

Figure 5-15: Variation of downdraft velocity at a distance of 0.6 m from the window for the case of $\theta = 1$

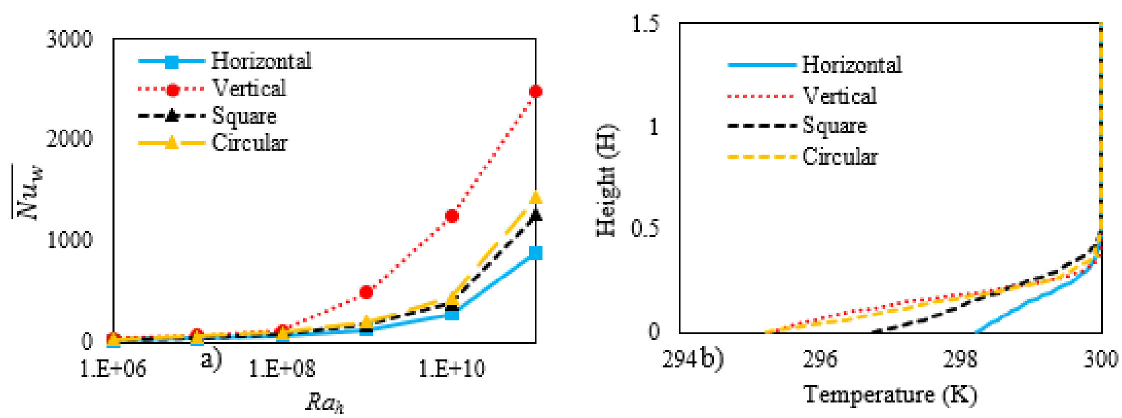

Figure 5-16: a) Variation of window Nusselt number with heater Rayleigh number for $\theta = 1$, and b) Variation of downdraft temperature at a distance of 0.6 m from the window for the case of $\theta = 1$

5.4.3.2 For the case of $\theta = 2$

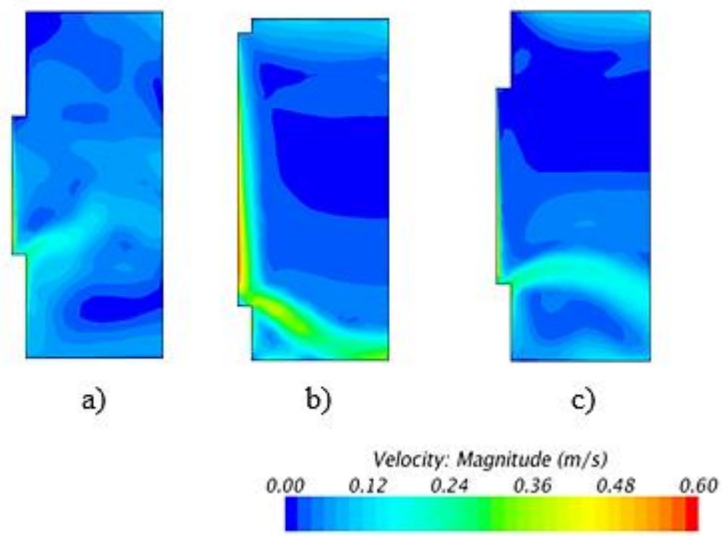

Figure 5-17: Plane section view of velocity contour for $\theta = 2$ and $Ra_h = 10^9$ for the case of a) horizontal -, b) Vertical – rectangular, c) square, and d) circular window configuration

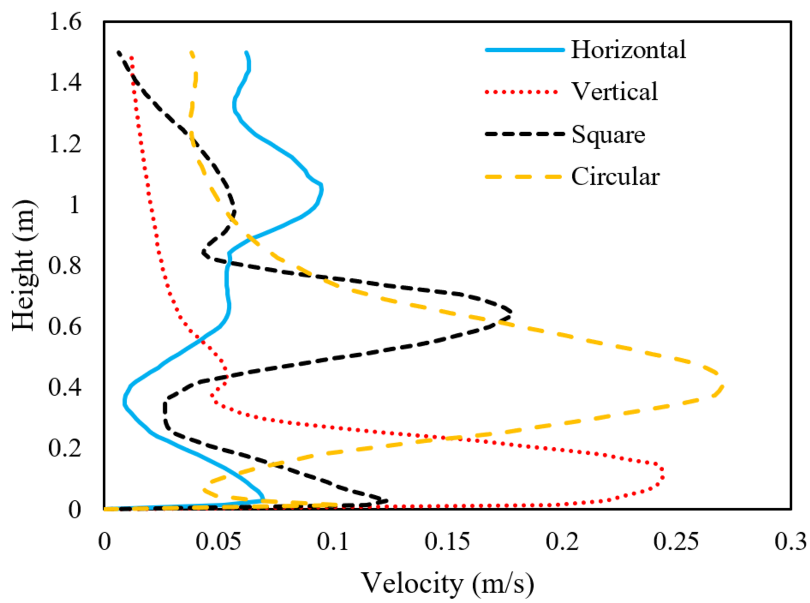

Figure 5-18: Variation of downdraft velocity at a distance of 0.6 m from the window for the case of $\theta = 2$

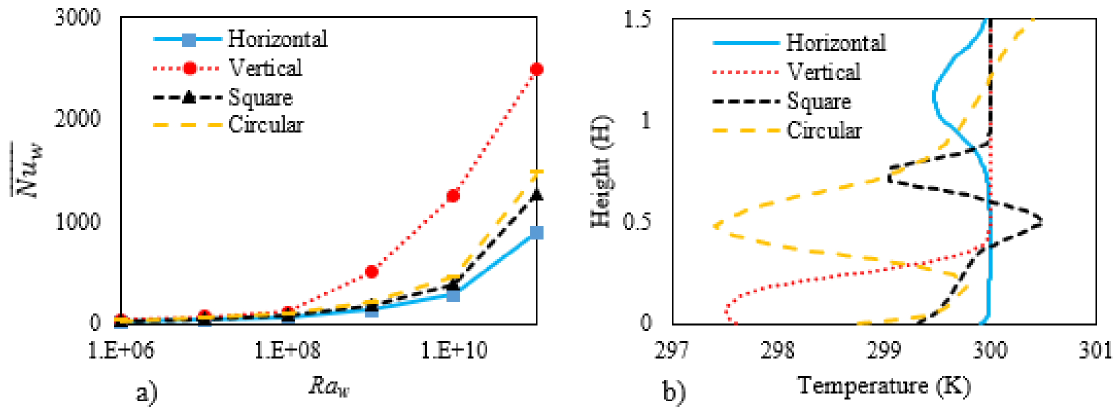

Figure 5-19: Variation of window Nusselt number with heater Rayleigh number for $\boldsymbol{\theta = 2}$ and for vertical rectangular configuration, and b) variation of downdraft temperature at a distance of 0.6 m from the window for the case of $\boldsymbol{\theta = 2}$

The changes in the direction of the flow are associated with the increase in θ. At low values of θ, the downward flow from the window dominates whereas at the higher values of θ the upward flow from the heater dominates. Therefore, it is essential to determine the minimum θ where the direction of the flow changes occur to maintain the thermal comfort of the room and save energy.

5.4.4 Flow patterns

The reference velocity associated with a natural convection flow over a vertical plane can be determined using Equation 5-12 (Oosthuizen & Naylor, 1999).

$$u_r = \frac{\alpha}{L}\sqrt{RaPr} \qquad \text{Equation 5-12}$$

where α is the thermal diffusion of air, Pr is the Prandtl number, and *Ra* is the Rayleigh number based on the height of the surface *L*. Thus, the change in flow pattern occurs when the u_r of the upward flow from the heater is equal to u_r of the downward airflow from the window. The downward flow from window represented in the left side of the Equation 5-13 and the upward flow are presented the right side of the Equation 5-13.

$$\frac{\alpha}{h_w}\sqrt{Ra_w Pr} = \frac{\alpha}{h_h}\sqrt{Ra_h Pr} \qquad \text{Equation 5-13}$$

From Equation 5-8:

$$Ra_w = \frac{\beta g (T_w - T_a) {h_w}^3}{\vartheta \alpha} \qquad \text{and} \qquad Ra_h = \frac{\beta g (T_h - T_a) {h_h}^3}{\vartheta \alpha}$$

Then

$$Ra_h = Ra_w \frac{\theta}{\left({}^{h_w}/_{h_h}\right)^3} \qquad \text{Equation 5-14}$$

From Equation 5-13:

$$Ra_h = Ra_w \left(\frac{h_h}{h_w}\right)^2$$

Therefore, the change is expected when:

$$\theta \left(\frac{h_h}{h_w}\right)^{-1} = 1 \qquad \text{Equation 5-15}$$

where h_w is the height of the window and h_h is the height of the heater. In this study, the height of the heater is defined as $h_h = 0.3h_w$.

Equation 5-15 defines flow pattern change can occur at a particular value of θ irrespective of the value of the Rayleigh number. However, this empirical formula (Equation 5-15) gives an approximation of the changes in the 2D flow patterns where the window and heater are in a vertically aligned position. It does not show a 3D spatial distribution of the air speeds and temperature, complex geometry of the window configurations, or the effects of the window recess and protrusion of the heater that can also affect the flow patterns (Oosthuizen & Paul, 2011; Oosthuizen, 2009). However, in realistic situations, the flow patterns are dependent upon the complex window configurations, heating systems and are sensitive to their geometrical configurations and exterior microclimates. Thus, the flow patterns for the four window configurations are determined using a high-resolution CFD approach under the specified boundary conditions.

Table 5-3: Flow pattern change

Window shapes	h_w/h_h	$\theta(Eq.15)$	$\theta(CFD)$
Horizontal rectangular	1/0.3	3.33	2
Vertical rectangular	2/0.3	6.67	4
Square	1.4/0.3	4.67	3
Circular	1.6/0.3	5.33	2.5

In the present case study, it is indicated that the flow direction change will occur at different θ for different window configurations as shown in Table 5-3. However, θ greater than two may pose safety concern with the higher heater temperature.

To analyze the flow direction variation for a hypothetical higher heater temperature θ values, the average window Nusselt number ($\overline{Nu_w}$) is normalized by the average window Nusselt numbers when there is no heater ($\overline{Nu}_{noHeat}$). Thus, the flow changes from moving dominantly downward to dominantly upward irrespective of the Rayleigh number occur at an approximate value of θ as illustrated in Figure 5-20.

It can be seen that the energy demand due to the increase in heater surface temperature counter the down draft for the horizontal rectangular windw configuration is the least. The vertical rectangular window configuration requires the most energy demand. This amounts to double "θ" derived for the horizontal window configuration.

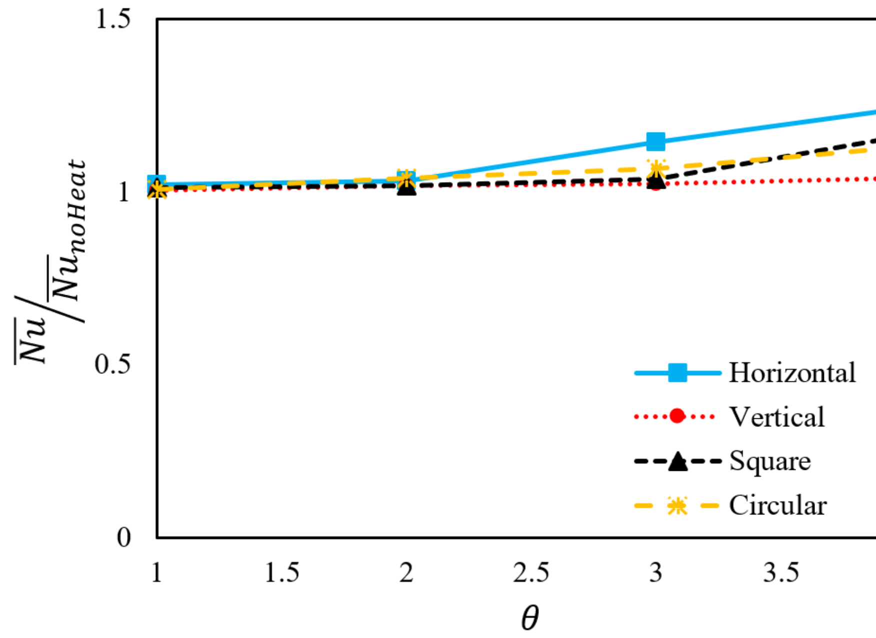

Figure 5-20: Comparison of window average Nusselt number with dimensionless heater temperature θ

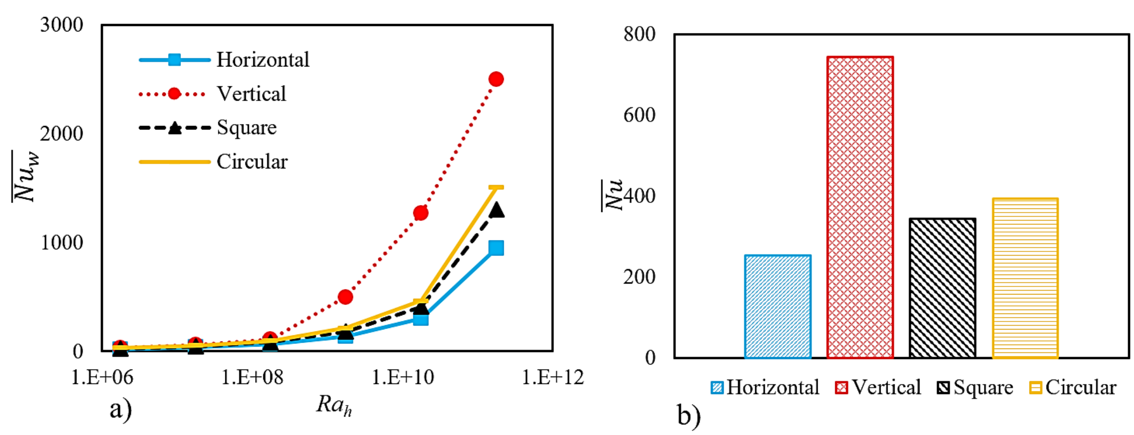

Figure 5-21: a) Comparison of window average Nusselt number for the range of dimensionless heater temperature θ (1 and 2), b) comparison of window average Nusselt number for all range *Ra* and θ

In summary, considering the average windows Nusselt number as shown in Figure 5-21 at the lower values of Rayleigh number, the variations in convective heat transfer rate are independent of the dimensionless heater temperature (θ) and the window configuration because the flow is laminar. However, at the higher values of Rayleigh numbers, the variations are dependent on the dimensionless heater temperature(θ), and the window configuration. Thus, the horizontal window configuration shows the least whereas the vertical shows the larger Nusselt number. Therefore, the horizontal window configurations require the least energy to maintain thermal comfort in a region of the room adjacent to the outdoor window. The overall thermal performance ranking from higher to lower is horizontal rectangular, square, circular and vertical rectangular window configuration, respectively.

5.5 Conclusion and further work

This study comparatively studied the convective heat transfer at the internal surface of the window to determine the convective thermal comfort and convective heat transfer rate for four different window configurations. A high-resolution 3D steady RANS simulation is used for the analysis. Initially, a CFD validation of the numerical model is carried out based on an experimental study of Churchill & Chu (1975) and numerical study of Oosthuizen, (2011). The results of the CFD validation showed that LRNM of Shear Stress Transport $k - \omega$ models could provide accurate results for the convective heat transfer rate. Based on the validated computational procedures and techniques, the downdraft velocity and convective heat transfer rates of a building are computed for four different full-scale windows with and without convective heaters. The following conclusions are deduced:

- Considering the window Nusselt number ($\overline{Nu_w}$), at the lower values of Rayleigh numbers (Ra_h), variations in convective heat transfer rate are independent of the window configuration, and the dimensionless heater temperature (θ). This is because the flow is mainly laminar. However, at the higher values of the Rayleigh number, variations are dependent on the window configuration and the dimensionless heater temperature. Thus, the horizontal-rectangular window configuration shows the least convective heat transfer rate value (Nusselt number) whereas the vertical rectangular configuration shows the largest convective heat transfer rate value.
- Considering the flow pattern near the floor, at the lower values of the dimensionless heater temperature, a downward flow from the window is observed, and the variation

of the window Nusselt number is independent of the window configuration. This flow pattern is approximately the same as the flow over a vertical plane without a heater.

- At the higher values of the dimensionless heater temperature, an upward flow from the heater is dominant, except for the vertical configuration where a downward flow is observed. In addition, the variation of the window Nusselt number is dependent on the window configuration and the dimensionless heater temperature values.
- On average, a change in the flow pattern occurs at the assumed dimensionless heater temperature value of, (θ) ~ 2, 4, 3, and 2.5 for horizontal, vertical, square, and circular window configurations, respectively. Thus, the Nusselt number, at a particular value of the Rayleigh number, increases as the dimensionless heater temperature increases, and the horizontal window configuration shows a minimum convective heat transfer rate.
- In general, considering the four window configurations that are investigated in the present study, the horizontal rectangular window configuration shows minimum downdraft velocity and convective heat transfer rate. The overall thermal performance ranking from higher to lower is horizontal rectangular, square, circular and vertical rectangular window configuration, respectively.

The present study is limited to heat transfer aspects of the windows, but as part of the on-going research, the authors are in the process of investigating optimal window configuration for minimum energy consumption. Along with the configuration of the window, many other objectives should be considered that influence the energy consumption, thermal and lighting performance of the building. Thus, a multi-objective optimization analysis will be required.

5.6 References

Ampofo, F., & Karayiannis, T. G. (2003). Experimental benchmark data for turbulent natural convection in an air-filled square cavity. *International Journal of Heat and Mass Transfer*, *46*(19), 3551-3572.

Bejan, A. (2013). *Convection heat transfer*. John wiley & sons.

Churchill, S. W., Chu, H. H. (1975). Correlating equations for laminar and turbulent free convection from a horizontal cylinder. International Journal of Heat and Mass Transfer, 18(9), 1049-1053.

Collins, M., Harrison, S. J., Naylor, D., & Oosthuizen, P. H. (2002). Heat transfer from an isothermal vertical surface with adjacent heated horizontal louvers: numerical analysis. *Transactions-American Society of Mechanical Engineers Journal of Heat Transfer*, *124*(6), 1072-1077.

Dalal, R., Naylor, D., & Roeleveld, D. (2009). A CFD study of convection in a double glazed window with an enclosed pleated blind. *Energy and Buildings*, *41*(11), 1256-1262.

de Vahl Davis, G. (1983). Natural convection of air in a square cavity: a bench mark numerical solution. *International Journal for numerical methods in fluids*, *3*(3), 249-264.

Eckert, E. R., & Jackson, T. W. (1950). *Analysis of turbulent free-convection boundary layer on flat plate* (No. NACA-TN-2207). National aeronautics and space administration Washington DC.

Ge, H. and Fazio, P. 2004, “Experimental Investigation of Cold Draft Induced by Two

Different Types of Glazing Panels in Metal Curtain Walls”. Building and Environment 39, 115 – 125.

Ghisi, E., & Tinker, J. A. (2005). An ideal window area concept for energy efficient integration of daylight and artificial light in buildings. *Building and environment*, *40*(1), 51-61.

Greenup, P. J., & Edmonds, I. R. (2004). Test room measurements and computer simulations of the micro-light guiding shade daylight redirecting device. *Solar Energy*, *76*(1), 99-109.

Handbook, A. S. H. R. A. E. (2017). Fundamentals, ASHRAE. *Atlanta*.

Heiselberg, P 1994, “Draught Risk from Cold Vertical Surfaces”. Building and Environment, 29: 297 – 301.

Kahsay M.T., Bitsuamlak G., Tariku F., (2017). Numerical study of the effect of window configuration on the convective heat transfer rate of a window. 15th Canadian Conference on Building science and Technology, Vancouver. Canada.

Lyons, P. R., Arasteh, D., & Huizenga, C. (2000). Window performance for human thermal comfort. *Transactions-American Society of Heating Refrigerating and Air Conditioning Engineers*, *106*(1), 594-604.

Lee, J. W., Jung, H. J., Park, J. Y., Lee, J. B., & Yoon, Y. (2013). Optimization of building window system in Asian regions by analyzing solar heat gain and daylighting elements. *Renewable energy*, *50*, 522-531.

Manz, H. and Frank, T. 2004, “Analysis of Thermal Comfort near Cold Vertical Surfaces by Means of Computational Fluid Dynamics”. Indoor Built Environment, 13: 233 – 242.

Machin, A. D., Naylor, D., Harrison, S. J., & Oosthuizen, P. H. (1998). Experimental study of free convection at an indoor glazing surface with a Venetian blind. HVAC&R Research, 4(2), 153-166.

National resources Canada, Heating Equipment. http://www.nrcan.gc.ca/energy/products/categories/heating/13740. Accessed Dec 24, 2016.

Ochoa, C. E., Aries, M. B., van Loenen, E. J., & Hensen, J. L. (2012). Considerations on design optimization criteria for windows providing low energy consumption and high visual comfort. *Applied Energy*, *95*, 238-245.

Oosthuizen, P. H., & Naylor, D. (1999). *An introduction to convective heat transfer analysis*. McGraw-Hill Science, Engineering & Mathematics.

Oosthuizen, P. H., Naylor, D. (2009). A numerical study of laminar-to-turbulent transition in the flow over a simple recessed window-plane blind system. In Proceedings of the 4th Canadian Solar Buildings Conference.

Oosthuizen, P. H., Naylor, D. (2010). A Numerical Study of the Effect of Blind Opening on Laminar-To-Turbulent Transition in the Flow over a Simple Recessed Window-Plane Blind System. In ASME 2010 International Mechanical Engineering Congress and Exposition (pp. 1487-1493).

Oosthuizen, P. H., Paul, J. T. (2011). Numerical Study of the Convective Heat Transfer Rate from a Window Covered by a Top Down–Bottom Up Plane Blind System to an Adjacent Room. Chemical Engineering, 25, 749.

Peng, S. H., & Davidson, L. (2001). Large eddy simulation for turbulent buoyant flow in a confined cavity. *International Journal of Heat and Fluid Flow*, *22*(3), 323-331.

Plumb, O. A., and Kennedy, L. A., 1977, "Application of a *k-e* Turbulence Model to Natural Convection from a Vertical Isothermal Surface," *ASME Journal of Heat Transfer*, 99, 79-85.

Posner, J.D., Buchanan, C.R., and Dunn-Rankin, D., 2003, "Measurement and Prediction of Indoor Air Flow in a Model Room," *Energy and Buildings*, 35(5), 515-526.

Rohdin, P., and Moshfegh, B., 2007, "Numerical Predictions of Indoor Climate in Large Industrial Premises. A Comparison Between Different k-ε Models Supported by Field Measurements," *Building and Environment* 42, 3872-3882.

STAR CCM+. CD-ADAPCO product. (2015). www.cdadapco.com/products/star-ccm Accessed on Oct. 12, 2016.

Savill, A.M., 1993, "Evaluating Turbulence Model Predictions of Transition. An ERCOFTAC Special Interest Group Project," *Applied Scientific Research*, 51(1-2), 555-562.

Schmidt, R.C., and Patankar, S.V., 1991, "Simulating Boundary Layer Transition with Low Reynolds Number *k-ε* Turbulence Models: Part 1- An Evaluation of Prediction Characteristics," *J. Turbomachinery* 113 (1), 10-17.

Straube, J. (2012). High performance Enclosure: design guide for institutional, commercial and industrial buildings in cold climate, *Building Science press,* 2nd edition, ISBN: 978-0-9837953-9.

SHARCNET is a consortium of colleges, universities and research institutes operating a network of high-performance computer clusters across south western, central and northern Ontario [Online]. Available: <www.sharcnet.ca>; 2016.

Stamou, A., and Katsiris, I., 2006, "Verification of CFD Model for Indoor Airflow and Heat Transfer," Building and Environment, 41(9), 1171-1181.

Standard, A. S. H. R. A. E. (2013). Standard 55-2013. *Thermal environmental conditions for human occupancy*.

Standard, A. S. H. R. A. E. (2010). ANSI/ASHRAE/IESNA Standard 90.1-2010. *Energy standard for buildings except low-rise residential buildings*.

Standard, A.S.H.R.A.E. (2014). ANSI/ASHRAE/USGBC/IES Standard 189.1-2014. Standard for the Design of High-Performance Green Buildings Except Low-Rise Residential Buildings.

Tariku, F., Kumaran, K., & Fazio, P. (2010). Integrated analysis of whole building heat, air and moisture transfer. *International Journal of Heat and Mass Transfer*, *53*(15), 3111-3120.

Toftum, J. (2004). Air movement–good or bad? *Indoor Air*, *14*(s7), 40-45.

Tzempelikos, A. (2005). *A methodology for integrated daylighting and thermal analysis of buildings* (Doctoral dissertation, Concordia University).

UNEP, United Nations Environment Program, http://www.unep.org/sbci/aboutsbci/background. asp. Accessed on Sep 11, 2016)

Xamán, J., Álvarez, G., Lira, L., and Estrada, C., 2005, "Numerical Study of Heat Transfer by Laminar and Turbulent Natural Convection in Tall Cavities of Façade Elements," Energy and Buildings, 37, 787-794.

Zhang, Z., Zhang, W., Zhai, Z., and Chen, Q., 2007, "Evaluation of Various Turbulence Models in Predicting Airflow and Turbulence in Enclosed Environments by CFD: Part 2-Comparison with Experimental Data from Literature," ASME HVAC & R Research, 13(6), 871-886.

Zheng, X., Liu, C., Liu, F., and Yang, C.-I., 1998, "Turbulent Transition Simulation Using the k-ω Model," International Journal for Numerical Methods in Engineering, 42(5), 907-926.

Zitzmann, T., Cook, M., Pfrommer, P., Rees, S., & Marjanovic, L. (2005, August). Simulation of steady-state natural convection using CFD. In *Proc. of the 9th International IBPSA Conference Building Simulation 2005* (pp. 1449-1456). Montréal: IBPSA.

Chapter 6

6 Optimization of window configuration on high-rise building

6.1 Introduction

The need for energy efficient buildings has increased due to the increase in urban development, environmental concerns, and rising energy costs. Building façade plays a crucial role in meeting the building efficiency and internal thermal comfort demands. The primary energy use in building for heating and cooling is due to the heat flow through the façades. Window systems alone could easily be the largest heat flow contributors for buildings. Previous studies by Lee et al. (2013) and Norris et al. (2012) have shown that about 20% to 40% of building energy is lost through windows. Therefore, improving window systems should take priority over improving the opaque wall thermal resistance that has often superior thermal performance. The building façade is a complex interface between the indoor-outdoor environments (see Figure 6-1). The annual energy consumption level is strongly dependent on the outdoor microclimate and the thermal performance of the envelope.

Previous studies (Greenup & Edmonds, 2004; Tzempelikos, 2005; Ghisia et al., 2005; Ochoa et al., 2012) have shown that design and selection of a proper window system is one of the essential passive strategies for saving energy in buildings. To minimize the energy consumption of a building, the window must minimize solar radiation in summer but maximize solar heat gain in winter; at the same time, it must provide appropriate daylighting and natural ventilation, which raises conflicting objectives, energy consumption and thermal comfort, in the selection of an appropriate size and position of a window. Choosing a window system and its corresponding configuration is one of fundamental decisions to be made in the early design stage, which is costly to be changed later. In practice, windows configured in high-rise buildings are architecturally driven and are based on, for example, the ASHRAE recommended approach (ASHRAE 90.1, 2010). Local microclimate, building geometry, building form, and orientation have a significant impact on windows performance, but typically are not comprehensively considered in practice.

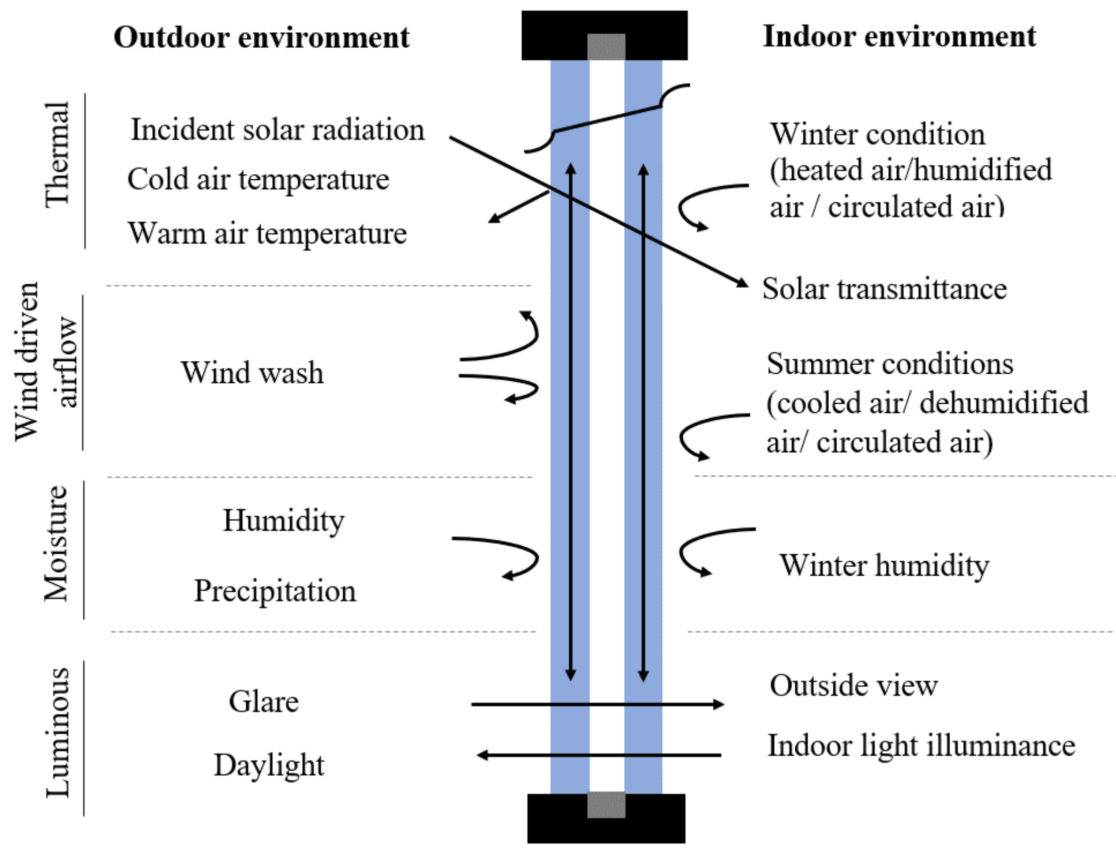

Figure 6-1: A window as an interface between indoor-outdoor environment

To investigate the effect of window configuration on building energy consumption, one of the conventional methods is assessing building energy consumption by changing a design parameter while other parameters remain constant. In the study of Susorova (2013), for instance, a window-to-wall ratio (WWR) was changed for a different direction of the building and this method was repeated for all building parameters. Since building energy simulation programs are based on a scenario-by-scenario process, this procedure is often time-consuming, and the exploration of the design space is usually not fully completed. Thus, it is ineffective in deciding the optimum solutions (Caldas & Norford, 2002; Rapone, 2012). In this respect, coupling a proper optimization procedure with a building energy simulation program makes it possible to analyze and optimize the characteristics and performance of buildings (Caldas & Norford, 2002; Rapone, 2012, Nguyen, 2014; Delgarm et al., 2016). Hence, due to the iterative nature of the procedure, simulation-based optimization tools are required.

Simulation-based optimization is a procedure that couples an optimization program to a simulation program whose function is to calculate a specific performance of a model. Simulation-based optimization has become an efficient measure to reach a cost-effective building design with reliable performance in a short time (Rapone, 2012; Nguyen, 2014). Many researchers use Building Energy Simulation (BES) programs, such as EnergyPlus, DoE-2, ESP-r, eQUEST, TRNSYS, or any custom-made programs (Liu, 2015; Ellis & Torcellini, 2005; Judkoff & Neymark, 1995). Using an optimization algorithm, it is possible to perform an automated search of a design domain for one or more optimal solutions. There are many different types of algorithms that can be used, and they can be classified into two main groups: a deterministic gradient-based algorithm or probabilistic algorithms. In building envelope design studies, the evolutionary algorithms, which is a family of the probabilistic algorithm, has been used (Naboni et al., 2013; Rapone, 2012; Delgarm et al., 2016) for optimization problems due to their capability to handle large amounts of variables. Evolutionary algorithms search for optimal solutions using the principles of evolution of a species or the behavior of groups of animals, some popular evolutionary algorithms include the Genetic Algorithm (GA), Evolutionary Neural Network (ENN), and Particle Swarm Optimization (PSO) (Rapone, 2012). Some of the studies on building façade designs using GA are Wright & Farmani (2001); Znouda et al. (2007); Rapone (2012); Delgarm et al. (2016). There are different types of tools, which are available in commercial and free resources. These tools are general optimization programs are not specific tools for design façade simulation. Yi & Malkawi (2009) used EnergyPlus and the GA optimization method to optimize the shape of a building based on heat flow, heat gain, heat loss, and volume. There are numerous studies on optimization of window configuration for low-rise buildings (Caldas & Norford, 2002; Rapone, 2012; Delgarm et al., 2016). However, there are limited studies regarding high-rise building window configuration optimization.

Therefore, the main aim of this study is to develop a novel framework of simulation-based optimization of window configuration (size and shape) in high-rise buildings. This framework integrates Computational Fluid Dynamics (CFD), which is used to develop new wind-driven $CHTC\text{-}U_{10}$ coefficients specific to a high-rise building, Building Energy Simulation (BES) program to analyze the annual energy consumption, and a numerical optimizer for iterative optimal window configuration selection based on the objective function such as energy and comfort. As an application of the proposed framework, a case study of an isolated 100 m, high-rise building with a floor-to-floor height of 3.33m and floor plane dimension of 30 m x 40 m. Test case rooms are at different floor height and locations of the building (corner and center zones) are investigated to optimize their annual energy consumptions. In the present study, a steady Reynolds Average Navier-Stokes (RANS) with *SST k-ω* turbulence simulation at full-scale are considered to investigate the impact of building height and room location on the $CHTC\text{-}U_{10}$ correlations. Furthermore, by dividing the building height into ten different floor-zones, a spatial distribution of local-*CHTC* over the entire windward façade is investigated. Once the new $CHTC\text{-}U_{10}$ correlation is developed, then it is integrated into the BES to replace the existing-*CHTC* correlations to perform window configuration optimization. This process can be used for other shapes of buildings.

This chapter is organized into five sections. Section 1 presents an introduction and literature review on the limitations of window optimization on high-rise buildings. Section 2 presents the development of new local-*CHTCs* using CFD simulations. Section 3 presents the implementation of simulation-based optimization. Section 4 discusses the results, while section 5 concludes the chapter.

6.2 CFD based *CHTC* development

6.2.1 CFD setup

A building exposed to open terrain conditions for five different wind speeds U_{10} = 1, 2, 3, 4 and 5 m/s at the reference height of 10 m is considered. The outdoor air temperature is kept constant at T_{ref} = 283 K, and the building has a fixed surface temperature of T_w = 303 K. The dimensions of the 3-D Computational Domain (CD) were defined based on the height of the building (H) and recommendations by Franke et al. (2007), Tominaga et al. (2008), and Dagnew & Bitsuamlak (2014) as illustrated in Figure 6-2. The distance between the inflow boundary wall and the building is 5H, with the outflow boundary 15H downstream of the building, to allow the wake-flow to develop. The lateral boundaries are set at 5H from the building surfaces, and the CD height is 6H. Three sub-grids with different control volumes were constructed to resolve the entire boundary layer to include the viscous sublayer and the buffer layer that dominate the convective heat transfer in the CD. The sub-computational domain volume (CV) are CV_1 (H/10), CV_2 (H/20), CV_3 (H/25) with different grid density and grid distribution are constructed. The CD is discretized using polyhedral control volumes with a refined grid near the exterior surfaces of the building. As illustrated in Figure 6-3, the surfaces of the buildings have a viscous boundary layer with ten prism layers, producing $y^+ < 5$ values. A dimensionless wall distance $y^+ = (u_* y_p)/v$ is used to characterize the grid resolution near the wall, where, u_* is friction velocity (m/s), y_p is the distance from the center point of the wall adjacent cell to the wall (m), and v is kinematic viscosity (m^2/s). The simulation uses a grid with cell centers at a minimum distance of 130 μm from the building surface. A total of 4.83 x10^6 grid cells are deployed. Convergence is assumed when all the scaled residual values level off and reach 10^{-7} for *x*, *y*, *z* momentum and energy, 10^{-5} for continuity and 10^{-6} for *k* and *w*.

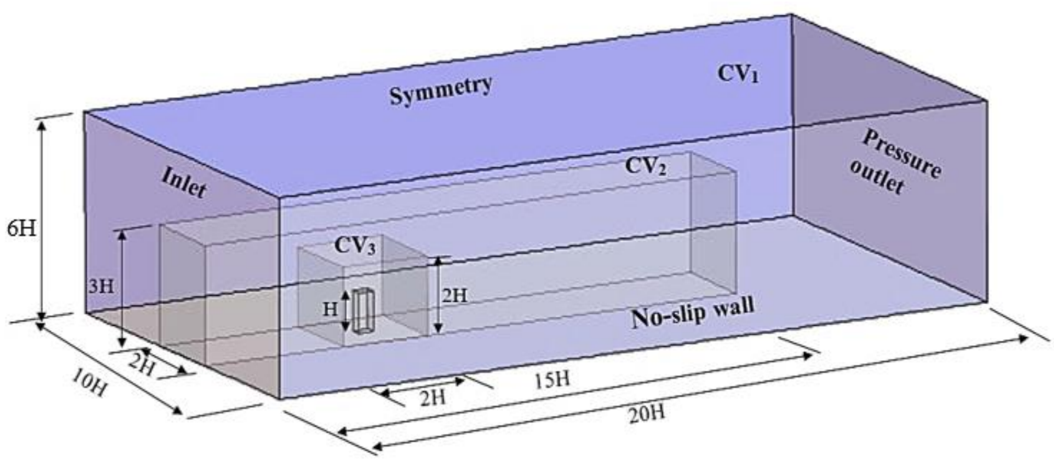

Figure 6-2: Computational domain geometry

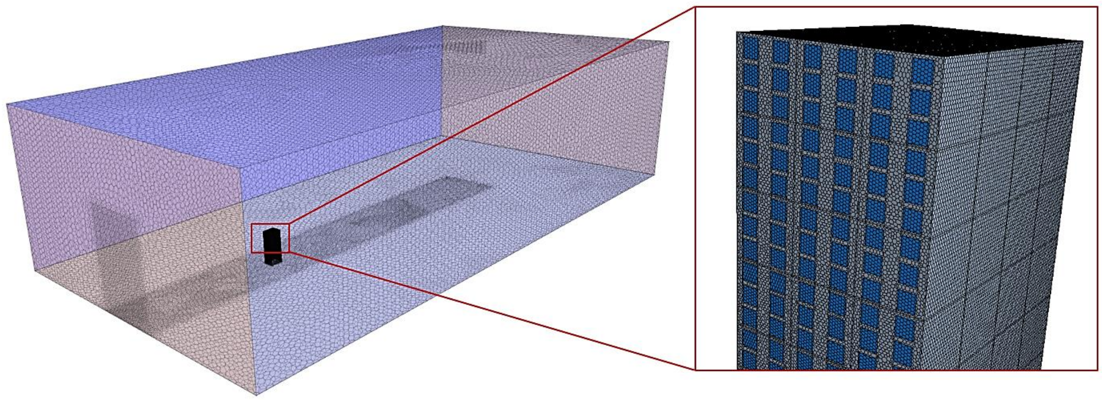

Figure 6-3: Grid distribution

6.2.2 Boundary conditions

The mean velocity and turbulent profiles are generated assuming an open terrain exposure. At the inlet of the domain, an atmospheric boundary layer (ABL) is imposed (see Equation 6-1 – 6-3). This boundary layer can be described by the logarithmic law, which constitutes a vertical profile of the mean horizontal wind speed, turbulent kinetic energy K (m^2/s^2) and turbulence dissipation rate ε (m^2/s^3) (Richards and Norris, 2011). These profiles represent a neutral ABL, where the turbulence originates only from friction and shear:

$$u(z) = \frac{u_*}{k} ln\left(\frac{z+z_0}{z_0}\right) \qquad \text{Equation 6-1}$$

$$K = 3.3u_*^2 \qquad \text{Equation 6-2}$$

$$\varepsilon = \frac{u_*^3}{k(z+z_0)} \qquad \text{Equation 6-3}$$

where z_0 is the aerodynamic dynamic roughness length which is assumed that the buildings are situated on a large grass-covered terrain z_0 = 0.03 m (ESDU, 2001), and k is the von Karman constant (~ 0.42). An adiabatic boundary condition is used for the ground surface. Symmetry boundary conditions are applied at the top and lateral sides of the computational domain. The ground surface is modeled as a no-slip wall with no roughness height ($k_s = 0$) since in Low Reynolds Number Model (*LRNM*) surface roughness values cannot be specified (Defraeye et al., 2010). Zero static pressure is applied to the outlet plane. For this simulation, only a forced convection heat transfer is considered. The Shear Stress Transport $k - \omega$ (*SST* $k - \omega$) is used as turbulent model closure in this study. Details on the CFD simulation validation from experimental data of Meinders et al. (1999) and grid sensitivity analysis are provided in Kahsay et al. (2018). The simulations are conducted using a commercial CFD package (STAR-CCM+ v.10.12, 2015) and the SHARCNET (www.sharcnet.ca, 2017) high-performance computing (HPC) facility at Western University.

6.2.3 *CHTC*-U_{10} expressions

To evaluate building energy consumption accurately, knowledge of the local-*CHTC* distribution over the facade of the building is essential. Thus, in this study, the evaluation of local-*CHTC* with the wind free stream velocity (*CHTC*-U_{10}) is the primary target, and the correlations are integrated into the building energy simulation.

The building aerodynamics play a crucial role in the local-*CHTC* distribution. The incoming wind flow is forced around the structure both on the sidewalls and the roof of the building (see Figure 6-4). The velocity increases around the leading-edge building corners, leading to higher surface friction velocity. As a result, a higher value of *CHTC* is observed at the leading top and corners zones of the building as illustrated in Figure 6-4. However, around the stagnation position and closer to the base of the buildings, lower values of *CHTC* are observed. Furthermore, the standing and horseshoe vortices around the bottom of the building, which increases the residence time of the air, leads to lower velocity, resulting in lower values of *CHTC*. The local-*CHTC* distribution for a specific room is directly dependent on its location within the building.

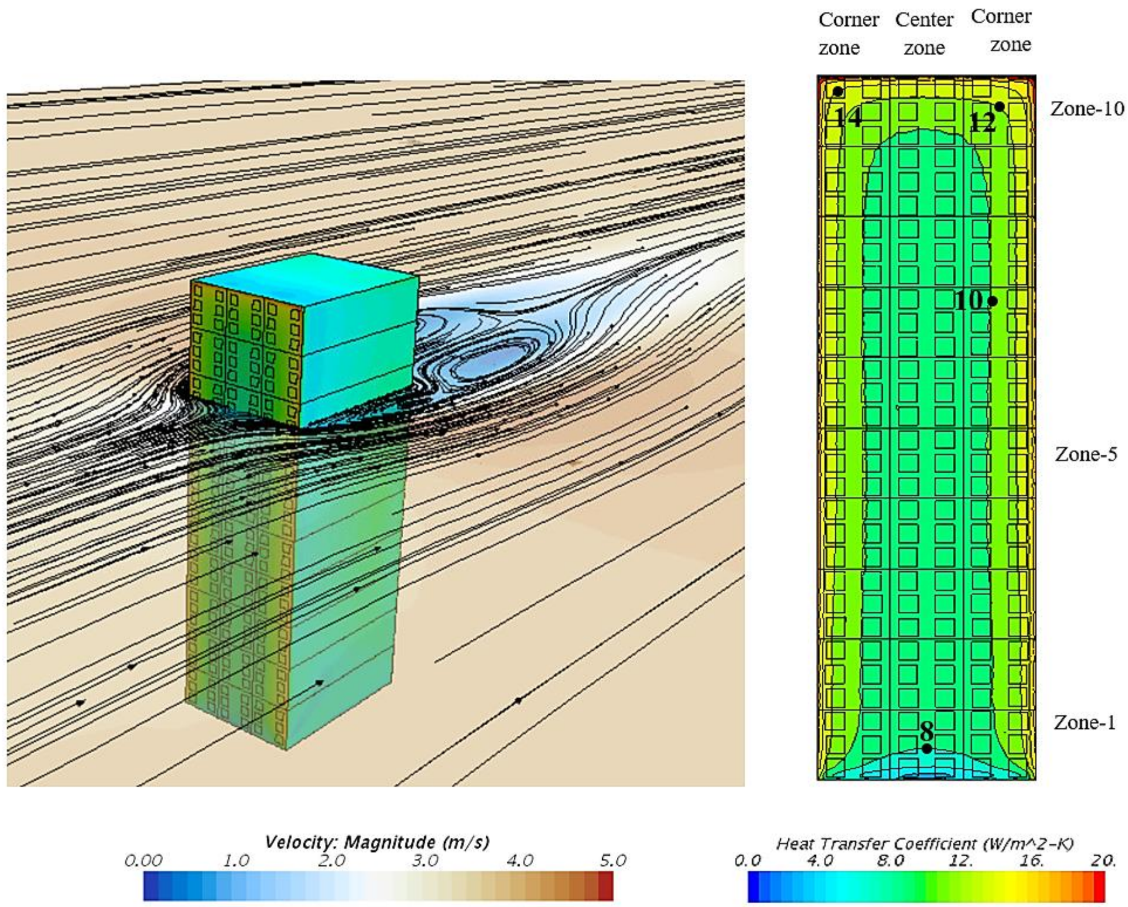

Figure 6-4: Velocity magnitude contours and *CHTC* distribution for a wind speed of 3 m/s at 10 m ref. height at the inlet.

Table 6-1 shows the local-*CHTC* correlations that have a high coefficient of determination (R^2) for different wind speeds at a corner- and center-zones of a building, respectively.

Table 6-1: Local-*CHTC* distribution on center and corner-zones of a 100 m tall of building for a windward side for a wind speed of 1 to 5 m/s at 10 m ref. height at the inlet.

Zone	Zone location	$CHTC_{avg} - U_{10}$ correlation for windward (W/m²K)	R^2 (-)
	Center-zone	$CHTC_{avg} = 3.29U_{10}^{0.78}$	0.9966
1	Corner-zone	$CHTC_{avg} = 4.16U_{10}^{0.8}$	0.9991
	Center-zone	$CHTC_{avg} = 3.7U_{10}^{0.81}$	0.997
2	Corner-zone	$CHTC_{avg} = 4.49U_{10}^{0.82}$	0.9988
	Center-zone	$CHTC_{avg} = 3.65U_{10}^{0.83}$	0.9975
3	Corner-zone	$CHTC_{avg} = 4.47U_{10}^{0.83}$	0.999
	Center-zone	$CHTC_{avg} = 3.66U_{10}^{0.83}$	0.9983
4	Corner-zone	$CHTC_{avg} = 4.51U_{10}^{0.83}$	0.9995
	Center-zone	$CHTC_{avg} = 3.60U_{10}^{0.83}$	0.9943
5	Corner-zone	$CHTC_{avg} = 4.58U_{10}^{0.83}$	0.9997
	Center-zone	$CHTC_{avg} = 3.68U_{10}^{0.80}$	0.9989
6	Corner-zone	$CHTC_{avg} = 4.61U_{10}^{0.81}$	0.997
	Center-zone	$CHTC_{avg} = 3.68U_{10}^{0.8}$	0.9987
7	Corner-zone	$CHTC_{avg} = 4.65U_{10}^{0.81}$	0.9997
	Center-zone	$CHTC_{avg} = 3.7U_{10}^{0.79}$	0.9986
8	Corner-zone	$CHTC_{avg} = 4.64U_{10}^{0.81}$	0.9993
	Center-zone	$CHTC_{avg} = 3.844U_{10}^{0.8}$	0.9988
9	Corner-zone	$CHTC_{avg} = 4.75U_{10}^{0.92}$	0.9996
	Center-zone	$CHTC_{avg} = 4.83U_{10}^{0.81}$	0.9996
10	Corner-zone	$CHTC_{avg} = 5.43U_{10}^{0.82}$	0.9998

$CHTC_{avg}$ surface-averaged convective heat transfer coefficient; U_{10} wind speed at ref. a height of 10 m; R^2: Coefficient of determination.

The new-*CHTC* developed for the corner and center-zone of the buildings, as shown in Table 6-1 are integrated into EnergyPlus to replace the existing-*CHTC*. Therefore, the building energy simulation in this stud is performed based on the actual exposure of the room to its local-*CHTC* distribution.

6.3 Building energy simulation analysis

6.3.1 EnergyPlus

The building energy simulation is conducted using EnergyPlus V8.9.0 software, developed by the US Department of Energy (DOE) (DOE, 2016). The energy simulation program can model a whole building and calculates the combined heat transfer of heating and cooling loads necessary to maintain the thermal control set points throughout a secondary HVAC system, as well as the consumption of the primary plant equipment. The energy simulation model is based on the fundamental principles of thermal balance (DOE, 2016) as shown in Equation 6-4. The input model consists of text files, which are interpreted by the simulation manager, which can also interact with external modules to interpret data coming from various sources. Formulating energy and moisture balances for the zone air is the basis for the zone and air system integration and to solve the resulting ordinary equations. The heat balance of air scheme is formulated as:

$$C_z \frac{dT_z}{dt} = \sum_{i=1}^{N_i} \dot{Q}_\imath + \sum_{i=1}^{N_{surf.}} h_i A_i (T_{si} - T_z) + \sum_{i=1}^{N_{zone}} \dot{m}_i C_p (T_{zi} - T_z) + \dot{m}_{inf} C_p (T_\infty - T_z) + \dot{Q}_{sys}$$

Equation 6-4

where:

$C_z \frac{dT_z}{dt}$ is heat stored in the air,

$\sum_{i=1}^{N_i} Q_i$ is the sum of convective internal loads?

$\sum_{i=1}^{N_{surf.}} h_i A_i (T_s - T_a)$ is convective heat transfer from the zone surface

$\sum_{i=1}^{N_{zones}} m_i C_p (T_i - T_a)$ is heat transfer due to inter-zone air mixing,

$\dot{m}_{inf}C_p(T_\infty - T_a)$ is heat transfer due to infiltration of outside air, and

$\dot{Q}_{sys}$ is air systems provide hot or cold air to the zones to meet heating or cooling loads.

If the air capacitance is neglected, the steady state system output is:

$$-Q_{sys} = \sum_{i=1}^{N_i} Q_i + \sum_{i=1}^{N_{surf.}} h_i A_i (T_{si} - T_z) + \sum_{i=1}^{N_{zone}} m_i C_p (T_{zi} - T_z) + \dot{m}_{inf} C_p (T_\infty - T_z)$$

Equation 6-5

The air system (Q_{sys}) is expressed in the form of the difference between the supply air enthalpy and the leaving air enthalpy.

$$\dot{Q}_{sys} = \dot{m}_{sys} C_p \left(T_{sup} - T_z\right)$$ Equation 6-6

If Equation 6-6 is substituted into Equation 6-5, we have:

$$C_z \frac{dT_z}{dt} = \sum_{i=1}^{N_i} Q_i + \sum_{i=1}^{N_{surf.}} h_i A_i (T_{si} - T_z) + \sum_{i=1}^{N_{zone}} m_i C_p (T_{zi} - T_z) + \dot{m}_{inf} C_p (T_\infty - T_z) + \dot{m}_{sys} C_p \left(T_{sup} - T_z\right)$$ Equation 6-7

Equation 6-7 shows that the sum of system output and zone loads are equal to the change in energy stored in the zone.

6.3.1.1 Description of the building model

To investigate the effect of wind-driven *CHTC* on window configuration and energy performance of a high-rise building, the proposed method is applied to a single test room, which is located at a different position of the building height as shown in the case study Table 6-2. As illustrated in Figure 6-5, the architectural schematic view of the baseline room are 5 m width, 10 m depth, and 3.33 m height and have a 100% window-to-wall ratio. In this study model, only the southern wall of the room is exposed to the sunlight and outside air. The high-rise building is made of lightweight construction with dimensions of 30 m width, 40 m length, and 100 m height. The exterior walls consist of 19 mm thick gypsum board on the interior, followed by a 13 mm wall airspace, and then 128 mm thick insulation panel with 1.5 mm thick metal cladding on the exterior. The roof consists of a 19 mm thick gypsum board, followed by a 650 mm thick fiberglass quilt, finally 100 mm thick concrete slab on top. The floor slab is composed of 100 mm thick concrete, followed by 100.3 mm insulation, and 19.1 mm thick acoustic tile. The partition wall is comprised of 19 mm thick of gypsum board, followed by 15 mm partition airspace, and 19 mm thick gypsum board. The physical and thermal properties of all these materials are presented in Table 6-3.

Table 6-2: Case studies

Floor zone	**Floor height**	**Window position**
Zone 1	2^{nd} Floor	Center window
Zone 5	15^{th} Floor	Center window
Zone 10	29^{th} Floor	Corner window

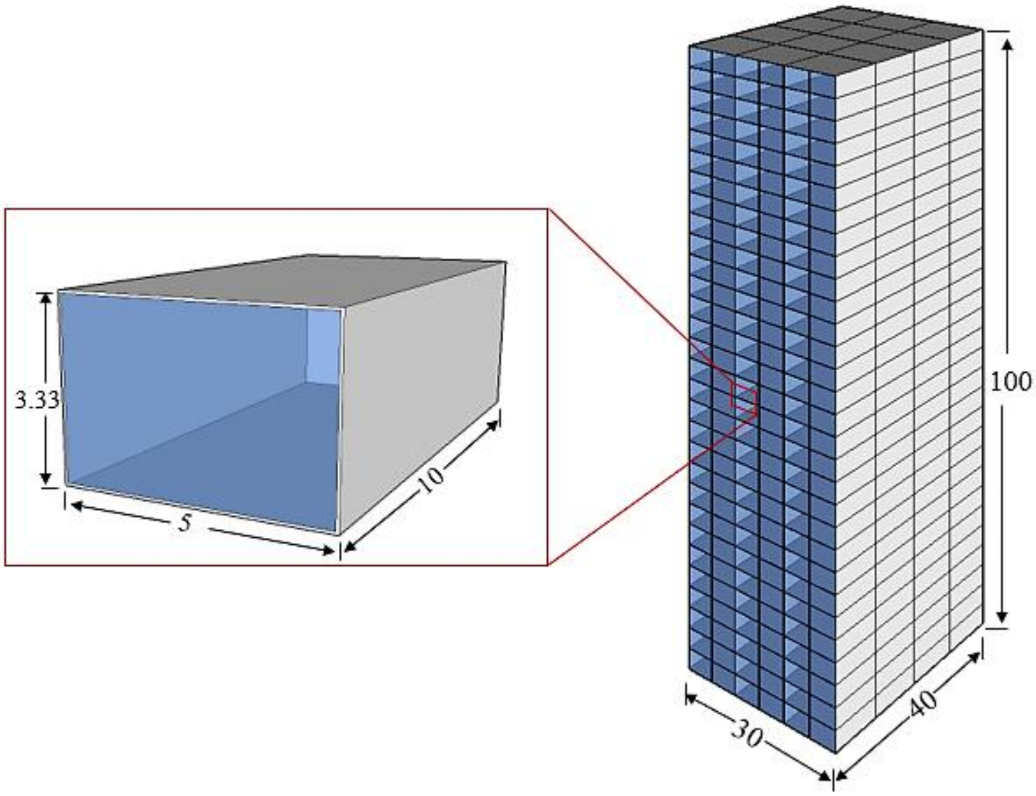

Figure 6-5: Schematic view of energy analysis baseline model

Table 6-3: Physical and thermal properties of materials that make up the building

Materials	Thermal conductivity (W/m K)	Thickness (m)	Thermal resistance (m^2 K/W)	Density (Kg/m^3)	Specific heat capacity (J/Kg K)
			Exterior wall assembly		
Metal clad	44.96	0.0015	3.33x10^{-5}	7688.86	410
Wall insulation	0.045	0.128	2.85	265	836
Wall airspace		0.013	0.15		
Gypsum board	0.16	0.019	0.11875	800	1090
			Insulated glass unit cladding		
Clear-glass	0.9	0.006	0.0067	2500	800
Window airspace		0.013	0.15		
Clear-glass	0.9	0006	0.0067	2500	800
			Partition wall		

Gypsum board	0.16	0.019	0.11875	800	1090
Partition airspace		0.013	0.15		
Gypsum board	0.16	0.019	0.11875	800	1090
			Ceiling		
Heavy weight concrete	1.95	0.1	0.051	2240	900
Ceiling air resistance			0.15		
Acoustic tile	0.06	0.0191	0.32	368	590
			Floor		
Heavy weight concrete	1.95	0.1	0.051	2240	900
Insulation	0.04	0.1003	25.075		
Acoustic tile	0.06	0.0191	0.32	368	590
			Roof		
Heavy weight concrete	1.95	0.1	0.051	2240	900
Fiberglass quilt	0.040	0.65	16.25	12.0	
Gypsum board	0.16	0.019	0.11875	800	1090

6.3.1.2 Boundary conditions and building operating conditions

The exterior boundary conditions for the walls and roof are generated from the weather data file while a constant 10^0C ground temperature is assumed for the room floor. The building is expected to operate with a continuous ventilation rate of 0.5 ACH (air-exchange per hour), and constant internal sensible heat gain of 800 W; 60% of the total heat gain is assumed to be radiative, and the remaining 40% is convective. It is assumed that all units are maintained at the same temperature so that there is no heat exchange between units and adiabatic boundary conditions are enforced. This assumption is valid for all units except the top and bottom floors. An ideal loads air system is used to control the temperature in the rooms. The room is equipped with a 10 W/m^2 compact fluorescent lamp (CFL) lighting system. Moreover, the model has a day-lighting controller sensor to automatically dim the lighting system with a threshold of 500 lx. When illuminance surpasses 500 lx, artificial lighting is not required, and the lighting system turns off. A generic office occupancy of 0.05 people/m^2 with an activity schedule of 8 am to 7 pm on workdays is considered. The heating and cooling set points are 20^0C and 27^0C, respectively for operating of the zone thermostat control. In this study, the local-*CHTC* expression integrated into the building energy consumption using EnergyPlus by defining the speed type referred as "parallel component with height adjust" which is used to modify the height of the room location and the parallel component velocity and local-$CHTC$-U_{10} distribution on the surface.

6.3.1.3 Climate to be considered

In this study, a study building is placed in Boston, MA, weather condition which is located at 42.2^0 north latitude and 71.03^0 west longitude and an altitude of 43 m is used. The annual wind speed is 5.5 m/s, and the annual average temperature high is 15^0C, and the low is 7^0C. Weather data from a typical metrological year (TMY) consists of hourly data that includes ambient temperature, relative humidity, wind speed and direction, solar radiation, cloud cover, and other metrological data over a year is used. The TMY weather data is available at the National Renewable Energy Laboratory, U.S. Department of Energy

6.3.2 jEplus

jEplus is an open-sourced tool that allows the user to manage a complex parametric simulation on building design using EnergyPlus or TRNSYS (Yi, 2009). It is developed in java file that links the weather file (*.epw*) and results extraction file as read variable input (*.rvi*) to the main (input data/macro file/*.idf*/*.imf*) file, which is necessary for a successful EnergyPlus simulation (Naboni et al., 2013; Delgarm et al., 2016). Based on the design variables and objective functions, this tool which consists of four modules is used for optimization: the input parameter database files, the Evolutionary Algorithm optimization software (*jEPlus+EA*), the energy simulation program, and the optimized output files. The objective functions are retrieved from EnergyPlus output files. Then a coupling function read variable extension (*.rvx*) is used as a hidden function, in this way the jEplus environment will completely control the EnergyPlus.

6.4 Multi-objective optimization (MOO)

Optimization is the selection of the best option concerning some criteria from a set of available candidates. When conflicting goals needed to be satisfied simultaneously, a single objective function is not sufficient to describe the problem, and multi-criteria procedure arise. Thus, the process of optimization that collect the objective functions in a systematically and simultaneously is called multi-objective optimization (MOO) (Marly et al., 2004). Multi-objective, multi-criteria or vector optimization is a process in which a number of objective functions are optimized. Optimization consists of maximizing and minimizing an objective function, and the problem is expressed mathematically as follow in Equation 6-8:

Minimize $F(\vec{x}) = (f_1(\vec{x}), f_2(\vec{x}), \ldots . f_k(\vec{x}))$ Equation 6-8

Subject to: $\begin{cases} \vec{g}(\vec{x}) \leq 0, \\ \vec{h}(\vec{x}) = 0 \end{cases}$

where the integer $k \geq 2$ is the number of objective functions, $\vec{g}(\vec{x})$ is the number of inequality constraints and their vector, $\vec{h}(\vec{x})$ is a number of equality constraints and their vector. $\vec{x} \in \Re^n$ is the vector of design variables (decision variable), where *n* is the number of decision variables x_i. $F(\vec{x}) \in \Re^k$ is their vector of the objective function in which $f_i(\vec{x}): \Re^n \to \Re^1$. The feasible design space (*X*) is defined as $\{\vec{x} | g_j(\vec{x}) \leq 0,\ j = 1,2,3 \ldots m \ and \ h_i(\vec{x}) = 0,\ \ i = 1,2,3 \ldots e\}$ where *m* is the number of inequality constraints and *e* is the number of equality constraints. The feasible criterion space (S) is defined as $\{F(\vec{x}) | \vec{x} \in X\}$. Feasibility implies that no constraint is violated.

In single objective optimization problems, a single solution can be achieved. However, in multi-objective optimization problems there is no a single global solution to determine for an optimum and the mathematical theory shows there is a set of trade-off solution, i.e., Pareto set or the Pareto frontier. Vilfredo Pareto (Censor, 1977), is one of the popular methods to present multi-objective solutions. In the solution, if no other feasible solution improves one objective without deteriorating at least another one, it is known as a Pareto or non-dominated solution. All points in the Pareto front are potentially are the optimum solution. Mathematically defined as "A *point,* $x^* \epsilon X$ *is Pareto optimal if there does not exist another point,* $x \epsilon X$*, such that* $F(x) \leq F(x^*)$*, and* $F_i(x) < F_i(x^*)$ *for at least one function".*

6.4.1 Design of the parameters

Any part of the building model is defined as a parameter. In each parameter, definitions contain a number of alternative values, which are assigned by users. Thus, each path from top to bottom of the tree represents one solution as illustrated in Figure 6-6.

6.4.1.1 Objective function and decision variables

In this study, three objective functions, the annual heating, cooling, and electric lighting demand are considered to investigate the energy performance of the case study room. The main aim is to examine optimum window configuration with minimum annual energy consumption in the room. The optimization problem consists of rooms at different floors heights and location of the building (corner and center), and window size as illustrated in Figure 6-7.

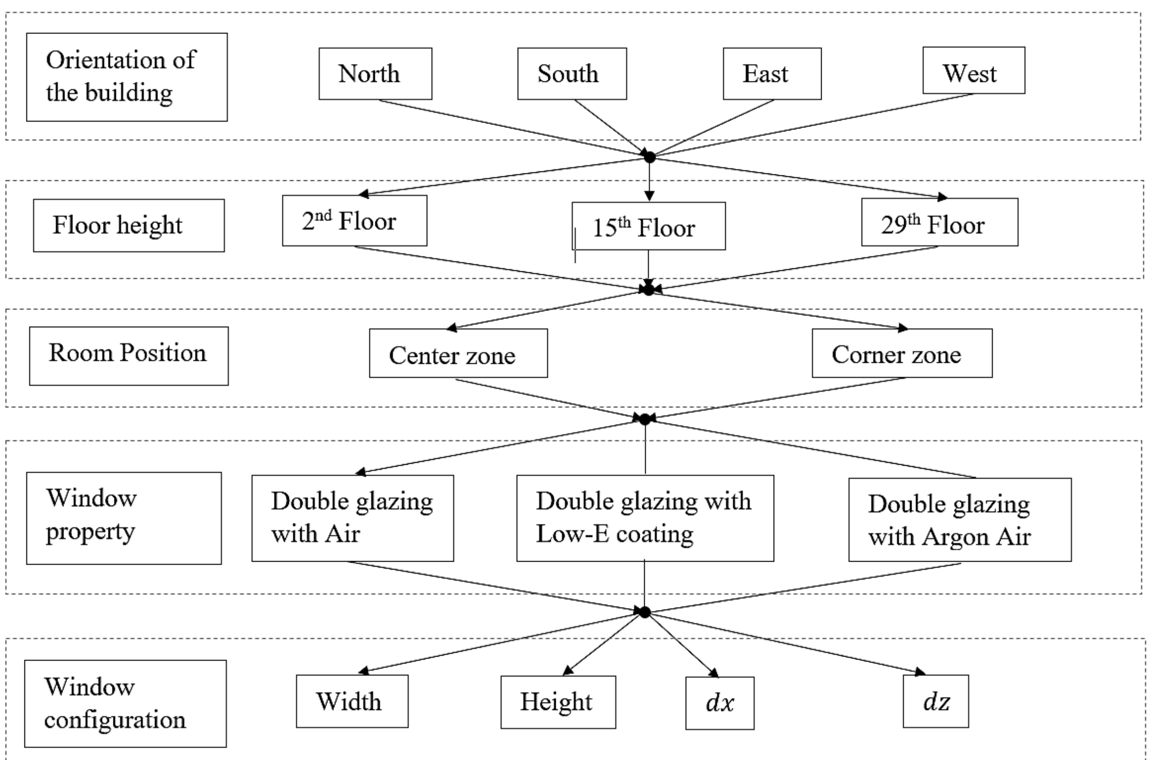

Figure 6-6: Diagram of parameter tree

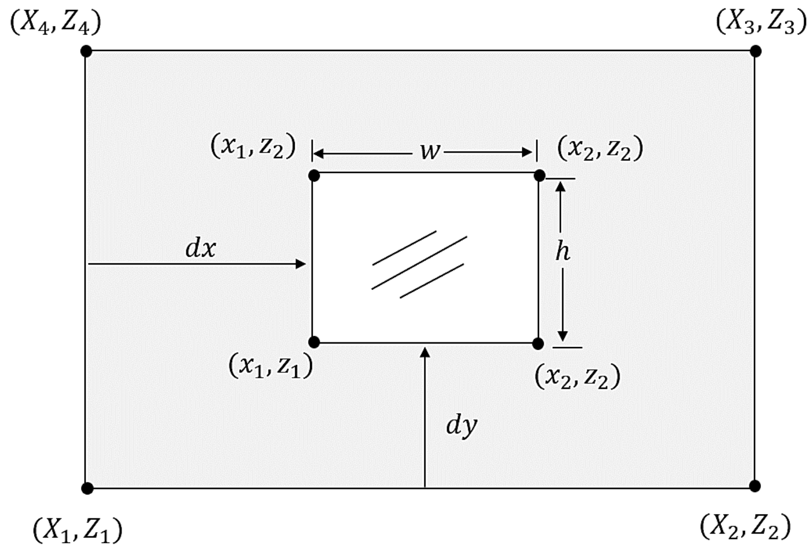

Figure 6-7: Definition of design parameters

The design parameters searching space area is between $0.1 \leq x \leq 4.9$ along the width and $0.2 \leq z \leq 3.23$ along the height of the window. The left side frame extends between $0.1 \leq x_1 \leq 4.8$ having five discrete values; and the right frame extends between $0.2 \leq x_2 \leq 4.9$ having five discrete values. The lower frame moves between $0.1 \leq z_1 \leq 3.13$ having seven discrete values: and the top frame moves between $0.2 \leq z_2 \leq 3.23$ having seven discrete values, thus the total searching space is 1225.

6.4.2 Simulation-based optimization

Simulation-based optimization is a process of integration of optimization techniques into the simulation analysis. Thus, a parametric simulation method is used to evaluate the performance of the system. To find the optimal solution in a minimum computational time, the problem is solved iteratively. In each iteration, the solution is closer to the optimal solution (Nguyen, et al., 2014). The simulation-based optimization procedure is implemented using a multi-objective and non-dominated sorting genetic algorithm (NSGA-II) code written in Java in the jEplus+EA (jEplus Evolutionary Algorithm) environment. The flowchart for the simulation-based optimization is illustrated in Figure 6-8.

6.4.2.1 Algorithm selection

There are many algorithms used for optimization problems, the choice of the optimization algorithm is dependent on the number and type of variables such as continuous and discrete, and the type of the objective function evaluated. A simulation-based optimization process where an external dynamic simulation is integrated can be highly discontinuous and non-differentiable. It is essential to use an algorithm that can complement these characteristics to compute the objective functions. Thus, Evolution algorithm is more suitable in these fields (Yi, 2009; Naboni et al., 2013; Delgarm et al., 2016).

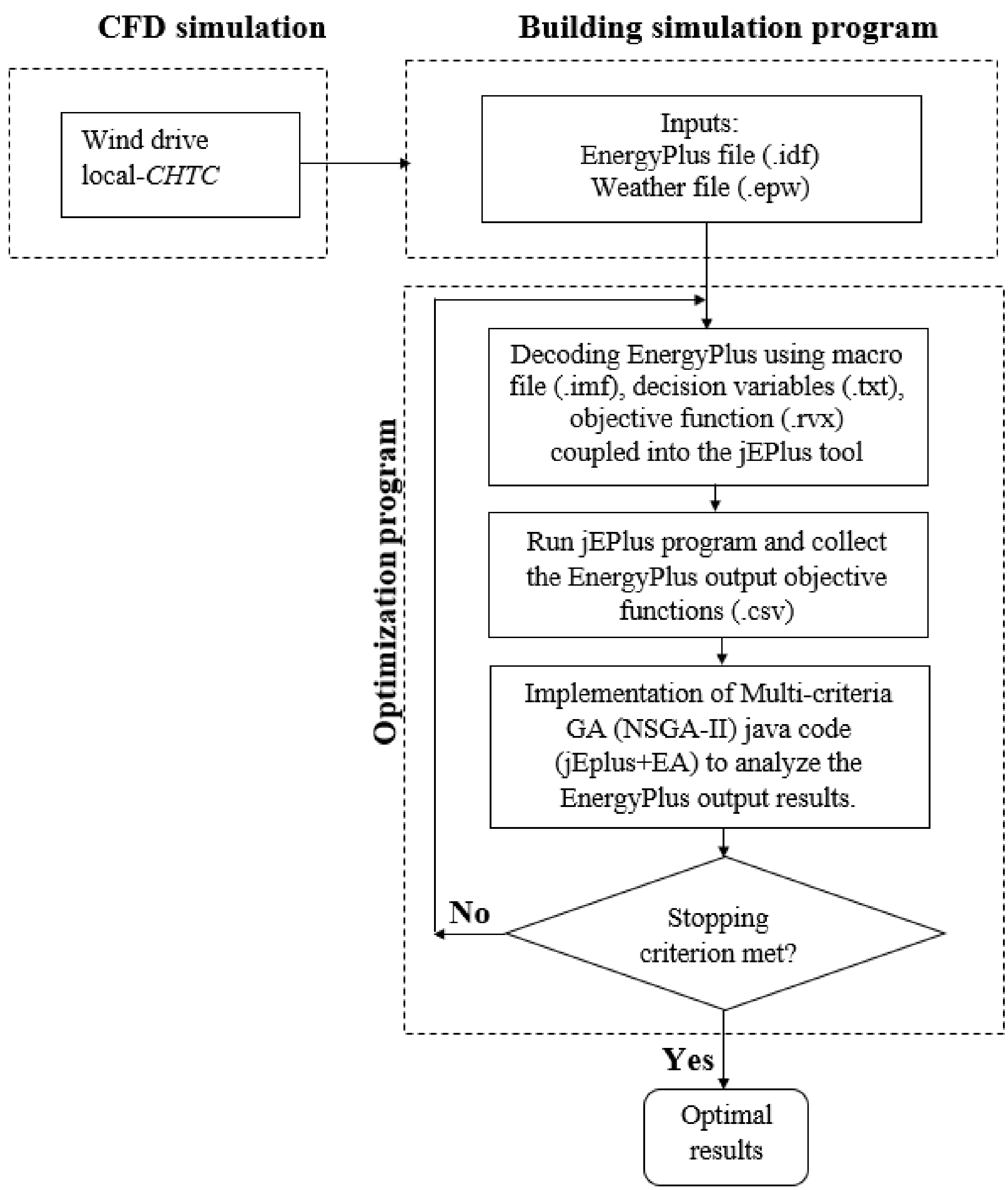

Figure 6-8: Flowchart of simulation-based optimization coupling CFD, BES, and optimization program.

6.4.2.2 Genetic Algorithm (GA)

John Holland (Holland, 1992) developed GA based on the mechanisms of natural adaptations. A genetic algorithm is population-based probabilistic method based on selection and genetic combination. One of the advantages of the GA over gradient-based techniques is that it can locate the extreme global value (i.e. maximum or minimum) with less probability of being trapped in local extreme values. The procedure involves initializations (random generated), selections, genetic operators, and termination (Rao, 2009). The general processes of GA's are illustrated in Figure 6-9.

The design variables are coded as real numbers. The optimization process starts by implementing an encoding scheme for numerically representing the problem variables. The encoding of a solution is called a "chromosome," in which each variable is encoded as a "gene". Accordingly, the optimization starts by randomly selecting candidates from the "initial population". At each step, the GA selects individuals from the current population to be *parents* based on their *fitness function* value (i.e., minimizing/maximizing their objective function values) and uses them to produce the *children* for the next *generation* through *crossovers and mutation.* Crossover and mutation are nature-inspired ways of creating new "offspring" from existing "parents". Crossover operators are applied to the candidates (parents) with higher fitness to produce better candidates (offspring's). While the mutation operators are applied to candidates with lower fitness to explore different regions in the search space and avoid stagnating in a local extreme value.

This procedure is applied to new generations, and it will continue until no significant improvements are obtained over the generations. Thus, the highest fitting candidate in the last generation will be considered the optimal solution. More detail discussion on GA can be found in (Parkinson et al., 2013). To implement the simulation-based optimization procedure, a multi-objective non-dominated sorting genetic algorithm (NSGA-II) code written in the Java environment is used. As explained before, the objective function is energy consumption (heating, cooling, and lighting) of the building required to be minimized while the design variables are geometric and property variables that controls the window configuration as illustrated in Figure 6-7.

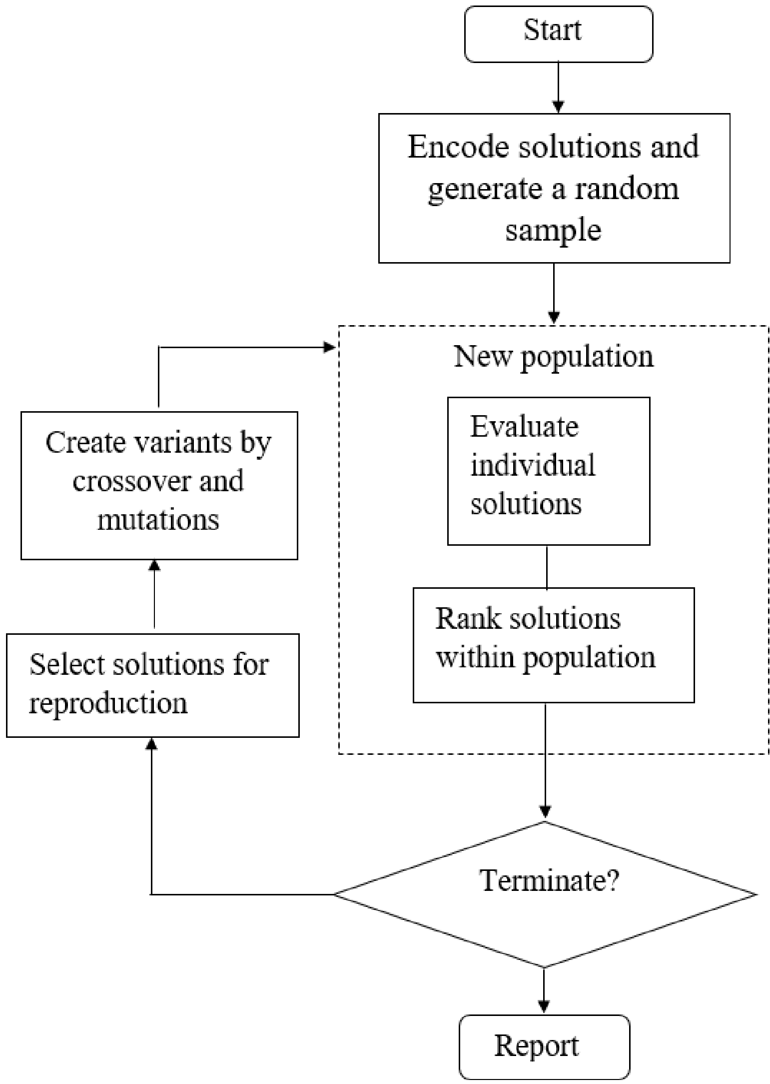

Figure 6-9: GA process flowchart

6.4.2.3 The setting of the Genetic algorithm parameters

In this study, the optimization procedure starts by randomly selecting 20 candidates to form the initial population. Then a maximum generation of 200, crossover rate is 1.0, a mutation rate of 0.2, and a binary tournament selector are selected to get the best tradeoff between the computational time and the reliability of the Pareto front.

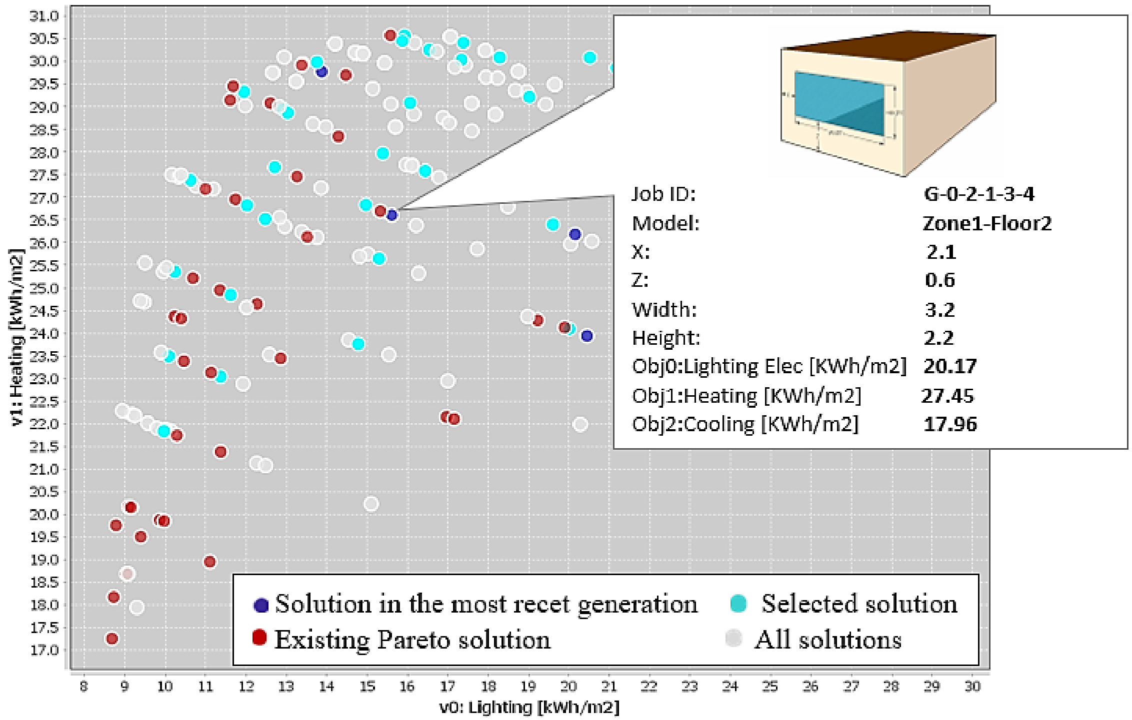

Figure 6-10: Single candidate represents one solution

As illustrated in the scattered plot of Figure 6-10, the single candidate is representing one solution, thus, the iteration is repeated until the stopping criteria is satisfied to confirm a convergence to the same optimal solution by avoiding trapping in a local minimum, i.e. the average change on the Pareto front becomes lower than the tolerance of the maximum generation is satisfied.

6.5 Results and discussions

After running the optimization procedure, a Pareto solution is created which is an archive of a tested window configuration and a series of optimal points. Figures 6-11, 6-13, and 6-15 show the optimum results of a multi-objective minimization in the form of three-dimensional Pareto front for the rooms located on the 2nd, 15th, and 29th floor rooms, respectively. Further, Figures. 6-12, 6-14, and 6-16 present a bi-objective optimization results in the forms of Pareto optimal curves for rooms located on the 2nd, 15th, and 29th floor, respectively. This prevails the conflicting objectives of both objective functions.

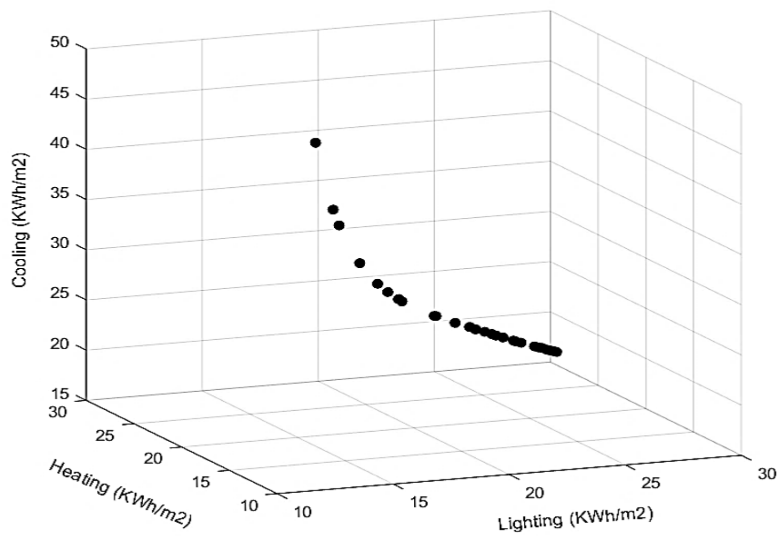

Figure 6-11: Pareto front for triple-objective optimization for case of room at the 2nd floor located at the center zone of the building

Figure 6-12 shows that as one of the objective decreases, the other ones increase. Hence, it is impossible to minimize all the objective functions simultaneously without sacrificing at least one criterion. Therefore, to choose a single optimum solution from the non-dominated set, decision-making or trade-off between criteria is required.

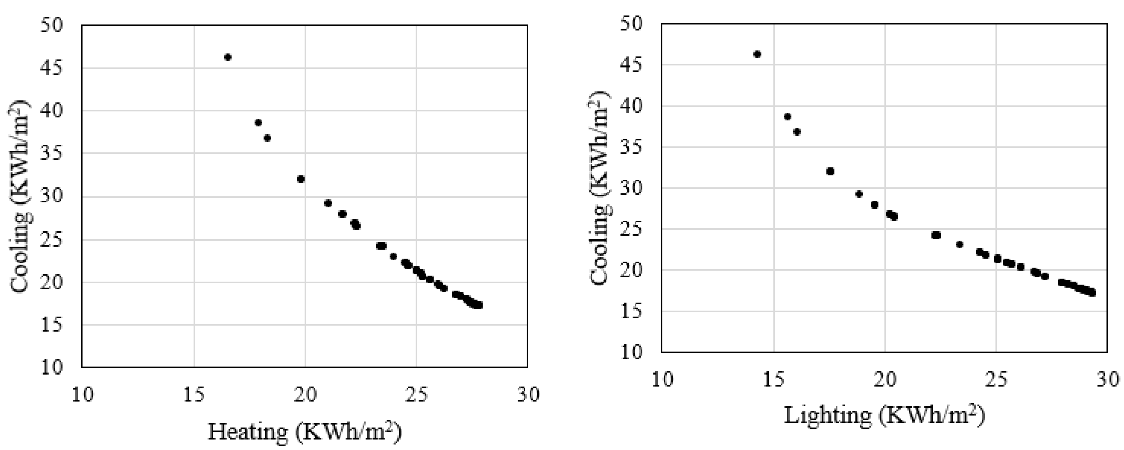

Figure 6-12: Pareto front for the bi-objective optimization for the case of room at the 2nd floor located at the center zone of the building

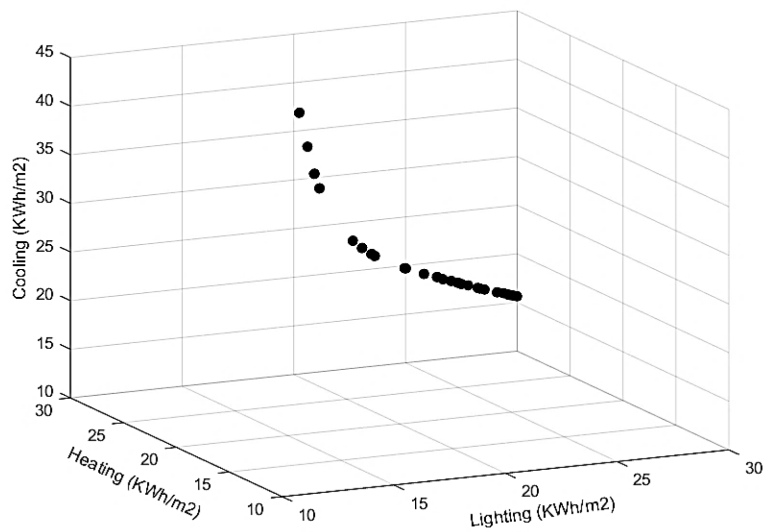

Figure 6-13: Pareto front for the triple-objective optimization for the case of room at the 15th floor located at the center zone of the building

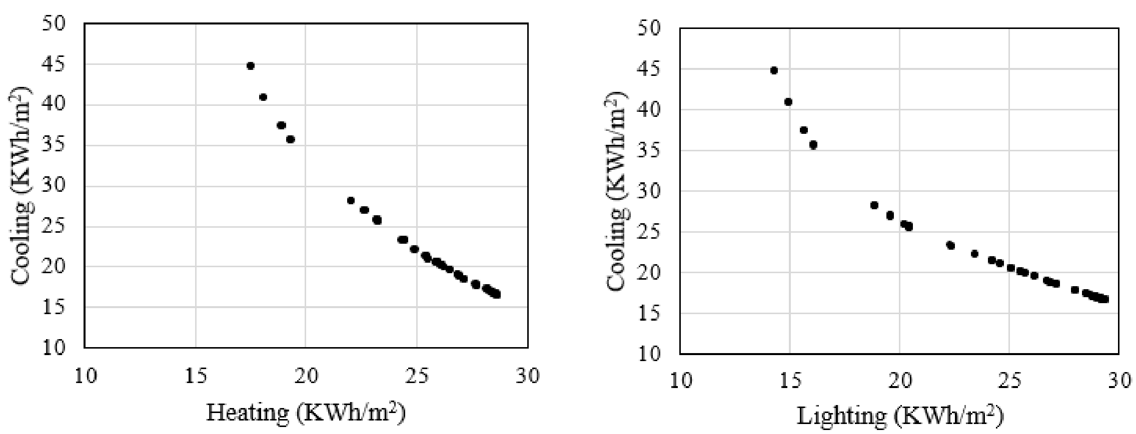

Figure 6-14: Pareto front for the bi-objective optimization for the case of room at the 15th floor located at the center zone of the building

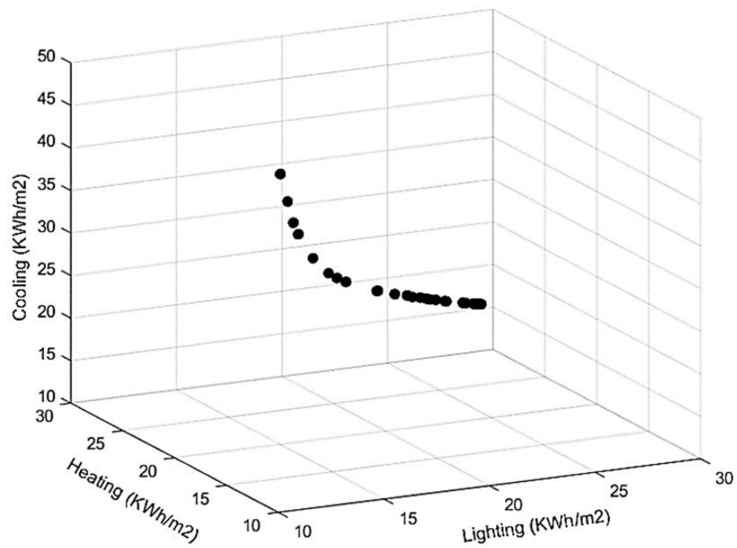

Figure 6-15: Pareto front for the triple-objective optimization for the case of room at the 29th floor located at the corner zone of the building

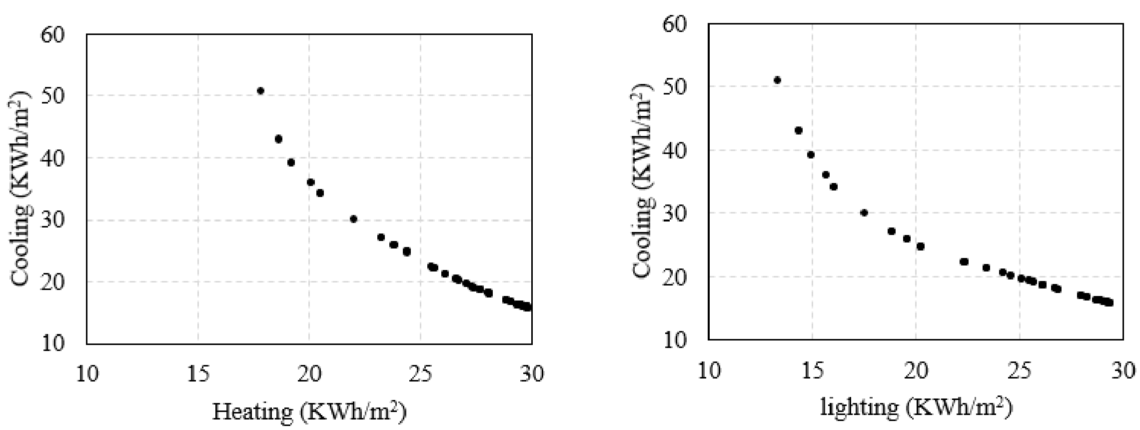

Figure 6-16: Pareto front for the bi-objective optimization for the case of room at the 29th floor located at the corner zone of the building

The multi-objective problem has an infinite number of Pareto optimal solutions. Thus, to determine a single optimal solution, it is necessary to incorporate user preference (Rao, 2009). To select the final optimum configuration among the available solutions, a decision-making process is required depending on the importance of each objective, characteristics, and performance of the system, and engineering experience. Accordingly, in this study, a weight-sum method (WSM) as shown in Equation 6-8 is used. WSM transfers the multi-criteria decision-making approach with multi-criteria optimization to mono-criteria optimization. The WSM uses the concept of multiplying each objective function by a relative weight and then sums up to a single value, which gives the designer an idea to the best solution. However, the problem with this method is that different users can assign different weights to each objective function, which will vary the optimal solution depending on the user. There are many variations of the WSM, all of which follow the same concept but with slightly altered methodologies (Marler & Arora, 2004). In this study, all consumed energy is in the form of electricity, it can be assumed that all objective functions are weighted equally. Thus, the designers may select the optimum window configuration based on their actual needs and interests.

$$U = \sum_{i=1}^{k} w_i F_i(x) \qquad \text{Equation } 6-8$$

where U is Pareto optimality; w is a vector of weights typically set by the decision maker; F is the objective function with variable x; i is initial and a subsequent number of objective functions; k maximum number of objective functions. Additional criteria based on the effect of window configuration on the convective heat transfer rate of a window and thermal comfort of occupants is included. These criteria are based on the previous work of Kahsay et al. (2017), on the numerical study of the effect of window configuration on the convective heat transfer rate of a window. A sensitivity of a window configuration on Nusselt number and room temperature distribution was examined, and the result show that horizontal window configuration has the least rate of convective heat transfer rate and down draft effect than other types of window configuration.

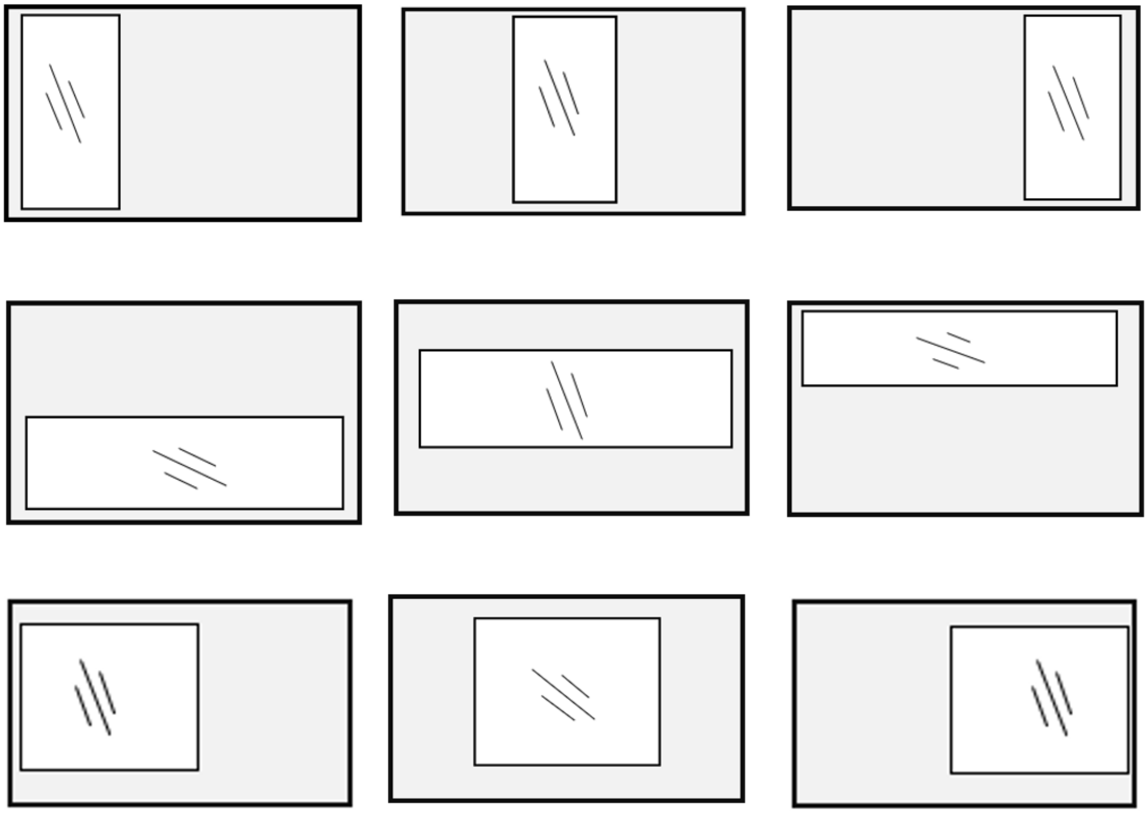

Figure 6-17: Window configurations alternatives presented as best solutions

After the WSM analysis is done, the least annual energy consumption a horizontal configuration located at the center of the wall is selected as optimum configuration for all cases. Figure 6-17 shows some of the alternative of best WWR configurations. Accordingly, considering the first case study (see Table 6-2) for a room located on the 2nd floor, the optimum values of the objective functions are presented in Table 6-4. The best optimal configuration is a window positioned at the center (1.1 m away from the edge) having 30% WWR with horizontal configuration is selected.

Table 6-4: Best values of objective functions for a room at zone 1 and floor 2nd

Optimal solution rank	Objective function	Optimal value (KWh/m²)	$U(x)$	x_1	z_1	x_2	z_2	WWR	Window position
1	Annual lighting Annual heating Annual cooling	18.9 21.11 29.04	23.0	0.1	0.6	2.2	3.2	32.8	Position: Right corner Shape: Square
2	Annual lighting Annual heating Annual cooling	19.6 21.75 27.78	23.1	1.1	1.1	4.2	2.7	29.8	Position: Centered Shape: Horizontal
3	Annual lighting Annual heating Annual cooling	19.6 21.75 27.78	23.1	0.1	1.1	3.2	2.7	29.8	Position: Right corner Shape: Horizontal
4	Annual lighting Annual heating Annual cooling	19.6 21.76 27.78	23.1	0.1	1.6	3.2	3.2	29.8	Position: Right corner Shape: Horizontal

Considering the second case study (see Table 6-2) for the case of a room located on the 15th floor, the best values of the objective functions are presented in Table 6-5. The best optimal configuration is a window positioned at the center (1.1 m away from the edge) having around 48% WWR with horizontal configuration is selected.

Table 6-5: Best values of the objective functions for a room at zone 5 and floor 15th

Optimal solution rank	Objective function	Optimal value (KWh/m²)	$U(x)$	x_1	z_1	x_2	z_2	WWR	Window position
1	Annual lighting Annual heating Annual cooling	18.89 22.08 28.03	23.0	0.1	0.6	2.2	3.2	32.8	Position: Left corner Shape: Vertical
2	Annual lighting Annual heating Annual cooling	18.89 22.08 28.03	23.0	2.1	0.6	4.2	3.2	32.8	Position: Right corner Shape: Vertical
3	Annual lighting Annual heating Annual cooling	19.59 22.66 26.83	23.01	0.1	1.1	3.2	2.7	29.8	Position: Right corner Shape: Vertical
4	Annual lighting Annual heating Annual cooling	16.11 19.35 35.48	23.6	1.1	0.1	4.2	2.7	48.4	Position: Centered Shape: Horizontal

The third case study (see Table 6-2) for the case of room located in the 29th floor, the best values of the objective functions are presented in Table 6-6. The best optimal configuration will be a window positioned at the center (1.1 m away from the edge) having around 30% WWR with horizontal configuration is selected.

Table 6-6: Best values of objective functions for a room at zone 10 and floor 29th

Optimal solution rank	Objective function	Optimal value (KWh/m^2)	$U(x)$	x_1	z_1	x_2	z_2	WWR	Window position
1	Annual lighting Annual heating Annual cooling	18.89 23.25 26.81	22.9	2.1	0.6	4.2	3.2	32.8	Position: Right corner Shape: Vertical
2	Annual lighting Annual heating Annual cooling	18.89 23.25 26.81	22.9	0.1	0.6	2.2	3.2	32.8	Position: Left corner Shape: Vertical
3	Annual lighting Annual heating Annual cooling	18.89 23.25 26.81	22.9	1.1	0.6	3.2	3.3	32.8	Position: Centered Shape: Vertical
4	Annual lighting Annual heating Annual cooling	19.59 23.83 25.64	23.1	0.1	0.1	3.2	1.7	29.8	Position: Right corner Shape: Horizontal
5	Annual lighting Annual heating Annual cooling	19.59 23.83 25.64	23.1	1.1	0.1	4.2	1.7	29.8	Position: Centered Shape: Horizontal

This study confirms that the outdoor microclimate and architectural design parameters are important factors in designing optimal window configurations, which has a significant influence on the building overall energy consumption. In the present case study, energy consumption is highly decreased while maintaining required illuminance by choosing optimal window configurations (as shown in Figure 6-18) according to the floor height and exposure to the wind.

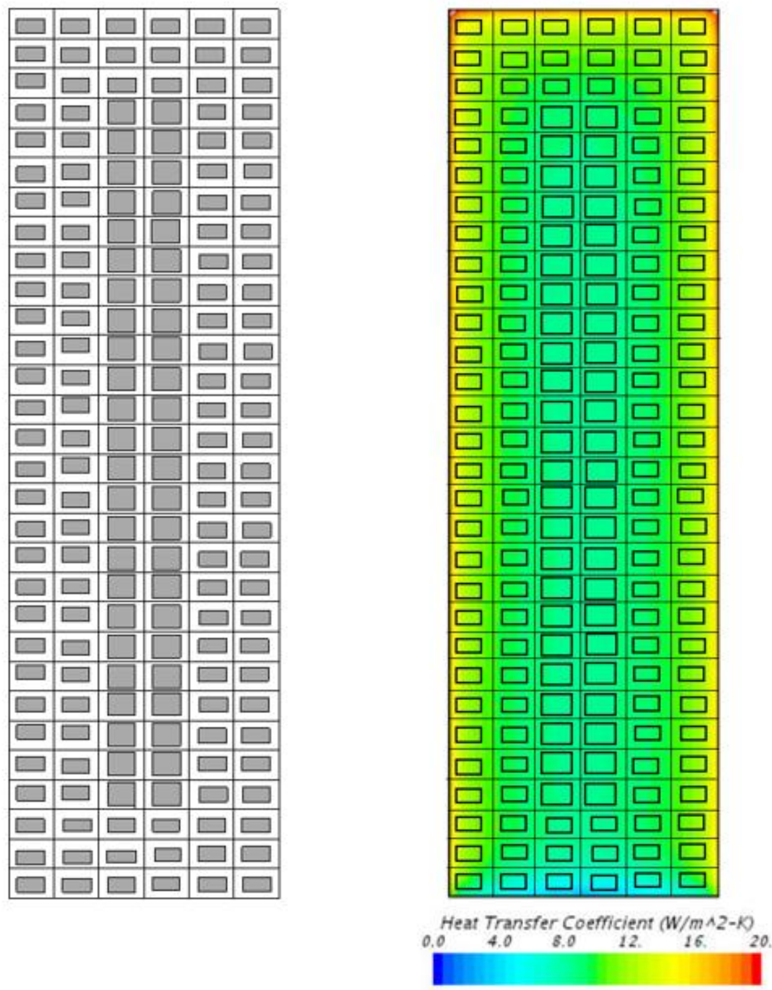

Figure 6-18: "Optimal" window configurations, 30% WWR around the corner & top and 48% WWR around the center of the building

Finally, a comparison between the optimal WWR and the baseline room model of having 100% WWR is performed. Thus, for the case of a window located in the 2nd, 15th, and 29th floor room of the high-rise building, a reduction of 31.7%, 26.1%, and 39.6%, respectively is observed on the annual energy consumption as shown in Table 6-7.

Table 6-7: Optimal value of objective function

Window floor height and location of room	Objective function	Baseline window (KWh/m^2)	Optimal window (KWh/m^2)	Diff. %
Floor 2 - center zone	Annual electric consumption	91.09	69.19	-31.7%
Floor 15 - center zone	Annual electric consumption	89.48	70.98	-26.1%
Floor 29 - corner zone	Annual electric consumption	96.42	69.08	-39.6%

6.6 Conclusion

A novel framework for simulation-based optimization of window configuration for a high-rise building is developed under opposing constraints of energy and comfort. This framework is applied on an isolated a 100 m case study high-rise building. Optimal window configurations for single room models located at different floors of the high-rise building located in Boston, MA, climatic condition is determined. The objective functions are to minimize the annual energy consumption for heating, cooling, and electric light. The decision parameters are window size and room location. The thermal comfort temperature set points and daylight illuminance are taken as constraints. In this multi-objective optimization, the optimum solutions were presented in the form of Pareto fronts to study the interaction between the objective functions and the window configurations. Finally, a weight-sum method is applied to obtain a single optimum solution. For the study case, for a rooms located in the center-zone at the second floor a 30% WWR, for room located in the center-zone of the fifteenth floor a 48%WWR, and for a room located in the corner-zone of the twentieth floor a 30% WWR is chosen.

In addition, an annual energy consumption comparison between the optimum window configuration and the base model of 100%WWR is performed. The study shows that a reduction more than, 32%, 26%, and 40% are obtained for rooms located on the 2nd, 15th, and 29th floor, respectively. From the case study, it is clear that the building height and window location affects the building lighting, heating, and cooling energy consumption. Overall, architectural details, window configuration parameters, and room location have a critical impact on the betterment of the building energy performance. Therefore, choosing an appropriate window configuration based on the convective heat transfer distribution on the façade can improve building energy performance significantly. Although in this study, only a smooth wall high-rise building is considered, other architectural elements such as external shadings have an effect of building energy performance. Further studies may be extended to analyze the effect of external shading on window optimization, thermal bridging, and internal surface condensation analysis. The optimization framework can also be applied to determine optimal window configurations for other building forms.

6.7 References

Caldas, L. G., & Norford, L. K. (2002). A design optimization tool based on a genetic algorithm. *Automation in construction*, *11*(2), 173-184.

Censor, Y. (1977). Pareto optimality in multiobjective problems. *Applied Mathematics and Optimization*, *4*(1), 41-59.

Dagnew, A. K., & Bitsuamlak, G. T. (2014). Computational evaluation of wind loads on a standard tall building using LES. *Wind and Structures*, *18*(5), 567-598.

Defraeye, T., Blocken, B., Carmeliet, J. (2010). "CFD analysis of convective heat transfer at the surfaces of a cube immersed in a turbulent boundary layer." Int. J Heat Mass Transf; 53:297–308.

Delgarm, N., Sajadi, B., Delgarm, S., & Kowsary, F. (2016). A novel approach for the simulation-based optimization of the building's energy consumption using NSGA-II: Case study in Iran. *Energy and Buildings*, *127*, 552-560.

DoE, U. S. (2016). Energyplus engineering reference. *The reference to energyplus calculations*.

Ellis, P. G., & Torcellini, P. A. (2005). Simulating tall buildings using EnergyPlus. In *International IBPSA conference* (pp. 279-286).

Engineering Sciences Data Unit (ESDU) 85020. (2001). Characteristics of atmospheric turbulence near the ground. Part II: Single point data for strong winds.

Franke, J., Hellsten, A., Schlünzen, H., Carissimo, B. (2007). Best practice guideline for the CFD simulation of flows in the urban environment COST 2007. Action 732.

Ghisi, E., & Tinker, J. A. (2005). An ideal window area concept for energy efficient integration of daylight and artificial light in buildings. *Building and environment*, *40*(1), 51-61.

Greenup, P. J., & Edmonds, I. R. (2004). Test room measurements and computer simulations of the micro-light guiding shade daylight redirecting device. *Solar Energy*, *76*(1), 99-109.

Holland, J. H. (1992). Genetic algorithms. *Scientific american*, *267*(1), 66-73.

Judkoff, R.; Neymark, J. (1995). Building Energy Simulation test (BESTEST) and diagnostic method. *NREL/TP-472-6231*. Golden, CO National Renewable Energy Lab.

Kahsay, M., Bitsuamlak, G., & Tarik, F., (2017). Numerical study of the effect of window configuration on the convective heat transfer rate of a window. CCBST 15th Canadian Conference on Building science and Technology.

Kahsay, M., Bitsuamlak, G., & Tarik, F., (2018). Numerical analysis of convective heat transfer coefficient for building facades. Journal of building physics.

Kahsay, M., Bitsuamlak, G., & Tarik, F., (2019). Effect of exterior convective heat transfer on high-rise building energy consumption.

Lee, J. W., Jung, H. J., Park, J. Y., Lee, J. B., & Yoon, Y. (2013). Optimization of building window system in Asian regions by analyzing solar heat gain and daylighting elements. *Renewable energy*, *50*, 522-531.

Liu, J., Heidarinejad, M., Gracik, S., & Srebric, J. (2015). The impact of exterior surface convective heat transfer coefficients on the building energy consumption in urban neighborhoods with different plan area densities. *Energy and Buildings*, *86*, 449-463.

Naboni, E., Zhang, Y., Maccarini, A., Hirsch, E., & Lezzi, D. (2013, January). Extending the use of parametric simulation in practice through a cloud based online service. In *IBPSA Italy-Conference of International Building Performance Simulation Association, Bozen, Italy*.

Nguyen, A. T., Reiter, S., & Rigo, P. (2014). A review on simulation-based optimization methods applied to building performance analysis. *Applied Energy*, *113*, 1043-1058.

Machairas, V., Tsangrassoulis, A., & Axarli, K. (2014). Algorithms for optimization of building design: A review. *Renewable and Sustainable Energy Reviews*, *31*, 101-112.

Marler, R. T., & Arora, J. S. (2004). Survey of multi-objective optimization methods for engineering. *Structural and multidisciplinary optimization*, *26*(6), 369-395.

Magnier, L., & Haghighat, F. (2010). Multiobjective optimization of building design using TRNSYS simulations, genetic algorithm, and Artificial Neural Network. *Building and Environment*, *45*(3), 739-746.

Meinders, E.R., Hanjalic, K., Martinuzzi R.J. (1999). “Experimental study of the local convection heat transfers from a wall mounted cube in turbulent channel flow.” Trans ASME J Heat Transf. 121:564–73.

Naboni, E., Zhang, Y., Maccarini, A., Hirsch, E., & Lezzi, D. (2013, January). Extending the use of parametric simulation in practice through a cloud based online service.

In *IBPSA Italy-Conference of International Building Performance Simulation Association, Bozen, Italy*.

Norris, N. E. I. L., Lawton, M., & Roppel, P. (2012, April). The concept of linear and point transmittance and its value in dealing with thermal bridges in building enclosures. In *Building enclosure science & technology conference*.

Ochoa, C. E., Aries, M. B., van Loenen, E. J., & Hensen, J. L. (2012). Considerations on design optimization criteria for windows providing low energy consumption and high visual comfort. *Applied Energy*, *95*, 238-245.

Parkinson, A. R., Balling, R., & Hedengren, J. D. (2013). Optimization methods for engineering design. *Brigham Young University*, *5*.

Rao, S. S. (2009). *Engineering optimization: theory and practice*. John Wiley & Sons.

Rapone, G. (2012). Optimisation of office building facades by means of genetic algorithms.

Richards, P. J., & Norris, S. E. (2011). Appropriate boundary conditions for computational wind engineering models revisited. *Journal of Wind Engineering and Industrial Aerodynamics*, *99*(4), 257-266.

Standard, A. S. H. R. A. E. (2010). ANSI/ASHRAE/IESNA Standard 90.1-2010. *Energy standard for buildings except low-rise residential buildings*.

SHARCNET is a consortium of colleges, universities, and research institutes operating a network of high-performance computer clusters across southwestern, central, and northern Ontario [Online]. Available: <www.sharcnet.ca>; 2015.

STAR CCM+. CD-ADAPCO product. (2015). www.cdadapco.com/products/star-ccm (accessed on Sep. 12, 2015)

Susorova, I., Tabibzadeh, M., Rahman, A., Clack, H. L., & Elnimeiri, M. (2013). *Energy and Buildings*, *57*, 6-13.

Tominaga, Y., Mochida, A., Yoshie, R., Kataoka, H., Nozu, T., Yoshikawa, M., Shirasawa, T. (2008). “AIJ guidelines for practical applications of CFD to pedestrian wind environment around buildings.” Journal of wind engineering and industrial aerodynamics, 96(10), 1749-1761.

Tzempelikos, A. (2005). *A methodology for integrated daylighting and thermal analysis of buildings* (Doctoral dissertation, Concordia University).

Wright, J., & Farmani, R. (2001, August). The simultaneous optimization of building fabric construction, HVAC system size, and the plant control strategy. In *Proceedings of the 7th IBPSA Conference: Building Simulation, Rio de Janeiro, Brazil* (Vol. 2, pp. 865-72).

Yi, Y. K., & Malkawi, A. M. (2009). Optimizing building form for energy performance based on hierarchical geometry relation. *Automation in Construction*, *18*(6), 825 833.

Zhang, Y. (2009). ‘Parallel’EnergyPlus and the development of a parametric analysis tool. In *11th Conference of International Building Performance Association (IBPSA), Glasgow, UK, July* (pp. 27-30).

Zhang, Y. (2012). Use jEPlus as an efficient building design optimisation tool. In *CIBSE ASHRAE Technical Symposium, London, Apr* (pp. 18-19).

Znouda, E., Ghrab-Morcos, N., & Hadj-Alouane, A. (2007). Optimization of Mediterranean building design using genetic algorithms. *Energy and Buildings*, *39*(2), 148-153.

Chapter 7

7 Conclusions and recommendations

7.1 Conclusions

This thesis introduces a new framework of simulation-based optimization of window configuration in buildings that combines Computational Fluid Dynamics (CFD) and heat transfer simulation, Building Energy Simulation (BES), and an optimizer algorithm. Intensive numerical analysis of wind-driven convective heat transfer from a building façade is performed. The numerical models are validated in comparison with experimental data from literature whenever applicable. Since the prediction accuracy of air flow and heat transfer in CFD depend on the accuracy of its boundary conditions, the emphasis is given in defining realistic microenvironment and geometrical boundary conditions. In the numerical analysis, a high-resolution of three-dimensional steady-state modeling with Reynolds-Averaged Navier-Stokes (RANS) simulation is used. To estimate the convective heat transfer coefficients (*CHTC)* accurately an *SST* κ-ω turbulence model closure is used. Detailed grid sensitivity analysis is also performed.

Detailed analysis of the aerodynamics (focusing on size) effects around five buildings with heights of 10.1 m, 33.7 m, 50.6 m, 67.4 m, and 100 m, respectively, and four different façade surfaces with and without- external shadings are investigated. The floor plan is adopted from the CAARC (Commonwealth Advisory Aeronautical Research Council) building which is a typical building used as a benchmark for various aerodynamics studies. The buildings are exposed to open terrain wind field conditions, having floor dimensions of 30 m width by 40 m in-depth and exposed to different local microclimate conditions (i.e. different cities) are considered.

Novel local-*CHTC* zoning is developed, motivated by the wind load zoning approach. New *CHTC*-U_{10} correlations for a building with-and without external shadings are developed. Futher, the impact of the existing-*CHTC* on building energy consumption is assessed by comparing with the newly developed *CHTC* correlations. The effect of different window configuration of the convective heat transfer of a window is investigated. Finally, a new simulation-based optimization framework of a window configuration is developed. As an application example, this framework is used to optimize a window configuration in a typical 100 m high building consistent with its local-*CHTC* distributions and aerodynamics effects around the buildings. Therefore, the proposed framework can be used for architects and designers to layout different window configuration with minimal energy consumption and maximum thermal and lighting comforts in a building.

7.2 Main contributions

The original contributions of the present study to scientific knowledge are presented below:

i. A CFD based procedural framework for an accurate analysis of convective heat transfer on building facades for a high-rise building is developed.

ii. A new approach to *CHTC*-zoning is introduced. This approach is used to understand the localized effect of convective heat transfer on buildings with glazed claddings. For example. the zoning information revealed zones of max and min convective heat loss regions that are useful among other things for optimizing window location, use of different R-values by the façade elements similar to use of different thickness glass for various pressure zones etc.

iii. A new surface average- and local- *CHTC*-U_{10} correlations are developed considering different building sizes, thus producing more accurate estimates that will enhance the energy consumption estimation by buildings.

iv. A new surface average- and local- *CHTC*-U_{10} correlations for high-rise buildings with and without external shading is developed. The effect of different external shading depths and forms on convective heat transfer of a building is also investigated. The benefits of architectural details such as egg crates are highlighted.

v. The impact of the existing-*CHTCs* on building energy performance is investigated and compared with new-*CHTC* developed using CFD.

vi. The effect of different window configurations on the convective heat transfer rate of a window is investigated for the first time. A detailed procedural framework for the analysis of convective heat transfer from the surface of a window is developed.

vii. A procedural framework for simulation-based optimization of window configuration in buildings is developed. This framework is also implemented in a typical high-rise building in a realistic environment. Different optimal window configurations are also proposed.

7.3 Recommendation for future work

The work presented in this thesis discusses several topics related to the effect of wind on building convective heat transfer and optimization of window configuration in a typical high-rise building. For the future development and improvement of the research, the following recommendations can be made:

i. Including urban topography effect and assessing their impact on building convective heat transfer is important to represent the realistic boundary conditions at the inlet.

ii. Large eddy simulation (LES) can be carried out to numerically investigate the unsteadiness characteristic of the flow around the building. This will improve the accuracy of the $CHTC\text{-}U_{10}$ correlations particularly around the lateral, top and leeward sides of the building.

iii. Extend the window configuration optimization process to include shading elements.

iv. Wind tunnel heat transfer experiments on building models of different heights with different architectural forms are highly recommended to analyze the wind effect around the corner sides of the building which are highly susceptible to loss of more energy and condensation effects.

Appendices

Appendix A

Governing equation

The governing equations, in CFD generally known as Navier-Stokes (N-S) equation consist of set of Partial Differential Equation (PDEs) includes: conservation of mass, conservation of momentum, and conservation of energy Equations A-1 – A-3.

$$\frac{\partial u_i}{\partial x_i} = 0 \qquad \text{Equation A-1}$$

$$\frac{\partial}{\partial x_j}\left(u_i u_j\right) = -\frac{1}{\rho}\frac{\partial p}{\partial x_i} + \frac{\partial}{\partial x_j}\vartheta\left(\frac{\partial u_i}{\partial x_j} + \frac{\partial u_j}{\partial x_i}\right) \qquad \text{Equation A-2}$$

$$\frac{\partial}{\partial x_j}\left(u_j T\right) = \frac{\partial}{\partial x_j}\left(\frac{k}{\rho C_p} + \frac{\partial T}{\partial x_j}\right) \qquad \text{Equation A-3}$$

where the vectors u_i and x_i are instantaneous velocity and position, p is instantaneous pressure, T is the instantaneous temperature, ρ is density, ϑ is the kinematic molecular viscosity, C_p is the specific heat capacity, and K is thermal conductivity. In this study, Reynolds-Average Navier-Stokes (RANS) equations with steady solver are employed to solve the fluid flow and energy equations.

Reynolds-Average Navier-Stokes

The basis for the RANS equation is the application of decomposition as the sum of a mean (ensemble-averaged or time averaged) and the fluctuating component as in Equation A-4:

$$u_i = \bar{u}_i + u_i' \qquad p = \bar{p} + p' \qquad T = \bar{T} + T' \qquad \text{Equation A-4}$$

where $\bar{u}_i$, $\bar{p}$, and $\bar{T}$ are mean values and u_i', p', and T' are the fluctuating components. By inserting Equation A-4 into Equation A1 -A3 and taking the ensemble average of the equations yields the RANS equations as shown in Equations A-5 – A-7.

$$\frac{\partial \bar{u}_i}{\partial x_i} = 0 \qquad \text{Equation A-5}$$

$$\frac{\partial}{\partial x_j}\left(\bar{u}_i \bar{u}_j\right) = -\frac{1}{\rho}\frac{\partial \bar{p}}{\partial x_i} + \frac{\partial}{\partial x_j}\vartheta\left(\frac{\partial \bar{u}_i}{\partial x_j} + \frac{\partial \bar{u}_j}{\partial x_i}\right) - \frac{\partial}{\partial x_j}\overline{\left(u_i' u_j'\right)} \qquad \text{Equation A-6}$$

$$\frac{\partial\left(\bar{T}\bar{u}_j\right)}{\partial x_j} = \frac{\partial}{\partial x_j}\left(\frac{k}{\rho C_p}\frac{\partial \bar{T}}{\partial x_j}\right) - \frac{\partial}{\partial x_j}\overline{\left(u_j' T'\right)} \qquad \text{Equation A-7}$$

In Equation A-6 the $\overline{\left(u_i' u_j'\right)}$ is called the Reynold stress (normal and shear stress) component and in Equation A-7 the $\overline{\left(u_j' T'\right)}$ is called turbulent heat flux. They represent the influence of turbulent in the mean flow and the heat transfer. The RANS equation does not form a closed set due to the presence of the Reynolds stress and turbulent heat fluxes which appear more unknowns than the equations and requires a closure or turbulence modeling.

Turbulence modeling

Generally, there are two types of modeling: First-order closure and Second-order closure. The first-order closure uses the Boussinesq eddy-viscosity hypothesis to relate the Reynolds stress to the velocity gradient in the mean flow by means of eddy-viscosity (ϑ_t), and the turbulent heat flux is to mean temperature gradients. The second-order closure or Reynolds stress modeling (RSM) refers to computing the Reynolds stress from their respective transport equation. Although RSM is more comprehensive, application in building simulation have not shown a consistent superiority as Boussinesq hypothesis approach (Ferziger 1997; Blocken, 2018). Thus, in this study the first-order closer which is expressed in terms of the turbulence eddy viscosity (ϑ_t) is used.

$$-\overline{u_i' u_j'} = \vartheta_t\left(\frac{\partial \bar{u}_i}{\partial x_j} + \frac{\partial \bar{u}_j}{\partial x_i}\right) - \frac{2}{3}k\delta_{ij} \qquad \text{Equation A-8}$$

$$\vartheta_t = \frac{\mu_t}{\rho} \qquad \text{Equation A-9}$$

The $(2/3)\ k\delta\_ij$ term is to insures that the normal stresses sum to $k = (3/2)u\_i\hat{}'2$

Where k is the turbulent kinetic energy associated with the fluctuations in the flow, μ_t is the dynamic viscosity, and δ_{ij} is the Kronecker delta:

$$k = \frac{1}{2}\overline{u_i' u_i'}$$ Equation A-10

$$\delta_{ij} = \begin{cases} 1 \text{ for } i = j \\ 0 \text{ for } i \neq j \end{cases}$$

Like the turbulent eddy viscosity, the turbulent heat flux $\overline{(u_j' T')}$ is expressed by means of turbulent heat diffusivity (K_T) which related to turbulent momentum diffusivity by the turbulent Prandtl number Pr_t.

$$\overline{u_j' T'} = K_T \frac{\partial \bar{T}}{\partial x_j}$$ Equation A-11

By analog with the molecular heat transfer to express the temperature gradients,

$$Pr = \frac{\mu C_p}{K} = \frac{\vartheta}{\alpha}$$ Equation A-12

$$Pr_t = \frac{\vartheta_t}{K_T}$$ Equation A-13

$$\overline{u_j' T'} = \frac{\vartheta_t}{Pr_t}\left(\frac{\partial \bar{T}}{\partial x_j}\right)$$ Equation A-14

where K_T, ϑ_t, and Pr_t are flow properties. In CFD the Pr_t is an assumed constant value between 0.7 to 1 which is an important for the simplification. Several turbulence models exist can model the turbulent eddy viscosity. In this study, the Shear Stress Transport (SST) $k - \omega$ turbulent model is mainly employed.

Shear Stress Transport (SST) $k - \omega$

This is a two-equation model presented by Menter (1994) which combines the original $k - \omega$ (Wilcox, 1988) model and the standard $k - \varepsilon$ model (Launder, 1974). A blending function, F_1, activates the Wilcox model near the wall in the viscous sub-layer and $k - \varepsilon$ model in the free stream.

$$\frac{\partial k}{\partial t} + u_i \frac{\partial k}{\partial x_i} = P_k - \beta^* k\omega + \frac{\partial}{\partial x_j}\left[(\vartheta + \sigma_k \vartheta_t)\frac{\partial k}{\partial x_j}\right]$$ Equation A-15

$$\frac{\partial \omega}{\partial t} + u_i \frac{\partial \omega}{\partial x_i} = \alpha S^2 - \beta\omega^2 + \frac{\partial}{\partial x_j}\left[(\vartheta + \sigma_\omega \vartheta_t)\frac{\partial \omega}{\partial x_j}\right] + 2(1 - F_1)\sigma_{\omega^2}\frac{1}{\omega}\frac{\partial k}{\partial x_i}\frac{\partial \omega}{\partial x_i}$$

Equation A-16

F_1 (Blending function)

$$F_1 = tanh\left\{\left\{min\left[max\left(\frac{\sqrt{k}}{\beta^*\omega y}, \frac{500\vartheta}{y^2\omega}\right), \frac{4\sigma_{\omega^2} k}{CD_{k\omega} y^2}\right]\right\}^4\right\}$$ Equation A-17

$$S = \frac{1}{2}\left(\frac{\partial \bar{u}_i}{\partial x_j} + \frac{\partial \bar{u}_j}{\partial x_i}\right)$$ Equation A-18

where P_k is the production limiter, k determines the energy in the turbulence, and ω determines the scale of turbulence (specific rate of dissipation of turbulent kinetic energy into thermal energy), and β^*=0.09, $\sigma_\omega = 2$, $\sigma_k = 2$, $\alpha = 5/9$, S is stress tensor.

$$\vartheta_t = \frac{k}{\omega} = \frac{\mu_t}{\rho} \quad \text{and} \quad \omega = C\frac{\varepsilon}{k}$$ Equation A-19

The unknown Reynolds stress tensor, $\overline{u_i' u_j'}$, is calculated from:

$$-\overline{u_i' u_j'} = \vartheta_t\left(\frac{\partial \bar{u}_i}{\partial x_j} + \frac{\partial \bar{u}_j}{\partial x_i}\right) - \frac{2}{3}\delta_{ij}\left(\rho k + \vartheta_t \frac{\partial \bar{u}_k}{\partial x_k}\right)$$ Equation A-20

Appendix B

Velocity and *CHTC* contour

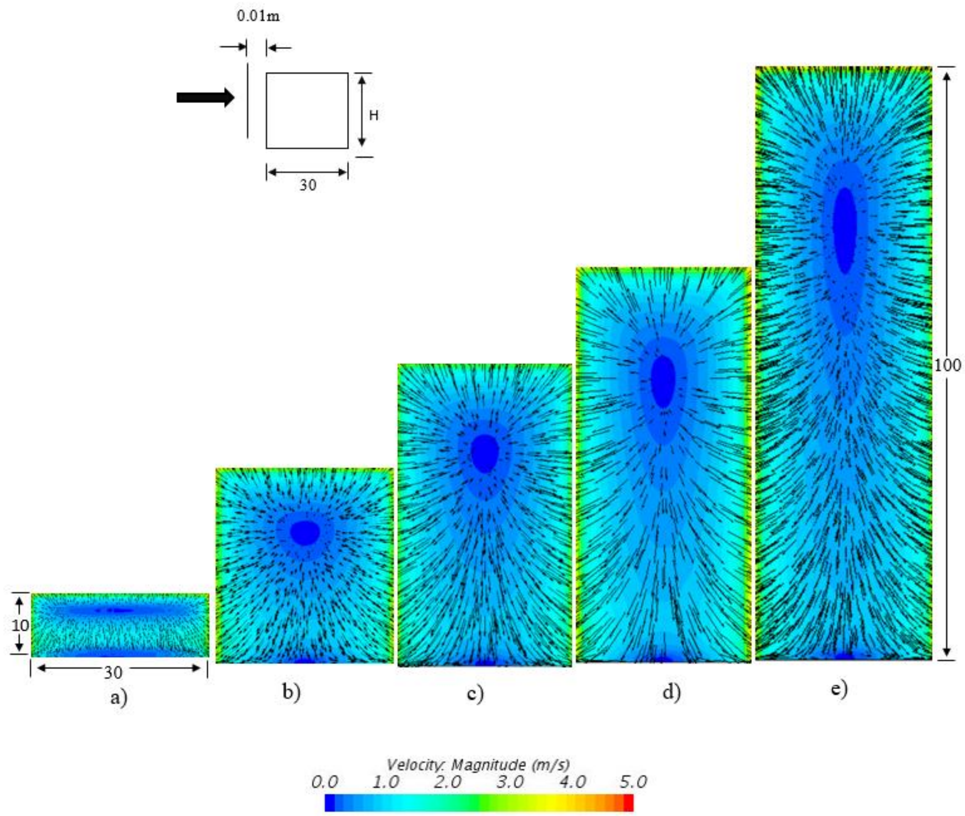

Figure B 1: Wind field vector and contour on a plane taken in front of the windward façade at 0.01 m from the wall of a building with height of a) 10.1 m, b) 33.7 m, c) 50.6 m, d) 67.4 m and e) 100 m heights (ref. wind speed of 3 m/s at the inlet)

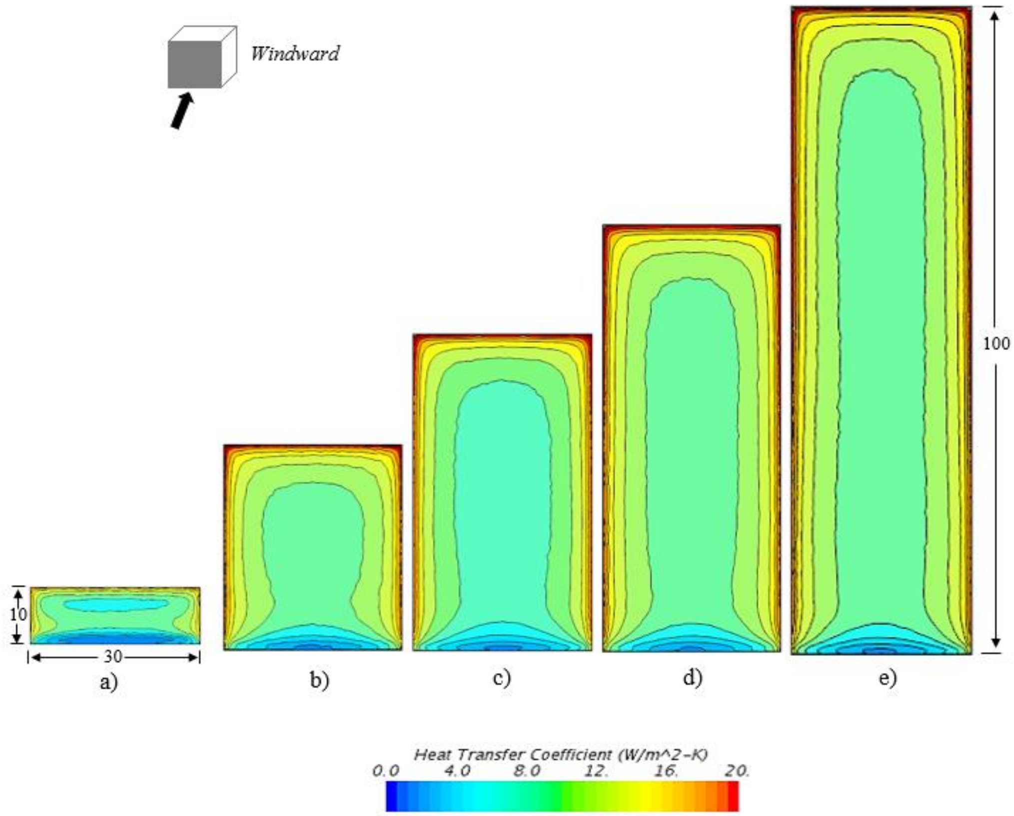

Figure B 2: Windward wall *CHTC* distribution (ref. wind speed of 3 m/s at the inlet) for building with a) 10.1 m, b) 33.7 m, c) 50.6 m, d) 67.4 m and e) 100 m heights

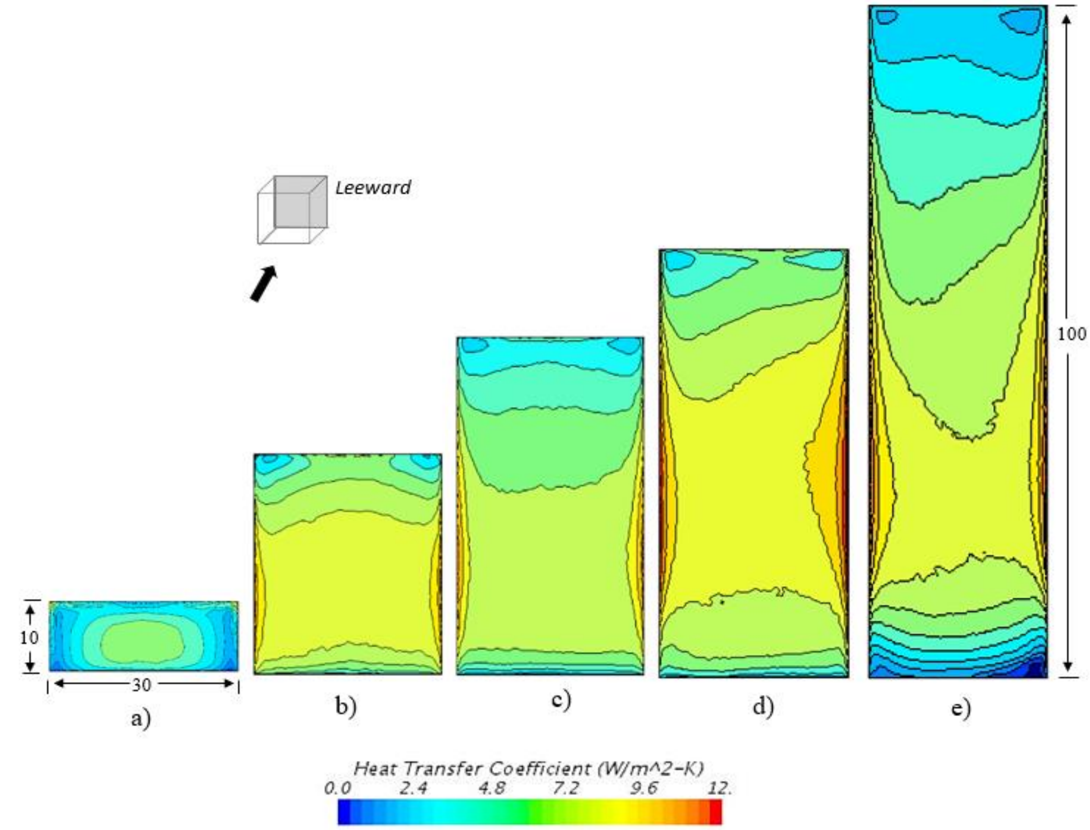

Figure B 3: Leeward wall *CHTC* distribution (ref. wind speed of 3 m/s at the inlet) for building with a) 10.1 m, b) 33.7 m, c) 50.6 m, d) 67.4 m and e) 100 m heights

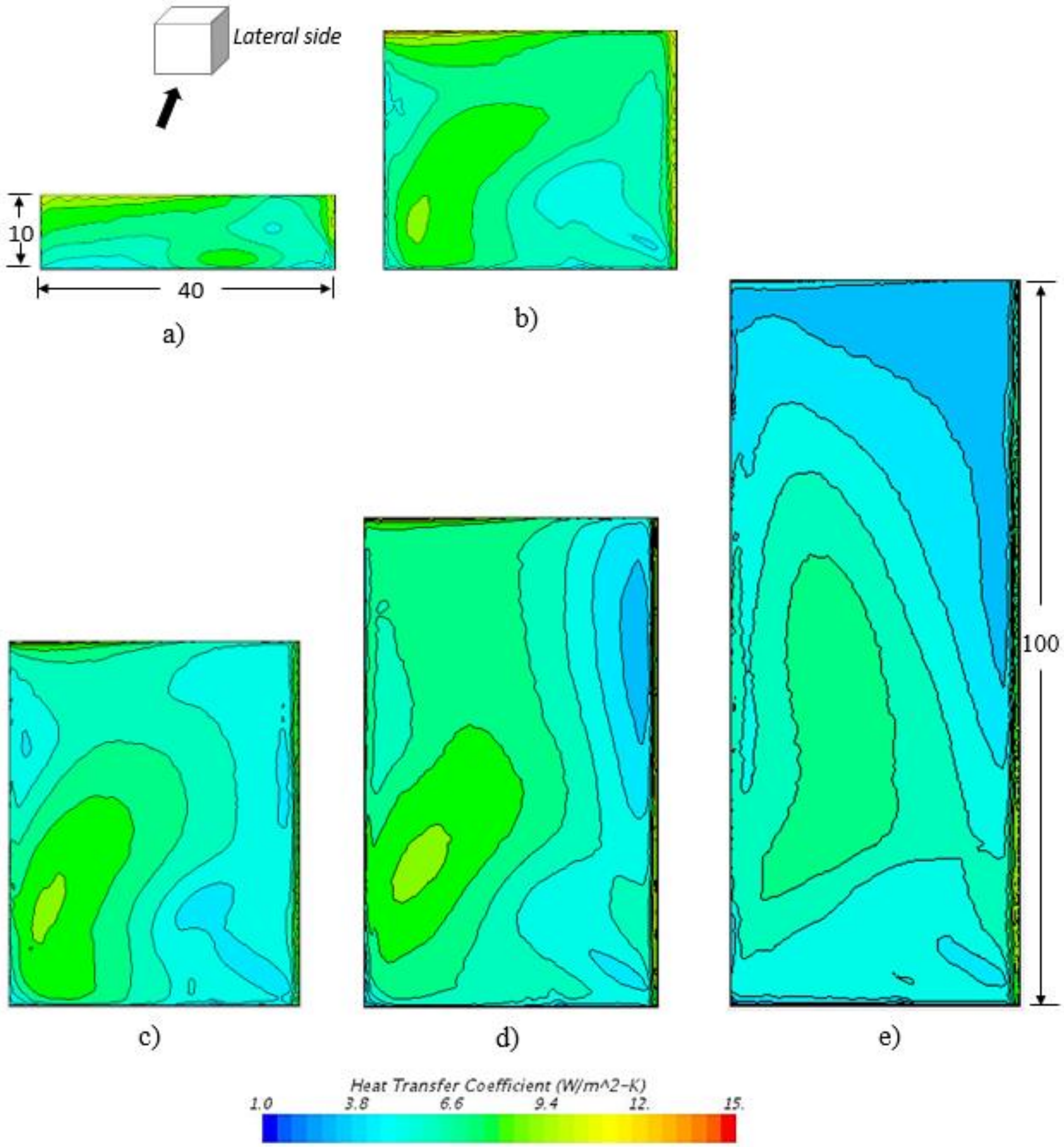

Figure B 4: Lateral sidewall *CHTC* distribution (ref. wind speed of 3 m/s at the inlet) for building with a) 10.1 m, b) 33.7 m, c) 50.6 m, d) 67.4 m and e) 100 m heights

Appendix C

CHTC-U₁₀ correlation with building height

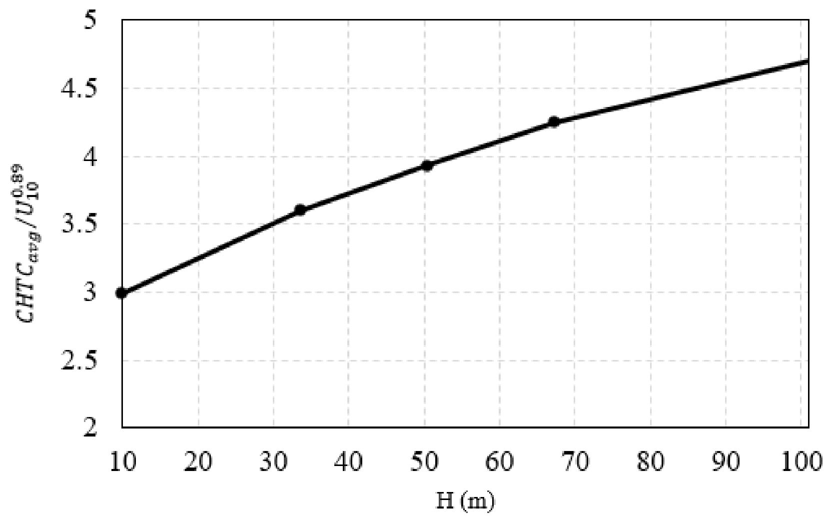

Figure C 1: Surface-averaged $CHTC_{\mathrm{avg}}/(\mathrm{U}_{10}^{0.89})$ correlation on the windward facade as a function of building height

Correlation between *CHTC* and U_z

The wind speed measured at a meteorological station can be extrapolated and transferred to another location using power law. Local wind speed U_z (at the building height) accounting for the different types of topography (ASHRAE, 2009) and altitude can be given with Equation C-1.

$$U_z = U_{10}\left(\frac{Z_{g-met}}{Z_{met}}\right)^{\alpha_1}\left(\frac{Z}{Z_g}\right)^{\alpha_2} \qquad \text{Equation C-1}$$

where U_z is wind speed at altitude z above the grade, U_{10} is wind speed at 10 m from the ground at the meteorological station, Z_{g-met} is the boundary layer thickness at the meteorological station, z_{met}, height above ground of the wind speed sensor, and α_1, wind speed profile exponent at the meteorological station, z is height above ground of the wind at the building site, z_g is wind speed profile boundary layer thickness at the building site, α_2,wind speed profile exponent at the site. The wind speed profile coefficients α_1, z_{g-met} , α_2, and z_g are variables that depend on the roughness characteristics of the surrounding terrain. The typical values of α range from 0.14 for the flat and the open country to 0.33 for towns and cities, while the values for z_g range from 270 m to 460 m for open and urban terrain types, respectively. The coefficient that connect the local wind speed and the reference wind speed obtained from meteorological station due extrapolations is calculated and summarized in Table B-1. Accordingly, Figure B-5 shows surface-averaged $CHTC/U_z^{0.89}$ as a function of building height H. While comparing Figure B-5 with Figure B-6, it is clear that the main reason that the *CHTC* changes with height of the building is the change in ref. velocity itself. But removing that effect of velocity as shown in Figure B-6 still indicate the impact of the building height on the *CHTC* coefficient albeit in a reduced scale.

Table C 1: Coefficient for conversion

	Building height (m)				
$\frac{U_z}{U_{10}}$	10.1m	33.7 m	50.6 m	67.4 m	101.1 m
	1	1.18	1.25	1.30	1.38

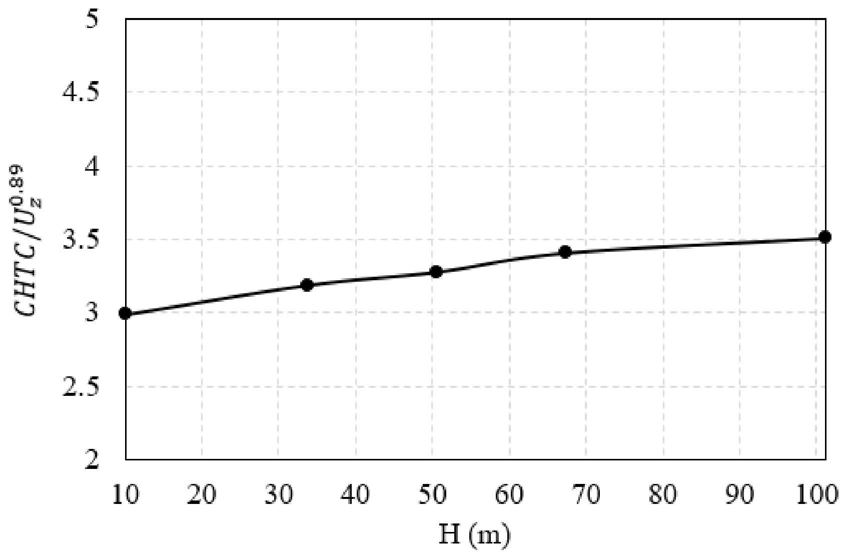

Figure C 2: Surface-averaged $CHTC_{avg}/(U_z^{0.89})$ correlation on the windward facade as a function of building height

References

ASHRAE. (2009). Fundamentals, SI ed. *American Society of Heating, Refrigerating and Air Conditioning Engineers: Atlanta, GA, USA.*

Blocken, B. (2018, October). LES over RANS in building simulation for outdoor and indoor applications: a foregone conclusion? In *Building Simulation* (Vol. 11, No. 5, pp. 821-870). Tsinghua University Press.

Ferziger, J. H. (1997). Large eddy simulation: an introduction and perspective. In *New tools in turbulence modelling* (pp. 29-47). Springer, Berlin, Heidelberg.

Launder, Brian Edward, and Dudley Brian Spalding. (1974). "The numerical computation of turbulent flows." *Computer methods in applied mechanics and engineering* 3, no. 2: 269-289.

Curriculum Vitae

Name:	Meseret Tesfay Kahsay
Post-secondary Education and Degrees:	**Western University** London, Ontario, Canada 2014 – 2019 Doctor of Philosophy Civil and Environmental Engineering
	Indian Institute of Technology Bombay (IITB) Mumbai, India 2008 – 2010 Master of Technology Thermal and Fluid Engineering
	Mekelle University Mekelle, Tigray, Ethiopia 2002 -2006 Bachelor of Science Mechanical Engineering
Honor and Awards	Western Engineering Scholarship Ontario Center of Excellence through Early Career Award and SOSCIP grants 2014 – 2019
Related works	Research and Teaching Assistant Western University 2014- 2019
	Lecturer and Research Assistant Mekelle University 2006 - 2013

Publications:

Journal Articles

i. Kahsay, M., Bitsuamlak, G., & Tarik, F., (2019). CFD simulation of external convective heat transfer coefficient effect on high-rise buildings with and without external shadings. *Building and Environment* (*accepted with revision*).

ii. Kahsay, M., Bitsuamlak, G., & Tarik, F., (2018). Numerical analysis of convective heat transfer coefficient for building facades. Published in the *Journal of Building Physics*. *https://doi.org/10.1177/1744259118791207*

iii. Kahsay, M., Bitsuamlak, G., & Tarik, F., (2018). The effect of building geometry on its convective heat transfer rate. *Journal of Wind Engineering and Industrial Aerodynamics*, special issue (*submitted*).

iv. Kahsay, M., Bitsuamlak, G., & Tarik, F., (2018). Effect of exterior convective heat transfer on high-rise building energy consumption. *Building Simulation* (*accepted with revision*).

Conference papers

i. Kahsay, M., Bitsuamlak, G., & Tariku, F., (2018). Influence of external shading on convective heat transfer of high-rise buildings. *Building Performance Analysis Conference and Sim-Build co-organized by ASHRAE and IBPSA-USA Chicago, IL September 26-28, 2018.*

ii. Kahsay, M., Bitsuamlak, G., & Tariku, F., (2018). Effect of building geometry on convective heat transfer rate. *The 7th International Symposium on Computational Wind Engineering 2018. June 18-22, 2018 in Seoul, Republic of Korea.*

iii. Kahsay, M., Bitsuamlak, G., & Tariku, F., (2017). Numerical study of the effect of window configuration on the convective heat transfer rate of a window. *15th Canadian Conference on Building Science and Technology.November 1-8, 2017 in Vancouver.*

iv. Kahsay, M., Bitsuamlak, G., & Tariku, F. (2017). Numerical Simulation of Forced Convective Heat Transfer Coefficients on the Facade of Low-and High-Rise Buildings. In *AEI, 2017* (pp. 266-278) *Oklahoma.*